Title

Effects of Tin Dispersed on Dealuminated BEA Zeolite on the Activity of Platinum for the Dehydrogenation of Propane

Author

Lefton, Natalie Grace

Publication Date

2023

Peer reviewed|Thesis/dissertation

Effects of Tin Dispersed on Dealuminated BEA Zeolite on the Activity of Platinum for the Dehydrogenation of Propane

By

Natalie Grace Lefton

A dissertation submitted in partial satisfaction of the

requirements for the degree of

Doctor of Philosophy

in

Chemical Engineering

in the

Graduate Division

of the

University of California, Berkeley

Committee in charge:

Professor Alexis T. Bell, Chair
Professor Alexander Katz
Professor T. Don Tilley

Fall 2023

Effects of Tin Dispersed on Dealuminated BEA Zeolite on the Activity of Platinum for the Dehydrogenation of Propane

Abstract

Effects of Tin Dispersed on Dealuminated BEA Zeolite on the Activity of Platinum for the Dehydrogenation of Propane

by

Natalie Grace Lefton

Doctor of Philosophy in Chemical Engineering

University of California, Berkeley

Professor Alexis T. Bell, Chair

The increasing demand for propene exceeds the capacity for its production by petroleum cracking and steam reforming of naphtha, creating what is called a "propene gap." This gap can be filled by the direct dehydrogenation of propane derived from the condensable fraction of natural gas produced by the fracking of shale. Prior research has demonstrated that supported Pt nanoparticles are quite effective for propane dehydrogenation (PDH) but readily poison due to coking. The rate of this process can be reduced by reducing the size of the Pt nanoparticles and alloying Pt with a non-noble metal such as Sn, Zn, Fe, etc. A further loss of activity with time on stream occurs due to particle agglomeration. This process can be impeded by anchoring Pt nanoparticles using a non-noble metal that is incorporated in the support and interacts strongly with Pt. This thesis explores the possibility of introducing Sn into the silanol nests of dealuminated BEA zeolites to produce Sn/DeAlBEA and then dispersing Pt onto this support to produce PtSn/DeAlBEA. Characterization of these materials by XRD, UV-vis spectroscopy, XANES, EXAFS, and IR spectroscopy of adsorbed pyridine, deuterated acetonitrile, and CO was used to develop a detailed understanding of the structures of Sn/DeAlBEA and PtSn/DeAlBEA. This information aided the interpretation of the effects of catalyst composition and structure on the performance of PtSn/DeAlBEA catalysts for PDH.

Chapter 2 provides a critical review of the literature on the use of infrared spectroscopy (IR) of adsorbed carbon monoxide (CO) to characterize supported Pt. It is noted that the position of IR bands for adsorbed CO can depend on CO surface coverage, support identity, Pt oxidation state and dispersion, and the identity of additives or promoters (e.g., Sn, Na, K, etc.). Increases in CO coverage result in increases in the frequency of adsorbed CO due to dipole-dipole interactions of neighboring adsorbates. Increases in Pt electron density (e.g., more negative Pt oxidation state, electron-donating promoters, less reducible supports, decreasing Pt particle size) result in decreases in the frequency of adsorbed CO. These trends are supported experimentally and theoretically. Deconvoluting the interactions of multiple effects is limited to a case-by-case basis. The compounding nature of these effects makes determining Pt structure based on the frequency of adsorbed CO alone very difficult, if not impossible. Notably, PtSn catalysts have been shown to exhibit both blue- and red-shifted IR frequencies of adsorbed CO relative to Pt alone. Therefore, while trends in the IR spectrum with increasing Pt/Sn ratio at a fixed Sn/Al ratio are informative, definitive statements based on this information are not possible.

Chapter 3 discusses the difficulties of using XAS to characterize PtSn/DeAlBEA because this material contains multiple Sn and Pt environments. The XANES portion of the XAS provides average oxidation states for Sn and Pt, whereas analyses of the EXAFS portion of the data can only provide average coordination numbers and backscattering distances between nearest neighbor atoms (e.g., Sn-Sn, Sn-O, Pt-Pt, Pt-Sn, Pt-O). Thus, the most effective use of XAS data is to reveal systematic changes in the oxidation state and environment as the loading of Sn and Pt in Sn/DeAlBEA and PtSn/DeAlBEA change.

Chapter 4 discusses the preparation and characterization of Sn/DeAlBEA and their PDH activity. XRD and UV-vis spectroscopy reveal the formation of SnO_2 for Sn/Al ratios above 0.36. Below this ratio, analysis of XAS data demonstrates that Sn/DeAlBEA contains four-coordinated Sn(IV) cations located in the BEA framework. Evidence for this species was confirmed by UV-vis spectroscopy and IR spectroscopy of adsorbed deuterated acetonitrile. The most effective means for introducing framework Sn(IV) sites is wetness impregnation with an ethanol solution of $SnCl_2 \bullet 2H_2O$. Sn/DeAlBEA was tested for its PDH activity. Sn/DeAlBEA exhibits stable activity and decent propene selectivity (>95%). The PDH activity per Sn atom increases as the Sn/Al ratio increases. Notably, the PDH activity of Sn/DeAlBEA is significantly lower than that of SnO_x/SiO_2 for the same Sn/nm^2 loading. This suggests that open ≡Sn-OH sites are more active for PDH than closed Sn(IV) sites. However, the PDH activity of Sn/DeAlBEA is low relative to that of PtSn/DeAlBEA.

Chapter 5 investigates the structure and PDH activities of PtSn/DeAlBEA catalysts as a function of the Pt/Al ratio. PtSn/DeAlBEA catalysts were prepared with a range of Pt/Al ratios (0.001-0.026) via wetness impregnation. These catalysts are characterized with IR of adsorbed probe molecules and XAS to understand the effect of changing Pt loading on the structure of Pt in PtSn/DeAlBEA. Pt dispersion on DeAlBEA produces Pt nanoparticles with an average Pt-Pt coordination number of 9 for Pt/Al ratios of 0.001. By contrast, dispersion of Pt on Sn/DeAlBEA (Sn/Al = 0.15) produces Pt oligomers with an average Pt-Pt coordination number of 3 for Pt/Al = 0.001, but for Pt/Al ratios > 0.013 Pt nanoparticles form which have a Pt-Pt coordination number of 9. This trend is confirmed by IR spectroscopy of adsorbed CO. PtSn/DeAlBEA exhibits high selectivity to propene (> 97%) and high dehydrogenation rates. Forward rate constants were calculated and compared to values determined and compared to values for various Pt and PtSn catalysts reported in the literature. PtSn/DeAlBEA exhibit significantly higher forward rate constants than previously reported for Pt and PtSn catalysts. The kinetics of PDH were measured for three PtSn/DeAlBEA catalysts with different Pt/Al ratios but identical Sn/Al ratios. In all cases, the kinetics are described by a Langmuir-Hinshelwood rate expression, which is first-order in propane and is inhibited by propane adsorption. The similarity of the apparent activation energies and enthalpies of propane adsorption for all three catalysts suggests that the active species are very small Pt_3Sn clusters tightly associated with the framework of DeAlBEA.

Dedication

To my family, who have always supported, encouraged, and believed in me.

Table of Contents

List of Figures

List of Tables

Acknowledgments

First, I want to thank my advisor, Prof. Alexis T. Bell. Over the last five years, Professor Bell has helped me tackle tough experimental and technical questions. I appreciate your attention to detail and patience every step of the way.

I would also like to thank all the members of the Bell Choir for the scientific and personal support they provided throughout my PhD. Danna Nozik – thank you for all your help in experimental training. Your meticulous methods have no doubt made me a better researcher. Neelay Phadke, thank you for providing a well-maintained experimental set-up and rigorous characterization and kinetic study to build my work. Julie Rorrer and Chris Ho – thank you for taking the time to answer stupid questions and explain how experiments work. Branden – thank you for all your experimental and theoretical help over the years, especially for always refilling the glovebox liquid N_2. Paul – thank you for all your efforts to keep the lab clean and functioning. Afnan – thank you for working through complex experimental challenges with me and being willing to discuss them together. Julie Fornaciari and Oyin Romiluyi – thank you for encouraging me and helping me through the PhD milestones, particularly qualifying exams. Liang Qi and Yanfei Zhang – thank you for all your assistance with experimental directions and discussions. Christianna – thank you for reminding me to take a step back. Henry Chen – thank you for bringing a fresh perspective and enthusiasm to the lab, for questioning, and for improving procedures.

I want to thank collaborators in the College of Chemistry, who reminded me that science extends far beyond my research project – Chao Chao, Raynald, Yaprak, Adrian, RJ.

I want to acknowledge the teachers and research mentors who have led me to this degree: Dr. Ali Mehdad, Dr. Young Jin Kim, Prof. Raul Lobo, Lisa Weist, Prof. Carsten Sievers, and Debra LeDoux.

I would also like to thank the friends I have lived with throughout my PhD. Ana Carneiro, Samantha Crowe, Emily Carvalho, and Monica Gurung – thank you for giving me a space to unwind and relax away from work. Our roommate dinners were always a source of respite in sometimes stressful and overwhelming weeks.

I also need to thank all my friends in the department who supported and encouraged me personally; a non-exhaustive list: Johnny Petrovick, Zach Konz, Zach Hoffman, Clay Batton, Eric Taw, Neel Shah, Doug Millar, Nick Oussail, Alison Lui, David Brown, Sarah Yang, Natalie Goh, Kara Fong. I would also like to thank the entire Class of 2018 for providing a community, especially as I started my PhD. I particularly would like to thank folks who organized and supported our efforts to unionize graduate student researchers – Takashi, Hailey, Abraham, Pedro, Josh, Tarini, and Helen.

I want to thank the Graduate Women in Engineering and all its members for providing context and community outside the department. I'd especially like to thank my co-chairs, Mahek Logantha and Natalie Goh.

I would also like to thank BASIS, particularly Tyler Chuck, Julie Rorrer, Julie Fornaciari, and Ana Carneiro, for facilitating science education and outreach. BASIS lessons continue to be some of my favorite memories of graduate school.

I want to thank the book clubs and reading groups I joined for reminding me about non-academic writing. Thank you, Luis, Sarah, Ana, Selin, Darby, Rafaela, Ashley, Johnny, Neel, Zach, and Sam, for providing accountability for reading for pleasure.

Thank you to all the friends who supported me and encouraged me regardless of how far apart we were – Kathy Zhang, Brooke Beatty, Joy Armstrong, Rebecca McCord, Drew Vidovich, Kellie Heom, Anelia Moore, Mary Adams, Lily Powell, Isabel Newsome, Lollie Newsome, Lizbeth Herger, Lexi Ritter, and Bella Reiss. Thank you for the calls, visits, and notes and for providing positive perspectives.

I would not be here without my family. Thank you to everyone for supporting me throughout this journey. I especially want to thank my sisters and parents – Monica Lefton, Hannah Lefton, Lew Lefton, and Enid Steinbart.

Lastly, I acknowledge that the University of California, Berkeley, where most of this research was performed, operates on Huichin, the unceded lands of the Ohlone people. Additional experiments were performed at SSRL on the ancestral land of the Muwekma Ohlone Tribe and at Argonne National Lab, which sits on the ancestral lands of the Bodwéwadmi (Potawatomi), Očhéthi Šakówiŋ, Myaamia, Kaskaskia, Kiikaapoi (Kickapoo), and Peoria Nations.

1 Introduction

1.1 Propane Dehydrogenation Motivation

Olefins are essential building blocks for bulk chemical production. Specifically, propene is a necessary precursor in the production of many high-demand chemicals, including polypropylene, acrylonitrile, and propylene oxide.[1] Historically, olefins (ethene, propene, butenes) have been produced as a by-product of steam cracking and fluidized catalytic cracking (FCC) of naphtha and, more recently, ethane.[2] Propene demand has continued to increase with time, compelling the development of novel pathways for its production.[3] Light alkane (methane, ethane, propane) production has recently increased due to increased shale gas production through hydraulic fracturing.[4] Light alkanes can be upgraded to olefins and further to aromatics (benzene, toluene, xylene) through dehydrogenation and dehydroaromatization processes, respectively. Therefore, increasing propene demand and growing propane production from shale gas support the direct dehydrogenation of propane to propene (PDH).[5] The endothermicity of PDH ($\Delta H = 124$ kJ mol^{-1}) results in equilibrium limitations at low temperatures and high partial pressures of propane. Often, PDH reactions are performed at high temperatures (> 773 K) and atmospheric pressures to avoid these thermodynamic limitations.

1.2 Pt and PtSn Catalysts for Propane Dehydrogenation

Supported Pt materials were identified as a dehydrogenation catalyst almost 100 years ago.[6] Since then, Pt catalysts have continued to be widely studied for PDH.[5,7–14] Pt- and Cr-based catalysts have achieved commercialization, but the toxicity of chromium oxide motivates the further investigation of Pt catalysts for PDH.[3,7] Recent research work has focused on identifying which factors affect the activity, selectivity, and stability of Pt catalysts for PDH. Highly dispersed Pt exhibits high activity for PDH,[15] and these smaller Pt domains exhibit less coking.[16] Unfortunately, even with high dispersion, supported Pt domains still deactivate during PDH.[17–19]

The introduction of Lewis acids (i.e., Sn, Zn, etc.) to disperse Pt produces better stability than Pt alone.[20,21] The addition of Sn results in more isolated Pt domains, decreasing coking rates and increasing PDH activity.[16,22–26] While the positive influence of Sn is relatively well-known, the proposed effect on Pt structure varies. Many different active sites have been proposed for these catalysts, including single Pt atoms, small Pt clusters, and PtSn bimetallic clusters.

The support also has a significant impact on the resulting Pt structure and PDH behavior. Brønsted acid sites on the support can catalyze propane cracking to form ethene and methane during PDH.[27] This undesired cracking activity can be reduced or eliminated by introducing metal sites via ion exchange with Brønsted acidic protons or by removing these acid sites altogether. Specifically, dealuminated BEA (DeAlBEA) has shown promise as a relatively well-defined siliceous support.[28–30] The removal of aluminum from the zeolite framework creates four terminal silanol groups in close proximity, known as a silanol nest. The silanol nests of DeAlBEA offer stable sites for anchoring Lewis acids (i.e., Zn, Sn), which, in turn, effectively disperse Pt, creating catalysts with increased Pt activity and selectivity to propene.[20,21,31,32]

While PtSn catalysts have shown promising activity and stability for PDH, rigorous characterization of dispersed Pt sites and thorough kinetic studies are lacking. Comparison of these many different studies is also difficult as each study chooses its own conditions (e.g., temperature, pressure, space velocity). Additionally, the impact of the Pt/Sn ratio on the Pt structure and resulting PDH activity has not been widely studied.

1.3 Supported Sn Catalysts for Propane Dehydrogenation

Although Sn catalysts are most often employed for sugar isomerization and other biomass conversion reactions,[33–35] recent studies have demonstrated that Sn supported on silica has considerable activity for propane dehydrogenation.[36–41] Several Sn active sites for PDH have been proposed, including Sn^{2+}-O-Si species, metallic Sn, and small Sn oxide domains. The characterization evidence for these sites remains relatively weak, lacking operando and post-reaction studies. Additionally, powerful techniques to investigate the Sn environment, like ^{119}Sn NMR and XAS, have not been applied to these catalysts despite their widespread use with other Sn catalysts.[42,43] The lack of thorough studies of Sn catalysts for alkane dehydrogenation and the promising stability reported for Sn on silica makes Sn catalysts interesting candidates for further research. Relative to PtSn/DeAlBEA, Sn/DeAlBEA exhibits lower propane dehydrogenation activity and similar selectivity to propene.[32]

1.4 Spectroscopic Characterization of Heterogenous Catalysts

Characterization of Pt-based PDH catalysts is crucial to establishing active site structures and comparing different types of catalysts. IR of adsorbed CO probes the electronic state of the metal site and is particularly widely used for Pt sites.[44–48] Evidence of metal structures from additional characterization is also useful for this process, as the Pt structure cannot be determined from IR of adsorbed CO alone.[49,50] X-ray absorption spectroscopy (XAS) offers an element-specific bulk analysis of the materials of interest.[51] The fine structure region of the XAS spectrum provides coordination numbers and bond distances, and the near-edge region provides information about the oxidation state and coordination environment. IR of adsorbed CO and XAS have been employed to identify the oxidation state of Pt in Pt and PtSn materials and interactions between Pt and Sn.[31,52–55]

In this thesis, Sn/DeAlBEA and PtSn/DeAlBEA catalysts for PDH are studied. Chapters 2 and 3 summarize the advantages and limitations of characterizing Pt- and PtSn-supported materials with IR of adsorbed CO and XAS, respectively. Chapter 4 investigates the structure and PDH activity of Sn/DeAlBEA materials. In Chapter 5, the nature of Pt sites in PtSn/DeAlBEA is examined for a range of Pt/Sn ratios, and the activity and kinetics of PDH over PtSn/DeAlBEA are measured. Specifically, the effects of the Pt/Sn ratio on Pt structure and the PDH activity and selectivity are investigated.

2 Effectiveness of Infrared Spectroscopy of Adsorbed CO as a Probe for Pt Environment

2.1 Introduction

Infrared spectroscopy (IR) of adsorbed carbon monoxide (CO) is a useful probe for identifying the electronic environment of many metals, including platinum. IR spectroscopy of adsorbed CO has an advantage over other characterization techniques, including X-ray absorption spectroscopy (XAS), in that it is specific to individual sites. This property allows adsorbed CO to probe many unique Pt sites simultaneously instead of providing an average of all Pt environments.

While CO is a widespread IR probe for characterizing platinum catalysts, it is well known that the speciation of Pt cannot be unambiguously determined with this technique alone.[49,50] The experimental observable is the frequency of adsorbed C-O stretch. Several factors can change the C-O stretching frequency, including the electronic environment of Pt and the CO surface coverage.[56] Pt electronic environment can be affected by the dispersion of Pt, Pt oxidation state, interactions with the other elements (e.g., Sn, K, Ce), and the support properties. CO surface coverage is a function of CO partial pressure, temperature, the time elapsed from dose, and the adsorption site identity. It is imperative to discern each of these effects in order to accurately interpret the IR frequency of CO adsorbed on Pt.

Many reviews on Pt catalysts[10,13,14,57,58] and IR of adsorbed CO over various metals[46,59–63] have been published; yet, a systematic examination of how these factors specifically influence the IR frequency of adsorbed CO is still lacking. Because the factors listed above are often changed simultaneously between different types of platinum catalysts and between reported literature studies, it is essential to consider each effect individually. In this chapter, we will review the influence of these parameters on CO frequency shift and investigate the effectiveness of IR of adsorbed CO as a probe for the Pt environment.

2.2 CO Bonding Models

Theoretical models of CO bonding to various transition metals have been developed; however, we will restrict the discussion to the bonding of CO to Pt. The Dewar-Chatt Duncanson (DCD) model was introduced to explain the adsorption of C_2H_4 on Pt,[64] but was subsequently used to describe CO absorption.[65–67] In the DCD model, electrons are donated from the 5σ orbital of CO to the unoccupied d_{z^2} orbital of the metal, and electrons are back-donated from the occupied d_{xz} orbitals of the metal to the 2π* orbital of CO.[68] Both electron donations strengthen the M-C bond; the σ donation strengthens the C-O bond (removes electrons from the antibonding 5σ CO orbital), while the π electron back-donation weakens it (adds electrons to antibonding 2π* CO orbital). The DCD model explains the redshift observed upon CO adsorption but fails to describe materials that exhibit blue shifts in CO frequency upon absorption.[68]

In 1964, Blyholder proposed a molecular orbital bonding model for CO adsorbed on metal sites.[69,70] In the Blyholder model, an M-C σ bond is formed between a metal d-orbital and a lone pair in an sp^2-hybrid orbital on the carbon. The CO σ orbitals are assumed to be the same as in the unbound CO. This model also includes a π system formed by the interaction of the C and O 2p orbitals and the d orbital of the metal. Mixing these three orbitals results in three new π molecular orbitals between the metal and CO: one bonding, one non-bonding, and one antibonding (2π*). The more electron-rich metal contributes more electron density to the 2π* orbitals of the CO, resulting in a lower CO stretching frequency; as the M-C bonding interaction strengthens, the C-O bond weakens, so the CO frequency also decreases. The Blyholder model has been found to be consistent with experimental IR observations for CO adsorbed on silica-supported Pt[71] and

theoretical, ab initio modeling for CO adsorbed on a Pt(111) system.[72] Notably, many studies have also applied the Blyholder model incorrectly, considering only 2π* interaction but not the entire hybridized π system.[73–76] Additionally, the full Blyholder model has been criticized for not accounting for the substantial observed σ orbital mixing or the σ repulsion.[77–81]

To address these concerns, Nilsson and Peterson provided an updated theoretical model of CO bonding that considers orbital hybridization and mixing, which is referred to as the Blyholder-Nilsson-Peterson (BNP) Model.[82–85] The orbital diagrams for the CO π and σ systems are shown in Figure 2.1. The π system of the BNP model has the same allylic configuration as the Blyholder and DCD models, but hybridization of the σ orbitals is also considered. The σ system hybridization also results in three orbitals: two bonding (4σ and 5σ, closely resembling CO MO's) and one antibonding (d_σ, more closely resembling metal, d orbital). Since the Pt d-bands are highly occupied, the σ system involves mostly occupied orbitals, resulting in the electron occupation of antibonding orbitals. The result is no net bonding in the σ system and a destabilizing effect on CO binding to the metal. The main impact of the σ system is the internal redistribution of electrons in CO rather than bonding interactions with the metal. X-ray emission spectroscopy (XES) and ab initio calculations support the BNP model of adsorbed CO.[84,85] Both σ and π interactions increase with increasing metal coordination, so these effects partially cancel each other out. Despite significant changes in the CO electronic environment, experimentally observed CO adsorption energies and IR frequencies do not change significantly.[83,84] These trends are consistent with the competing effects between π and σ molecular orbitals of the adsorbate-metal complex in the BNP model.

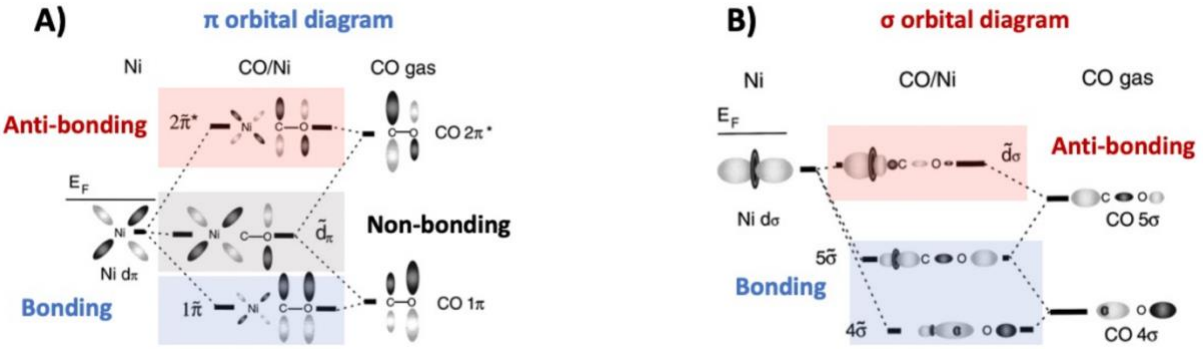

Figure 2.1. Orbital diagrams for the A) π and B) σ interactions. These models are based on the adsorption of CO to a single Ni atom. Adapted from [84].

The BNP model predicts that the σ interactions will destabilize the adsorbate-substrate complex and predicts that increasing π interactions will weaken the C-O internal bond while increasing σ interactions will strengthen it. Both the BNP and Blyholder bonding models can be used to explain the observed trends in CO coverage and Pt electronic environment, and they capture the observed CO frequency decrease with increasing metal electron density.

2.3 Discussion

2.3.1 Effects of CO Coverage

Isolated Pt species show no change in CO frequency with changes in the fraction of sites occupied by CO.[47] For non-isolated Pt sites, increasing CO coverage results in a blueshift in frequency, as illustrated in Figure 2.2. As the CO coverage is increased by increasing CO partial pressure, the CO band frequency will shift to higher frequencies (i.e., closer to that of gas-phase CO).

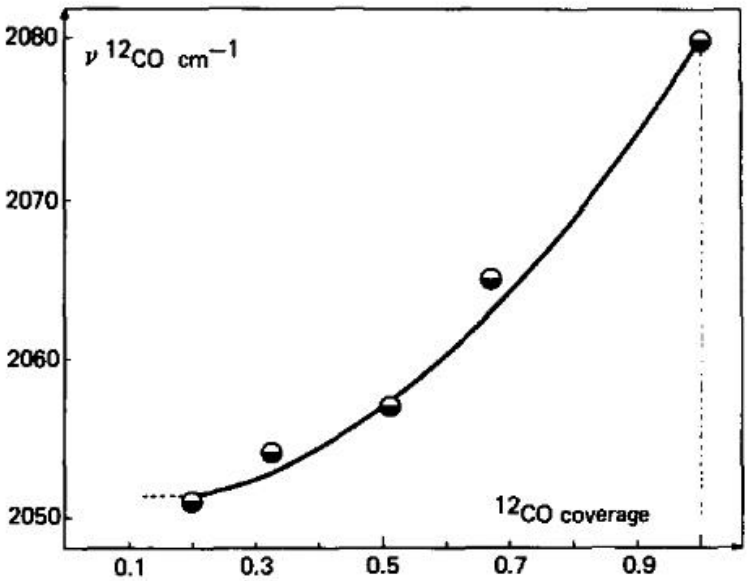

Figure 2.2. Change in ν^{12}CO frequency with CO coverage. Various coverages were obtained by desorption at increasing temperatures of the Pt/Al_2O_3 sample fully covered by CO at 298K. [86]

The BNP and DCD models do not address the effects of CO coverage. However, Blyholder offered two explanations for the blue shift in the C-O vibrational frequency observed with increasing CO coverage: decreased available electrons and site heterogeneity.[69] In the first case, higher coverage results in more competition for electrons, leading to fewer electrons in each orbital and an increase in the C-O stretching frequency for adsorbed CO. For the second explanation, if different sites exist, the weaker adsorbing Pt sites will only adsorb CO at higher coverages, resulting in a band shift to a higher wavenumber. As the CO coverage increases with increasing CO partial pressure, the CO band frequency will shift to higher frequencies (i.e., closer to that of gas-phase CO). As an alternative, Hammaker proposed that dipole-dipole interactions of neighboring CO adsorbates influence the shift in C-O frequency.[87] As CO coverage increases, the number of neighboring adsorbed CO molecules on the surface increases. Repulsion between these neighboring CO adsorbates weakens the strength of CO adsorption, increasing the C-O frequency. Experimental IR studies with mixtures of ^{13}CO and ^{12}CO have measured a 30 cm^{-1} change in the frequency of CO from coverage fractions of 0.1 to 1.[56,86,88–92] DFT studies have validated a dipole-dipole contribution to shifts in CO frequency.[56] It should be noted that this dipole-dipole explanation for the observed blue shift in the CO vibrational frequency is most commonly given in the experimental literature. While some authors have claimed that dipole-dipole interactions are the sole reason for any CO frequency shift with coverage; however, evidence to support this claim universally is still lacking.[93] In summary, increasing CO coverage results in a blue shift IR peak for adsorbed CO; CO dipole-dipole interactions, decreased electron availability, or differences in CO heats of adsorption can explain this shift.

The observed blue shift with increasing CO coverage is extremely important to consider when comparing literature results and investigating other effects of IR spectroscopy of adsorbed CO. Reported results are commonly measured at low CO coverages, but exact coverage values are not included. While most studies consistently control CO coverage (i.e., taking spectra at the constant temperature and time point after CO dose), many do not report the CO pressure, the flow rate of CO, or CO coverage at the time of measurement. If included, conditions are often different, making comparisons at constant CO coverage across literature complex if not impossible. Additionally, one should note that the frequency shifts reported by different authors working with

dispersed Pt nanoparticles, as opposed to single crystal facets of Pt, cannot be readily compared because of differences in the size and morphology of the Pt nanoparticles and their coverage by CO, issues that are discussed in more detail below. The blue shift in IR frequency of adsorbed CO observed with increasing CO coverage can complicate the direct comparison of results between different studies.

2.3.2 Platinum Oxidation State

Platinum readily occurs in 0, 2^+, and 4^+ oxidation states. IR peaks above 2100-2101 cm^{-1} are attributed to CO adsorbed linearly on positively charged Pt species.[44–46] This assignment can be explained theoretically. For positively charged Pt species, there are fewer d-electrons to be back donated to CO, resulting in a stronger C-O bond and a higher frequency. These high-frequency IR peaks are observed for CO adsorbed on positively charged supported Pt species[44–46] and positively charged Pt organometallic complexes.[94,95] These IR peaks of adsorbed CO are also found to disappear with reduction and reappear with oxidation,[96] further supporting their assignment to Pt species in higher oxidation states. Metallic Pt species interacting with linearly adsorbed CO exhibits IR peaks in the range of 2050-2100 cm^{-1}. [48] Reduction experiments also support this assignment.[96] Additionally, DFT and experimental results agree that CO on Pt_{38} alone exhibits a peak at 2075 cm^{-1}.[48]

CO can also exhibit peaks in the range of 1900-1550 cm^{-1}, corresponding to CO bridging across two neighboring metal sites.[46] These bridging peaks are generally seen for zero valent metallic particles,[97–100] but have also been observed for organometallic complexes.[101] The bridging bands are broader and have lower relative extinction coefficients than linear CO.[47] Because of this, it is easy to miss these bridging peaks, especially when they are low in intensity. While a peak in this lower frequency range indicates Pt clustering, its absence cannot definitively indicate that Pt clusters do not exist.

To summarize, CO peaks observed above 2100 cm^{-1} are attributable to positively charged Pt; CO peaks between 2100-2050 cm^{-1} are attributable to metallic Pt; and CO peaks observed between 1900-1550 cm^{-1} are attributable to bridge bonded CO.

2.3.3 IR Frequencies of CO on Unsupported Platinum

2.3.3.1 Platinum Complexes

Stretching frequencies for various homogeneous Pt complexes are presented in Table 2.1. These results highlight the effect of oxidation state, with positive Pt species exhibiting higher CO frequencies (>2150 cm^{-1}) and Pt^0 and Pt clusters exhibiting CO frequencies below 2060 cm^{-1}. Organometallic Pt clusters show an increase in CO frequency with increasing Pt coordination numbers.[102] It is important to note that there are potential effects of other ligands on the electronic state of Pt; complexes with ligands such as Br and Cl have been excluded for comparison here.[95] In addition to illustrating the effects of Pt oxidation state and clustering, this platinum complex data set shows the wide range of potential CO stretching frequencies.

Table 2.1.IR Stretching Frequencies of CO in Unsupported Pt Complexes

Species	CO IR Frequencies (cm^{-1})	Reference
$Pt(CO)_4$	2053	45103
$Pt(CO)_3$	2049	103
$Pt(CO)_2$	2059	103
Pt(CO)	2054	103
$[[Pt(CO)_3]_2]^{2+}$	2195, 2186, 2174	94
cis-$[Pt(CO)_2]^{2+}$ (solv.)	2218, 2182	94
$[Pt_3(CO)_3(\mu_2CO)_3]^{2-}{}_2$	1990, 1818, 1795	101
$[Pt_3(CO)_3(\mu_2CO)_3]^{2-}{}_3$	2030, 1855, 1842, 1835, 1810	101
$[Pt_3(CO)_3(\mu_2CO)_3]^{2-}{}_4$	2045, 2025, 1880, 1860, 1840, 1828	101
$[Pt_3(CO)_3(\mu_2CO)_3]^{2-}{}_5$	2055, 1890, 1870, 1840, 1825	101
$[Pt_6(CO)_{12}]^{2-}$	1970, 1790	102
$[Pt_9(CO)_{18}]^{2-}$	2005, 1810	102
$[Pt_{12}(CO)_{24}]^{2-}$	2025, 1830	102
$[Pt_{15}(CO)_{30}]^{2-}$	2040, 1850	102

Pt^0, Pt^{2+}, Pt clusters

2.3.3.2 Platinum Single Crystals

For bulk single crystals, the Miller indices of the surface and the CO coverage affect the CO stretching frequencies. Low Miller index facets exhibit CO frequencies in the ranges of 2062-2105 cm^{-1} and 1850-1877 cm^{-1}, attributed to linear and bridging CO on $Pt^{0,}$ respectively. Different facets will have a different number of broken bonds: the {110} facet has five broken bonds, the {100} facet has four broken bonds, and the {111} facet has three broken bonds. CO bonding models and experiments suggest that with increasing undercoordination (i.e., more broken bonds), the CO frequency will decrease. In other words, the higher CO adsorption energy on undercoordinated sites will result in lower CO frequency vibration, while increasing coordination number will result in higher CO frequency.[104]

A summary of literature reported CO frequencies over Pt{111}, Pt{110}, and Pt{100} single crystals are presented in Figure 2.3. For the most part, the data reported in the literature follows the trend of CO adsorbed on the {110} surface having the highest frequencies, followed by {100} and {111}. The difference in CO coverage can partially explain these deviations from this trend. These samples exhibit blueshifts of 35-18 cm^{-1} with increasing CO coverage, which easily compensate for variations.

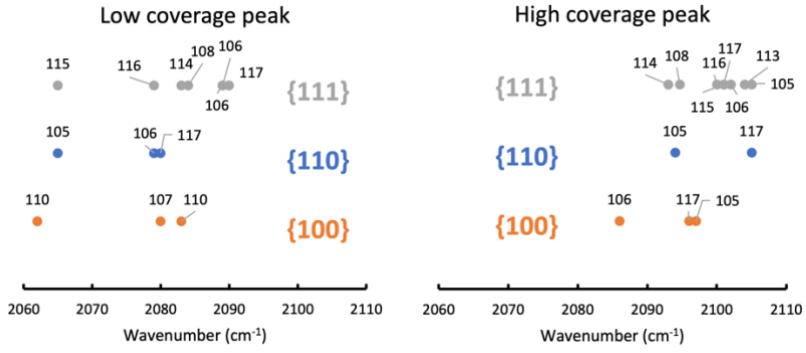

Figure 2.3. Reported IR Frequencies of CO Adsorbed on Pt Single Crystals. (A) reported values at low CO coverage (<0.2); (B) reported values at high coverage (>0.8). Data from references: [105–117]

In summary, platinum single crystals exhibit CO vibrational frequencies corresponding to linear CO on Pt^0 (2062-2105 cm^{-1}) and bridging CO on Pt^0 (1850-1877 cm^{-1}).

2.3.4 Supported Isolated Platinum

The vibrational frequency for CO adsorbed on isolated Pt sites does not exhibit shifts with CO coverage.[118] Isolated Pt atoms have no neighboring Pt atoms to adsorb CO and hence do not experience dipole-dipole interactions with neighboring adsorbates or site heterogeneity to cause the blueshift. Consequently, IR spectroscopy of adsorbed CO with temperature programmed desorption (TPD) is a good indicator of Pt site isolation, in addition to established techniques such as extended x-ray absorption fine structure (EXAFS) and high-angle annular dark-field scanning transmission electron microscopy (HAADF STEM).[58] It is worth noting that the definitive characterization of single-atom catalysts is complex, especially in determining active site geometry. Additionally, the characterized structure is not guaranteed to be maintained under reaction conditions.[14]

Isolated Pt species often exhibit CO frequencies higher than those seen for Pt^0 nanoparticles.[118–123] This blue shift can be partially explained by increased support interactions for single Pt atoms. Since these supports are metal oxides, they are less electron-donating than Pt, which creates more electron-deficient Pt. For example, Christopher has reported the frequency of CO adsorbed on isolated Pt (confirmed by CO desorption) as 2102 cm^{-1}.[47,124] This blue shift in CO frequency relative to CO adsorbed on Pt clusters is consistent with an electronically deficient Pt in strong interaction with reducible TiO_2 support.

Peak position alone cannot be used to assign Pt isolation because the oxidation state of the atom and its interaction with the support can also influence the C-O vibrational frequency. Table 2.2 compares the IR frequency of adsorbed CO on isolated Pt for a variety of supports. Each of these samples has confirmed Pt isolation via CO TPD, HAADF STEM, or XAS. Some debate around the degree of isolation of Pt on CeO_2 exists due to the ability of CeO_2 to oxidize Pt and easily interconvert Pt between raft-like structures and single atoms.[50] This behavior could explain some of the disparity of reported CO frequencies for Pt/CeO_2.

Table 2.2. IR of Adsorbed CO on Isolated Pt Over Different Supports

Pt wt.%	Support	EA* (eV)	IR (cm^{-1})	CO TPD	HAADF STEM	XAS	ref
0.3	Al_2O_3	12.82	2070		Y	Y	[53]
0.2	Al_2O_3	12.82	2084		Y	Y	[125]
1	CeO_2	7.64	2090		Y	Y	[126]
1	CeO_2	7.64	2112		Y	Y	[121]
1	CeO_2	7.64	2098		Y	Y	[122]
0.22	CeO_2	7.64	2089		Y		[127]
0.27	CeO_2	7.64	2095		Y	Y	[128]
1	CeO_2	7.64	2095	Y	Y		[129]
0.17	Fe_2O_3		2080	Y	Y	Y	[130]
0.25	meso Fe_2O_3		2073	Y	Y		[131]
0.05	MgO	9.79	2085		Y	Y	[132]
0.82	Mn_2O_3		2099	Y	Y	Y	[123]
0.82	Mn_3O_4		2099	Y	Y	Y	[123]
0.025	TiO_2	4.53	2112	Y	Y		[133]
0.025	TiO_2	4.53	2112	Y		Y	[118]
0.5	HZSM-5	7.44	2115	Y	Y		[120]
0.22	Y	7.44	2116		Y	Y	[119]

* EA is energy affinity from reference [134]

In summary, isolated Pt exhibits no shift in C-O vibrational frequency with CO coverage and a blueshift in the CO frequency (2116-2070 cm^{-1}) relative to CO adsorbed on bulk Pt. Support composition can also have a significant influence on these vibrational frequencies.

2.3.5 Effect of Pt Dispersion

Previous work has shown some agreement between supported Pt and homogenous Pt complexes.[135] Small platinum particles result in low CO vibrational frequencies.[136] This redshift is consistent with stronger binding of CO to smaller Pt particles relative to larger ones. Stronger Pt binding will result in a weaker C-O bond, causing a lower frequency stretch.[137] Additionally, well-coordinated Pt sites have been shown to result in higher CO frequencies than under-coordinated Pt sites.[138,139] This assignment partially explains Pt dispersion effects on IR frequency of adsorbed CO. Well-coordinated Pt sites exhibit higher CO frequencies; small particles have fewer of these sites and therefore exhibit lower frequencies.[137] These trends are nicely presented in the combined DFT and DRIFTS study showing the redshift with decreasing particle size and how the fraction of sites changes with particle size.[140] This trend in site changes with particle size is illustrated in Figure 2.4. In brief, decreasing Pt particle size leads to a decrease in CO frequency.

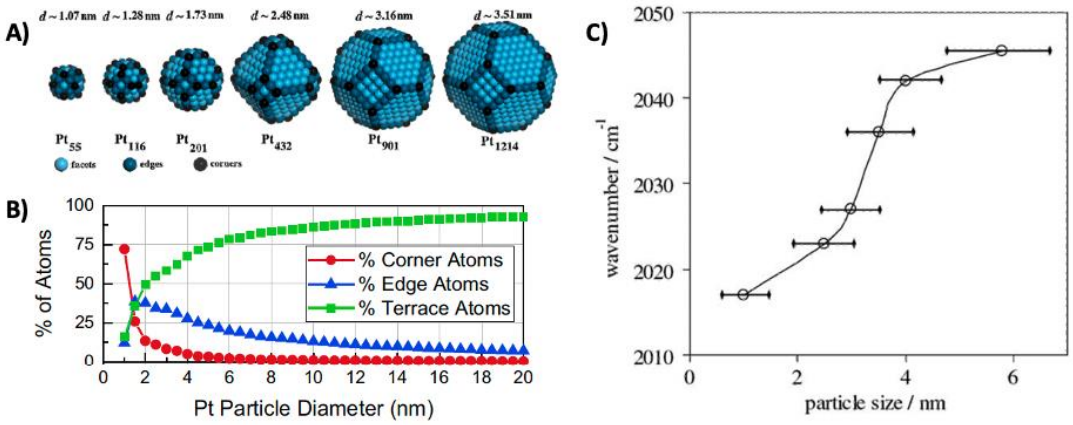

Figure 2.4. Effect of Pt Particle Size. A) Hard sphere models of Pt nanoparticles of different sizes between 1.07 nm (55 atoms) and 3.51 nm (1214 atoms). Adapted from [140] B) Calculated total and relative number of corner, edge, and terrace atoms for Pt particles of different sizes, assuming a truncated octahedron geometry and perfectly uniform particle size distribution. Adapted from [141] C) Evolution of the CO_{ads} stretch frequency as a function of the Pt particle size. The horizontal lines indicate the particle size distribution. Results are for Pt colloid solutions. Adapted from [136]

2.3.6 Effect of Support Material

Theoretically, a support can donate or withdraw electron density from Pt atoms. If support withdraws electron density from Pt, the CO frequency will increase; if support contributes electron density to Pt, then the CO frequency will decrease. It is also important to note that supports can influence Pt morphology, with some supports more readily stabilizing more dispersed Pt nanoparticles than others. In this way, even samples prepared in the same way with the same loading can have dispersion and support influences on Pt-CO interaction.

Metal oxide supports can be grouped into reducible and non-reducible.[142,143] While technically all metal oxide supports can be reduced, this distinction is based on the ease of oxygen vacancy formation, which is an important step for metal oxide reduction. More reducible supports will withdraw more electron density from Pt, leading to higher frequency CO stretches, including those associated with positive Pt species. Reducible supports include TiO_2, ZrO_2, CeO_2, and SnO_2, and non-reducible supports include Al_2O_3, MgO, MgAlO.

Several studies have directly compared the IR frequency for CO adsorbed on Pt on different supports. For TiO_2, ZrO_2, and Al_2O_3, the support reducibility increases the strong metal-support interaction (SMSI) effect; Al_2O_3 (non-reducible) exhibits lower CO stretches (2082 cm^{-1}) than reducible supports [ZrO_2 (2189, 2131, 2098, 2084 cm^{-1}) and TiO_2 (2186, 2087 cm^{-1})] at the same conditions.[97] There is little difference in the frequency of CO adsorbed on 0.4 wt.% Pt on MgO (2088, 2075cm^{-1}) and 0.4 wt.% Pt on Al_2O_3 (2075 cm^{-1}).[100] MgO and Al_2O_3 are both non-reducible supports. For Pt supported on TiO_2, a more reducible support, Pt becomes electron-rich Pt, and the CO frequency shifts accordingly (2121, 2067, 2060, and 1832 cm^{-1}).[144] This difference in support interactions for TiO_2 vs. Al_2O_3 is consistent with XPS measurements. It is important to note that Pt dispersion is different on these supports for the same Pt loading: for Pt/TiO_2, the Pt particles have a diameter of 26 Å, while for Pt/Al_2O_3, the particles have diameters of 9-11 Å.[144] These differences in particle size could also partially explain the blueshift of Pt on TiO_2 compared to Pt on Al_2O_3. Generally, these studies find that reducible supports result in higher CO frequency stretches than those for non-reducible supports. Still, these studies do not control the size and shape of Pt particles.

Identifying specific support effects on IR frequencies of CO adsorbed on Pt is difficult using the published literature because Pt dispersion and CO coverage are commonly different between reported results. While holding the Pt dispersion and CO coverage constant can circumvent this issue, the comparison remains challenging as every paper chooses different CO dosing procedures, leading to different CO coverages. Additionally, many studies do not report Pt dispersion. A selection of reported literature IR frequencies of CO adsorbed to Pt on various support materials is shown in Figure 2.5. Generally, the CO frequencies can be grouped into bridging CO and linear CO on Pt^0 and Pt^{n+}, but no other trends emerge because of the confounding effects of dispersion and CO coverage.

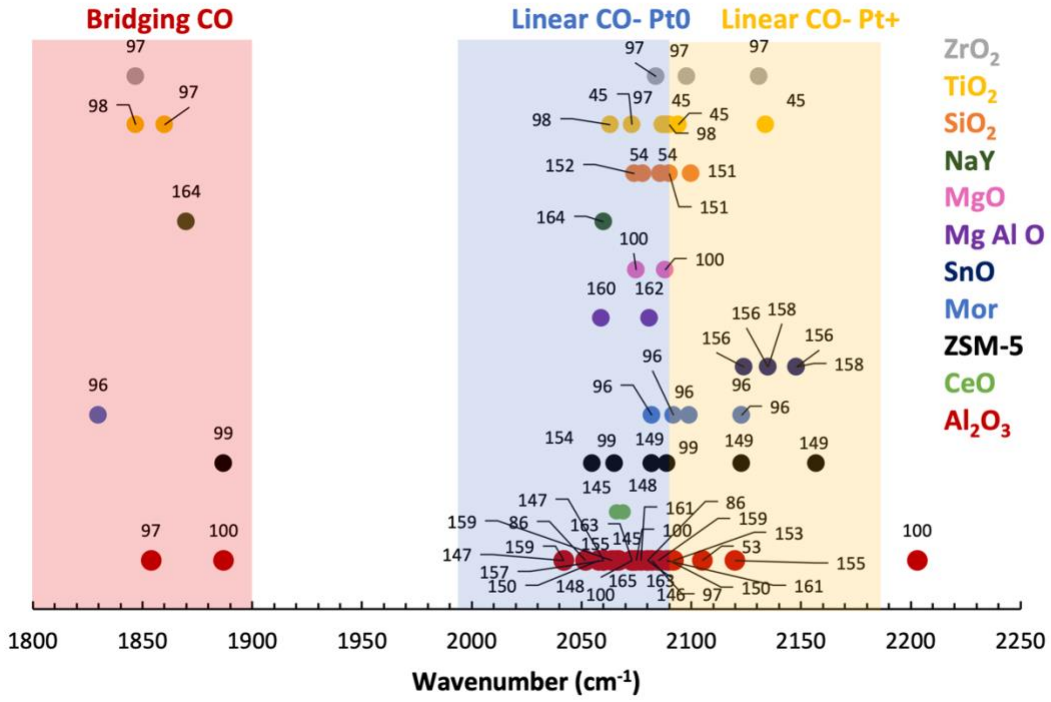

Figure 2.5. Summary of Reported IR Frequencies of CO Adsorbed on Pt across a Variety of Supports. Data from references:[45,53,54,86,96–100,145–165]

To avoid the effects of CO coverage and Pt dispersion, we can examine the vibrational frequency of CO adsorbed on isolated Pt sites. Only isolated Pt sites confirmed via CO TPD, XAS, or HAADF STEM are included in Figure 2.6. The reducibility of the support is often described by the ease of oxygen vacancy formation.[166] DFT studies on oxygen vacancy formation, electronic localization, and band gaps have shown all parameters trend with reducibility but found that one descriptor cannot capture reducibility trends.[134] In general, isolated Pt atoms show increasing frequencies with increasing reducibility of the support. Facile interconversion between isolated Pt and raft-like Pt structures on ceria could explain the spread of CeO_2 samples.[50] A positive Pt oxidation state could explain the significant deviation over zeolitic samples, where isolated Pt likely sits in ion exchange sites, compensating for negatively charged oxygens with neighboring aluminum atoms.

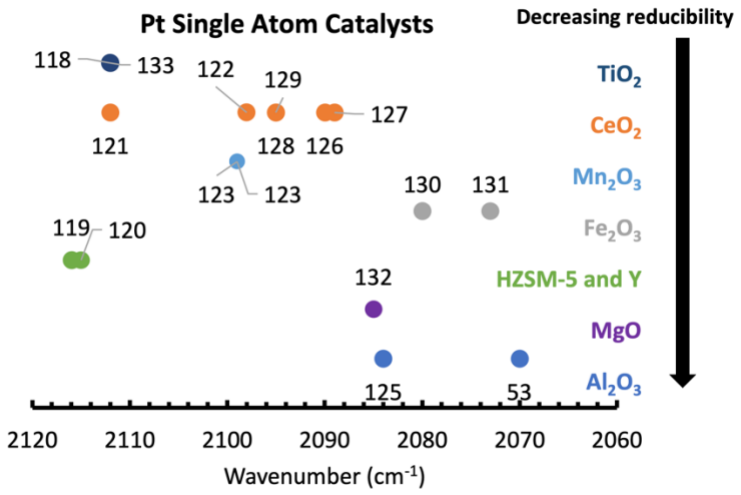

Figure 2.6. Reported IR Frequencies of CO Adsorbed on Isolated Pt Sites on a Variety of Supports. Data from references:[53,118–122,125–133,167]

In conclusion, CO adsorption on Pt supported on non-reducible supports exhibits lower frequency CO peaks than for Pt supported on reducible supports, a result of the larger withdrawal of electron density from Pt, leading to higher CO frequencies.

2.3.7 Effect of Sn with Pt on CO Vibrational Frequency

CO adsorbed on PtSn bimetallics and alloys is affected by all the previous parameters (support, CO coverage, dispersion) discussed above. Additionally, CO adsorption can result in structural modification.[13] This restructuring can take the form of surface segregation if one metal preferentially adsorbs CO.[13] Pt interacting with Sn can cause red or blue shifts in the CO vibrational frequency relative to Pt alone. Changes in CO frequencies on PtSn structure relative to Pt are included in Figure 2.7. CO adsorbed on PtSn nanoalloys[48] exhibits IR peaks at 2047 cm^{-1}, red-shifted from Pt NP alone (2075 cm^{-1}).[48] Many papers cited observe a CO frequency decrease with Sn addition.[48,54,159,160] This redshift can be attributed to the following:

1) Sn can isolate the Pt atoms from one another, with the consequence that CO dipole-dipole interactions are less important. This decrease in CO dipole-dipole contribution causes a red shift relative to CO adsorbed on Pt clusters.
2) Sn alloyed with Pt can donate electrons to Pt, which results in greater electron density on Pt, thereby increasing back donation to the CO $2\pi^*$ orbitals. This electron donation results in a weaker C-O bond and a lower frequency stretch.

Other studies, especially those involving Ce and other promoters, report that Sn addition to Pt results in a blue shift of the CO frequency relative to that observed for Pt alone.[145,148,165] Theoretically, this blue shift can be explained by the Pt interacting with Sn being more electron deficient than Pt alone, causing a higher C-O vibrational frequency. This blue shift in CO frequency has been observed for Pt interacting with Sn within a zeolite framework[21,31] and with tin oxide.[158] Despite likely decreases in Pt cluster size with Sn interaction, electron interactions with promoters win out. Some studies observe a combination of both blue and red-shifted peaks. This difference in trends is consistent with multiple Pt species, at least one of each of the previous two examples. [21] Finally, some studies report no shift, which indicates little structural/ environmental change for Pt with Sn addition. [31,32] This lack of change is consistent with Pt clusters with little Sn interaction.

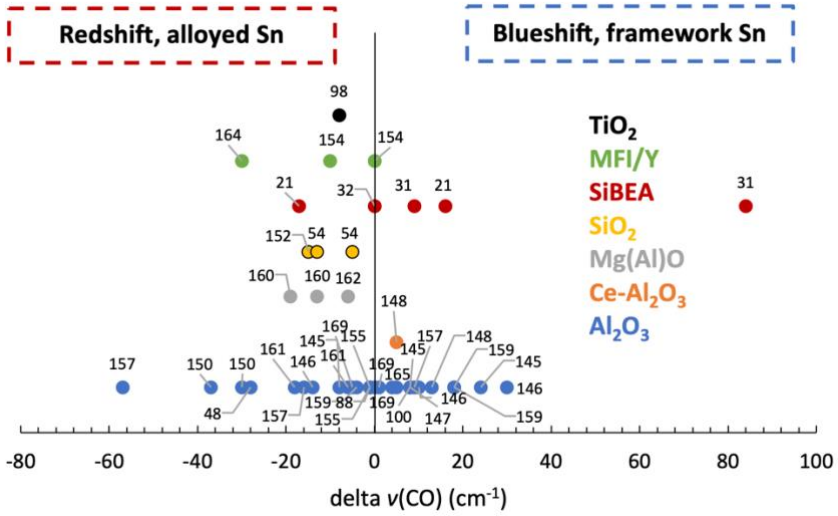

Figure 2.7. Change in IR Vibrational Frequency of CO Adsorbed on Pt with Sn Across a Variety of Supports. Values are reported in $\Delta\nu$(CO) (cm^{-1}) relative to Pt catalyst without Sn. Data from references: [21,31,32,48,54,88,98,100,145–148,150,152,154,155,157–162,164,165,168–170]

To summarize, Pt interaction with Sn in the support results in electron withdrawal from Pt and consequently a blue shift of the CO frequency; Sn alloyed with Pt results in a red shift in the position of the CO peak because Sn donates electrons to Pt that are then back donated to CO.

2.3.8 Effects of Other Promoters Interacting with Pt

Similarly to Sn addition, other additives can have a blue or red shifting effect on CO stretches depending on whether they withdraw or donate electrons, respectively. The effects of Ce, La, and K are detailed in Table 2.3 and Figure 2.8. Ce addition results in blue shifted CO peaks, suggesting that it promotes more electron-deficient Pt.[145,148] These shifts are consistent with the electron-withdrawing nature of Ce and the reducibility of CeO_2. Similarly to Ce, La addition to Al_2O_3 results in blue-shifted CO peaks.[155] This increasing blue shift with increasing La addition is consistent with La withdrawing electron density from Pt. Unfortunately, this study does not compare the effect of La addition on Pt alone, only with PtSn. Conversely, K addition results in strongly red-shifted CO peaks for linear and bridged CO species and increases in linear relative to bridged CO on Pt.[100,154,171] The increase in alkalinity reduces the acidity of the support, in turn making the support less electron withdrawing. More electron density on Pt will lead to lower frequency CO stretches. These results are supported by Nilsson's XES data showing how the presence of alkali decreases σ repulsion.[172]

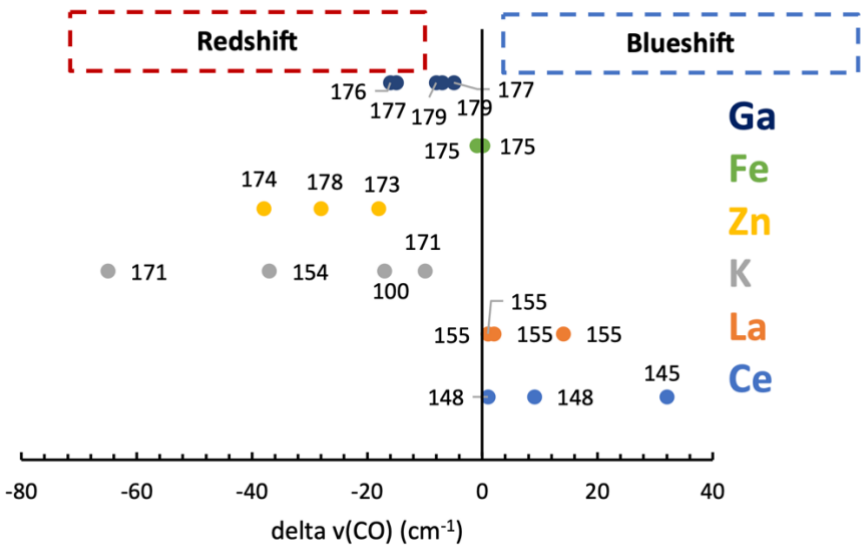

Figure 2.8. Effect of Additive on IR Frequencies of CO Adsorbed on Pt. Values are reported in Δν(CO) (cm^{-1}) relative to Pt catalyst without additive. Data from references: [100,145,148,154,155,171,173–179]

Table 2.3. Effect of Additive on the IR Frequency of Adsorbed CO on Pt

Additive	Support	Catalyst	Pt only (cm^{-1})	Pt with additive (cm^{-1})	Δν(CO) (cm^{-1})	Reference
Ce	Al_2O_3	Pt/Al_2O_3	2060	2069	9	[148]
Ce	Al_2O_3	$PtSn/Al_2O_3$	2073	2074	1	[148]
Ce	Al_2O_3	Pt/Al_2O_3	2066	2098	32	[145]
La	Al-SI	PtSn/Al-SI-1	2066	2068	2	[155]
La	Al-SI	PtSn/Al-SI-1	2129	2130	1	[155]
La	Al-SI	PtSn/Al-SI -20	2066	2080	14	[155]
La	Al-SI	PtSn/Al-SI -20	2129	2130	1	[155]
K	MFI	Pt@MFI	2055	2018	-37	[154]
K	Al_2O_3	Pt/Al_2O_3	2051	2034	-17	[100]
K	SiO_2	Pt/SiO_2	2060	2050	-10	[171]
K	SiO_2	Pt/SiO_2	1830	1765	-65	[171]

Other metals besides Sn have been frequently used as Pt promoters, e.g., Fe, Zn, Ga, and Cu. Some promoters adsorb CO at room temperature, such as copper, gold, and silver.[46,180] Here, we will compare promoter metals that do not adsorb CO at room temperature in the same range as Pt to provide a clear picture of the effect on Pt. Like Sn, many metals (e.g., Zn, Ga) alloy with Pt, and correspondingly, IR measurements of the CO vibrational frequency on PtM show a redshift in CO stretches relative to Pt alone.[167,178] This shift is consistent with the added metal donating electron density to the platinum atom. Conversely, iron platinum catalysts show little changes in CO stretches relative to platinum catalysts alone.[175] Ultimately, additives can withdraw or donate electrons to Pt, allowing for both red and blue-shifted CO frequencies, depending on the additive identity and system.

2.4 Perspective

IR spectroscopy of adsorbed CO is a powerful tool, but the results must be interpreted carefully. Coverage studies are critical for determining site isolation, especially for reducing supports, such as CeO_2, where more positively charged Pt sites can easily be mistaken for isolated Pt sites. Given the overlapping impacts of CO coverage across studies, Pt dispersion across

supports, and support effects, it is difficult to compare and draw definitive conclusions for the full range of supports used for Pt. The same can be said of promoters and additives to Pt. Determining the electronic effects on Pt can often be clouded by differences in Pt dispersion and supports. Figure 2.9 illustrates the overlapping ranges for many different Pt species.

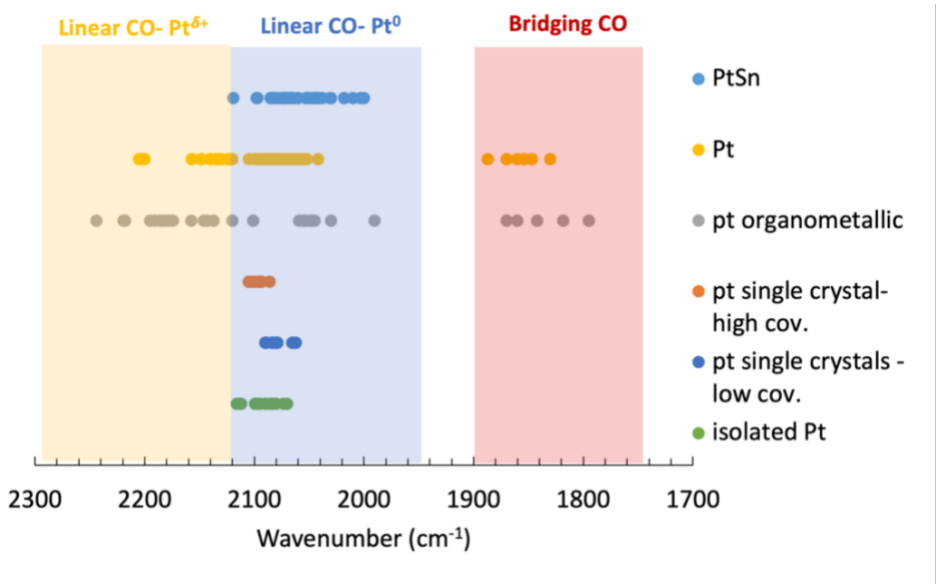

Figure 2.9. IR Frequency of CO Adsorbed on a Variety of Pt Species.

2.5 Conclusion

Many factors affect the IR frequency of CO adsorbed on Pt. Here, we have examined the effects of support identity, additives/promoters, Pt oxidation and dispersion, and CO coverage. It is important to consider all these effects and control them as much as possible in order to accurately interpret IR spectra for CO adsorbed on Pt. The effects and their impacts on observed IR frequencies of adsorbed CO are summarized in Table 2.4. Additional characterization (e.g., XAS, HAADF STEM) is crucial for accurately interpreting IR spectra. Increasing CO coverage results in a blue shift of the C-O frequency. This change with CO coverage can result from dipole-dipole CO repulsions at high coverages or from heterogeneity of sites, where the sites with the strongest adsorption (lowest frequency) adsorb CO first, followed by sites with lower adsorption energies. Positive Pt species exhibit higher frequency CO stretches (>2100 cm^{-1}); less electron-dense Pt donates fewer electrons to the $2\pi^*$ orbital of CO, resulting in a stronger C-O bond and, in turn, a higher stretching frequency. Decreasing Pt particle size results in a lower CO frequency for Pt clusters. The exception to the trend is isolated Pt atoms, which appear at high frequencies (>2100 cm^{-1}) if support interactions are strong. Support effects are particularly challenging to deconvolute from the effects of Pt dispersion and CO coverage across studies. Reducible supports withdraw electron density from Pt, resulting in higher CO stretching frequencies than observed for Pt supported on non-reducible supports. The addition of Sn has a red-shifting effect for alloyed, metallic Sn and a blue-shifting effect for framework or oxidized Sn relative to Pt alone interacting with CO. Other additives (e.g., Ce, La, K) can have blue or red shifting effects on the CO stretching frequencies depending on whether they withdraw or donate electrons to the Pt.

Table 2.4. Summary of Effects on IR Frequency of CO Adsorbed on Pt

Influence	Direction of Shift of CO Frequency	$\Delta\nu$(CO) (cm^{-1})	Ref
CO coverage	↑ With increasing CO coverage	**~ 30**	86
Pt Oxidation State	↑ With increasing Pt oxidation state	**~ 50 to 75**	96
Isolated Pt	↑ Relative to clusters	**35-52**	47
Pt dispersion	↑ With increasing Pt cluster size ↑ With increasing Pt coordination	**~ 40**	136
Support effects	↑ With increasing reducibility of support	**~ 50**	53,118–133
Pt-Sn interaction	↑ With Sn-framework interactions* ↓ With bimetallic and alloyed Sn*	**~ 81 to 1** **~ -60 to -1**	145,148,165 48,54,159,160
Pt-Other additives	↑ With electron withdrawing additves (Ce, La)* ↓ With alakaine additves*	**~ 1 to 30** **~ -10 to -60**	100,154,171

*Relative to Pt alone

3 Examination of X-ray Absorption Spectroscopy to Characterize Pt and Sn Catalysts

3.1 Introduction

X-ray Absorption Spectroscopy (XAS) is a powerful, element-specific, bulk characterization technique. Hard X-rays have high enough energies to eject a core electron. This electron excitation has characteristic energies for each element, allowing the average electronic and geometric structure of all sites of a single element to be precisely measured. In this way, XAS can be applied to nearly every element. The scattering of ejected electrons can be modeled to gain detailed insights into the element of interest. XAS spectra are divided into two regions: 1) X-ray Absorption Near-Edge Structure (XANES) which probes oxidation state and local symmetry, and 2) Extended X-ray Absorption Fine Structure (EXAFS), which provides information about coordination number, the distance between nearest neighbors, and neighboring species identity.[181] XAS can probe atomic environments, such as those of elements in supported metal particles and isolated sites.[182] XAS provides an average of all sites' geometric and electronic structures.[183] An additional strength of XAS is its ability to probe catalysts in situ and operando.[184]

Several textbooks[51,185] and reviews[186–190], have been written about XAS. Here, the use of XAS for Pt and Sn characterization is summarized, and the impact of changing the Pt and Sn environment on XAS results is examined. Tin and platinum can exist in various structures (e.g., isolated sites, bimetallic and monometallic nanoparticles), analyzing even common catalysts complex. The oxidation state, dispersion, geometry, support, and neighboring atom identity will all affect the observed XAS results. This chapter evaluates these effects in order to determine to what extent XAS can provide definitive evidence of Pt and Sn interactions.

3.2 XAS Models and Theory

The X-Ray Absorption Near Edge Structure (XANES) region includes the pre-edge and up to 50-110 eV above the edge, and the Extended X-Ray Absorption Fine Structure (EXAFS) region extends from 50-110 eV above the edge to 1000 eV above the edge.[191] The physics of these regions are coupled, but the spectral ranges are typically analyzed separately. XAS experiments are performed at synchrotron beamlines since high-energy X-rays (4 - 30 keV) are needed to excite the core electrons of metal atoms. Synchrotron beamlines also provide a high flux (i.e., high brilliance) of these high-energy X-rays to enhance signal-to-noise relative to benchtop instruments. The design of these synchrotrons is discussed extensively elsewhere.[182] Because XAS experiments require synchrotron radiation, catalyst characterization by XAS is less common than by benchtop methods (IR, UV-vis, XRD, etc.), especially for Sn.[192] In situ and operando experimental setups for XAS have become more common.[184] Appropriate sample preparation has also been covered extensively elsewhere.[51,181] Good sample preparation is critical to acquiring high-quality data so that particle size and orientation artifacts do not influence the recorded spectra.

XANES probes the oxidation state and site symmetry of the element of interest. The analysis of XANES is mainly qualitative as there is no equivalent equation to the EXAFS equation for XANES.[181] By comparing the spectrum of a sample to spectra of known standards, it is possible to identify the oxidation state and symmetry of the element in the sample.[51,193] Because the XANES signal is stronger than the EXAFS signal, quality XANES spectra can be acquired at lower element concentrations than EXAFS data. The XANES edge position is sensitive to the oxidation state of the atom. Specifically, the white line height and the edge energy increase with increasing oxidation state. White line height is a measure of the unoccupied d-electrons.[194] As the oxidation state increases, so does the white line intensity. This effect is powerful compared to the influence of

dispersion, chemical identity, and support on white line intensity and edge energy.[195] The coordination symmetry of the scattering element primarily impacts the pre-edge region of the XANES spectrum. Specific electronic transitions can result in observed pre-edge peaks, which are often sensitive to the oxidation state and the symmetry of the ligands surrounding the scattering element.[196] Pre-edge features are not commonly observed in XANES spectra of Pt and Sn catalysts.

EXAFS spectra reflect the coordination number and immediate local geometry (up to ~6 Å)[197] of the absorbing element. The physics EXAFS scattering (equation 1) has been solved precisely with the following equation, first derived by Sayer:[198]

$$\chi(k) = S_0^2 \sum_i Ni \frac{fi(k)}{kR_i^2} e^{-\frac{2Ri}{\lambda(k)}} e^{-2k2\sigma_i^2} \sin(2Rik + \delta i(k)) \quad (1)$$

Several parameters appear in the EXAFS equation. Table 3.1 lists these parameters, their physical significance, and their acceptable ranges. The amplitude reduction factor (S_o^2) approximates intrinsic losses in the EXAFS spectrum. These losses can originate from the rearrangement of electrons to compensate for the core hole formed by the ejected electron, the excitation of an outer electron, or the ejection of an outer electron from the atom. All of these processes decrease the amplitude of the EXAFS signal and are relatively independent of k and R within the fitted EXAFS region (< 10% deviations). [51] The degeneracy (N) is the number of unique instances of a specific scattering path. N is equivalent to the coordination number for a single scattering path and must be greater than or equal to zero. A good upper bound for N is the coordination number of the bulk metal (often 6 or 12). The Mean Square Relative Displacement (σ^2) accounts for the thermal and static disorder. σ^2 is also called the pseudo-Debye–Waller factor or the 2nd cumulant (C_2). The values of σ^2 increase with increasing disorder in the system. The half path length (D) is the average distance between the absorbing and scattering atoms. D is equivalent to the bond length for a single-scatterer. The reference energy (E_o) is the effective energy origin for EXAFS. E_o is used to align experimental spectra to the calculated spectra.[188] Less commonly, the third and fourth cumulants are also used to fit. The third cumulant (C_3 or σ^3) addresses asymmetry, and the fourth cumulant (C_4 or σ^4) accounts for size distribution tails. Third and fourth cumulants are commonly zero. The fifth and higher cumulants are rarely used.

These parameters can be grouped into those that mainly change the amplitude (N, S_o^2, C_2/σ^2, C_4/σ^4) and those that mainly change the phase (D, E_o, C_3/σ^3). S_o^2 and N are closely correlated, so fitting one at a time is essential. S_o^2 is generally considered independent of k and R. S_o^2 can be fit for each path individually or held constant (if chemical environments are similar between paths. Because of the interdependent nature of the parameters in the EXAFS equation, it is crucial to critically evaluate all fitted parameters to ensure they have acceptable values.

Table 3.1. Summary of EXAFS Equation Parameters and Their Acceptable Constraints and Errors

Parameter	S_o^2	N	D (Å)	σ^2 (Å^2)	E_o (eV)	σ^3 (Å^3)	σ^4 (Å^4)
Physical meaning	k- and R-independent amplitude suppression	Number of unique scattering paths	Half path length	thermal and structural disorder	Effective energy origin	asymmetry	size distribution
Constraints/ Acceptable Ranges	0.7 - 1.05 [51] 0.7 - 1.0 [184]	≥0	≥0	0.002-0.03 [51] 0.001-0.012 [183]	-10 - 10	<0.001Å^3	<0.0001 Å^4
Acceptable Error	10%		1%	5%	0.1 +/- 5%		

3.2.1 Analysis of XANES Spectra

XANES is commonly used to gain information about the oxidation state of the element of interest. The edge position and white line intensity can determine the oxidation state, with more oxidized species exhibiting higher edge energies and more intense white lines. XANES data analysis primarily involves the comparison of spectra of known standards and structures with experimental data. This technique provides qualitative information about the oxidation state and the geometry of the element of interest. Calculations can accurately predict spectra, which enables the evaluation of proposed structures.[183,186] However, it is not possible to fit structural parameters (e.g., coordination numbers, bond distances) from experimental XANES data.

Positive species have higher edge energies and exhibit higher white-line intensities. These trends have been shown for Pt complexes, with Pt(II) complexes exhibiting a lower absorption maximum (1.45) than Pt(IV) complexes (2.4).[199] This increase in white line intensity with increasing oxidation state holds for single atoms.[121] Additionally, peak height can be used to quantitatively determine the fraction of Pt oxidation state in binary systems. These shifts in white line intensity and edge energy have also been confirmed with oxidation and reduction experiments.[200,201] Similarly, more positive Sn species have higher edge energies and white line intensities. For example, the white line height of tin standards follows this trend: Sn Foil< SnO< SnO_2.[21,202,203] XANES edge position can also be used to identify the oxidation state, as the edge position shifts up to 6 eV with changes in the oxidation state.[203,204] It should be noted that neighboring atom identity can also shift the edge energy.[205] The oxidation of PtSn catalysts has also confirmed these shifts in white line intensity and edge energy.[206] In summary, increasing the oxidation state increases the white line intensity and the edge energy. These systematic changes can be used to quality fractions of species in binary systems.

3.2.2 Fitting of EXAFS Spectra

EXAFS data fitting relies on fitting the Fourier transform of the experimental data to theoretically generated paths (equation 3). Early EXAFS studies primarily investigated coordination numbers and nearest neighbor distances.[207] Today, advanced software exists to analyze EXAFS data and fully fit it to the EXAFS equation. These programs provide the best choice of fitting parameters (N, S_o^2, C_2/σ^2, D, E_o) as well as quantitative metrics of the goodness of fit (i.e., R-factor, χ^2). These programs are summarized elsewhere,[183] and many books and tutorials discuss their use.[51,181] Users can also generate XAFS signals from structural models (FEFF[208], GNXAS, Corvus, FDMNES), process EXAFS data (Athena, ProQEXAFS, EXAFS-Neo), perform EXAFS fits and data analysis (Artemis and Larch), and incorporate theoretical calculations, such as Reverse Monte Carlo (EvAX) and DFT (QuantEXAFS), into the structure search. The first shell fit is routine.[186] The quality of EXAFS fit depends on the models used to fit.[183] These data reduction and analysis processes are illustrated in Figure 3.1.

XAFS data are collected in the energy domain. These data are normalized to an edge step of 1 and then converted to frequency (k) domain using the following equation:

$$k = \frac{1}{\hbar}\sqrt{2m_e\left(E - E_o\right)} \tag{2}$$

Data is converted to the radial distribution (R) domain by taking the Fourier transform of absorption intensity in the k space (Equation 3). The k-weight (w) is generally 1, 2, or 3 and should increase with decreasing atomic mass of the scatterer.[51] The choice of k-weight should not significantly change the final fitting results.[51]

$$\tilde{\chi}(R) = \frac{1}{\sqrt{2\pi}} \int_{k_{min}}^{k_{max}} k^w \chi(k) e^{i2kR} dk \quad (3)$$

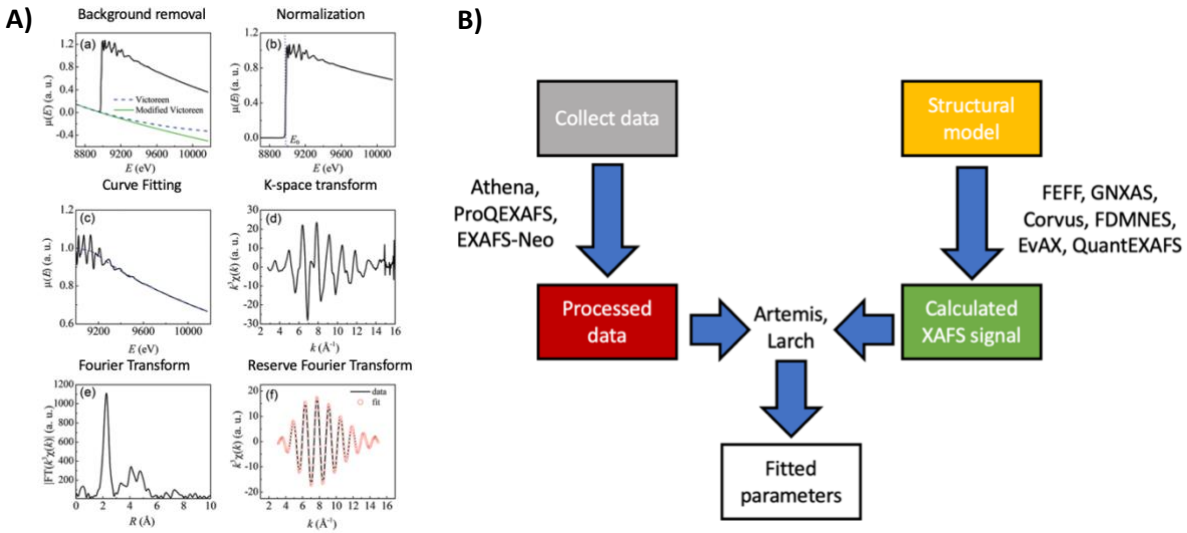

Figure 3.1. A) Typical EXAFS data processing and analysis procedure: (a) pre-edge background removal, (b) normalization, (c) curve fitting of μ0, (d) conversion to k-space and weighting, (e) Fourier transformation to R-space, and (f) reverse Fourier transform and fitting in the k-space. Adapted from [209] B) XAFS fitting and modeling processes.

To compare the interpretation of EXAFS data for related material, it is necessary to understand the goodness of fit. The R-factor is often used as a measure of fit since it measures the deviation of the data from the model, and the lower the R-factor, the better the fit. An R-factor of 0.05 or less is considered acceptable.[51,183] χ^2 is the sum of squared deviations weighted by the estimated uncertainty, and the reduced χ^2 (χ_ν^2) is the χ^2 per degrees of freedom. χ_ν^2 accounts for the number of fitting parameters and independent variables available in the k- and R-ranges. χ_ν^2 is preferred to the R-factor but must be compared over the same k and R ranges, making comparisons of χ_ν^2 across different studies difficult. Lower χ_ν^2 values correspond to a better fit. Additionally, χ_ν^2 should not be compared for fits where the measurement uncertainty is significantly different (i.e., different materials, different conditions).[51] χ_ν^2 is best used to compare fits of the same or similar data taken over the same ranges in k- and R-space. Conversely, the R-factor can be used to compare the goodness of fit between samples regardless of the type of material or fitting ranges used. It is also essential to consider the physicality of the fitted parameters, not just the goodness of fit.

Good data processing is crucial to produce a reasonable fit.[51,181] The first step for ensuring a reasonable fit is to check for nonsensical values (e.g., negative values of N or σ^2 or S_o^2, σ^2, or ΔE out of acceptable range); even if the error of the fit is low, if the fitted parameter values are out of range, the fit is not physically significant. It is necessary to compare χ_ν^2 values to prevent overfitting. Using material standards with similar composition and structure to the sample of interest will also enable a better fit. Additional characterization (e.g., IR, XRD, UV-vis, TPR, STEM) can inform the predicted structure, supporting or opposing the proposed XAFS structures. S_o^2 must be fit first to a reference material containing the same element as that of the sample being characterized so that this parameter does not skew fitting results for the material of interest (i.e., CN). To compare materials directly, data processing and fitting must be performed methodically and consistently. When fitting, it is essential to consider various structural models. To evaluate

these models, the χ_v^2 and R-factor should be compared, and fitted parameters checked to ensure they make physical sense.

3.3 Discussion

3.3.1 XAS of Standards and References

3.3.1.1 XAS of Pt Standards and References

Because the Pt K edge is very high in energy (78,394.8 eV), the L_3 edge (11,536.7 eV) is used most often to investigate Pt. The L edge involves the excitation of p electrons into unoccupied d orbitals.[185] Occasionally, the L_2 edge (13,272.6 eV) is also used. Reported fitting parameters for Pt foil and PtO_2 standards are included in Table 3.2. Table 3.2 shows that the EXAFS fits of standard Pt-containing materials exhibit a range of fitted parameters; these differences can be attributed to differences in fitting procedures (e.g., k- and R-space ranges, data reduction procedures). Generally, for a known material structure, the degeneracy of the path is fixed to the known value for the crystal structure so that the amplitude reduction factor can be fit appropriately. The bond distances do not change much across these fits, but the fitted values for σ^2 and ΔE exhibit more variation between different studies. It should be noted that fitting software provides the error for these fitted parameters, but often these errors are not reported in the literature. This issue is especially prevalent for standard reference materials, e.g., Pt foil.

Table 3.2. EXAFS fits of Experimental Pt Standards

Ref	Standard	R factor	S_0^2	Path	N	R (Å)	σ^2 (x10^3)	ΔE (eV)
[210]	Pt foil	0.002	0.91	Pt-Pt	12	2.77	5	4.8
[154]	Pt foil	0.0017	0.89	Pt-Pt	12	2.763	4.8	6.7
[118]	Pt foil	0.002	0.78	Pt-Pt	12	2.77	4	8.1
[211]	Pt foil	0.0024	0.787	Pt-Pt	12	2.76	4.4	7.5
[211]	PtO_2	0.0073	0.79	Pt-O	6	2.02	1.4	13.3
[156]	PtO_2	0.045	0.83	Pt-O	6	2.02	3.1	12.7

The Pt-O and Pt-Pt paths from these Pt materials with known structures are used as initial guesses to fit the paths for unknown samples. However, the structure and phase of the reference can affect the fitting results; this effect is more significant at larger shells ($n \geq 2$) because the phase of the reference material starts to influence the structure. Surprisingly, very few papers report the structure of the reference material used as an initial guess. Table 3.3 lists the bond distances for various Pt crystallographic structures. Several structures (e.g., tetragonal, hexagonal, cubic) of Pt, PtO, and PtO_2 exist. For Pt-Pt paths, the crystallographic bond distances of these standards do not change significantly (~2.700 Å), but there is variation in the Pt-O bond lengths for different morphologies of PtO_2 and PtO (1.94 - 2.31 Å), with PtO exhibiting longer bond distances than PtO_2. For PtSn reference materials, several different compositions and morphologies exist (e.g., SnPt, $SnPt_3$, Sn_4Pt) with Pt-Sn bond distances between 2.69 and 2.85 Å. Experimental crystallographic results for organometallic PtSn complexes report Pt-Sn bond distances between 2.62 and 2.83Å.[212,213] The variations in these bond distances highlight the importance of choosing reference materials for initial guesses.

Table 3.3. Crystallographic bond distances for Pt-Pt paths, Pt-O paths, and Pt-Sn paths in standard Pt materials. CIF files of these standard materials were obtained from The Materials Project.[214]

Material	**Path**	**$R_{crystallographic}$ (Å)**
Pt^0	Pt-Pt	2.79
PtO, cubic	Pt-O	2.31
PtO, tetragonal	Pt-O	2.07
PtO_2, cubic	Pt-O	1.94
PtO_2, tetragonal	Pt-O	2.01, 2.04
	Pt-Pt	3.25
PtO_2, hexagonal	Pt-O	2.04
PtSn	Pt-Pt	2.74
	Pt-Sn	2.76
Pt_3Sn	Pt-Pt	2.85
	Pt-Sn	2.85
Pt_2Sn_3	Pt-Pt	2.79
	Pt-Sn	2.69, 2.80
$PtSn_4$	Pt-Sn	2.814

3.3.1.2 XAS of Sn Standards and References

Generally, the K edge is used to characterize the local properties of Sn (29.2 keV), but the L_2 and L_3 edges are also used occasionally.[215] It is best practice to extract the amplitude reduction factor from the fit of a standard material (e.g., Sn foil, SnO_2) in order to isolate the amplitude reduction factor from the degeneracy, since the two parameters are closely correlated. However, many Sn XAS studies assume S_0^2 to be 1.0 without fitting to a standard material. Additionally, when S_0^2 is extracted from a fit to a standard material, the other fitting parameters (e.g., σ^2 and ΔE) are often not reported. Because fewer Sn XAS studies exist than Pt ones, finding complete fits for Sn XAS is challenging. For this reason, incomplete reports of XAS fits for Sn are included. Reported fitting parameters for Sn foil and SnO_2 standards are listed in Table 3.4. The degeneracies (N) of the scattering paths (Sn-Sn and Sn-O) are fixed during the fitting of Sn reference materials. Across literature studies, the fitted bond lengths agree for Sn-O and Sn-Sn paths, respectively. Reported values of σ^2 and ΔE for these materials vary more widely. Notably, fewer Sn XAS studies report values of the R-factor, ΔE, and S_0^2 for the fit. Additionally, several reported fitted parameters are outside of acceptable ranges listed in Table 3.1 (e.g., $\sigma^2 > 30$, $\Delta E > 10$, R-factor > 0.05).

Table 3.4. EXAFS fits of Experimental Sn Standards

Ref	Standard	R factor	S_0^2	Path	N	R (Å)	σ^2 (x10^3)	ΔE (eV)
[216]	Sn Foil	0.147	1	Sn-Sn	4	3.001	16	n.r.
[217]	Sn Foil	n.r.	n.r.	Sn-Sn	4	3.022	70	n.r.
[216]	SnO_2	0.194	1	Sn-Sn	2	3.2	9	n.r.
[218]	SnO_2	n.r.	n.r.	Sn-O	6	2.06	n.r.	n.r.
[98]	SnO_2	n.r.	n.r.	Sn-O	4	2.04	1.3	11.8
				Sn-O	2	2.06	2.7	13
[219]	SnO_2	n.r.	n.r.	Sn-O	6	2.05	5	n.r.
[216]	SnO_2	0.194	1	Sn-O	6	2.041	7	n.r.
[220]	SnO_2	0.009	n.r.	Sn-O	6	2.06	58	n.r.
[221]	SnO_2	0.01	n.r.	Sn-O	6	2.045	1.8	28
[217]	SnO_2	n.r.	n.r.	Sn-O	6	2.068	70	n.r.
[222]	SnO_2	n.r.	n.r.	Sn-O	6	2	4.49	n.r.

In addition to the reported fits of experimental data of Sn standards, the FEFF-calculated EXAFS parameters for different crystal structures of Sn materials can be compared. Table 3.5 includes the crystallographic bond distances for these Sn materials. The Sn-Sn bond distances for these reference materials are in the range of 2.84 to 3.54 Å, and the Sn-O bond distances are between 2.07 and 2.23 Å. These Sn-Sn and Sn-O bond distances overlap with Pt-Pt and Pt-O bond distances because of the similar atomic size of Sn and Pt. Because these paths cannot be distinguished from a radial distribution plot, more advanced EXAFS fitting to account for atom identity must be used to differentiate between Sn and Pt. Specifically, paths with Pt or Sn can be fit with Artemis or Larch, and the quality of the fits can be compared. The differences in these Sn paths again emphasize the importance of material structure choice in XAFS fitting. It is recommended to use a reference path that most closely resembles the fitting path; if information about the fitting path is unknown, multiple reference paths should be tested.

Table 3.5. Crystallographic bond distances for Sn-Sn paths and Sn-O paths in standard Sn materials. CIF files of these standard materials were obtained from The Materials Project. [214]

Material	Path	$R_{crystallographic}$ (Å)
β-Sn, body-centered tetragonal	Sn-Sn	3.05, 3.20
α-Sn, diamond cubic	Sn-Sn	2.84
SnO	Sn-O	2.23
	Sn-Sn	3.54
SnO_2	Sn-O	2.07
	Sn-Sn	3.21

3.3.2 Effect of Dispersion on XAS

Increasing the metal dispersion decreases the average metal-metal coordination number as the surface site fraction increases. In the XANES region, this decrease in metal interaction increases the white-line intensity and edge energy if the nearest-neighbor atom is less electron-donating than the metal. In the EXAFS fit, lower coordination numbers will reduce the fitted value of degeneracy for that path. Decreasing the degeneracy will decrease the scattering amplitude in both k- and r-spaces.[51] If the metal is dispersed on a support, an increase in white line intensity (i.e., a decrease in d electrons) is expected.

Isolated Pt sites only show one intense peak in R space at 2 to 3 Å, which corresponds to a single Pt-O scattering path.[118,154,200] Further evidence for Pt isolation can be demonstrated with a good fit, including $N_{Pt\text{-}Pt}$ scattering path of zero or a better fit if Pt-Pt scattering is excluded from the model. As cluster size increases, so does the degeneracy of the Pt-Pt path. Figure 3.2 shows how Pt cluster size changes the fitted Pt-Pt coordination number, Pt-Pt distance, and XANES region. Increasing coordination numbers with particle size follows a sub-linear trend.[223] Additional studies investigating the effects of Pt dispersion confirm these results.[224–226] The Pt-Pt bond distance increases slightly with increasing Pt particle size until it reaches the bulk value. The XANES edge energy increases with decreasing Pt particle size, which has been attributed to cluster-size dependent band gaps of Pt as no change in Pt oxidation state was observed with XPS.[227] It should be noted that the oxidation state cannot be unambiguously assigned with XANES as a result of these compounding effects.[118]

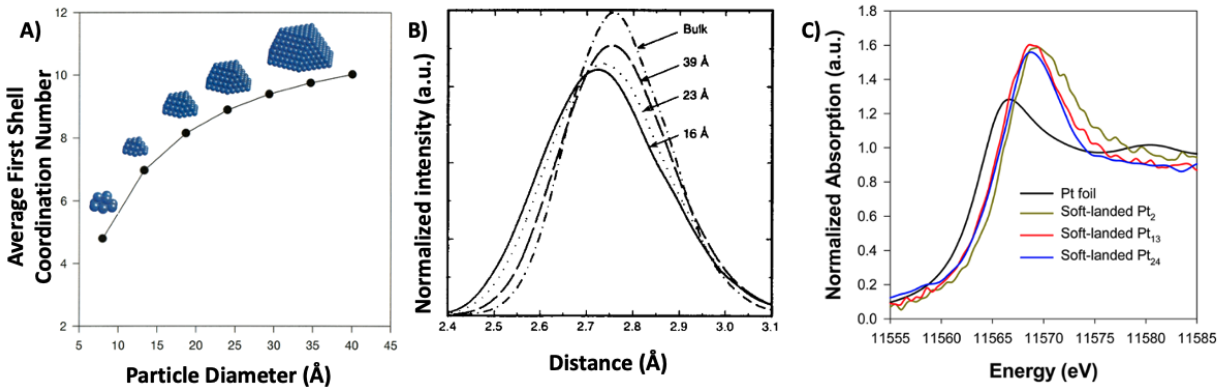

Figure 3.2. A) Coordination number vs. particle diameter for Pt clusters, adapted from[223] B) Effect of particle size on Pt-Pt distance, adapted from[226] C) Effect of XANES edge energy with changing particle size, adapted from[227]

XANES spectra of supported Pt clusters of increasing particle size (Pt_2, Pt_{13}, Pt_{24} supported on SiO_2) show a slight decrease in white line intensity and a reduction in edge energy.[227] XPS results confirm that Pt remains in the zero oxidation state, but XANES edge energies and white line resemble bulk, oxidized Pt. Often the XANES spectra of these isolated Pt species closely resemble bulk PtO_2.[128,227] There is ambiguity in assigning XANES features to the effects of size and oxidation state. XAS of small Pt particles can resemble that of bulk standards (e.g., PtO_2) because of the effects of particle size on electronic levels. Increasing Pt nanoparticle size leads to a decrease in white line intensity.[228,229] This trend can be explained by decreasing support interactions and increasing Pt-Pt interactions with increasing Pt clustering, ultimately increasing the occupancy of d-electrons.

The same trends exist for Sn, although fewer examples are present in the literature. Many articles only consider bulk Sn compounds and dispersed Sn samples but vary multiple parameters in this comparison (e.g., support, dispersion). Still, the trends observed for increasing Pt cluster size are expected to persist for Sn XAS. One study compares two different SnO_2 nanoparticles and finds a shift in the absorption edge toward higher energies with smaller nanoparticles. This change is attributed to differences in SnO_2/SnO and Sn distribution with particle size.[197]

To summarize, increasing dispersion will decrease $N_{M\text{-}M}$ and increase white line intensity. As metal interactions with support increase and metal-metal interactions decrease, the observed XAS of dispersed metal sites will often resemble that for a bulk metal oxide.

3.3.3 Effect of Neighbor Identity on XAS

The mass of a neighbor can generally be determined within an atomic mass of five by XAS.[181] Higher-mass neighbors are usually larger in atomic radius and sit further apart. This difference in spacing with neighbor atomic mass is exemplified by comparing metal-metal and metal-oxygen path fits (e.g., Pt-O vs. Pt-Pt in Table 3.3). Other studies have shown similar trends for similarly different atomic mass nearest neighbors. Pt dispersed on MoN and α-MoC were compared by XAS; Pt/MoN samples displayed a Pt-N distance of 2.04 Å and the Pt/α-MoC samples showed a Pt-Mo distance of 2.82 Å.[230] The effect of neighbor identity on XAS has also been investigated with adsorption experiments. The adsorption of hydrogen[231] to Pt shows significant changes to the Pt L_3 edge XAS spectra. A reduction in Pt white line intensity was observed upon hydrogen adsorption, attributed to a decrease in Pt-Pt scattering interactions and an increase in weaker scattering Pt-H paths. These effects are most evident in the near-edge region of the spectrum.

Many Sn examples only consider O or Sn nearest neighbors, but the same trends of increasing effective distances with increasing atomic mass exist. Differences in scattering intensity and bond distance easily differentiate between tin and oxygen neighbors, and even more similar neighbors can be distinguished. One study compared SnO_2 and Sn on N-doped graphene.[232] While Sn-C and Sn-N had very similar effective bond distances to Sn-O, the intensity of the white decreased for the Sn/N-C sample, and the edge shifted to lower energies. These changes are consistent with lower electron donation from N and C relative to O, resulting in more electron-poor Sn.

In this way, atomic mass and electronic differences in scatters can be used to determine the identity of the neighboring atom. The adjacent atom's identity primarily affects the core element's electronic state (e.g., white line intensity, edge energy), bond distances, and fitted degeneracies.

3.3.4 Effect of Support Identity on XAS

Support effects are difficult to determine because of the interacting impacts of dispersion, oxidation state, and electronic interactions with the support. Different supports or even the same support treated in different ways has been shown to produce different Pt morphologies.[144,205] Generally, stronger metal-support interactions increase the white line intensity (more electron-deficient metal) relative to metallic interactions.[205] There are two explanations for these changes with support.[185] The first explanation attributes changes with different support solely to particle size effects. As the metal-metal interactions are replaced with metal-support interactions, the white line intensity of the metal XAS increases. The second interpretation includes electronic effects. The direct interaction of the metal with the support will change the electron density of the metal particle, in turn affecting the XAS spectrum. More reducible supports will be more electron-withdrawing, increasing the white line intensity.

Experimental evidence for support effects is often difficult to disentangle from other influences (e.g., dispersion of Pt, changes in scatterer identity). Investigation of isolated Pt atoms eliminates the potential for dispersion and neighbor identity effects. Isolated Pt on TiO_2 and Al_2O_3 exhibit similar white line intensities and positions.[229] Pt nanoparticle samples display more differences, with TiO_2 showing higher white line intensities than Al_2O_3, suggesting a more electron-deficient Pt.[229] For bulk Pt, the comparison of PtSn on SiO_2 and Al_2O_3 results in longer Pt-Sn bonds (2.80 vs. 2.61 Å), higher Pt-Sn coordination numbers (N_{Pt-Sn}: 4.7 vs. < 0.5), and more Pt-Pt interactions on SiO_2 than Al_2O_3 (N_{Pt-Pt}: 6.5 vs. 3.2).[203] It is clear that in this study there are morphological changes resulting from the change in the support. The investigation of Pt particle size on Pt/SiO_2 and Pt/Al_2O_3 finds that at the same Pt particle size, Pt/SiO_2 materials exhibit more negative energy shifts than Pt/Al_2O_3 relative to the Fermi level.[227] In addition to changing the support composition, the structure of the support material also influences particle morphology; zeolites usually have smaller, more uniform particles than macroporous supports.[185] These differences make it challenging to isolate the effects of the support.

Studies of Sn/Beta have shown how different crystallographic sites within the Beta zeolite result in different Sn geometries and EXAFS-fitted bond distances.[233] Specifically, Sn is preferentially inserted into T5/T6 sites of Sn/BEA prepared via a fluoride hydrothermal synthesis route.[233] The EXAFS results of specific Sn crystallographic sites were modeled and compared to experimental results, with the T5/T6 Sn sites providing the best fit. Because different supports have different local structures, it is expected that these differences observed within unique crystallographic sites of Beta zeolite will also persist across other supports. Comparing different types of supports, $PtSn/SiO_2$ exhibits longer Sn-Pt bonds (2.79 vs. 2.62 Å) and higher Sn-Pt coordination numbers (6.8 vs. < 0.5) than $PtSn/Al_2O_3$.[203] Additionally, Sn and Pt both had more oxygen interactions on Al_2O_3 than SiO_2.

Support identity affects multiple XAS parameters (e.g., R, N). Additionally, different supports disperse metals to different extents, so dispersion effects must also be considered when comparing results between different supports.

3.3.5 Effect of Sn on Pt XAS

In addition to changes in the Pt electronic environment, Sn can promote the isolation of Pt atoms. This structural change often leads to more Pt-O interactions with the support and fewer Pt-Pt interactions, in addition to interactions with Sn.[234] In this way, it is difficult to isolate the effects of Sn introduction on Pt XAS as dispersion and neighbor identity effects are also present.

Because of their similar sizes (atomic radius of Sn: 140 pm, atomic radius of Pt: 139 pm), Pt-Sn and Pt-Pt path lengths overlap. The Pt-Sn distance in the SnPt standard is 2.78 Å, while the Pt-Pt distance in Pt foil is 2.81 Å.[235] Crystallographic results for $(C_8H_{12},)_3Pt_3(SnCl_3)_2$ complex exhibits a greater Pt-Sn bond distance (2.80 Å) than Pt-Pt bond distance (2.58Å).[236] Because of these similar bond distances, the fitting results for Pt-Sn bond distances in supported PtSn materials can be longer than,[201,221,237] shorter than,[200,201,203,206] or equal to the Pt-Pt bond distance.[200,238] In this way, the magnitude of the Fourier transform (FT) cannot be used unequivocally to assign Pt-Sn or Pt-Pt paths; instead, fitting with EXAFS software must be used to distinguish between Pt and Sn neighbors. EXAFS software fitting will manipulate all the scattering parameters and consider real and imaginary FT space to provide the best fit. Often, scattering paths can have destructive interference in the real part of the FT, resulting in little change in the magnitude of the FT, but EXAFS fitting software will take this interference into account.

Other fitting parameters do not show distinct trends when comparing Pt-Pt vs. Pt-Sn. The pseudo-Debye-Waller factor increases[237,238] or stays the same with Sn introduction.[201,239] Systematic changes in ΔE with Sn introduction are also not evident. Upon Sn introduction, the Pt d-band vacancy increases, causing an increase in XANES white line intensity.[203,205,238] This result is consistent with Sn interaction causing a more electron-poor Pt.[201] In terms of bond lengths, an increase in the lattice parameter (i.e., larger Pt-Pt bond distances) is observed when Sn is introduced.[238]

Different environments can change the morphology of PtSn structures as well.[200,206] Reduction of PtSn catalysts decreases the white line intensity, and oxidation increases it.[200,206] Additionally, Pt_3Sn/C can be prepared with increasing Sn-Pt mixing by changing gas environments (PtSn alloying increases in air < He < H_2 annealing); XRD, HRTEM, and XPS results show an increase in metallic Sn and Pt_3Sn species and a decrease in SnO_2 and metallic Pt particles with air < He < H_2 annealing. XAS of Pt_3Sn/C shows increasing Pt-Sn coordination number with increasing extent of alloying, as well as decreases in Sn-Pt distances and increases in Pt-Pt distances.[237] It was observed that Pt_3Sn is more readily oxidized than PtSn, though both samples have surface-segregated Sn.[206]

Generally, Sn disperses and withdraws electrons from Pt, increasing white line intensities and edge energies. Pt-Sn scattering paths can be distinguished from Pt-Pt paths with thorough EXAFS fitting. EXAFS fitting of Pt-Pt and Pt-Sn paths must be performed carefully as their bond distances overlap. Specifically, the comparison of multiple fitting paths (e.g., Pt-Pt path, Pt-Sn path, Pt-Pt and Pt-Sn path) must be employed to achieve the most representative structure. Finally, thoughtful experiment control and planning must be implemented to ensure measurements are collected in meaningful environments for these catalysts (e.g., dehydrated or pre-treated).

3.3.6 Effect of Pt on Sn XAS

If Sn is in excess of Pt, most Sn atoms do not interact with Pt, so Sn-Pt paths become harder to fit. In these cases, often just the Sn-O path is fit.[221,238] Still, information about the effect of Pt on the Sn electronic state can be gleaned from these fits. Small decreases in Sn-K edge (< 2 eV) are seen with increased Pt content on SnO_2, indicating an increase in Sn electrons.[221] This decrease in white line intensity can be explained by higher electronegativity for Sn than Pt.[221] This increase in electron density of Sn is also consistent with the decrease in electron for Pt seen in the Pt edge XAS results. While PtSn samples often have higher edge energy and white line intensity than Sn foil, dispersion effects could partially explain this.[200,203,238]

As mentioned for Pt, the reaction environment can restructure PtSn particles. For example, Pt_3Sn/C can be prepared with increasing Sn-Pt mixing by changing gas environments (PtSn alloying increases in air < He < H_2); these samples exhibit decreasing Sn-Pt distances as the Sn-Pt coordination number increases.[237] It should be noted that the fitted coordination numbers do not match between Sn-Pt and Pt-Sn shells. Oxidizing or reducing PtSn catalysts can also shift Sn edge energy and change the white line intensity.[200,235] The limited available data makes trends in other fitting parameters (e.g., Debye-Waller factor, ΔE) hard to discern. In addition to Sn-Pt paths, in zeolitic or siliceous supports PtSn, an Sn-O-Pt path is often fit.[21] In these cases, the Sn-Pt distance is longer (> 3 Å).

In summary, Pt introduction to Sn material decreases Sn K-edge energy and white line intensity relative to SnO_2 and increases relative to Sn foil. These trends are consistent with a donation of electrons from Pt to Sn and the dispersion effects of PtSn mixing.

3.4 Perspective

The lack of published XAS parameters often makes evaluating reported fits of EXAFS data highly challenging. Many studies publish only some fitting parameters, and only some share the fitting strategies or procedures. Additionally, the fitted reference structures are very rarely included. Frequently, studies only publish the one best fit without including alternative fits as proof of the quality of this fit. This information is essential when EXAFS is the primary evidence for a specific structure. The XAS literature would benefit from more detailed and standardized reports of fitting procedures and bases used to draw deductions and more thorough comparisons of experimental data with standard structures and previously recorded spectra of similar materials. In many ways, more consistent and transparent data processing and fitting are necessary to compare different reported literature studies.

3.5 Conclusion

This chapter has examined the effects of oxidation state, dispersion, support, and neighbor identity on Pt and Sn XAS data. Table 3.6 summarizes these effects. Increasing the oxidation state increases white line intensity and absorption edge due to decreased electrons (XANES). Increasing metal clustering increases coordination numbers and often reduces white line intensity due to neighbor identity differences (EXAFS, XANES). The support can affect XAS signals in two ways: changing particle size and changing the electron density. More reducible supports will withdraw more electron density, causing an increase in the white line energy and intensity. Sn interacting with Pt results in a decrease in electron occupation and an increase in the lattice spacing. Pt interacting with Sn results in an increase in electron occupation and a reduction in the lattice spacing. It is essential to evaluate fits critically. Researchers should confirm that the reported parameters make sense and are consistent with similar literature or analogous standards. XAS

results depend on the interplay of multiple parameters, so considering results from additional characterization techniques to support structure assignment is essential.

Table 3.6. Effects of changing environment on Pt and Sn XAS

Effect	White Line	Edge energy	$N_{first\ shell}$	$R_{first\ shell}$
Increasing Oxidation State	**increases**	**increases**	-	-
Increasing Dispersion	**increases**	**increases**	**decreases**	**decreases**
More reducible Support	**increases**	**increases**	**decreases**	**decreases**
Pt Sn interaction: Pt edge (relative to Pt-Pt)	**increases**	**increases**	**decreases**	**increases or decreases**
Pt Sn interaction: Sn edge (relative to Sn-Sn)	**decreases**	**decreases**		**decreases**

4 Effect of Preparation Method and Sn Loading on Sn/DeAlBEA Catalysts for Propane Dehydrogenation

4.1 Introduction

The rise in domestic shale gas production heightens the need for efficient conversion of light alkanes. Light alkanes can be upgraded to olefins (e.g., ethene, propene, butenes) and to aromatics (benzene, toluene, xylene) through dehydrogenation and dehydroaromatization processes. Cracking also occurs as an undesired side reaction, creating lower alkenes and alkanes, including methane. Isolated metal sites have shown high activity and high olefin selectivity for propane dehydrogenation (PDH). Still, additional unselective activity can come from both the support and thermal cracking and dehydrogenation (if the reaction is performed at high enough temperatures). Elucidating the role of Lewis acids is critical in effective catalyst design for light alkane dehydrogenation.

Tin is an effective Lewis acid catalyst for Baeyer Villiger,[240–243] glucose isomerization,[244,245] and hydrogen transfer[246] reactions and recently, such catalysts have been shown to be active for PDH.[36,38–41,247] Beta zeolite (BEA) has often been chosen as a support for Sn Lewis acid catalysts because of its ability to stabilize isolated Sn framework sites. There are several reported techniques for the post-synthesis introduction of Sn into siliceous and zeolitic supports, including ion exchange (IE),[218,248] wetness impregnation (WI),[249] incipient wetness impregnation (IWI),[36,41] and solid-state ion exchange (SSIE).[250] Despite the many preparation procedures, only a few studies directly compare different preparation techniques or justify the choice of one over another. Furthermore, only one study investigates Sn/DeAlBEA for PDH.[247] The details of preparation are lacking, and rigorous investigation and comparison of PDH activity are lacking.

Several characterization techniques can be used to determine the structure and oxidation state of Sn, including ultra-violent visible spectroscopy (UV-vis),[43,251,252] X-ray absorption spectroscopy (XAS),[42,253] X-ray diffraction (XRD),[31,41,42,254] and infrared (IR) spectroscopy of adsorbed CD_3CN [244,255,256] and pyridine.[257–259] This work utilizes these characterization techniques to examine the effects of the preparation method and Sn loading on the structure and oxidation state of Sn in DeAlBEA. This chapter summarizes and evaluates various preparation methods for Sn/DeAlBEA, the effect of Sn loading on the structure of Sn/DeAlBEA, and the activity of Sn/DeAlBEA for propane dehydrogenation activity.

4.2 Experimental Methods

4.2.1 Catalyst Preparation

H-BEA was prepared by heating NH_4-BEA (Alfa Aesar, Si/Al = 12.5) in quartz boats placed in a tubular quartz tube at 5 K/min to 773 K and holding at 773 K for 4 h in dry synthetic air (Praxair, ultra-zero, 100 mL/min). The H-BEA samples were dealuminated in 13M HNO_3 for 20 h at 373 K with stirring. The solution was filtered and washed extensively with deionized water. The filter cake was dried at 393 K overnight to yield dealuminated BEA (DeAlBEA). This technique has been shown to fully remove framework Al species.[20]

Metals were introduced to dealuminated BEA via wetness impregnation and dry impregnation. For wetness impregnation, $SnCl_2{*}2H_2O$ (98.0-103.0%, from Alfa Aesar) or $SnCl_4{*}5H_2O$ (98%, from Sigma Aldrich) was dissolved in ethanol with a concentration of 0.16 M. In procedures with acid addition, 3 M HCl was added to the tin ethanol solution in a 1:1 ratio. Each solution was stirred for 30 min before impregnation. The desired weight loading determined the

amount of metal, while the amount of liquid was kept constant for the same amount of siliceous support (2.8 mL liquid per 1 g support. The solution was added to the siliceous support, and the mixture was ground until all the liquid evaporated (~30 min). For dry impregnation, tin (II) acetate (99%, from Strem Chemicals) was ground with DeAlBEA to produce the desired Sn/Al ratio. All samples were then dried at 393 K overnight in air, followed by calcination in air at 873 K for 2 h.

4.2.2 Catalyst Characterization

Specific surface areas of samples were determined by N_2-adsorption using Brunauer–Emmett–Teller (BET) with a Micrometrics Gemini VII. 40-45 mg of catalysts were dehydrated overnight in vacuum at 453 K. Then nitrogen was adsorbed at 77 K to measure an adsorption isotherm. BET calculation details are included in the supplemental information. Elemental analysis was performed by Galbraith Laboratories, Inc.; metal content was measured with inductively coupled plasma-optical emission spectrometry (ICP-OES), and chlorine content was measured with potentiometric titration.

Fourier transform infrared (IR) spectra were collected in transmission mode using a Nicolet 6700 spectrometer. Samples (~35 mg) were pressed into thin pellets and loaded into an infrared cell equipped with CaF_2 windows. Helium (Praxair, 100mL/min) was used as a carrier gas. The sample was then dehydrated at 573 K for 2 h before the collection of spectra. Spectra were collected by averaging 64 scans at a resolution of 1 cm^{-1} at 473 K and 393 K. For pyridine adsorption IR experiments, 2 μL of pyridine or deuterated acetonitrile (CD_3CN) was injected into the helium feed stream heated to 373 K with heating tape. Spectra were recorded at 10, 20, and 30 min after injection. Spectra were baseline corrected with a spline function and normalized to the intensity of Si−O−Si framework overtone bands occurring between 1700 and 2000 cm^{-1}. The IR spectra of adsorbed pyridine presented here have had the initial spectrum of the sample taken at 393 K subtracted out.

Diffuse reflection ultraviolet-visible spectroscopy (DRUV-vis) was performed after dehydration at 573 K for 2 h. Catalyst samples were ground, sieved, and packed. Spectra were collected from 190 to 500 nm with a resolution of 2 nm at room temperature.

Powder X-ray diffraction (XRD) patterns were collected with a D8 Discover GADDS Powder XRD instrument using Cu-Kα radiation. XRD patterns were collected at room temperature, scanning between 7.5° and 80° with 5 frames. Depending on the noise and crystallinity of the samples, 60 or 300 seconds per frame of equilibration time was used. The XRD pattern for SnO_2 was generated from a reference structure from The Materials Project crystallographic database.

X-ray absorption spectroscopy (XAS) was performed at the Advanced Photon Sources at Argonne National Lab. The Sn K edge was probed at BM-10B using the six-shooter sample holder. Sn/DeAlBEA samples were dehydrated before measurement at 823 K for 1 h.

4.2.3 Catalyst Activity

To test propane dehydrogenation activity, 50 mg of catalyst was loaded into a quartz bubble reactor (10 mm inner diameter). Quartz wool was used to support the catalyst bed. Tests were performed at atmospheric conditions and at 873 K. Catalysts were heated to 873 K at 15 K/min in air and held in air at 873 K for 30 min. A pretreatment of 1 h in hydrogen at 873 K was also applied. Propane 20.2% in He (Praxair) was diluted with He (Praxair, ultra-zero). A He flow rate of 20 mL/min with 1 mL/min propane (4.67 kPa propane) was used as a reference condition. Additional conditions with different total flow rates at the same partial pressure of propane and different partial pressures of propane at the same spacetime of propane were also used. Reaction products were analyzed with an in-line 7890A Agilent Gas Chromatograph equipped with a 25 m

HP-PLOT Q column and a flame ionizing detector (FID). Conversion and selectivity are reported on a molar basis. Net Site-Time Yield (STY) of propene is reported as moles of propene per hour per mole Sn. Equations for calculating conversion, selectivity, and STY are included in the Appendix.

4.3 Results and Discussion

4.3.1 Investigation of Sn introduction methods

Hydrothermal synthesis can introduce Sn into the zeolite framework directly[43,240,244,260] For BEA, a two-step procedure of aluminum removal followed by tin introduction has been shown to successfully introduce framework tin, bypassing the need for direct Sn zeolite synthesis.[42,261] Here, we will evaluate methods to introduce Sn into DeAlBEA.

A number of techniques for introducing Sn into siliceous and zeolitic supports have been reported; these can be broken into solvent-based and non-solvent-based processes. A summary of these studies is included in Table S4.1. The most common methods for solvent-based metal exchange into zeolites are ion exchange (IE), incipient wetness impregnation (IWI), and wetness impregnation (WI). These techniques are typically performed with water as the solvent. IE, IWI, and WI are distinct in the volume of solution used. IE uses large volumes of solution, followed by filtering and washing. IWI uses a solvent volume equivalent to the pore volume of the material, and WI uses a small amount of solution. In both IWI and WI methods, the solvent is allowed to dry rather than being filtered or washed away. All three of these techniques require a soluble metal precursor and have the potential for back exchange of protons from solvent during drying. IWI also suffers from mass transfer limitations due to small solution volumes, leading to under-exchange.

Non-solvent-based techniques have also been developed to address issues concerning precursor solubility and the potential for back exchange. Solid-state ion exchange (SSIE) entails dry grinding of a metal precursor with the support material, followed by heating. SSIE has the advantage of avoiding bulk metal oxides. Additionally, any solubility problems or potential of H+ addition from the solvent are circumvented by eliminating the solvent. However, in order to fully exchange, the precursor must have sufficient volatility to reach the internal silanol sites. Chemical vapor deposition (CVD) involves heating a volatile reservoir of metal precursor; once gaseous, this precursor can travel to the support chamber and deposit. CVD has been shown to create isolated and uniform sites, but it requires a sufficiently volatile precursor.

Several Sn precursors have been used for introduction of Sn (e.g., $SnCl_2*2H_2O$, $SnCl_4*5H_2O$, $Sn(C_2H_3O_2)_2$).[262,263] The volatility and solubility of tin precursors are included in Figure 4.1. Many tin precursors have low solubility in water. Non-aqueous solvents (e.g., ethanol) and acids (e.g., HCl) have been used to increase the solubility of these tin species.[242,264] Non-solvent-based methods can also be used to circumvent this issue (e.g., chemical vapor deposition (CVD), solid-state ion exchange (SSIE)). Several tin precursors have appreciable vapor pressures at elevated temperatures. The very low volatility of Sn metal and high volatility of SnH_4 and $SnCl_4$ exclude them from use for CVD or SSIE. Hydrolysis and insolubility in water are common for many tin precursors, but the use of ethanol and the addition of HCl can increase the solubility of these tin species.

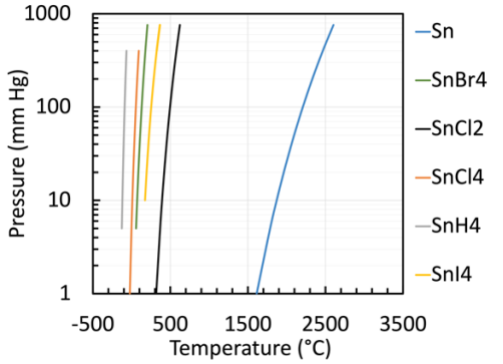

Precursor	Solubility in H_2O (g/100g)	Alternative solvents
$SnCl_2$	178	Ethanol, ethyl ether, acetone
$SnCl_2*2H_2O$	178	Ethanol, NaOH, HCl
$SnCl_4$	hydrolyzes	Ethanol, acetone
$SnCl_4*5H_2O$	very soluble	Ethanol
$Sn(C_2H_3O_2)_2$	hydrolyzes	Dil. HCl
SnF_2	31	-
$SnBr_2$	85	Ethanol, ethyl ether, acetone
$SnSO_4$	18.8	-

Figure 4.1. A) Vapor pressure of Sn precursors vs. temperature. B) Solubility of Sn precursors. Information from CRC handbook.[265]

To evaluate the effectiveness of different preparation methods, we used IR spectroscopy of adsorbed deuterated acetonitrile (CD_3CN). Sn/DeAlBEA was prepared with the same Sn weight loading to allow for a fair comparison. IR of adsorbed CD_3CN can distinguish between framework and extraframework tin sites and detect silanol nests, allowing quantitative measures of material Lewis acidity as preparation procedures change. Figure 4.2 shows the IR results of adsorbed CD_3CN on Sn/DeAlBEA prepared in different ways. Table S4.2 includes the integrated areas of these peaks. The amount of tin introduced into the framework will correlate with the Lewis acidity of the catalyst. Tin oxide moieties will not contribute to Lewis acidity. IR of adsorbed pyridine exhibits peaks corresponding to CD_3CN adsorbed to Lewis acid sites (2316 - 2308 cm^{-1}) and silanol nests (2275 - 2285 cm^{-1}).[255,256] Additionally, the CD_3CN frequency can be used to distinguish between different framework tin sites. Open Sn sites display a frequency of adsorbed CD_3CN at 2316 $cm^{-1,}$ while closed sites have a peak at 2308 cm^{-1}.[244,266,267] The wavenumber shift has also been attributed to potential solvent effects[268] or a distribution of Sn sites[267], but the lack of clear shoulders on the 2308 cm^{-1} peaks for these Sn/DeAlBEA suggests the majority of Sn sites are closed. All the preparation methods result in a peak at 2308 $cm^{-1,}$ indicating closed tin sites are present. Ethanol wetness impregnation with an $SnCl_2$ precursor results in the largest Lewis acid peak and the most significant decrease in silanol nest peak, indicating this method is most effective at producing framework Sn sites.

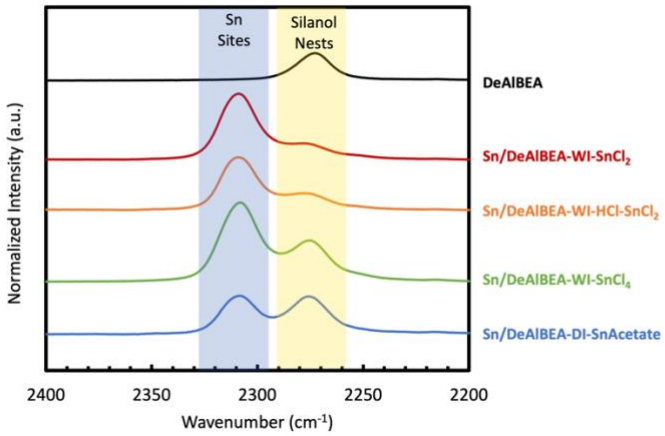

Figure 4.2. IR of deuterated acetonitrile on DeAlBEA and Sn/DeAlBEA catalysts.

In summary, several tin introduction techniques were investigated. IR of adsorbed CD_3CN indicates that wetness impregnation with ethanol is the most effective preparation technique to introduce tin into the framework sites of DeAlBEA.

4.3.2 Effect of Sn loading

While other studies have studied the effect of Sn loading on Sn/DeAlBEA structure, the Sn was introduced via hydrothermal synthesis or not well characterized. Here, we have prepared Sn/DeAlBEA with ethanol wetness impregnation at different Sn loadings and will characterize these samples to determine the effect of Sn loading on the Sn/DeAlBEA structure. The physicochemical properties, metal weight loading, and metal atom distribution are reported in Table 4.1. Surface area analysis with BET and pore volume analysis with all samples show a slight decrease in surface area with Sn introduction. The small changes in surface area with metal introduction support the lack of large particles, as these would result in significant decreases in surface area with increasing weight loading. Elemental analysis confirms that tin remains in the catalyst after calcination at 873 K. Elemental analysis results indicate that while most Sn has been exchanged with the supports, a small amount of chlorine from the $SnCl_2$ precursor remains in the catalyst system, especially for higher tin loadings.

Powder XRD patterns are included in Figure 4.3. Powder X-ray diffraction (XRD) can be used to detect crystalline domains. This technique detects crystalline structures, like BEA zeolite framework and bulk tin species (e.g., SnO_2, $SnCl_2$). The presence of BEA zeolite peaks in dealuminated samples confirms that the dealumination and tin introduction do not affect the crystalline structure of the zeolite framework. The additional peaks in the Sn/DeAlBEA samples can be attributed to tin oxide particles, indicated by the reference diffraction pattern at the bottom of the chart. The detection of SnO_2 by XRD in the as-prepared samples is consistent with similar Sn/SiO_2 catalysts reported in the literature.[41] At higher Sn loadings (Sn/Al > 0.4), peaks corresponding to bulk SnO_2 appear. The intensities of these SnO_2 peaks increase with increasing tin weight loading. Additionally, the lack of peaks for $SnCl_2$ indicates the absence of unreacted precursors in the catalyst samples. This result implies that the chlorine detected via elemental analysis exists as chlorine ligands on Sn, silanol groups, or small tin chloride clusters, not bulk $SnCl_2$ particles. XRD can only detect nanoparticles greater than 2.5-2 nm in size and ~1% by volume.[269–272] The absence of these XRD peaks does not entirely negate the existence of these extra-framework particles. Instead, it indicates that these domains are either absent or smaller than the XRD detection limit.

Table 4.1. Surface area and metal loading for Sn/DeAlBEA at different Sn loadings.

Sample	Sn wt.%	Cl wt.%	Sn/Al	Si/Sn	Sn atom /nm^2	Surface Area (m^2/g)	Pore Volume (cm^3/g)
DeAlBEA	0	0	0	-	0	515.6	0.37
H-BEA	0	0	0	-	0	469.7	0.33
Sn/DeAlBEA-0.67	8.17	1.3	0.67	18.7	0.84	492	0.35
Sn/DeAlBEA-0.4	5.15	0.71	0.40	31.6	0.51	511.9	0.37
Sn/DeAlBEA-0.28	3.76	<0.6	0.28	45.0	0.36	534.5	0.37

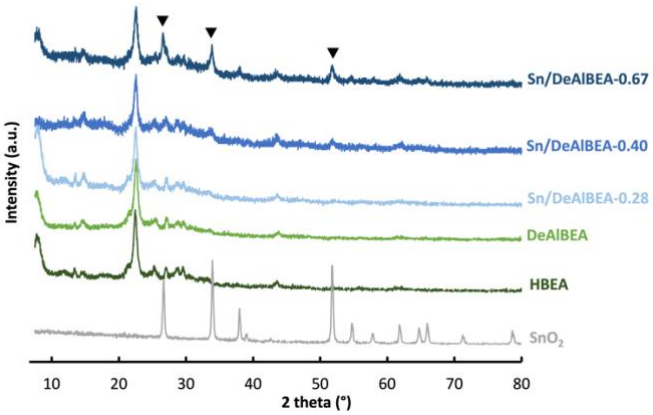

Figure 4.3. XRD patterns of HBEA, DeAlBEA, Sn/DeAlBEA, and SnO_2.

Ultraviolet-visible spectroscopy (UV-vis) can provide additional information about the structure of Sn in these materials. Specifically, previous studies have used UV-vis to distinguish between tetragonal framework Sn (200 - 220 nm), nano-SnO_2 clusters (230 - 255nm), and bulk SnO_2 particles (280 - 290 nm).[33,43,273,274] DRUV-vis spectra of Sn/DeAlBEA catalysts and bulk SnO_2 are shown in Figure 4.4. The DRUV-vis spectrum of tin oxide exhibits a broad absorption band between 200 and 300 nm. The DRUV-vis spectra of Sn/DeAlBEA-0.2, Sn/DeAlBEA-0.36, and Sn/DeAlBEA-0.5 all show a peak at 200 nm corresponding to isolated tetrahedral Sn. The DRUV spectrum of Sn/DeAlBEA-0.5 exhibits a peak at 250 nm, which can be attributed to SnO_2. These results suggest that SnO_2 particles begin to form around 0.36 Sn/Al and increase with increasing Sn loading, consistent with the XRD results from Figure 4.3. The edge energies of these materials can also be compared with a Tauc plot (Figure 4.4C). Increasing Sn content results in decreasing edge energy for Sn/DeAlBEA catalysts. The 250 nm peak in the Sn/DeAlBEA-0.5 spectrum exhibits a similar edge energy (4.03 eV) to that calculated for the bulk SnO_2 (3.97 eV), further confirming the. These peak positions and edge energies are also consistent with previous literature studies of SnO_2.[275–277] UV-vis suggests framework Sn(IV) sites exist for all Sn/DeAlBEA catalysts, and some SnO_2 species are present at the highest Sn loadings (Sn/DeAlBEA-0.5). UV-vis cannot distinguish between open and closed Sn sites.

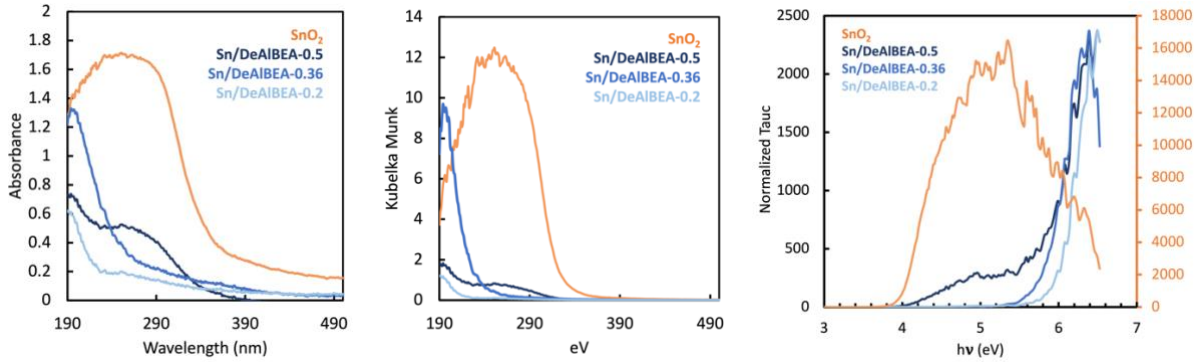

Sample	Peak (nm)	Edge Energy (eV)	Peak (nm)	Edge Energy (eV)
SnO_2	251	3.97	-	-
Sn/DeAlBEA-0.2	-	-	190	5.97
Sn/DeAlBEA-0.36	-	-	195	5.93
Sn/DeAlBEA-0.5	250	4.03	192	5.58

Figure 4.4. DRUV-vis spectra of Sn/DeAlBEA catalysts and SnO_2 in absorbance, Kubelka-Munk Units, and Tauc plots.

The IR spectra for DeAlBEA and Sn/DeAlBEA are shown in Figure 4.5A. The sharp peaks at 3745 cm^{-1} are attributed to the OH vibration of isolated, acidic silanols, while the broader peak at 3674 cm^{-1} is attributed to vicinal and bulk OH groups.[278] The 3610 cm^{-1} peak in the H-BEA sample can be attributed to Brønsted acid OH vibrations.[30,279,280] The broad peak at ~3500 cm^{-1} evident for the DeAlBEA spectrum originates from OH vibrations from silanol nests. For Sn/DeAlBEA, a decrease in the areas of the silanol nest peak (3500 cm^{-1}) and of the isolated silanol peak (3745 cm^{-1}) with metal introduction supports the idea that the exchange of Sn species occurs with the protons in these OH groups. For all the samples except H-BEA, the absence of peaks around 3610 cm^{-1} confirms the lack of Brønsted acid sites in the catalysts.

IR spectra of adsorbed pyridine are used to identify relative amounts and strengths of Brønsted and Lewis acid sites. IR spectra of adsorbed pyridine are shown in Figure 4.5B. The peaks at 1445 cm^{-1} and 1600-1612 cm^{-1} correspond to pyridine interacting with Lewis acid sites. Increases in the frequency of the pyridine peak above 1600cm^{-1} indicate increasing Lewis acid strength.[257] The peaks at 1544 cm^{-1} and 1640-1630 cm^{-1} correspond to pyridine coordinated to Brønsted acid sites. The peak at 1490 cm^{-1} corresponds to pyridine interactions with both Lewis and Brønsted acid sites. The peak at 1544 cm^{-1} for H-BEA is assigned to the pyridinium ion, indicating Brønsted acidity. In the H-BEA spectra, the 1630-1640 cm^{-1} peaks correspond to pyridine bonded to Brønsted acid sites, while peaks around 1450 cm^{-1} correspond to the vibration of the neutral pyridine ring.[258] Dealuminated BEA exhibits peaks at 1592 and 1445 cm^{-1}, which can be ascribed to the interaction of pyridine with H atoms of the Si−OH groups in the silanol nests.[259] No peaks corresponding to Brønsted acid sites (1544 cm^{-1}) are present for DeAlBEA or Sn/DeAlBEA. In the spectra of pyridine adsorbed on Sn/DeAlBEA, the decrease in the areas of the peaks for pyridine adsorption on Si-OH groups in silanol nest upon introduction of Sn suggests that this element is incorporated into the silanol nests. The residual peaks corresponding to silanol nests indicate some silanol nests remain, potentially inaccessible to tin. The consistent peak silanol peak areas across weight loadings suggest that the remaining silanol groups may not be accessible for tin exchange. Additionally, the lack of increase in peak area is consistent with the formation of tin oxide at higher Sn loadings, as evidenced by XRD. Notably, SnO_2 does not adsorb pyridine at these conditions.

IR spectra of adsorbed CD_3CN adsorbed on Sn/DeAlBEA, shown in Figure 4.5C, were used to identify open and closed Sn sites and silanol nests. IR spectra of adsorbed CD_3CN are. Similarly to the results at an intermediate loading for different preparation methods (Figure 4.2), all Sn/DeAlBEA catalysts exhibit peaks corresponding to closed Sn sites (2308 cm^{-1}) and silanol nests (2275 - 2285 cm^{-1}).[244,255,256] There is no evident shoulder or other evidence for open Sn sites (2316 cm^{-1}).[244,266,267] A consistent decrease in silanol peak area is observed for Sn/Al ratios from 0.16 to 0.40, but the highest loading Sn/DeAlBEA exhibits a larger silanol nest peak. This change at high Sn/Al ratios also coincides with the formation of SnO_x species detected by XRD and UV-vis spectroscopy. The IR peak of CD_3CN adsorbed to Sn-OH species has been calculated as red-shifted from CD_3CN adsorbed to Si-OH.[281] The lack of red-shift in the peak suggests that the observed increase in the 2275 cm^{-1} peak is not a result of Sn-OH formation. Likely, this increase in peak intensity is due to the creation of Si-OH groups upon Sn_xO_y formation.

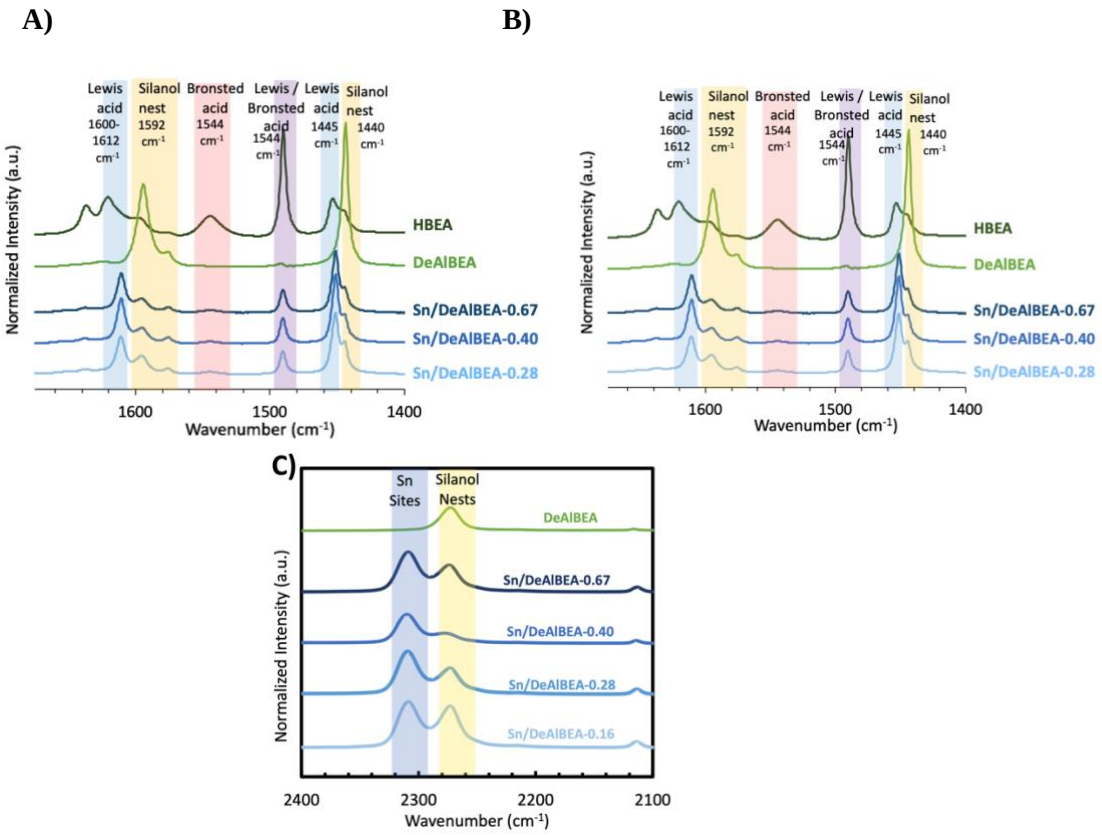

Figure 4.5. IR spectra of A) dehydrated supports and Sn/DeAlBEA and B) Pyridine adsorbed on supports and Sn/DeAlBEA. C) CD_3CN adsorbed on DeAlBEA and Sn/DeAlBEA.

X-ray absorption spectroscopy (XAS) was also used to probe the oxidation state and environment of Sn for two Sn loadings on Sn/DeAlBEA. Figure 6 shows the XAS spectra for Sn/DeAlBEA and tin reference materials and the relevant fitting parameters. The fit is presented in Figure S1. The XANES edge position and white line height of Sn/DeAlBEA closely resemble those of SnO_2, suggesting Sn(IV) with oxygen nearest neighbors. The EXAFS fitting results for both loadings suggest four Sn-O bonds, consistent with framework Sn(IV). The magnitude of the Fourier transform shows one clear peak at a distance consistent with an Sn-O path. Additional fits, including Sn-Sn and Sn-Cl paths, are included in Table S3, but these paths do not improve the level of fit (i.e., reduced χ^2 and R-factor). Sn metal (Sn foil) and $SnCl_2$ are included as reference materials for comparison, but the EXAFS spectra for these materials are quite different from that of Sn/DeAlBEA. Our fitting results are consistent with previous XAS studies of Sn/BEA[42,253] and support the identification of Sn in Sn/DeAlBEA as Sn(IV) sites within the BEA framework.

In summary, XAS, UV-vis spectroscopy, and IR of adsorbed CD_3CN provide characterization support for the creation of framework Sn(IV) upon Sn introduction to DeAlBEA. The decrease in IR peaks corresponding to silanol nests after Sn introduction also supports this structure. As tin loading increases, SnO_x species begin to form (Sn/Al > 0.4), as evidenced by IR of adsorbed pyridine, XRD, and UV-vis spectroscopy. No evidence of Sn^0 is present for these Sn/DeAlBEA materials.

A)

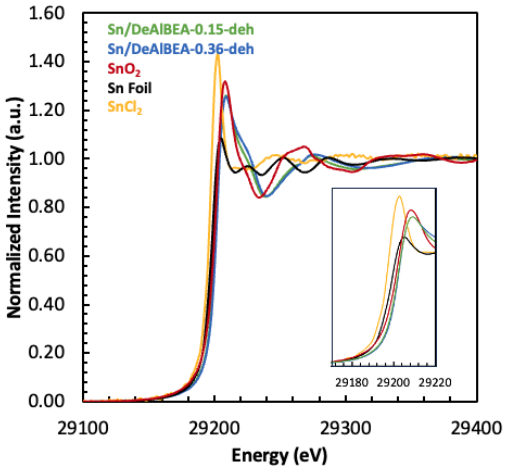

B)

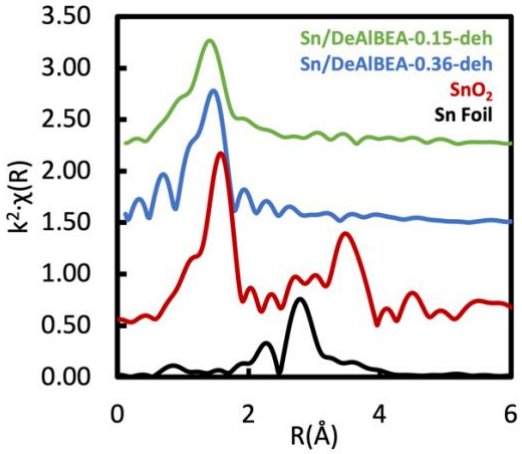

C)

Catalyst	Red. chi-square (χ_ν^2)	R-factor	Path	N	R (Å)	σ^2 (10^{-3}Å^2)	ΔE_0 (eV)	R range (Å)	k range
Sn/DeAlBEA-0.15	832.85	0.019	Sn-O	4.43 ± 0.38	1.92± 0.0097	6.43 ± 1.28	0.96 ± 1.31	1-3	3-12.5
Sn/DeAlBEA-0.36	1518.2	0.032	Sn-O	4.05 ± 0.33	1.91± 0.0087	3.15 ± 1.06	4.00 ± 1.26	1-3	3-12.5

Figure 4.6. A) XANES spectra and B) EXAFS of dehydrated Sn/DeAlBEA-0.15, Sn/DeAlBEA-0.36, and tin reference materials. C) Fitting parameters for dehydrated Sn/DeAlBEA-0.15 and Sn/DeAlBEA-0.36. Amplitude reduction factor determined from SnO_2 and fixed in Sn/DeAlBEA fitting to 0.770.

4.3.3 Propane Dehydrogenation Activity Results

DeAlBEA exhibits some activity for dehydrogenation and cracking above 773K, although the bulk of this activity can be attributed to thermal cracking and dehydrogenation. The activities of DeAlBEA and the blank reactor are included in Table S4.1 of the supplemental information. The empty reactor was tested by running a reaction with no catalyst present, only quartz wool. The conversion as a result of thermal cracking and dehydrogenation is accounted for in the activity of the supports. To determine the effects of tin alone, the activity of the supports, which is primarily represented by the thermal activity, was subtracted from the results for the metal-exchanged catalysts. The results presented indicate whether they are raw data or are corrected for the effects of DeAlBEA.

In the literature for Sn on siliceous supports, the catalyst is typically reduced in hydrogen prior to use for propane dehydrogenation.[36,38,41] To validate the need for this pretreatment and elucidate its effect, reactions were run with and without the hydrogen pretreatment. The comparison of these results is included in Figure S4.2. The impact of the hydrogen pretreatment noticeably increases conversion and propene selectivity. Figure 4.7 shows the conversion, selectivity, site-time yield (STY), and forward rate constant (k_f) for PDH over Sn/DeAlBEA. All Sn/DeAlBEA catalysts exhibit stable conversion and high C_3H_6 selectivity. The highest Sn loading of Sn/DeAlBEA shows the highest propane dehydrogenation activity. Additionally, increasing Sn systematically increases STY and the forward rate constant for Sn/DeAlBEA. These initial increases in rates with increasing Sn content are consistent with previous studies changing Sn content in Sn/SiO_2 and Sn/BEA. Further increases in Sn content have also shown an increase

initially, followed by decreases at higher Sn loadings.[36,39,41,247] As the amount of tin increases, there are noticeable differences in the activity of Sn/DeAlBEA, further suggesting a change in the tin speciation with changes in tin composition. DFT calculations have suggested that open Sn sites are more active for PDH than closed Sn sites.[247] Increasing amounts of Sn open sites at intermediate Sn loadings could explain these increases in activity with increasing Sn loading.

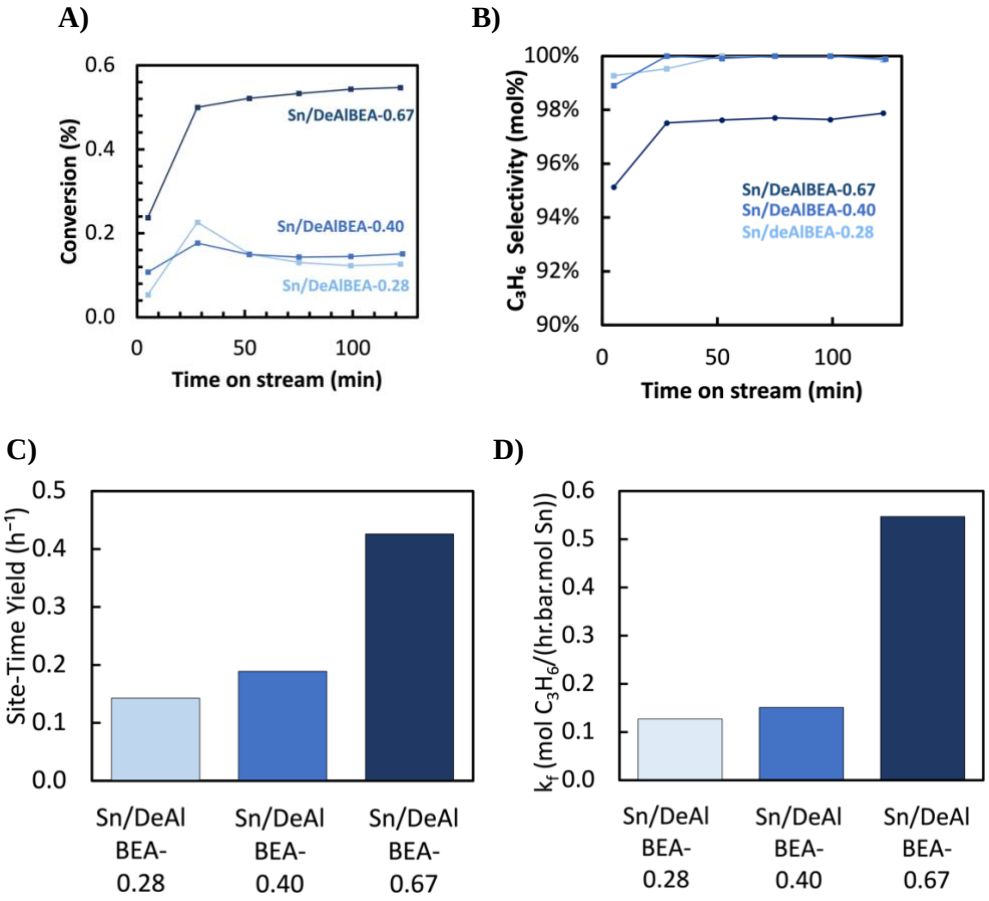

Figure 4.7. Propane dehydrogenation activity of Sn/DeAlBEA at different Sn/Al ratios. A) conversion, B) C_3H_6 selectivity, C) STY (mol C_3H_8/mol Sn h^{-1}), and D) forward rate constant.

Figure 4.8 shows the effect of propane partial pressure on the propane conversion and selectivity to propene. Sn/DeAlBEA exhibits first-order propane partial pressure dependence in agreement with previous studies of PDH over Sn/BEA.[247] First-order kinetics are also consistent with other PDH studies over Lewis acid sites.[280,282]

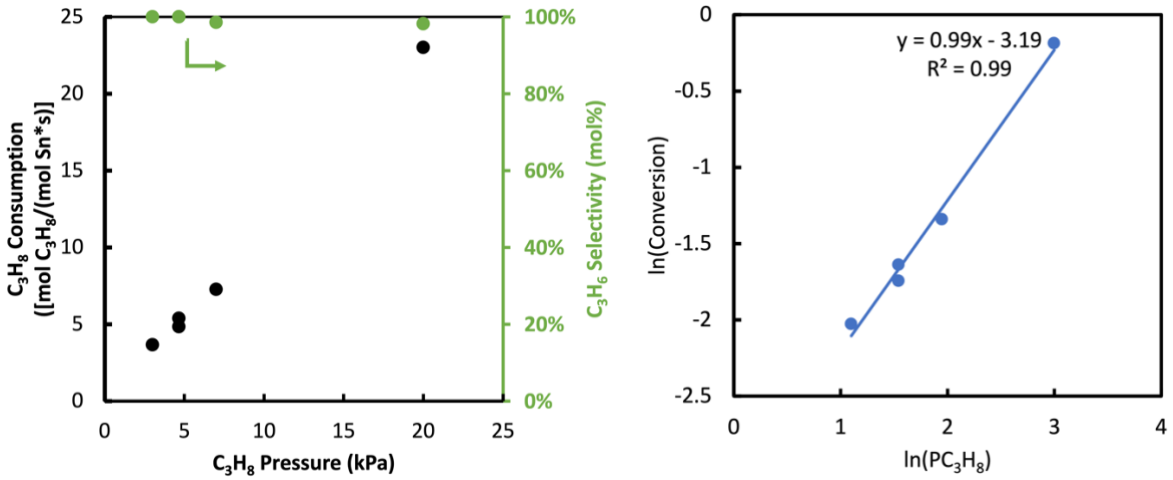

Figure 4.8. Partial pressure dependence of PDH over Sn/DeAlBEA-0.28.

The value for k_f was calculated to enable comparisons with previous studies of PDH conducted with supported Sn catalysts carried out at different temperatures, propane partial pressures, and flow rates. The derivation of k_f is included in the supplemental information. This metric accounts for differences in the conditions and conversions by including the approach to equilibrium. Figure 4.9 shows the forward rate constants for Sn/DeAlBEA and Sn/SiO_2. It should be noted that Sn/SiO_2 exhibits higher values of k_f than Sn/BEA. A similar result was in the present work (Figure S4.3), even when Sn surface loading was controlled to account for the differences in surface areas. The Sn/DeAlBEA catalysts exhibit similar activities to previously prepared Sn/BEA catalysts but lower k_f values than Sn/SiO_2.[36,38,40,41,247] The large range of forward rate constants for Sn/SiO_2 and Sn/meso-SiO_2 can be explained by the range of Sn loadings (0.83 - 30.0 wt.% Sn) as well as the differences in preparation methods by different authors. The higher forward constants for Sn/SiO_2 catalysts could be explained by a higher fraction of open Sn sites, which have been calculated to have higher activity.[247] Table 4.2 includes the DFT calculated apparent activation energies and resulting calculated relative PDH rates for different Sn open and closed sites. Notably, an 83 kJ/mol decrease in activation energy for PDH from closed Sn sites to open Sn sites with three hydroxyls results in 4 orders of magnitude increase in the reaction rate. An increase in open Sn sites on silica supports can account for the dramatic increase in the forward rate constants for Sn/SiO_2 compared to Sn/DeAlBEA.

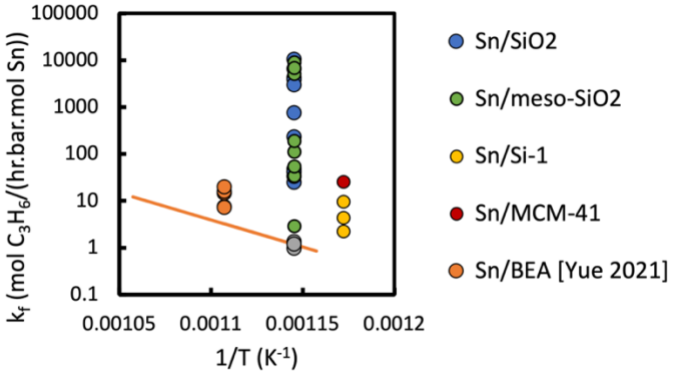

Figure 4.9. Comparison of forward rate constant for Sn/DeAlBEA, Sn/SiO_2, and Sn/MCM-41 catalysts. The reported activation energy for Sn/DeAlBEA[247] is included as an orange line.

Table 4.2. Activation Energies and Relative Rates for PDH over Different Sn Sites. Sn structures and activation energies from [247]. A temperature of 873K was used to calculate the rate.

Sn Site	E_a (kJ/mol)	Relative PDH Rate
Sn-(O-Si)$_4$ (closed) – direct PDH Mechanism	300	1
Sn-(O-Si)$_4$ (closed) – indirect PDH Mechanism	266	108
HO-Sn-(O-Si)$_3$ (open)	237	5884
(HO)$_2$-Sn-(O-Si)$_2$ (open)	220	61214
(HO)$_3$-Sn-(O-Si) (open)	217	92546

4.4 Conclusion

Several Sn introduction techniques (e.g., wetness impregnation and solid-state ion exchange) and combinations of Sn precursors were evaluated for Sn Lewis acid introduction into DeAlBEA. This evaluation concluded that ethanol wet impregnation is the most effective means for introducing Sn(IV) into silanol nests of DeAlBEA, as confirmed by IR of adsorbed CD_3CN. Introduction of Sn results in Lewis acidity in Sn/DeAlBEA catalysts, as evidenced by CD_3CN and pyridine IR. Additionally, IR of adsorbed pyridine confirms the absence of Brønsted acid sites on these Sn/DeAlBEA catalysts. IR spectra of adsorbed CD_3CN support the conclusion that Sn is introduced in a closed framework site for all loadings (Sn/Al = 0.16 - 0.67). In addition to framework Sn sites, XRD and UV-vis spectroscopy show evidence of SnO_2 particles in the as-prepared catalyst samples at Sn/Al > 0.4. XRD also confirms that the introduction of Sn into DeAlBEA does not alter the BEA framework structure. XAS and UV-vis spectroscopy of Sn/DeAlBEA corroborate that framework Sn(IV) species dominate at Sn/Al $\leq$ 0.4. Sn sites in Sn/DeAlBEA exhibit low propane dehydrogenation activity but high stability and propene selectivity. The STY for propane dehydrogenation increases with Sn loading for Sn/DeAlBEA, attributable possibly to the formation of more open Sn sites. The forward rate constant for Sn/DeAlBEA prepared in this study is lower than that of Sn/SiO_2 but similar to that reported previously for Sn/DeAlBEA. The higher values of k_f for Sn/SiO_2 are possibly due to a greater fraction of Sn open sites when Sn is dispersed on SiO_2 as opposed to its introduction into the silanol nests of DeAlBEA.

4.5 Acknowledgments

This research used resources of the Advanced Photon Source, a U.S. Department of Energy (DOE) Office of Science user facility operated for the DOE Office of Science by Argonne National Laboratory under Contract No. DE-AC02-06CH11357.

4.6 Supporting Information

4.6.1 Sn Catalyst Preparation Summary

Table S4.1. Summary of Sn preparation Methods

Ref	Support	Prep	Wash	Calcine	Sn precursor	Solvent	Reaction	Sn species	Evidence?
[262]	SBA-15	WI	N	dry, calcine at 823 K for 6 h	$SnCl_4*5H_2O$; $Sn(CH_3COO)_2$	EtOH	n.r.	Sn(IV), Sn(II)	Mossbauer
[263]	FAU	HS	H_2O	calcine	$SnCl_2*2H_2O$, $SnCl_4*5H_2O$	sol gel	n.r.	Sn *(F)*	XRDM SiNMR
[283]	Y	SSIE	Y		$SnCl_2*2H_2O$	N	n.r.	SnO2	XRD
[233]	BEA	HS	N	dry and calcine	$SnCl_4*5H_2O$	sol gel	Ox. Anisaldehyde, Cyclohexanone	Sn(IV) *(F)*; SnO_2	XAFS, EDS, STEM, TEM,
[34]	BEA	HS	H_2O	dry; calcine at 853 K for 6 h	$SnCl_4*5H_2O$ or $SnMe_4*5H_2O$	sol gel	sugar iso.	Sn (IV) *(F)*	UV-vis, IR, Sn NMR
[43]	BEA, SiO_2	HS; IWI	H_2O	dry, calcine at 853 K for 10 h	$SnCl_4$ or SnO_2	Sol gel ; H_2O	Iso. glucose to fructose	SnO_2; Sn(IV) open and closed	NMR, SEM, XRD, DRUV-vis
[284]	SiO_2	graft THF	N	calcine for 6 h at 773 K	$[(Si(CH_3)_3)_2N_2]Sn$	THF	isobutanol dehydration	Sn(IV), Sn(II)	XPS
[285]	SBA-15	HS	H_2O	dry 323 K overnight. Calcine at 773 K for 12 h	$SnCl_4*5H_2O$	sol gel	n.r.	Sn(IV) isolated, SnO_2	SAXS, XRD, UV-vis
[286]	silicates	HS			$SnCl_4*5H_2O$	sol gel	n.r.		
[287]	BEA, MCM-41	HS	H_2O	dry at 333 K for 24 h; 813K for 1 h in N_2, 6 h in air	$SnCl_4*5H_2O$	sol gel	MPV	Sn(IV) *(F)*	NMR, py-IR, XRD, AAS
[288]	MCM-41	graft	Toluene	dry at 373 K; calcine for 3 h at 853 K	nBu_3SnCl, nBu_2SnCl_2, $nBuSnCl_3$,Me_2SnCl_2, $Sn(OtBu)_4$	toluene; triethylamine	BV	Sn(IV)	IR, AAS,
[33]	Sil-1, MFI	HS	H_2O	dry at 338 K, calcine at 823 K for 5 h	$SnCl_4*5H_2O$	sol gel	Glucose iso.	Sn(IV) *(F)*; small SnO2	UV-vis
[289]	MCM-48	add to gel post synth			$SnCl_2$	sol gel post synth	Ox. benzyl alcohol to benzaldehyde	Tet. Sn	UV-vis
[290]	Sil-1	HS	H_2O	dry at 423 K, calcine at 773 K for 2 h; or at 773 K in N_2 then introduce O_2 for 5 h	$SnCl_4*5H_2O$	sol gel	n.r.	Sn(IV) *(F)*	IR, NMR, Mossbauer
[291]	Sil-1	HS	H_2O	dry at 373 K, calcine at 573K for 3 h, and 823 K for 7 h	$SnCl_4*5H_2O$	sol gel	n.r.	Sn *(F)*	
[292]	ZSM-5, Y, SiO_2, Al_2O_3	SSIE			Sn^0	n/a	n.r.		
[293]	BEA	SSIE	N	heat to 823 K in N_2 (3 h) then air (3 h)	$Sn(CH_3COO)_2$	n/a	BV	Sn(IV) *(F)*	
[42]	BEA	SSIE	N	heat to 823 K in N_2 (3 h) then air (3 h)	$Sn(CH_3COO)_2$	n/a	MPV, glucose iso.	Sn(IV) and Sn_xO_y	UV-vis, XAFS, XRD, Sn NMR
[218]	TN	IE	H_2O	dry in vacuum	$SnCl_2*2H_2O$	MeOH, H_2O	BV	Iso. $[Sn(IV)(OH)_x(H_2O)_{5-x}]^{(4-x)+}$	XAFS, Sn NMR, XRD
[294]	SnO_2	Precip.	MeOH	dry at 373 K	SnC_2O_4	IPA + aq NH_4OH	cyclohexanol DH	SnO_2	
[295]	FAU	TIE			$SnCl_2$	n/a	n.r.	Sn(II) with Cl clusters	crystallography

[296]	Y,MOR, FER, Si-1	SSIE	N	323 K for 30 min, vacuum 3 h, 373 K; 20 h 473 K, 20 h.; 673 K for 1.5 h in O_2	$SnCl_2$*2H_2O	n/a	n.r.	SnO_2, $SnCl_2$	Mossbauer
[297]	MOR	SSIE	H_2O	673 K for 1.5 h in O_2	$SnCl_2$*2H_2O	n/a	n.r.	$Sn^{?+}$, SnO_2at high wt. %	XRD, HF analysis
[298]	SBA-15	CVD	2M KOH	dry 1 day at 413 K	tin chloride?	n/a	n.r.	SnO_2	EDS,
[248]	ZSM-5, Y, USY	AqIE			$SnCl_2$	EtOH	OPDH		
[299]	SiO_2	CVD			$SnBu_4$	n/a	isobutane DH	Si-O-$SnBu_3$	NMR
[242]	MMT	WI	H_2O	dry at 333 K in vacuum for 24 h	$SnCl_2$*2H_2O	H_2O, HCl	oxidation of ketones	Positive Sn	FTIR
[40]	SiO_2	HS	H_2O	dried overnight at 353 K and calcined 823 K in air for 6 h	$SnCl_4$	H_2O, sol gel	PDH	Sn^0, Sn(II), Sn(IV), SnO_2	XPS, XRD, H_2 TPR
[300]	Sil-1, Sil-2, ZSM-5	HS	H_2O	dry at 383 K, calcine at 773 K	$SnCl_4$*5H_2O	sol gel	Ox. toluene, meta-Cresol, hydroxylation of phenol	Sn(IV) *(F)*	XRD, FTIR, Sn NMR, elemental analysis
[301]	Sil-1	HS	H_2O	dry at 383 K, calcine at 773 K	$SnCl_4$*5H_2O	sol gel	hydroxylation of phenol	Sn(IV) and SnO_2	Sn NMR, FTIR,
[204]	AlPO-5	HS	H_2O	dry; calcine for 12 h at 973 K	$SnCl_4$*5H_2O	sol gel	n.r.		
[302]	BEA	HS	N	dry; calcine at 853 K	$SnCl_4$*5H_2O	sol gel	BV	isomorphous Sn (IV), SnO_2	XAFS, TEM, XRD, EDS
[303]	Sil-1	HS	H_2O	dry at 383 K , calcine at 813 K for 12 h	$SnCl_4$*5H_2O	sol gel	hydroxylation of phenol	Sn(IV) isolated	
[304]	SBA-15	IE	EtOH	dry at 393 K overnight; calcine	$SnCl_4$*5H_2O	EtOH	carbohydrates to methyl lactate	Sn(IV); SnO_2 at high wt.%	UV-vis, FTIR, TEM, Mossbauer, Raman, TEM
[305]	MCM-36	deBor; SSIE			$SnCl_4$*5H_2O	n/a	BV	Tet. Sn *(F)*	UV-vis, XRD
[306]	Mag	HS, IE			$SnCl_4$*5H_2O or Na2SnO3	H_2O	n.r.	Sn(IV)	DRUV-vis, H_2 TPR
[307]	SBA-15	HS, organo silane, NH4F	H_2O	dry; boil with EtOH, calcine at 773 K for 5 h	$SnCl_4$	sol gel	BV, MPV	Sn(IV) *(F)*	XRD, FTIR, DRUV-vis, NMR, TEM
[308]	SBA-15	HS	H_2O	dry overnight at 373 K, Calcine at 813 K for 6 h	$SnCl_4$*5H_2O, $Sn(CH_3COO)_4$	sol gel	n.r.	Sn(IV) *(F)*	
[309]	BEA	IE	H_2O	dry at 353 K, calcine at 823 K for 4 h	$SnCl_2$*2H_2O	H_2O	Strecker	Sn(II), SnO_2	
[264]	SBA-15	WI	N	calcine at 823 K for 6 h	$SnCl_4$*5H_2O	EtOH	transesterification diethyl malonate	Si-O-Sn^{2+}-O-Si, SnO_2	NH_3TPD, Mossbauer, Si, Sn NMR,
[310]	SBA-15	IWI	N	dry, calcine at 823 K for 6 h	$SnCl_4$*5H_2O; $Sn(CH_3COO)_2$	EtOH	transesterification	Sn(IV), Sn(II)	Mossbauer
[311]	Sil-1, MFI	HS	H_2O	dry at 353 K calcine at 373 K for 1 h and 823 K for 8 h	$SnCl_4$*5H_2O	sol gel	n.r.	Sn tet. *(F)*	UV-vis
[312]	Y	SS			SnF_2	H_2O	n-butane cracking	Sn(II) *(F)*	
[313]	SiO_2 xerogel	HS	N	dry	$Sn(NEt_2)_4$	sol gel	MPV	SnO_2; Sn^0	FTIR, NMR?, XRD, SEM; XRD

[314]	BEA	HS	H_2O	dry at 353 K, calcine at 823 K for 4 h	$H_2{}^{119}SnCl_6$; $SnCl_4*5H_2O$	H_2O	isobutene oligomerization	Sn(IV) *(F)* oct. (hyd.), Sn(IV) *(F)* tet. (deh.)	NMR, IR
[315]	BEA	HS	H_2O	dry at 353 K in air; heat at 823 K in air for 6 h	$SnCl_4*5H_2O$; $(NH_4)_2SnF_6$	H_2O; sol gel	DHA CH_3OH → $CH_3CH(OH)CO_2CH_3$	Sn(IV) *(F)*, SnO_2	XRD, SEM, SEM-WDS, ICPOES
[316]	Sil-1	HS	H_2O	dry at 383 K, calcine at 823 K for 5 h	$SnCl_4*5H_2O$, $SnCl_4$	sol gel	n.r.	Sn(IV) *(F)*	
[36]	SiO_2	IWI			$SnCl_2*2H_2O$	EtOH	PDH	Sn^0, Sn(II), Sn(IV) *(F)*	XRD, XPS
[39]	HMS	HS	H_2O	calcine for 5 h at 823 K; reduce for 0.5 h at 873 K	tin chloride	EtOH; sol gel	PDH	Si-O-Sn^{2+}; SnO_2	XPS; XRD
[41]	SiO_2	IWI	H_2O (on half)	dry in vacuum 24 h; calcine (873 K 3 h); OR wash, dry (303 K, 24 h) and calcine (873 K, 3 h)	$SnCl_4*5H_2O$	H_2O	PDH	At low wt.%: Sn(II), Sn(IV); at high wt.%: SnO, Sn^0	UV-vis, XPS, XRD,H_2 TPR
[38]	MCM -41, Si-1, Si-2	IWI			$SnCl_2*2H_2O$	EtOH	PDH	Si-O-Sn^{4+}, Si-O-Sn^{2+}, SnO_2 (dep. on wt.%)	UV-vis, H_2 TPR; UV-vis, XRD
[317]	Y	graft	N	vacuum for 10 h	$SnMe_4$	n/a	n.r.	Si-O-Sn-Me_3	XAFS
[261]	DeAlBEA	SSIE	N	calcine at 823 K	$Sn(CH_3COO)_2$	n/a	glucose iso.	Sn(IV) oct., SnO_2	NMR, Mossbauer, DFT
[274]	ZSM-5, Si-1	HS	H_2O	Calcine (823 K, 6 h.); 5% NH_4Cl at 353 K for 4 h, filter, wash, dry. Calcine at 823 K for 6 h	$SnCl_4*5H_2O$	sol gel	BV	Sn(IV) *(F)*	UV-vis, XPS, EDS,
[273]	Def. S-1 zeolite	DP with $SnCl_2$	N	dry at 383 K; calcine at 823 K for 6 h	$SnCl_2*2H_2O$	alcohol	Cond. $C_2H_4(NH_2)_2$ to TEDA and PIP	nano and bulk SnO_2	UV-vis, FTIR, SEM, H_2 TPR

SSIE: Solid state ion exchange; WI: wetness impregnation; IWI: incipient wetness impregnation; TIE: Thallous ion exchange; HS: hydrothermal Synthesis; deBor: deboronation
(*F)*: framework Sn; Tet- tetrahedral; Oct- octahedral
MPV: Meerwein Ponndorf Verley; BV: Baeyer Villiger; PDH: Propane dehydrogenation

4.6.2 Spectroscopy

Table S4.2. Integrated peak areas IR of Adsorbed CD_3CN normalized to DeAlBEA.

	Physisorb (2214 cm^{-1})	SiOH (2275 cm^{-1})	Open Sn site (2308 cm^{-1})
Sn/DeAlBEA-WI-$SnCl_2$	9.62	0.53	4.56
Sn/DeAlBEA-WI-$SnCl_2$-HCl	6.84	0.64	3.49
Sn/DeAlBEA-WI-$SnCl_4$ - HCl	8.99	1.46	4.68
Sn/DeAlBEA-DI-Sn(acetate)	8.32	1.46	2.41
DeAlBEA	1.00	1.00	0.00

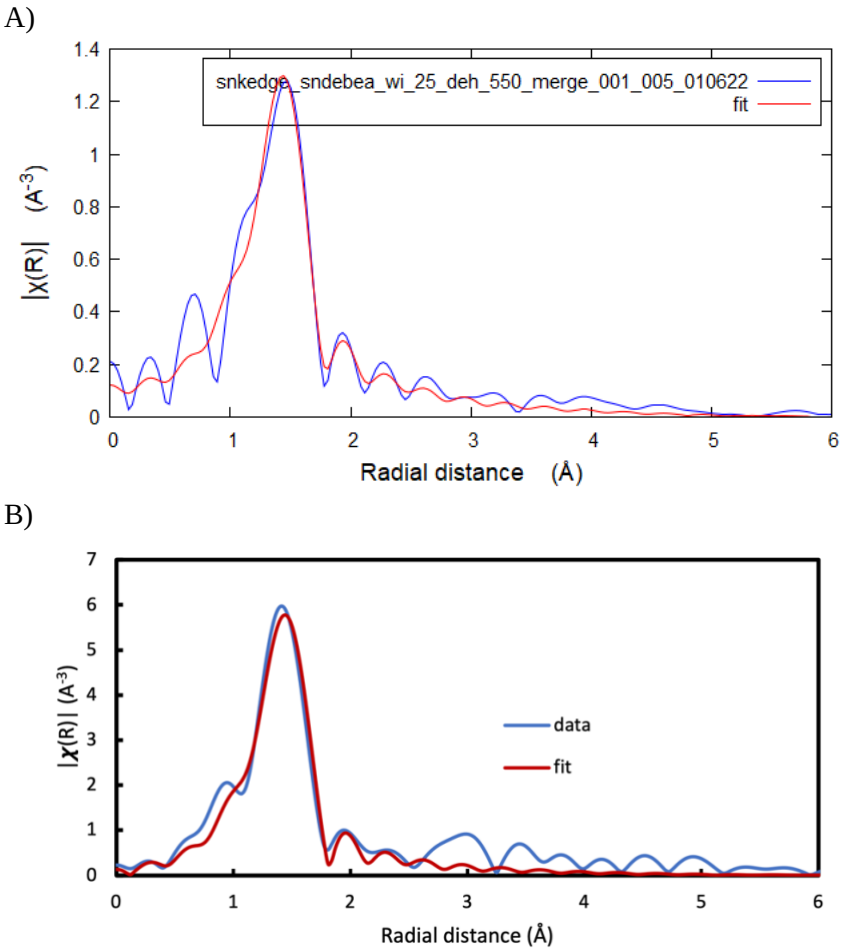

Figure S4.1. A) EXAFS fit of Sn/DeAlBEA-0.36. Fit 1b in Table S3. B) EXAFS fit of Sn/DeAlBEA-0.15.

Table S4.3. Fitting parameters for Sn/DeAlBEA-0.36. Amplitude reduction factor determined from SnO_2 and fixed in Sn/DeAlBEA fitting to 0.770.

fit	Red. chi-square (χ_v^2)	R-factor	Path	N	R (Å)	σ^2 (10^{-3}Å^2)	ΔE_0 (eV)	R range (Å)	k range
1a	1551.5	0.033	Sn-O	3.11 ± 0.258	1.91 ± 0.0087	2.96 ± 1.07	5.41 ± 1.26	1-3	3-12.5
1b	1518.2	0.032	Sn-O	4.05 ± 0.33	1.91 ± 0.0087	3.15 ± 1.06	4.00 ± 1.26	1-3	3-12.5
2	1600.9	0.023	Sn-O	4.14 ± 0.60	1.91 ± 0.0093	3.43 ± 1.13	3.79 ± 1.37	1-3	3-12.5
			Sn-Sn	0.377 ± **0.755**	2.54 ± 0.036	**1.16 ± 9.79**			
3a	1630.6	0.0254	Sn-O	4.163 ± 0.421	1.91 ± 0.010	3.36 ± 1.20	4.17 ± 1.72	1-3.5	3-12.5
			Sn-Sn	2.67 ± 3.07	3.15 ± 0.044	14.4 ± 11.3			
			Sn-Cl	1.41 ± 4.28	2.85 ± 0.107	23.3 ± 50.99			
3b	1782.2	0.0215	Sn-O	4.14 ± 0.38	1.91 ± 0.0098	3.41 ± 1.18	3.66 ± 1.29	1-3.0	3-12.5
			Sn-Sn	0.67 ± 0.45	3.11 ± 0.032				
			Sn-Cl	0.26 ± 0.36	2.79 ± 0101				
4	1915.9	0.030	Sn-O	4.29 ± 0.59	1.92 ± 0.014	3.61 ± 1.49	4.38 ± 1.98	1-3	3-12.5
			Sn-Cl	0.17 ± **0.31**	2.22 ± 0.096				

4.6.3 BET Calculation[318,319]

BET surface area was calculated from a linear regression of B_I vs P_{rel_I}

$$B_I = \frac{P_{rel_I}}{(1 - P_{rel_I}) * N_{ads_I}}$$

Where B_I is in g/cm^3 at standard temperature and pressure, P_{rel_I} is relative pressure, and N_{ads_I} is gas adsorbed after equilibration at the Ith dose in cm^3 at standard temperature and pressure.

The surface area is then calculated as follows:

$$SA_{BET} = \frac{CSA * 6.023 * 10^{23}}{22414\ cm^3 STP * 10^{18} \frac{nm^2}{m^2} * (S + Y_{INT})}$$

Where CSA is the adsorbate molecular cross-sectional area in nm^2 (0.162 nm^2 for N_2), S is the slope of the B_I vs P_{rel_I} fitting in g/cm^3 at standard temperature and pressure, Y_{INT} is the intercept of the B_I vs P_{rel_I} fitting in g/cm^3 at standard temperature and pressure.

4.6.4 Conversion, selectivity, STY, and forward rate constant calculations

The conversion was calculated on a molar basis, using the equation below:

$$Conversion\ \% = \frac{Inlet\ mol\ C_3H_8 - Outlet\ mol\ C_3H_8}{Inlet\ mol\ C3H8} * 100\%$$

Carbon selectivity was calculated using the following equation:

$$carbon\ selectivity\ \% = \frac{mol\ of\ product * C\#}{\sum(mol\ product * C\#)} * 100\%$$

Molar selectivity was calculated using the following equation:

$$mol\ selectivity\ \% = \frac{mol\ of\ product}{\sum(mol\ product)} * 100\%$$

Net Site-Time Yield was calculated using the following equation:

$$STY\ (h^{-1}) = \frac{\frac{mol\ propylene\ formed}{h}}{mol\ metal\ in\ catalyst\ mass}$$

Derivation of k_f:

This derivation makes the following assumptions:

- Propane dehydrogenation and propene hydrogenation reactions are reversible.
- The reaction occurs at low occupancy of Sn active sites, i.e., the inhibition of adsorbed products is negligible.
- The rate of propane dehydrogenation is first-order in propane partial pressure. Similar kinetics are applied for the reversible hydrogenation reactions.

$$C_3H_8 \leftrightarrow C_3H_6 + H_2$$

Net rate of propane dehydrogenation can be represented as :

$$R_{PDH} = k_{f-PDH}\ p_{C3H8} - k_{r-PDH}\ p_{C3H6}\ p_{H_2}$$

$$R_{PDH} = k_{f-PDH} p_{C3H8} \left[1 - \frac{1}{K_{ePDH}} \frac{\left(p_{C3H6} p_{H_2}\right)}{p_{C3H8}}\right]$$

$p_{C3H8} = \frac{p^0_{C3H8}(1-X)}{1+y^0_{C3H8}X}$; $p_{C3H6} = \frac{p^0_{C3H8}X}{1+y^0_{C3H8}X}$; $p_{H_2} = p_{C3H6} + p^0_{H_2} = \frac{p^0_{C3H8}(X+\theta_{H_2})}{1+y^0_{C3H8}X}$; $\theta_{H_2} = \frac{p^0_{H_2}}{p^0_{C3H8}}$

$$R_{PDH} = -F^0_{C3H8}\frac{dX}{dW}$$

$$-F^0_{C3H8}\frac{dX}{dW} = k_{f-PDH}\frac{p^0_{C3H8}(1-X)}{1+y^0_{C3H8}X}\left[1 - \frac{1}{K_{ePDH}} \frac{\left(\frac{p^0_{C3H8}X}{1+y^0_{C3H8}X}\frac{p^0_{C3H8}\left(X+\theta_{H_2}\right)}{1+y^0_{C3H8}X}\right)}{\frac{p^0_{C3H8}(1-X)}{1+y^0_{C3H8}X}}\right]$$

The forward rate constant (k_f) was calculated using the following equation:

$$k_{f-PDH} = \frac{F^0_{C3H8} MW_{Sn}}{m_{Sn} p^0_{C3H8}} \int_0^X \frac{(1 + y^0_{C3H8} X)}{\left((1 - X) - \frac{(p^0_{C3H8}) X \left(X + \theta^o_{H_2} \right)}{K_{ePDH}(1 - X)} \right)} dX$$

Table S4.4. Activity of DeAlBEA and the thermal activity of the blank reactor (with quartz wool). Reaction conditions: 873K, 4.67 kPa C_3H_8, 1 atm, 20 mL/min total, 50. mg cat.

Sample	Conversion (%)	CH_4 Selectivity (%)	C_2H_4 Selectivity (%)	C_3H_6 Selectivity (%)
DeAlBEA	0.89	29	29	42
Blank	1.02	29	30	40

Table S4.5.Turnover frequencies for Sn/DeAlBEA catalysts. Raw data

Sample	Conversion (%)	C_3H_6 selectivity (%)	TOF ((mol C_3H_6/h)/ mol M)
Sn/DeAlBEA – 0.4	0.82	57.35	0.80
Sn/DeAlBEA – 0.5	0.92	54.36	0.62
Sn/DeAlBEA – 0.8	1.27	77.81	0.68
DeAlBEA	0.89	42	-

Table S4.6. Turnover frequencies for Sn/DeAlBEA catalysts. Activity of the supports (including thermal activity) subtracted from results.

Sample	Conversion (%)	C_3H_6 selectivity (%)	TOF ((mol C_3H_6/h)/ mol M)
Sn/DeAlBEA – 0.4	0.084	100.	0.14
Sn/DeAlBEA – 0.5	0.15	100.	0.19
Sn/DeAlBEA – 0.8	0.57	95	0.43
DeAlBEA	0.89	42	-

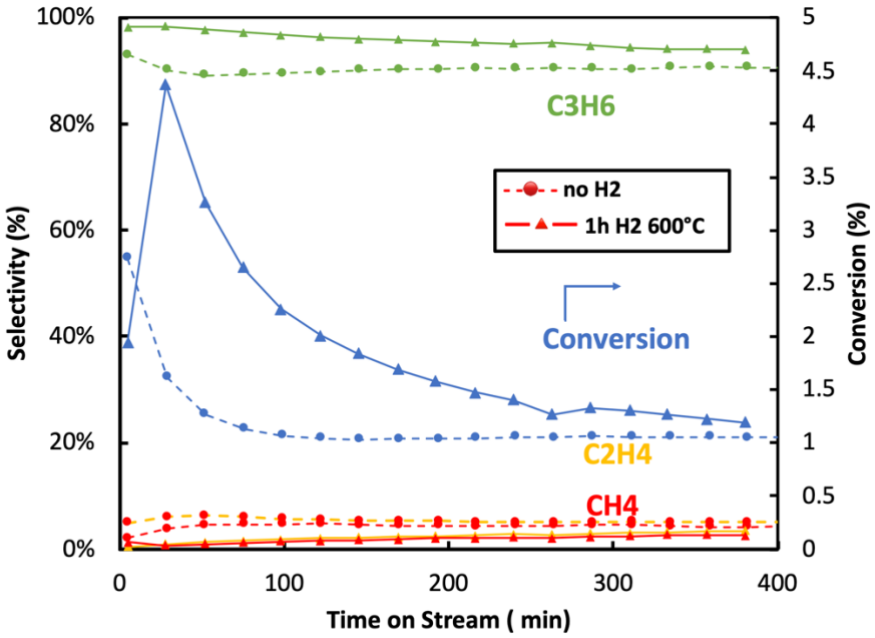

Figure S4.2. Effect of 1 h H_2 pretreatment on Sn/DeAlBEA PDH performance.

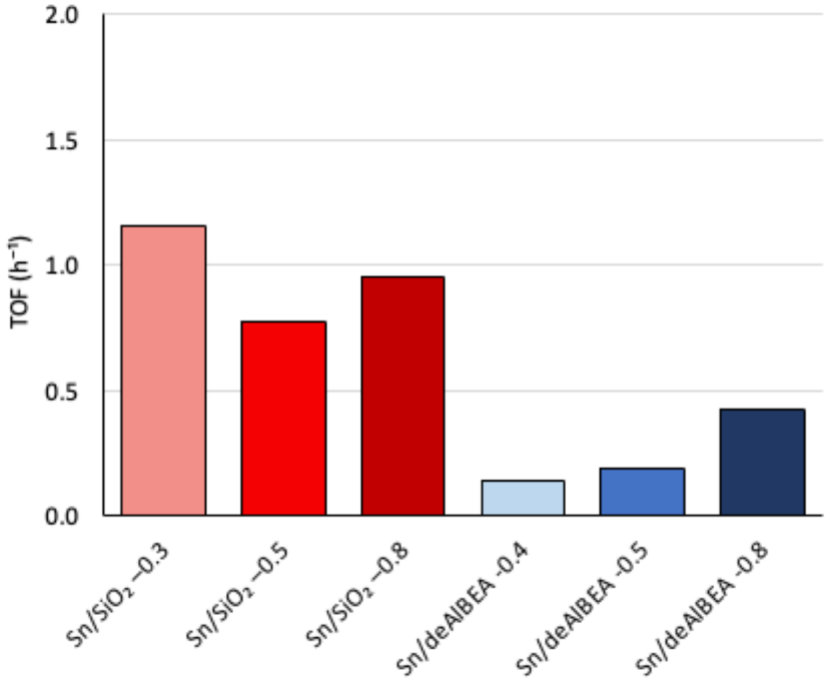

Figure S4.3. Turnover frequencies for PDH over Sn/SiO_2 and Sn/DeAlBEA catalysts. Samples are labeled with Sn/nm^2 loading. Reaction data was collected at 873K, 4.67 kPa C_3H_8, and 20 mL/min total flow.

4.6.5 Summary of Tin PDH Catalysts

Table S4.7. Activity of Sn/DeAlBEA and Sn/SiO_2 catalysts.

Ref	Support	Prep	Sn wt. %	Surface area (m^2/g)	M atom/nm^2	P_{C3H8} (kPa)	T (K)	Spacetime (mol Sn*s/ mol C_3H_8)	Conv. (%)	Select. C_3H_6 (%)	k_f (mol C_3H_6/ (h.bar.mol Sn)
[40]	Sn/SiO_2	Iso	32.8	637	2.61	101	873	139.31	10	80	2.90
[40]	Sn/SiO_2	Iso	4.52	598	0.38	101	873	19.20	15	85	34.04
[40]	Sn/SiO_2	Iso	3.34	670	0.25	101	873	14.17	17	88	54.09
[40]	Sn/SiO_2	Iso	1.74	750	0.12	101	873	7.41	18	87	111.61
[40]	Sn/SiO_2	Iso	0.69	611	0.06	101	873	2.91	13	73	188.43
[36]	Sn/SiO_2	IWI	30.0	378	4.02	100	873	0.48	17	86	229.26
[40]	Sn/SiO_2	IWI	20.0	378	2.68	100	873	0.72	28	87	748.45
[40]	Sn/SiO_2	IWI	10.0	378	1.34	100	873	1.45	35	88	2964.95
[40]	Sn/SiO_2	IWI	7.52	378	1.01	100	873	1.92	35.4	88.5	4241.82
[40]	Sn/SiO_2	IWI	5.00	378	0.67	100	873	2.89	37	87	6460.41
[40]	Sn/SiO_2	IWI	2.00	378	0.27	100	873	7.23	32	86	10345.65
[39]	Sn/SiO_2	Iso	10.0	799	0.63	100	873	1.04	36	93	5125.93
[40]	Sn/SiO_2	Iso	2.00	1065	0.10	100	873	5.19	22	87	6863.30
[40]	Sn/SiO_2	Iso	5.00	950	0.27	100	873	2.08	42	91	8990.73
[41]	Sn/SiO_2	IWI	3.82	311	0.62	101	873	78.60	30	90	24.71
[41]	Sn/SiO_2	IWI	2.57	315	0.41	101	873	52.88	28.5	90	32.73
[41]	Sn/SiO_2	IWI	0.83	329	0.13	101	873	17.08	13.5	85	33.62
[41]	Sn/SiO_2	IWI	1.36	327	0.21	101	873	27.98	22.5	89	40.66
[41]	Sn/SiO_2	IWI	1.96	322	0.31	101	873	40.33	28	90	41.37
[41]	Sn/SiO_2	IWI	1.78	327	0.28	101	873	36.62	28.5	90	47.26
[38]	Sn/MCM-41		5.12	1121	0.23	101	853	105.34	30	96.32	25.36
[38]	Sn/Sil-1		7.88	416	0.96	101	853	162.07	9	96.17	2.23
[38]	Sn/Sil-2		5.12	288	0.90	101	853	105.34	11	95.21	4.32
[38]	Sn/Sil-1		5.12	416	0.62	101	853	105.34	20	96.33	9.50
[247]	NaSn/DeAlBEA	WI	7.19	451	0.81	20	903	205.61	32	94	7.12
[247]	NaSn/DeAlBEA	WI	4.41	457	0.49	20	903	126.01	40	92	15.81
[247]	NaSn/DeAlBEA	WI	2.72	456	0.30	20	903	77.83	33	91	19.58
[247]	Sn/DeAlBEA	WI	7.19	416	0.88	20	903	205.61	33	92	7.41
[247]	Sn/DeAlBEA	WI	2.72	460	0.30	20	903	77.83	26	79	14.45
[247]	Sn/DeAlBEA	WI	4.41	461	0.48	20	903	126.01	38	84	14.68
-	Sn/DeAlBEA	WI	12.8	496	1.31	4.67	873	74.57	1.27	68	0.62
-	Sn/DeAlBEA	WI	4.16	539	0.39	4.67	873	24.25	0.81	57	1.20
-	Sn/DeAlBEA	WI	7.02	516	0.69	4.67	873	40.93	0.98	55	0.86

5 Characterization and Kinetics of PtSn/DeAlBEA for Propane Dehydrogenation

5.1 Introduction

Recent interest in the direct dehydrogenation of propane to propene has been motivated by the growing industrial demand for propene and the realization that it cannot be met by catalytic cracking of petroleum and steam cracking to naphtha.[3,5] At the same time, propane has become increasingly available from shale gas. Hence, propane dehydrogenation (PDH) offers a way to close the gap between propene demand and its availability from petroleum.[320] The most extensively investigated catalysts for PDH are supported Pt and bimetallic PtSn.[5,12] Previous studies have found that Pt is quite active for PDH but suffers from deactivation and poor selectivity.[17–19] However, the activity, propene selectivity, and stability of Pt improve with decreasing particle size and are best for isolated Pt atoms.[15,16] Both experimental and theoretical studies have shown that the addition of Sn increases the dispersion of Pt, enhances the rates of PDH, and reduces the rate of coke formation.[22–26] PtSn catalysts contain a variety of structures and Pt/Sn ratios, e.g., Pt particles, PtSn bimetallic alloys (e.g., Pt_3Sn, PtSn), small, supported PtSn bimetallic particles, and isolated Pt atoms interacting with Sn,[3] the nature of these structures depending on the catalyst preparation procedure, Pt/Sn ratios, and support composition.[21,144,321–323] Pt_3Sn is often cited as the most active bulk alloy,[23] although PtSn has also been shown to be active.[52] The addition of hydrogen to the feed propane has been reported to enhance the rate of PDH by up to 4-fold, with an optimum propane-to-hydrogen ratio of 1:1.[24,324] Hydrogen addition also decreases the deactivation of PtSn catalysts due to coking by removal of coke precursors through reaction with atomically adsorbed hydrogen,[24] an interpretation supported by theoretical studies.[325,326] Hydrogen addition has also been found to cause restructuring of PtSn particles and increase Pt-Sn interactions.[154,327,328]

The resistance of Pt and PtSn clusters and nanoparticles to sintering can be improved by encapsulating them within the pores of a zeolite. Of particular interest has been the idea of using dealuminated Beta zeolite (DeAlBEA) containing non-noble metal sites (Zn, Sn,...). DeAlBEA is formed by removal of framework aluminum atoms to create silanol nests that can then be used to host non-noble metals in the form of $(\equiv SiO)_{n-m}M^{n+}\text{-}(OH)_m$ (n is the oxidation state of M ranging from 1+ to 4+ and $0 \leq m \leq n$). These groups then serve as anchors for Pt and facilitate the achievement of a high dispersion of Pt.[5,12,20,21] A further advantage of using a siliceous/non-acidic support is elimination (or at least reduction) of Brønsted acid sites that can promote coking and, hence, reduce propene selectivity and catalyst stability. In the absence of supported Pt, Sn/DeAlBEA is not very active for PDH.[39,40,247] However, dispersion of Pt on Sn/DeAlBEA produces a highly active, selective, and stable catalyst for PDH.[21,31,32,256] The active site in PtSn/DeAlBEA has been proposed to be single Pt atoms[21] or small clusters of Pt atoms stabilized by Sn in the zeolite framework.[21,31,32] Different methods of PtSn/DeAlBEA preparation and pretreatment have been reported. Previous investigations that varied Sn and Pt loadings found that the optimum PDH activity is achieved for Sn/Pt = 3, Sn/Pt = 1, or Sn/Si = 80 (Sn/Pt = 9.9).[21,32] An important finding of catalyst pretreatment is that direct reduction of PtSn/DeAlBEA results in a more stable and active catalyst than calcination followed by reduction due to the formation of smaller Pt domains upon direct reduction.[21]

Despite substantial previous work on PtSn/DeAlBEA as a catalyst for PDH, the details of how Pt interacts with Sn in these materials are not fully clear. We also note that most previous studies of PtSn/DeAlBEA have not investigated the effects of catalyst composition and structure on the reaction kinetics. Moreover, comparison of the activities of catalysts reported by different investigators is difficult because most report the net rate of propene production without considering the effects of propane conversion and the approach to equilibrium of this intrinsically reversible reaction. While some reports have isolated the apparent, first-order rate coefficient for propane dehydrogenation, most do not.[20,329,330] Therefore, it is not possible to define how catalyst composition and structure affect catalyst activity for propane dehydrogenation.

Here, we describe the preparation and characterization of Sn/DeAlBEA and Pt/SnDeAlBEA with the aim of establishing how Sn is anchored to DeAlBEA and how the environment of Pt changes with Sn/Pt ratio at a fixed Sn content. We then investigate how the dispersion of Pt and its interactions with Sn affects the PDH activity and kinetics of PtSn/DeAlBEA. The forward rate constant for PDH ($k_{f,app}$) is calculated from measurements of the net rate of propene formation to properly account for the effects of reaction conditions (T, P_{C3H8}, weight-hourly space velocity (WSHV), etc.), which affect the propane conversion and the approach to thermodynamics equilibrium. We find that Sn interacts with the silanol nests of DeAlBEA to form Sn(IV) cations that are four-fold coordinated as $(\equiv Si\text{-}O)_4Sn$ structures within the zeolite framework, that PtSn/DeAlBEA contains multiple types of Pt sites, and that the interactions of Pt with Sn change with Sn/Pt ratio. We also find that the value of $k_{f,app}$ decreases as the Pt/Al ratio increases (at a fixed Sn/Al ratio), suggesting that highly dispersed Pt structures are the most active for PDH. Our EXAFS data suggest that the most active form of Pt is a Pt_3 cluster interacting with Sn(IV) in the framework of BEA. Compared to previously reported PtSn catalysts, the PtSn/DeAlBEA catalysts reported here exhibit exceptionally high values of $k_{f,app}$.

5.2 Experimental Methods

5.2.1 Catalyst Preparation

H-BEA was prepared by heating NH_4-BEA (Alfa Aesar, Si/Al = 12.5) in a quartz boat placed in a quartz tube at 5K/min to 773 K and maintained at this temperature for 4 h in dry synthetic air (Praxair, ultra-zero, 100 mL/min). H-BEA was dealuminated in 13 M HNO_3 for 20 h at 373K with stirring. The solution was filtered and washed extensively with deionized water. The filter cake was dried at 393 K overnight to yield dealuminated BEA (DeAlBEA). This technique has been shown by ^{27}Al NMR to remove framework and extra-framework Al completely.[20]

Sn and Pt were introduced sequentially to DeAlBEA via wetness impregnation. $SnCl_2{\cdot}2H_2O$ (98.0-103.0%, from Alfa Aesar) was dissolved in ethanol and stirred for 30 min prior to impregnation. The amount of metal was determined by the desired weight loading, while the amount of liquid was kept constant for the weight of DeAlBEA (5.6 mL liquid per gram of DeAlBEA). The solution was added to the siliceous support, and the mixture was ground until all the liquid evaporated (~30 min). The samples were then dried overnight in air at 393 K, followed by calcination in air at 873 k for 2 h. Pt was introduced to both Sn/DeAlBEA and DeAlBEA. To do so, $Pt(NO_3)_4(NH_4)_2$ was dissolved in water and stirred for 30 min prior to impregnation. The amount of metal was determined by the desired weight loading, while the amount of liquid was

kept constant relative to the weight of Sn/DeAlBEA (2.8 mL liquid per gram of Sn/DeAlBEA). The solution was added to the siliceous support, and the mixture was ground until all the liquid evaporated (~60 min). Samples were then dried at 393 K for 2 h in static air, followed by heating to 623 K for 2 h. These samples are designated as PtSn/DeAlBEA-XX, where XX indicates the Pt/Al ratio.

5.2.2 Catalyst Characterization

Specific surface areas of samples were determined by N_2-adsorption using a Micrometrics Gemini VII instrument. 40-45 mg of catalysts were dehydrated overnight in vacuum at 453 K. Then, nitrogen (Praxair, UHP) was adsorbed at 77 K to measure an adsorption isotherm. Calculations of the Brunauer–Emmett–Teller (BET) surface area are included in the supplemental information (SI S.1). Metal content was measured with inductively coupled plasma-optical emission spectrometry (ICP-OES).

Infrared (IR) spectra were collected in transmission mode using a Nicolet 6700 Fourier transform spectrometer. Samples (~35 mg) were pressed into thin pellets and loaded into an infrared cell equipped with CaF_2 windows. Helium (Praxair, ultra-zero, 100mL/min) was used as a carrier gas. The sample was then dehydrated at 573 K for 2 h to acquire spectra. Spectra were collected by averaging 64 scans at a resolution of 1 cm^{-1} at 473 k and 293 K. For IR studies of adsorbed pyridine, 2 μL of adsorbate was injected into the helium feed stream heated to 373 K with heating tape. Spectra were recorded at 10, 20, and 30 min after injection. To obtain IR spectra of adsorbed CO, 1% CO/He (Praxair, CSG) was flowed over the sample for 20 min. Then, the IR cell was flushed with He, and spectra were recorded. Spectra were baseline corrected with a spline function and normalized to the intensity of Si−O−Si framework overtone bands occurring between 1700 and 2000 cm^{-1}. The IR spectra of the adsorbed probe molecule presented were corrected by subtracting the initial spectrum of the sample taken at the adsorption temperature.

Powder X-ray diffraction (XRD) patterns were collected with a D8 Discover GADDS Powder XRD instrument, which uses Cu-Kα radiation. XRD patterns were collected at room temperature, scanning between 7.5° and 80° with 5 frames. Depending on the noise and crystallinity of the samples, 60 or 300 s of contact of the adsorbate with the solid was used to achieve equilibrium.

X-ray absorption spectroscopy (XAS) was performed at the Stanford Synchrotron Radiation Laboratory (SSRL). XAS measurements were performed in fluorescence mode. The monochromator energy was calibrated with Pt foil. The Pt L_3 edge was probed at beamline 9-3 using the 3 mm capillary sample holder. The flow rate of gases to the sample holder was regulated with digital mass flow controllers. The outlet gas was monitored with an in-line mass spectrometer. Ambient samples were measured in flowing He (Praxair, ultra-zero); samples were then heated to 823 K in flowing He and held for 30 min. Samples were then cooled to room temperature, and XAS spectra were collected. XAS data analysis was performed with the Athena/Artemis software using the FEFF routine.

5.2.3 Catalyst Activity

Studies of propane dehydrogenation were carried out using 5 mg of catalyst loaded into a quartz tube reactor (4 mm inner diameter). Quartz wool was used to support the catalyst bed. Tests were performed at atmospheric pressure and 823 K. Catalysts were heated to 823 K at 15 K/min

in air and held in He (Praxair, ultra-zero) at 823 K for 30 min. Then, 20.2% C_3H_8/He (Praxair, CSG) diluted with He (Praxair, ultra-zero) to achieve a desired C_3H_8 composition was fed to the reactor. A total flow rate of 200 mL/min (0.7 kPa propane) was used as a reference condition. Reaction products were analyzed with an in-line 7890A Agilent Gas Chromatograph equipped with a 25 m HP-PLOT Q column and a flame ionizing detector (FID). Conversion and selectivity are reported on a molar basis. Net Site-Time Yield (STY) of propene is reported as moles of propene per hour per mole Pt. Equations for calculating conversion, selectivity, and STY are given in the SI.

5.3 Results and Discussion

The metal weight loading and metal atom distribution for each catalyst are reported in Table 5.1. The BET surface area of all samples is essentially the same (498.2 ± 19.6 m^2/g) and does not change notably upon the introduction of Sn and Pt. Powder XRD patterns presented in Figure 5.1 show that all of the samples are identical to that of the parent H-BEA, confirming the maintenance of the BEA crystal structure through dealumination and introduction of metals. No peaks indicative of bulk Pt or PtSn nanoparticles are observed. Since XRD can only detect nanoparticles greater than 2.5-2 nm in size and ~1% by volume,[269–272] the absence of diffraction peaks does not entirely eliminate the presence of these particles but only means that their particle size is below the XRD detection limit. These XRD results suggest that adding Pt at high loadings (Pt/Al = 0.2) does not change bulk structures in these PtSn/DeAlBEA catalysts. The absence of peaks for Pt or PtSn nanoparticles is also true for lower loadings of Pt in PtSn/DeAlBEA.

Table 5.1. Characteristics of HBEA, DeAlBEA, Sn/DeAlBEA, Pt/DeAlBEA, and PtSn/DeAlBEA.

Sample Name	Pt wt.%	Sn wt.%	Pt/Al	Sn/Pt	Sn/Al	BET area (m^2/g)
HBEA	0	0	0	-	-	469.7
DeAlBEA	0	0	0	-	-	515.6
Pt/DeAlBEA-0.001	0.03	0	0.001	-	-	495.5
Pt/DeAlBEA-0.026	0.62	0	0.026	-	-	490.4
PtSn/DeAlBEA-0.001	0.03	1.9	0.0014	96.7	0.13	454.4
PtSn/DeAlBEA-0.002	0.05	1.8	0.0021	59.2	0.13	477.0
PtSn/DeAlBEA-0.003	0.06	1.8	0.0026	47.8	0.13	522.9
PtSn/DeAlBEA-0.013	0.32	2.4	0.013	12.6	0.17	509.9
PtSn/DeAlBEA-0.015	0.36	2.4	0.0150	10.8	0.16	497.0
PtSn/DeAlBEA-0.020	0.48	2.2	0.0199	7.674	0.15	502.7
PtSn/DeAlBEA-0.026	0.62	2.5	0.0258	6.63	0.17	517.0

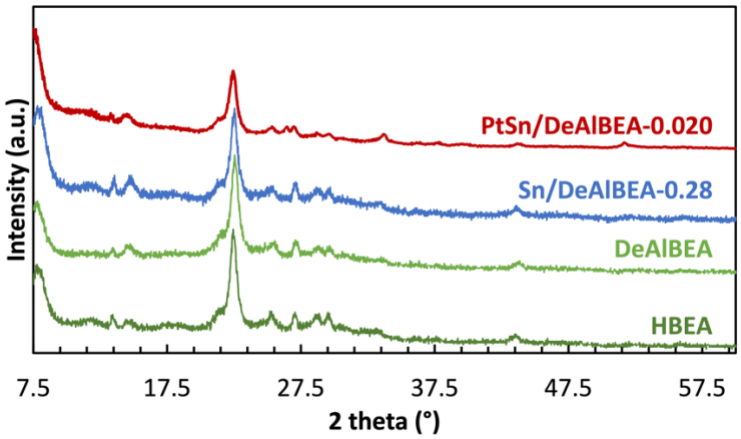

Figure 5.1. XRD patterns of HBEA, DeAlBEA, Sn/DeAlBEA, and PtSn/DeAlBEA.

5.3.1 IR Spectra of pyridine adsorbed on Sn/DeAlBEA, Pt/DeAlBEA, and PtSn/DeAlBEA

IR spectra of adsorbed pyridine can be used to identify the relative amounts and strengths of Brønsted and Lewis acid sites. IR spectra of adsorbed pyridine on DeAlBEA, Sn/DeAlBEA, Pt/DeAlBEA, and PtSn/DeAlBEA are shown in Figure 5.2. Distinct peaks are evident corresponding to pyridine interacting with silanol nests (1592 cm^{-1} and 1445 cm^{-1}) and Lewis acid sites (1600-1612 and 1450 cm^{-1}), and pyridinium ions formed via interaction of pyridine with Brønsted acid sites (1544 cm^{-1}).[244,251,331,332] Blue shifts in the frequency of the pyridine peak above 1600 cm^{-1} indicate increasing Lewis acid strength.[32,257] The peak at 1490 cm^{-1} corresponds to pyridine interactions with both Lewis and Brønsted acid sites. Dealuminated BEA exhibits peaks at 1592 and 1445 cm^{-1} ascribed to the interaction of pyridine with H atoms of the Si−OH groups in the silanol nests of DeAlBEA,[259] but no peaks are present corresponding to Brønsted acid sites (1544 cm^{-1}). It is notable that the spectrum of pyridine adsorbed on Pt/DeAlBEA is very similar to that of DeAlBEA. The absence of a change in the intensity of the peaks for pyridine interacting with silanol groups suggests that the introduction of Pt does not perturb or consume these groups. When pyridine is adsorbed on Sn/DeAlBEA, the presence of Lewis acid sites is clearly evident, and a significant reduction occurs in the intensity of the bands at 1592 and 1445 cm^{-1} for pyridine interacting with silanol groups. Introduction of Pt to Sn/DeAlBEA results in a reduction in the peaks for pyridine interacting with Sn Lewis acid sites (1600-1612 and 1450 cm^{-1}), suggesting this is due to the interaction of Pt with Sn cations. In summary, the IR spectra of adsorbed pyridine confirm the presence of Sn Lewis acid sites in Sn/DeAlBEA and show a decrease in these Sn-pyridine interactions upon Pt introduction to form PtSn/DeAlBEA.

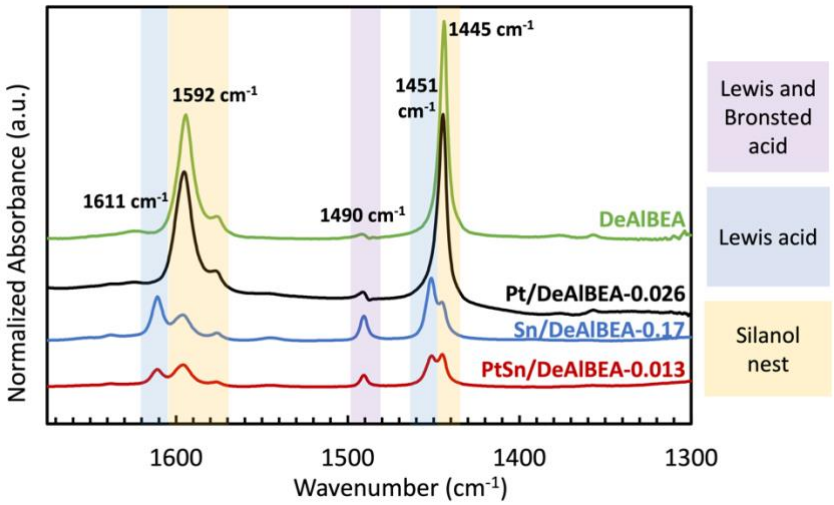

Figure 5.2. IR spectra of pyridine adsorbed on DeAlBEA, Sn/DeAlBEA-0.13, Pt/DeAlBEA, and PtSn/DeAlBEA-0.013.

5.3.2 IR of CO Adsorbed on Pt/DeAlBEA and PtSn/DeAlBEA

The IR spectra of CO adsorbed on Pt/DeAlBEA and PtSn/DeAlBEA are shown in Figure 5.3. For PtSn/DeAlBEA-0.001, the IR spectrum of adsorbed CO exhibits peaks at 2068 cm^{-1} and 2136 cm^{-1}. As the Pt/Al ratio increases, a peak at 2097 cm^{-1} appears for PtSn/DeAlBEA-0.003 and is maintained until the Pt/Al ratio reaches 0.02. At an intermediate Pt/Al ratio (0.013), the spectrum of adsorbed CO exhibits also displays a peak at 2089 cm^{-1}. This peak is maintained at higher Pt/Al ratios as well. At the highest Pt/Al ratio (0.026), the IR spectrum of adsorbed CO on PtSn/DeAlBEA exhibits peaks at 2092 cm^{-1} and 2127 cm^{-1}. The IR spectra of CO adsorbed on Pt/DeAlBEA with low and high Pt/Al ratios (0.001 and 0.026) are also shown for comparison. The IR spectrum of CO adsorbed on Pt/DeAlBEA-0.001 displays one broad peak at 2092 cm^{-1}, whereas the spectrum for Pt/DeAlBEA-0.026 exhibits two peaks at 2090 cm^{-1} and 2112 cm^{-1}.

All samples of PtSn/DeAlBEA also exhibit a peak above 2120 cm^{-1}; as the Pt/Al ratio increases, this peak becomes broader, and the area below 2130 cm^{-1} increases. At higher Pt/Al ratios (>0.013), the IR spectrum of adsorbed CO shows a broad peak centered between 2085-2095 cm^{-1}. At low Pt/Al ratios (0.001-0.003), a peak at 2068 cm^{-1} is also present. The IR spectrum for PtSn/DeAlBEA-0.026 resembles that for Pt/DeAlBEA-0.026, but the peak above 2120 cm^{-1} is blue-shifted relative to that for Pt/DeAlBEA-0.026. For Pt/DeAlBEA-0.001, a blue shift in the frequency of the IR band of adsorbed CO is seen relative to the major peak for Pt/DeAlBEA-0.026.

After PDH, a decrease occurs in the intensity of the CO peaks appearing above 2120 cm^{-1} for both PtSn/DeAlBEA and Pt/DeAlBEA catalysts relative to those for the dehydrated catalysts (Figure S5.2). At Pt/Al ratios less than or equal to 0.020, a small peak above 2120 cm^{-1} persists for PtSn/DeAlBEA; this high-frequency CO IR peak disappears completely for PtSn/DeAlBEA-0.026 and Pt/DeAlBEA-0.026 after reaction. After the PDH, PtSn/DeAlBEA with Pt/Al ratios from 0.001 to 0.020 also exhibit peaks at 2089 cm^{-1} and 2068 cm^{-1}.

The IR frequency of CO adsorbed on Pt is influenced by the CO coverage and the electronic state of the Pt (i.e., oxidation state, support composition, neighboring elements, and dispersion), discussed in detail in Chapter 1 of this thesis. IR peaks for linearly adsorbed CO on Pt can be

grouped into those for CO interacting with positively charged Pt (2110-2300 cm^{-1}) and zero-valent Pt (2050-2100 cm^{-1}).[44–46,333] Therefore, the peaks observed between 2140 and 2120 cm^{-1} in Figure 5.2 are consistent with CO adsorbed on positively charged Pt.[45,96,99,149] This assignment is supported by the observed decrease in the areas of these peaks after exposure of PtSn/DeAlBEA to reducing conditions during PDH. (Figure S5.2). Molecular orbital theory also supports this assignment; more positively charged Pt species will have less significant back-donation of electrons to adsorbed CO and, in turn, a stronger C-O bond and a higher stretching frequency.[69,84,85] The increase in the frequency of the band < 2100 cm^{-1} for CO adsorbed on PtSn/DeAlBEA relative to Pt/DeAlBEA suggests that Pt is more electron-deficient when supported on Sn/DeAlBEA than DeAlBEA.

The IR peak for adsorbed CO observed at 2097 cm^{-1} is consistent with Pt interacting with framework Sn or oxygen. Similar shifts in ν(CO) (~10 cm^{-1}) relative to Pt/DeAlBEA have also been reported for PtSn/DeAlBEA prepared by other investigators.[31] Additional studies have observed blue-shifted CO peaks when Pt interacts with Sn due to electron-withdrawing interactions of Pt with Sn.[145,148,165] This assignment suggests that Pt interacting with a framework Sn or O species has a lower electron density than large Pt clusters. The absence of a peak at 2097 cm^{-1} for CO adsorbed on Pt/DeAlBEA, even at low Pt/Al ratios, suggests that Sn is necessary to create positively changed Pt, narrowing the potential species to Pt-Sn or Pt-O-Sn interactions. Either way, the peak at 2097 cm^{-1} can be assigned to Pt interacting closely with electron-withdrawing species in the BEA framework.

The peaks for adsorbed CO appearing at 2080-2095 cm^{-1} correspond to CO linearly adsorbed on metallic Pt clusters.[54,138,149,159,334] This region accounts for the majority of the spectral peak area for Pt/DeAlBEA and PtSn/DeAlBEA at high Pt/Al ratios (0.026). The growth of the area of this peak after reaction (Figure S5.2) also supports this assignment. For Pt/DeAlBEA-0.001, the blue shift in this peak position relative to that for Pt/DeAlBEA-0.026 is inconsistent with a decrease in Pt particle size and increasingly undercoordinated Pt sites but can be attributed to a stronger support interaction at low Pt/Al ratios.[136] The observed IR frequency for CO adsorbed on Pt/DeAlBEA-0.001 is still lower than that for CO adsorbed on Pt interacting with Sn or fully isolated Pt.[21,31,118–123] Notably, these C-O stretching frequencies are slightly red-shifted relative to those observed for PtSn/DeAlBEA, consistent with electron withdrawal and increased Pt dispersion due to the interaction of Pt with Sn.

The peak at 2068 cm^{-1} can also be attributed to CO interacting with Pt-Sn species. The red shift of this peak relative to other observed CO frequencies is consistent with more electron-rich Pt species. Several studies have observed similar peak positions for PtSn and Pt_3Sn alloys.[48,54,55,145,159,335] We note that there is no evidence for the formation of PtSn alloys in the samples of PtSn/DeAlBEA prepared for this study.

To summarize, the IR spectra of adsorbed CO suggest that, at low Pt/Al ratios, PtSn/DeAlBEA contain both positively charged Pt species (ν_{CO} = 2136 cm^{-1}) and Pt interacting with Sn (ν_{CO} = 2068 cm^{-1}). Pt clusters (ν_{CO} = 2089 cm^{-1}) are formed as the Pt/Al ratio increases (≥ 0.013). At the highest Pt/Al ratio (0.026), CO adsorbed on PtSn/DeAlBEA only exhibits IR peaks corresponding to positively charged Pt (ν_{CO} = 2136 cm^{-1}) and metallic Pt clusters (ν_{CO} = 2089 cm^{-1}). Pt/DeAlBEA exhibits CO IR peaks characteristic of metallic Pt clusters at high and low Pt/Al ratios (0.026 and 0.001). Thus, IR spectroscopy of adsorbed CO confirms the importance of Sn in the dispersion of Pt supported on DeAlBEA.

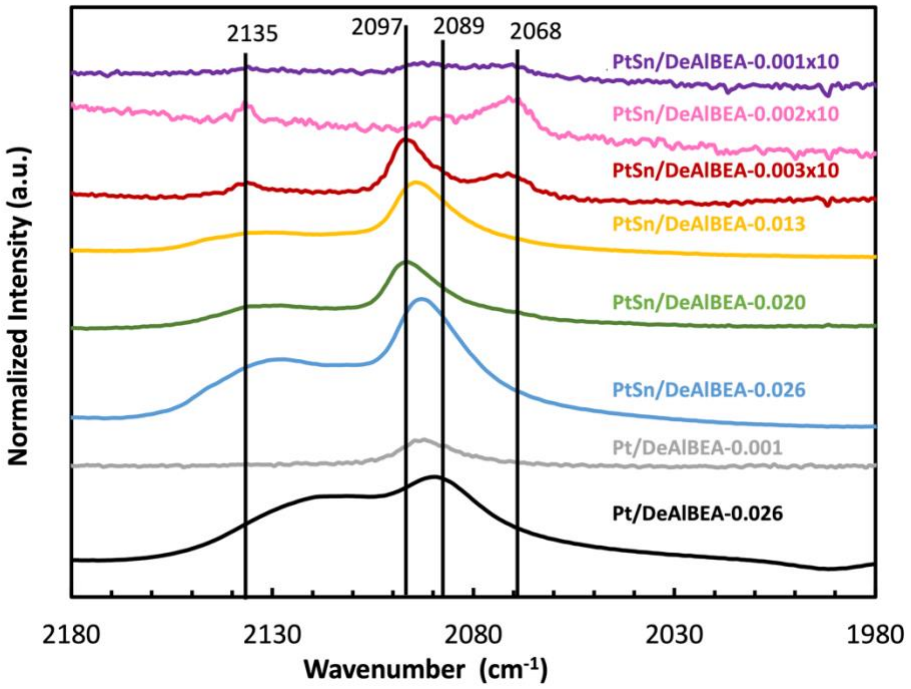

Figure 5.3. Infrared spectra of CO adsorbed on Pt/DeAlBEA and PtSn/DeAlBEA at 303 K under flowing He. Spectra are offset for clarity.

IR spectra were also collected during CO desorption from PtSn/DeAlBEA and Pt/DeAlBEA, as shown in Figure S5.1. The spectra of CO desorbing from Pt/DeAlBEA-0.076, PtSn/DeAlBEA-0.026, and PtSn/DeAlBEA-0.013 all exhibit shifts in peak position for the peak corresponding to CO linearly adsorbed to Pt^0 (2080-2095 cm^{-1}) both with desorption of CO at 303 K as a function of time and upon heating. By contrast, the spectra of CO adsorbed on PtSn/DeAlBEA-0.001 do not exhibit a shift in the position of the IR peaks for adsorbed CO during CO desorption. Shifts in the IR frequency of adsorbed CO with CO coverage are characteristic of CO desorption from Pt clusters.[47,56,118,124] If neighboring Pt sites adsorb CO, the neighboring CO molecules experience dipole-dipole interactions, causing a blue shift in the observed frequency. As the CO desorbs, a red-shift in the CO frequency is observed as these dipole-dipole interactions diminish. As CO desorbs from PtSn/DeAlBEA-0.013, a new peak appears at 2110 cm^{-1} between the broad peaks at 2135 cm^{-1} and 2090 cm^{-1}. This peak can be attributed to CO linearly adsorbed on isolated Pt atoms.[336] These CO desorption experiments indicate Pt nanoparticles exist on Pt/DeAlBEA and PtSn/DeAlBEA samples with Pt/Al ratios $\geq$ 0.013. For PtSn/DeAlBEA-0.001, the IR spectra of adsorbed CO do not show evidence of a shift in peak position with changes in CO coverage, indicating that Pt is atomically dispersed either as single atoms or very small Pt_x clusters.

5.3.3 XAS characterization of Pt/DeAlBEA and PtSn/DeAlBEA

The coordination and local environment of Pt were also probed with XAS. The intricacies of XAS analysis of Pt and PtSn materials have been thoroughly discussed in Chapter 2. To summarize, Pt XANES edge energies shift with the oxidation state and local environment, and careful fitting must be done to comprehensively analyze and interpret EXAFS data. XANES data for the Pt-L_3 edge are presented in Figure 5.4A. Pt foil exhibits an edge energy of 11563.2 eV and a modest white line height, consistent with zero-valent Pt with Pt neighbors. XANES spectra of

Pt/DeAlBEA show a slight increase in edge energy (11563.7 eV) relative to Pt foil (11563.2 eV), as do the XANES spectra of PtSn/DeAlBEA-0.001 and PtSn/DeAlBEA-0.013, which both exhibit small increases in edge energies relative to Pt foil (11563.5 and 11563.6 eV, respectively). All DeAlBEA samples show higher white line intensities than that seen for Pt foil (1.28). The white line intensity decreases slightly with increasing Pt loading (1.51 for PtSn/DeAlBEA-0.001 vs 1.49 for PtSn/DeAlBEA-0.013) and increases with the addition of Sn (1.44 for Pt/DeAlBEA-0.001 vs. 1.51 for PtSn/DeAlBEA-0.001). The increases in edge energies and white line intensities relative to Pt foil for Pt/DeAlBEA and PtSn/DeAlBEA are consistent with a slight decrease in the electron density of Pt. Increases in the white line intensity have also been shown to correlate with reductions in Pt nanoparticle size.[228,229] The XANES data shown in Figure 5.4A are consistent with positive and zero-valent Pt species identified by IR spectroscopy of adsorbed CO on Pt/DeAlBEA and PtSn/DeAlBEA. The observed decrease in the electron density of Pt with increasing Pt dispersion obtained from XANES data also agrees with the findings deduced from IR spectroscopy of adsorbed CO.[206,227] The similarity in the value of edge energy observed for PtSn/DeAlBEA to that for Pt foil suggests that most of the Pt in PtSn/DeAlBEA-0.013, PtSn/DeAlBEA-0.001, and Pt/DeAlBEA-0.001 exists as Pt^0, with only a minority of the Pt present in a higher oxidation state.

EXAFS data for the Pt-L_3 edge are presented in Figure 5.4B, and the fitting parameters are presented in Table 5.2. The EXAFS spectra for Pt foil are used to determine the amplitude reduction factor (0.798) and as a reference for metallic Pt-Pt interactions (R_{Pt-Pt} = 2.77 Å, CN_{Pt-Pt} = 12 (fixed)). The features in the R-space for Pt foil can be attributed conclusively to Pt-Pt interactions. The EXAFS fitting results for Pt/DeAlBEA-0.001 show Pt-Pt scattering paths (R_{Pt-Pt} = 2.76 Å, CN_{Pt-Pt} = 9.05 ± 1.70) as well as Pt-O scattering paths (R_{Pt-O} = 1.92 Å, CN_{Pt-O} = 1.03 ± 0.69). PtSn/DeAlBEA-0.0013 and PtSn/DeAlBEA-0.001 are best fit with Pt-Pt, Pt-O and Pt-Sn paths. Fits of the EXAFS data for PtSn/DeAlBEA closely resemble those for Pt/DelABEA-0.001 with the addition of a Pt-Sn path. On the other hand, PtSn/DeAlBEA-0.001 exhibits fewer Pt-Pt scatterers (R_{Pt-Pt} = 2.74 Å, CN_{Pt-Pt} = 3.90 ± 1.92) and more Pt-O scatterers (R_{Pt-O} = 2.03 Å, CN_{Pt-O} = 3.24 ± 0.60) relative to Pt/DeAlBEA-0.001 and PtSn/DeAlBEA-0.013. Additionally, there is a slight decrease in the Pt-Pt scattering distance. Decreases in the Pt-Pt distance and coordination number have previously been shown to coincide with decreases in Pt cluster size.[223,226]

The EXAFS data for all samples exhibit Pt-Pt interactions (R_{Pt-Pt} = 2.74-2.77 Å, $N_{Pt-Pt} > 1$), indicating some degree of Pt-Pt clustering. The lowest Pt/Al ratio shows the lowest number of Pt-Pt interactions (CN_{Pt-Pt} = 3), consistent with higher Pt dispersion for this loading. We note that even at intermediate Pt/Al ratios, the EXAFS pattern of PtSn/DeAlBEA resembles that of Pt foil. Specifically, high Pt-Pt coordination numbers are observed. The trends in Pt-Pt coordination numbers suggest that Pt dispersion increases with a reduction in the Pt/Al ratio and with the inclusion of Sn in the DeAlBEA framework. At all Pt/Al ratios, there are minimal Pt-Sn interactions ($CN_{Pt-Sn} \leq 1$), suggesting that Pt and Sn do not form alloys in PtSn/DeAlBEA. Therefore, analysis of the EXAFS data is consistent with the presence of small, metallic Pt clusters that interact with framework Sn sites together with a small number of isolated Pt atoms that are positively charged, and as the Pt/Al ratio increases, the formation of small Pt nanoparticles with a CN_{Pt-Pt} = 9, which corresponds to a particle size of ~ 25 Å.

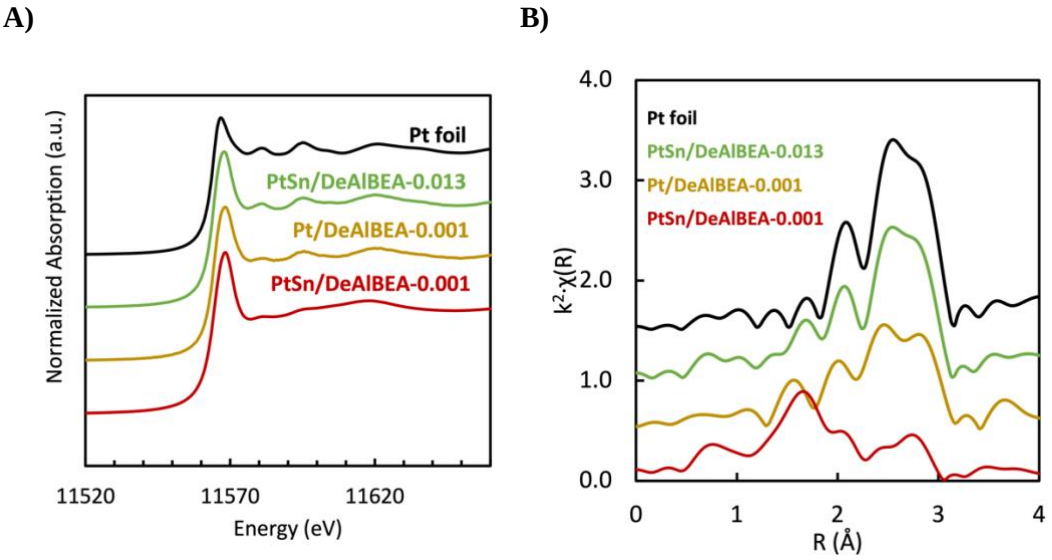

Figure 5.4. A) Normalized Pt L_3-edge XANES spectra and B) the magnitude of the Fourier-transformed k^2-weighted EXAFS spectra of PtSn/DeAlBEA and Pt/DeAlBEA Catalysts at ambient conditions. Spectra are offset for clarity.

Table 5.2. EXAFS Fitting Parameters for Pt L_3-edge spectra of Pt/DeAlBEA and PtSn/DeAlBEA Catalysts.

Sample	Red. chi^2 (χ_v^2)	R-factor	Path	CN	R (Å)	σ^2 (10^{-3} Å^2)	ΔE_0 (eV)
Pt foil	1031.9	0.0021	Pt-Pt	12 (fixed)	2.77± 0.005	4.2 ± 2.6	7.36 ± 0.36
Pt/DeAlBEA-0.001	71.3	0.021	Pt-Pt Pt-O	9.05 ± 1.70 1.03 ± 0.69	2.76 ± 0.01 1.92 ± 0.04	5.18 ± 1.28 5.41 ± 9.29	6.60 ± 1.64
PtSn/DeAlBEA-0.001	291.7	0.015	Pt-Pt Pt-Sn Pt-O	3.90 ± 1.92 1.07± 0.80 3.24± 0.60	2.74± 0.03 2.92±0.05 2.03± 0.02	6.51 ± 4.48 6.14 ± 2.78	7.56±5.27 13.94±2.01
PtSn/DeAlBEA-0.013	53.2	0.0014	Pt-Pt Pt-Sn Pt-O	9.98 ± 1.45 0.74 ± 0.58 1.81±0.72	2.77 ± 0.001 2.89±0.07 2.07±0.04	4.63 ± 1.32 8.41±6.21	6.34 ± 3.09 17.32± 3.49

$S_0^2 = 0.798$

The XAS results reported here for Pt foil agree closely with those reported previously for the Pt L_3 edge.[118,125,154,211] We also note that the Pt-Pt and Pt-O distances identified in this study (2.69-2.74 Å) are similar to those reported in other studies of PtSn/DeAlBEA. The observation of large Pt clusters and evidence of Pt-Sn interactions have been reported previously for PtSn/DeAlBEA.[337] Previous XAS studies of PtSn/DeAlBEA-0.014 have also reported evidence for isolated Pt in the as-prepared material ($CN_{Pt-Pt} = 0$) and small Pt clusters ($CN_{Pt-Pt} = 3$) following reduction.[21] However, this study did not report Pt-Sn interactions but suggested that Pt interacts with Sn via Pt-O-Sn linkages. Attempts to fit Pt-O-Sn paths in our work resulted in non-sensical coordination numbers or worse fits than those obtained only using Pt-Sn paths. The different activities may be due to different pretreatment conditions; the samples in earlier work were reduced (in H_2) at 773 K, while samples in the present study were treated in air at 623 K - a procedure chosen because it resulted in better Pt dispersion in Pt-Zn-DeAlBEA.[20] Additionally, the Sn/DeAlBEA used in the earlier study was synthesized through hydrothermal structural reconstruction (dealumination, followed by hydrothermal introduction of Sn) rather than sequential dealumination and impregnation, as was done here. While XAS data for Pt/DeAlBEA at low Pt/Al ratios have not been reported previously, such data are available for isolated Pt sites

and Pt clusters on other supports. Evidence for significant Pt clustering (CN_{Pt-Pt} = 8) has also been reported previously for Pt/DeAlBEA (Pt/Al=0.014).[21] These XAS results are similar to those presented here for Pt/DeAlBEA-0.001. XAS studies of isolated Pt on other supports (Pt_1/CeO_2 and Pt/SiO_2) have shown that the EXAFS pattern of isolated Pt often resembles PtO_2.[128,227] These observations are consistent with the increases in edge energy and white line intensity for PtSn/DeAlBEA-0.001. In summary, the XAS results for PtSn/DeAlBEA-0.013 resemble those reported previously for PtSn/DeAlBEA, but these results exhibit unique Pt-Sn interactions (i.e., absence of alloying or bonding to oxygen).

5.3.4 Characterization Summary

To summarize, evidence from characterization of Pt/DeAlBEA and PtSn/DeAlBEA by UV-vis spectroscopy, IR spectroscopy of adsorbed pyridine and CO, and XAS suggests that these materials contain two types of Pt, as illustrated in Figure 5.5. The first is atomically dispersed Pt atoms interacting with either Sn(IV) contained in the zeolites framework or with O atoms associated with ≡SiOH groups in silanol nests. Such Pt atoms are partially charged due to electron transfer from the Pt atom to either framework Sn(IV) cations or the O atoms of silanol groups. The second form of Pt is small to medium-sized clusters in which one of the Pt atoms of the cluster interacts with framework Sn(IV) cations or the O atoms of silanol groups. When Pt is added to Sn/DeAlBEA, the Sn(IV) cations in the zeolite framework facilitate the dispersion of Pt into isolated Pt atoms and small Pt clusters. High Pt dispersion is achieved for Pt/Al <0.020 at a constant Sn/Al ratio of 0.15. For higher Pt/Al ratios, small nanoparticles are formed in PtSn/DeAlBEA, and in the case of Pt/DeAlBEA, for all Pt/Al ratios down to Pt/Al = 0.001.

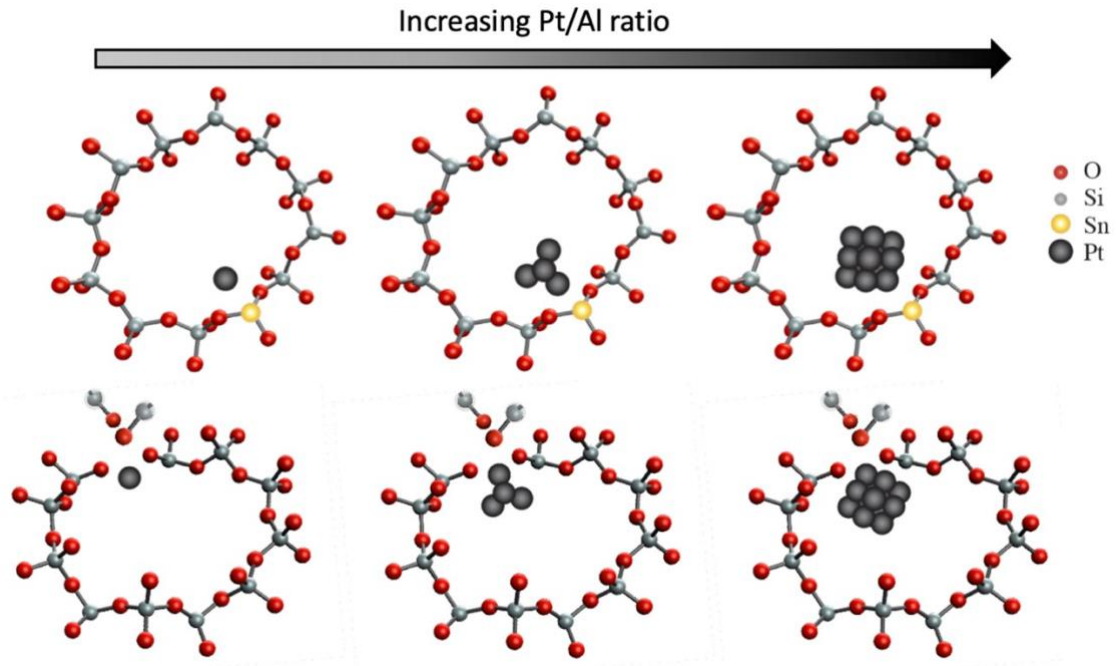

Figure 5.5. Potential Pt Structures in PtSn/DeAlBEA and Pt/DeAlBEA as a function of Pt/Al ratio. Hydrogen atoms are omitted for clarity.

5.3.5 Propane Dehydrogenation on Pt/DeAlBEA and PtSn/DeAlBEA

The PDH activity and selectivity of Pt/DeAlBEA and PtSn/DeAlBEA catalysts are shown in Figure 5.6. The activities of both DeAlBEA and Sn/DeAlBEA are negligible compared to those of Pt/DeAlBEA and PtSn/DeAlBEA (Figure S5.6A). Time on stream data for PDH over PtSn/DeAlBEA are presented in Figure S5.6. All PtSn/DeAlBEA catalysts exhibit high selectivity to propene (> 97%). Additionally, PtSn/DeAlBEA exhibits better stability (k_d = 0.002 h^{-1} for Pt/Al = 0.002 to k_d = 0.071 h^{-1} for Pt/Al = 0.026) than Pt/DeAlBEA (k_d = 0.19 h^{-1} for Pt/Al = 0.026) (Table S3). The PDH activity per total Pt atoms is highest at the lowest Pt/Al ratio, decreases with increasing Pt/Al ratio, and then plateaus at high Pt/Al ratios. This trend indicates that the most active Pt sites in PtSn/DeAlBEA are formed at the lowest Pt/Al ratios. The data shown in Figure 5.6A are adjusted for the dispersion of Pt using the integrated intensity of the IR spectrum of adsorbed CO to estimate the fraction of accessible Pt sites (Figure 5.3, Table S5.1; Additional details of dispersion estimations are included in 5.6.2.1). As seen in Figure 5.6B, differences in Pt dispersion do not fully account for the significant decrease in dehydrogenation rate at high Pt/Al ratios. This figure also shows that even after adjustment for Pt dispersion, the activity of Pt/DeAlBEA-0.026 is significantly lower than that of PtSn/DeAlBEA, suggesting that a major part of the activity in the latter catalyst is attributable to small Pt clusters containing three or so atoms that interact with a Sn(IV) cation in the framework of Sn/DeAlBEA.

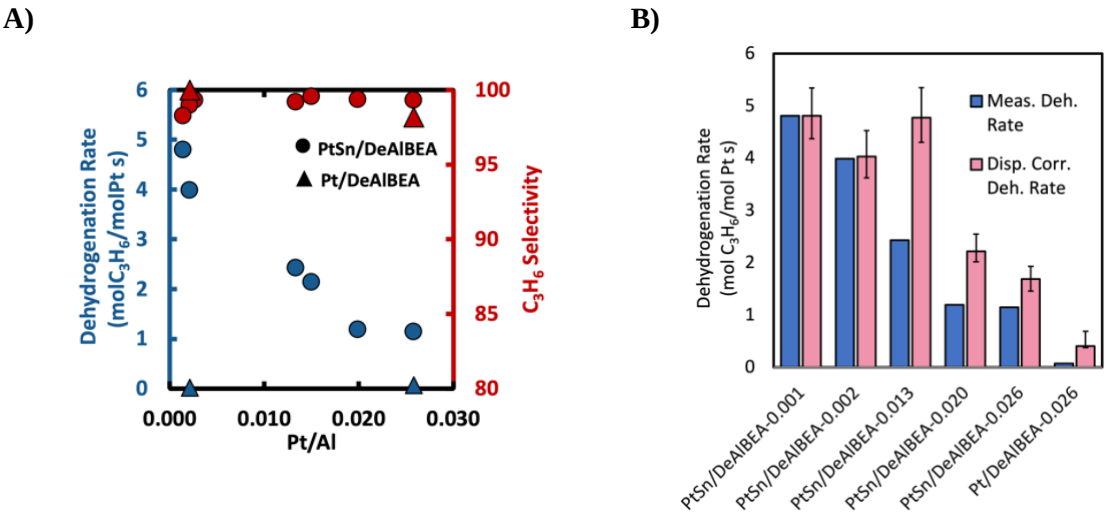

Figure 5.6. A) Propane Dehydrogenation Activity of PtSn/DeAlBEA as a Function of Pt/Al ratio. Reaction Conditions: 823 K, 0.7 kPa C_3H_8, 200 mL/min total flow. Sn/Al ratios are constant (Sn/Al = 0.2). B) Effect of Dispersion on Propane Dehydrogenation rate. Dispersion estimates derived from IR of adsorbed CO results (Table S5.1).

5.3.6 Kinetics of PDH over PtSn/DeAlBEA Catalysts

Figure 5.7 shows the dependence of the rate of PDH on the propane partial pressure measured at different reaction temperatures for three samples of PtSn/DeAlBEA. As noted in Table 5.3, all data were collected under conditions where the propane conversion ranged from 2.5% to 26%, but the approach to thermodynamic equilibrium was much less than 2%. Consequently, the measured rates of propene formation can be regarded as the true forward rate of propane dehydrogenation, neglecting the reverse reaction, propene hydrogenation. For the purposes of fitting a rate expression to the data, the reactor was assumed to behave as a plug-flow reactor (PFR). This mode of data treatment is particularly important when the propane conversion

is > 5%. As discussed in S.8 of the SI, the basic form of the rate expression assumes that the rate-limiting step for PDH is the dissociation of adsorbed propane and that the only relevant surface intermediates are adsorbed propane. This mechanism has been used successfully to interpret the rate of propane dehydrogenation over PtZn/DeAlBEA.[20] Interestingly, a Langmuir-Hinshelwood rate expression considering appreciable propene site occupation also fit the data well; however, accounting for propene and propene site occupation simultaneously provided a worse fit (Table S5.8). IR spectroscopy was performed after the PDH reaction to look for evidence of adsorbed propene with the aim of distinguishing these rate laws (Figure S5.3). While the resulting spectra displayed C-H vibrational modes at 2950, 2919, and 2838 cm^{-1} attributable to adsorbed propane or propene, similar to what was observed in studies of PDH on Pt/SiO_2,[338–340] no evidence was found for C=C vibrational modes at 1650 cm^{-1} characteristic of molecular propene.[341,342]

The rate laws and the corresponding rate parameters that give the best fit for each catalyst are shown in Table 5.3. The apparent activation energy is nearly the same (within error) for all Pt/Al ratios. Previous studies that varied Sn content at constant Pt loading also found that the activation energy for PDH remains nearly constant (58 - 62.7 kJ/mol for PtSn/NaY).[343] The heat of propane adsorption becomes slightly more negative with increasing Pt/Al, although the significant errors in these values do not allow for definitive determination of this parameter. We note that the magnitude of this error is similar to that reported in previous studies.[344–347] The similarity in the magnitude of the rate parameters for the three Pt/Al ratios suggests that similar active sites exist at all Pt/Al ratios, which suggests that the observed decrease in overall activity with increasing Pt/Al ratio, seen in Figure 5.6, is caused by dilution of active sites with much less active Pt species at high Pt/Al ratios. In other words, only the highly dispersed Pt species interacting with Sn are responsible for the observed PDH activity. This hypothesis is consistent with recent theoretical work showing that small Pt clusters interacting with Sn (e.g., Pt_2Sn and Pt_3Sn) are the most active and stable structures for PDH.[348]

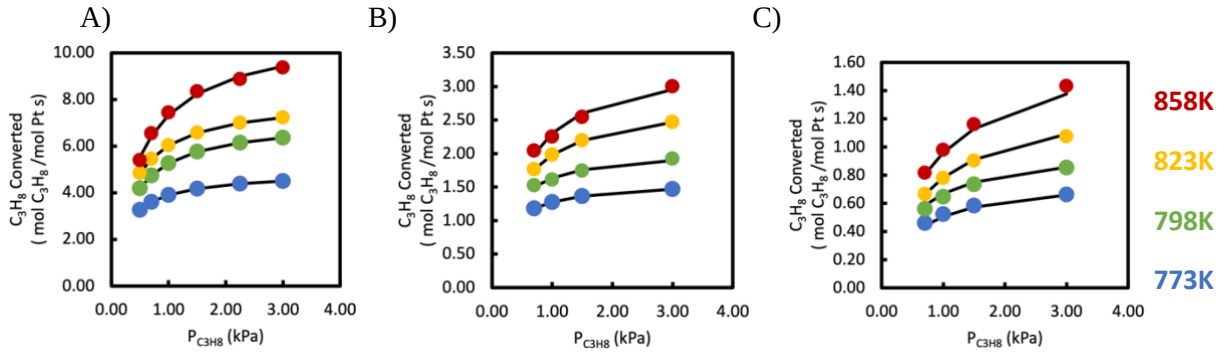

Figure 5.7. The dependence of the moles of converted C_3H_8 per mol Pt per s with propane partial pressure over PtSn/DeAlBEA was measured at different temperatures and 9.4 moles of propane/s per moles of Al for A) PtSn/DeAlBEA-0.001, B)PtSn/DeAlBEA-0.013, and C)PtSn/DeAlBEA-0.026. Colored circles indicate experimental data collected at various temperatures, and black curves show the calculated value obtained from the fitted kinetic parameters in Table 5.3.

Table 5.3. Fitted Kinetic Rate Laws of PtSn/DeAlBEA catalysts.

Catalyst	Conv. (%)	Frac. Appr. to Equil.	Rate law	E_1 (kJ/mol)	Ln(A_1)	ΔH (kJ/mol)	ΔS (J/mol K)	E_{app} (kJ/mol)	Ln(A_{app})	R^2
PtSn/DeAlBEA-0.001	2.5 – 6.9	0.0001 –0.0018	$\frac{k_1 K_{C_3H_8} P_{C_3H_8}}{1 + K_{C_3H_8} P_{C_3H_8}}$	50.68 ± 6.31	9.51 ± 0.94	-40.90 ± 11.43	-3.05 ± 14.09	9.78 ± 17.74	9.14 ± 2.63	0.981
PtSn/DeAlBEA-0.013	7.7 – 24	0.0011– 0.015	$\frac{k_1 K_{C_3H_8} P_{C_3H_8}}{1 + K_{C_3H_8} P_{C_3H_8}}$	52.53 ± 4.70	8.65 ± 0.70	-51.37 ± 10.68	-15.52 ± 13.16	1.16 ± 15.38	6.78 ± 2.28	0.996
PtSn/DeAlBEA-0.026	7.7 – 26	0.0011– 0.019	$\frac{k_1 K_{C_3H_8} P_{C_3H_8}}{1 + K_{C_3H_8} P_{C_3H_8}}$	55.06 ± 3.36	8.32 ± 0.50	-33.16 ± 13.12	1.54 ± 16.17	21.90 ± 16.48	8.51 ± 2.44	0.982

Where $k_{app} = k_1 K_{C_3H_8}$

Apparent activation energies for PDH over PtSn catalysts reported in the literature range from 26 to 212 kJ/mol (Table S5.10).[344,345,349–352] This wide range has been attributed to differences in the size of Pt particles, dispersion, and Pt surface site accessibility for these different Pt catalysts.[351] The apparent activation energies for PtSn/Al_2O_3 (44.7 to 169.7 kJ/mol) and PtSn/Mg(Al)O (34.6 to 81 kJ/mol) are generally higher than those reported here. The fitted enthalpies of propane adsorption for PtSn/DeAlBEA fall within the range previously reported for propane adsorbed on Pt and PtSn catalysts (-7.7 to -85.8 kJ/mol).[345,350–353,353] It is notable, though, that the enthalpy for propane adsorption reported for supported Pt and PtSn catalysts is much smaller in magnitude than that for propane adsorption on Pt single crystal surfaces (-247.9 to -283.8 kJ/mol).[354]

5.3.7 Comparison of PDH Activity for PtSn/DeAlBEA to Those Reported in the Literature

Comparison of the activities of the PtSn/DeAlBEA catalysts reported in this study to those for Pt and PtSn catalysts reported in the literature is challenging because the temperature, propane partial pressure, hydrogen partial pressure, propane conversion, and approach to equilibrium in each study are different. For this reason, all catalysts are compared on the basis of the apparent forward rate coefficient for PDH ($k_{f,app}$) calculated as described in S.5 of the SI. To compensate for the sublinear dependence of the forward rate of PDH on the propane partial pressure observed in our study, the values of $k_{f,app}$ were calculated for data collected at a low propane partial pressure (0.7 kPa) and a high temperature (823K). A comparison of $k_{f,app}$ to k_1 and K_{C3H8} for PtSn/DeAlBEA catalysts is included in Table S5.9. It is noted that a similar approach could not be used to determine values of $k_{f,app}$ from data reported for other Pt and PtSn catalysts, and hence, the values determined (see Table S5.4) may be underestimated for the reasons discussed below.

Several variables affect the accuracy of the calculated value of $k_{f,app}$. These include 1) the approach to equilibrium, 2) the effect of hydrogen in the reactor feed, and 3) the adsorption of reactants and/or products. As already noted, most authors described the rate of PDH by Langmuir-Hinshelwood kinetics,[344,345,347,349–352] in which case the calculated $k_{f,app}$ may be underestimated because it does not account for site blockage by adsorbed propane, propene, and hydrogen. The extent of underestimation of $k_{f,app}$ depends on the propane, conversion, and the heats of adsorption of propane, propene, and hydrogen. These individual effects are estimated to result in 2- to 4-fold increases in $k_{f,app}$ (an increase of 0.7 to 1.4 in ln($k_{f,app}$), with propene site-blocking having the most significant potential impact. The effect of site blocking on $k_{f,app}$ is discussed further in S.5.1. To

minimize these effects on the values of $k_{f,app}$ determined from data reported in the literature, data points collected with high approaches to equilibrium (> 0.6) and with high partial pressures of propene (>0.15 bar) were excluded from Figure 5.8 but are included in Table S5.4. The effects of Pt or PtSn dispersion were accounted for when metal dispersion was reported (see Table S5.4). Studies in which H_2 was added to the feed are identified explicitly.

Figure 5.8 shows values of $k_{f,app}$ for different Pt and PtSn catalysts. The values of $k_{f,app}$ for the PtSn/DeAlBEA catalysts prepared in this study are significantly higher than those previously reported for PtSn and Pt catalysts when compared at the same temperature (823 K) and in the absence of H_2 addition to the feed. It is notable that values of $k_{f,app}$ for PtSn catalysts reported in Ref. 31 in which H_2 was co-fed with propane are comparable to those observed for PtSn/DeAlBEA in the absence of added H_2. To assess the effect of H_2 addition on the activity of PtSn/DeAlBEA catalysts reported here, PDH was carried out with H_2 co-fed over PtSn/DeAlBEA-0.001 (Figure S5.6B). The addition of H_2 (1:1 C_3H_8:H_2) resulted in a 25% increase in propane conversion, corresponding to a 26-fold increase in the value of $k_{f,app}$, and the selectivity to propene increased slightly from 98 to 100%.

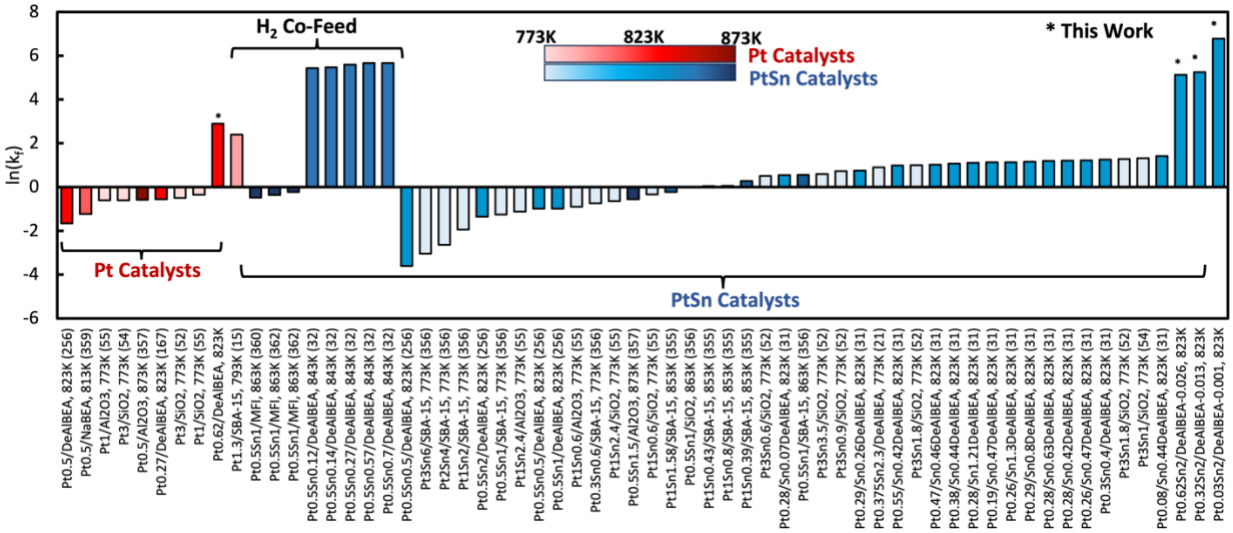

Figure 5.8. Comparison of apparent first-order forward rate constant ($k_{f,app}$) for various Pt and PtSn catalysts. Stars note catalysts from this work. Red bars are Pt-based catalysts, and blue bars are PtSn catalysts. Details concerning catalyst composition/structure and reaction conditions are reported in Table S5.4. References: [17,21,31,52,54,55,256,355–362]

The differences in values of $k_{f,app}$ for PtSn/DeAlBEA found in this study relative to those derived from data presented in the literature may be a consequence of the method used for catalyst preparation and pretreatment. Sequential grafting of Sn and Pt precursors results in the formation of alloyed PtSn nanoparticles coordinated to framework Sn sites.[32] By contrast, sequential impregnation of Sn and Pt precursors, the method employed here and in other studies, results in framework Sn coordinated with isolated Pt species or small Pt clusters.[21,31,256] The PtSn/DeAlBEA catalysts reported here were prepared with higher Sn/Pt ratios (Sn/Pt = 97 - 6.6) than those used in earlier studies (Sn/Pt = 0.5 - 10.1).[21,31,256] Additionally, the Pt loading in the PtSn/DeAlBEA catalysts (0.03 – 0.62 wt.%) reported here is generally lower than that used in previous studies (0.3 – 1 wt.%).[21,31,256] One study also reports that direct reduction of PtSn/DeAlBEA results in a more stable and active catalyst relative to sequential calcination and reduction steps.[21] This stability is

attributed to forming smaller Pt domains (Sn-O-Pt) with direct reduction.[21] By contrast, we found that pre-reduction decreased the stability relative to pretreatment in He.

The characterization data reported here suggests that the most active species in PtSn/DeAlBEA are small Pt clusters, containing on average three Pt atoms that interact with a Sn(IV) cation contained in the framework of DeAlBEA. This conclusion is also drawn in a recent theoretical investigation of Pt_x (x = 1, 2, 3, 4) and Pt_xSn_y (x = 1, 2, 3 and y = 1 or x = 2 and y = 2) structures, which reported tradeoffs in PDH activity with increasing Pt nuclearity.[348] Significant differences in rate-limiting steps and adsorbed species were found depending on the structure, but ultimately, Pt_3Sn was identified as the most active and stable species for PDH.

It is also interesting to compare the activity of PtSn/DeAlBEA to that of PtZn/DeAlBEA reported by the present authors.[20] The most active PtSn/DeAlBEA catalyst (Pt/Al = 0.001) has a value of $k_{f,app}$ = 878 mol C_3H_6/(mol Pt·s·bar)) at 823 K, which is considerably higher than that for PtZn/DeAlBEA, $k_{f,app}$ = 37 mol C_3H_6/(mol Pt·s·bar))). We note, though, that PtSn/DeAlBEA deactivates more rapidly (k_d = 0.002 to 0.071 h^{-1} for Pt/Al = 0.001 to 0.026) than PtZn/DeAlBEA (k_d = 0.004 to 0.014 h^{-1} for Pt/Al = 0.04 to 0.1) This suggests that Zn is more effective than Sn in suppressing the formation of coke, the primary cause of deactivation. These findings are consistent with previous work that reported higher coking rates on $PtSn/Al_2O_3$ than $PtZn/Al_2O_3$ catalysts.[173] The decrease in coking rate was attributed to the ability of zinc to stabilize more highly dispersed Pt species.[173] The differences in activity and stability of PtSn/DeAlBEA and PtZn/DeAlBEA may be due to differences in the number of heteroatoms (Zn or Sn) interacting with Pt. For instance, Pt in PtZn/DeAlBEA interacts with 4-6 Zn(II) sites, while Pt in PtSn/DeAlBEA only interacts with one framework Sn(IV) site and possibly a small number of other Pt atoms. This may be the reason for the high activity of PtSn/DeAlBEA, but also its greater susceptibility to deactivation relative to PtZn/DeAlBEA.

5.4 Conclusions

PtSn/DeAlBEA catalysts were prepared by adding Pt to Sn/DeAlBEA, a support derived by the reaction of Sn with silanol nests produced by the dealumination of BEA zeolite. Characterization of Sn/DeAlBEA showed that Sn is incorporated in the zeolite framework as Sn(IV) cations, replacing Al and the charge compensating proton in the parent H-BEA. The presence of Sn(IV) cations in Sn/DeAlBEA stabilizes Pt in the form of very small Pt clusters and Pt nanoparticles. By contrast, Pt introduction into DeAlBEA produced predominantly Pt nanoparticles. While Pt could be dispersed largely as small Pt clusters (containing ~ 3 Pt atoms) in PtSn/DeAlBEA for Pt/Al ratios ≤ 0.013, increased formation of large Pt clusters and nanoparticles occurred at higher Pt/Al ratios.

The specific activity (i.e., per Pt atom) of PtSn/DeAlBEA for PDH, measured under conditions far from thermodynamic equilibrium, shows a decrease with Pt/Al ratio for Pt/Al > 0.013, even after compensation for the dispersion of Pt in catalysts with Pt/Al ratios > 0.02. The kinetics of propane dehydrogenation can be described by a Langmuir-Hinshelwood expression that is first-order in the partial pressure of propane but is inhibited by propane adsorption. The nearly identical rate parameters observed across all Pt/Al ratios suggest that the active site is the same in all cases. The nuclearity of Pt in the lowest loading catalyst (Pt/Al = 0.001) is three based on EXAFS characterization, suggesting that the active sites are Pt_3Sn species closely coupled to the BEA framework. This conclusion is consistent with recent theoretical analyses showing that Pt_3Sn clusters are particularly active for PDH. Therefore, the decline in specific activity observed

with increasing Pt/Al ratio is attributed to dilution of Pt_3Sn clusters by increasingly large Pt clusters or nanoparticles that exhibit minimal interaction with Sn cations in the BEA framework.

The PDH activity of PtSn/DeAlBEA was compared with those of supported Pt and PtSn catalysts reported in the literature based on calculated values of the apparent first-order rate coefficient for PDH, $k_{f,app}$. The values of $k_{f,app}$ for PtSn/DeAlBEA are significantly higher than those reported previously for Pt and PtSn catalysts, including those supported on DeAlBEA. The high activity for catalysts reported here is attributed to highly dispersed Pt species interacting with Sn cations introduced into the framework of BEA.

5.5 Acknowledgments

This work was supported by the Office of Science, Office of Basic Energy Sciences of the U.S. Department of Energy under Contract No. DE-AC02-05CH11231. NGL also acknowledges support through a fellowship from Chevron Energy Corporation. Use of the Stanford Synchrotron Radiation Lightsource, SLAC National Accelerator Laboratory, is supported by the U.S. Department of Energy, Office of Science, Office of Basic Energy Sciences under Contract No. DE-AC02-76SF00515.

5.6 Supporting Information

5.6.1 BET Calculation[318,319]

BET surface area was calculated from a linear regression of B_I vs P_{rel_I}

$$B_I = \frac{P_{rel_I}}{(1 - P_{rel_I}) * N_{ads_I}}$$

Where B_I is in g/cm^3 at standard temperature and pressure, P_{rel_I} is relative pressure, and N_{ads_I} is gas adsorbed after equilibration at the Ith dose in cm^3 at standard temperature and pressure.

The surface area is then calculated as follows:

$$SA_{BET} = \frac{CSA * 6.023 * 10^{23}}{22414\ cm^3 STP * 10^{18} \frac{nm^2}{m^2} * (S + Y_{INT})}$$

Where CSA is the adsorbate molecular cross-sectional area in nm^2 (0.162 nm^2 for N_2), S is the slope of the B_I vs P_{rel_I} fitting in g/cm^3 at standard temperature and pressure, Y_{INT} is the intercept of the B_I vs P_{rel_I} fitting in g/cm^3 at standard temperature and pressure.

5.6.2 IR of Adsorbed CO on PtSn/DeAlBEA Catalysts.

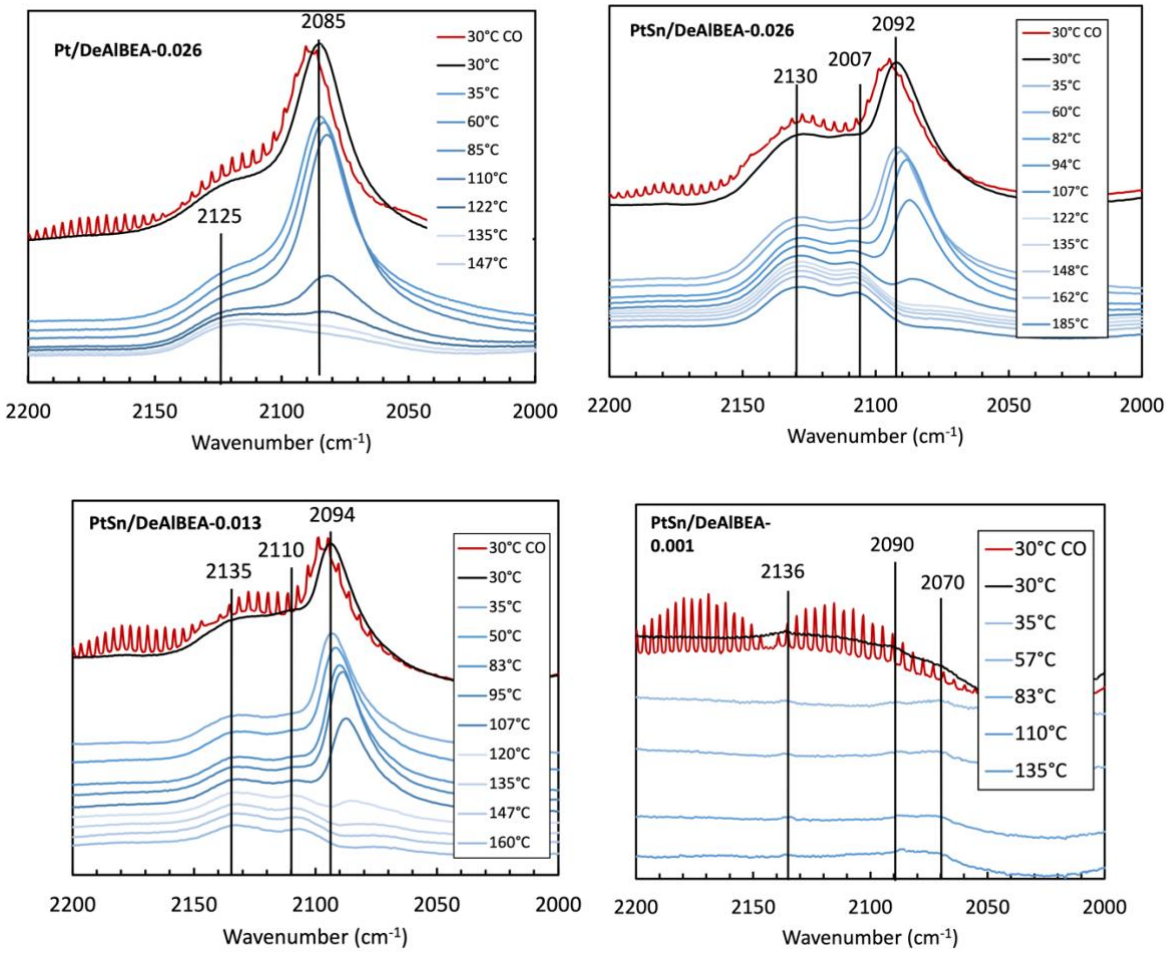

Figure S5.1. IR spectra of CO desorption as a function of temperature. Spectra are offset for clarity.

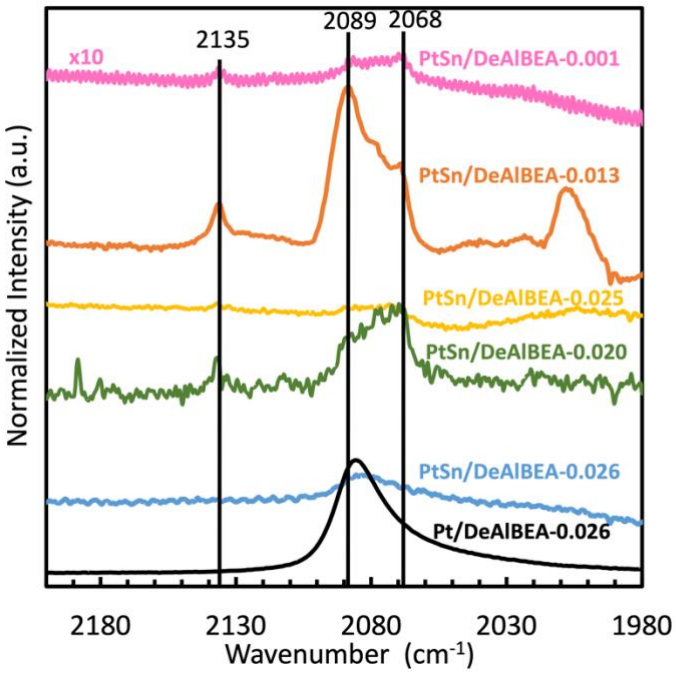

Figure S5.2. IR of adsorbed CO acquired after PDH on PtSn/DeAlBEA and Pt/DeAlBEA.

A) B)

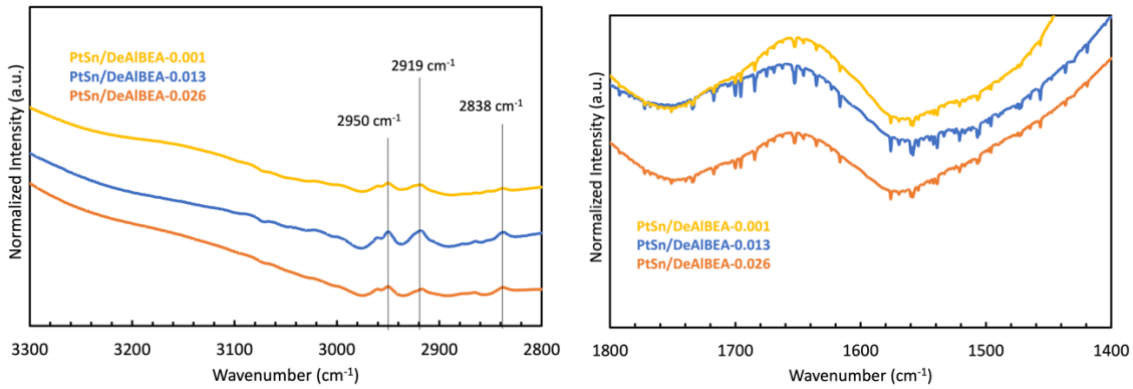

Figure S5.3. IR of PtSn/DeAlBEA catalysts acquired after PDH. Spectra collected after cooling to 303 K. Reaction run for 30 min of 0.7 kPa C_3H_8 at 773K. (A) 2800 - 3300 cm^{-1} and (B) 1500 -1800 cm^{-1} regions.

5.6.2.1 Estimation of Dispersion

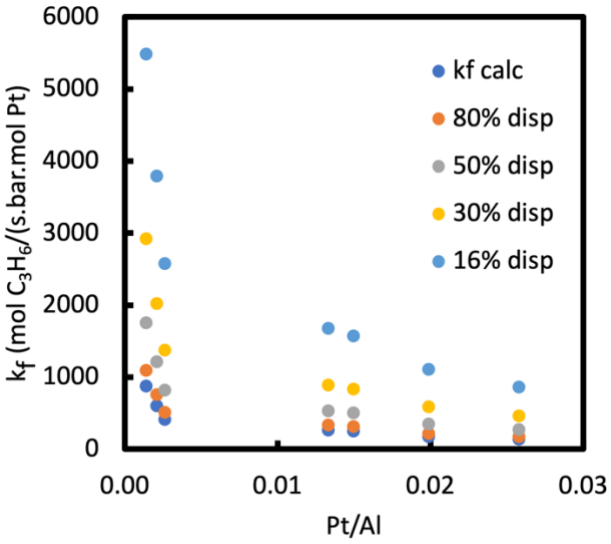

Figure S5.4. Estimation of dispersion of Pt in PtSn/DeAlBEA with different Pt/Al ratios.

For decreasing dispersion to account for the trends in reducing reaction rates, the dispersion of the highest Pt/Al ratio would have to be 16%. We can estimate the dispersion with an extinction coefficient using IR of adsorbed CO. The peak areas and CO adsorption values are included in the table below.

Table S5.1. Dispersion estimate based on IR peak areas of adsorbed CO.

Catalysts	Norm. peak area of adsorbed CO (a.u.)	Pt wt.%	peak area/ wt.	Assuming lowest loading is 100% disperse
PtSn/DeAlBEA-0.001	0.003	0.033	0.09	100%
PtSn/DeAlBEA-0.002	0.005	0.050	0.10	89%
PtSn/DeAlBEA-0.003	0.005	0.050	0.11	80%
PtSn/DeAlBEA-0.013	0.032	0.320	0.12	47%
PtSn/DeAlBEA-0.015	0.028	0.360	0.08	76%
PtSn/DeAlBEA-0.020	0.075	0.478	0.16	55%
PtSn/DeAlBEA-0.026	0.118	0.620	0.19	45%
Pt/DeAlBEA	0.234	0.620	0.38	23%
Pt/DeAlBEA-red	0.364	0.620	0.59	15%

5.6.3 XAS fitting parameters

Table S5.2. EXAFS fitting parameters for Pt L_3-edge spectra of as prepared and dehydrated PtSn/DeAlBEA and Pt/DeAlBEA.

Sample	Red. chi^2 (χ_v^2)	R-factor	Path	N	R (Å)	σ^2 (10^{-3} Å^2)	ΔE_0 (eV)
Pt foil	1031.9	0.0021	Pt-Pt	**12**	2.767± 0.005	4.2 ± 2.6	7.36 ± 0.36
Pt/DeAlBEA-0.001	71.3	0.021	Pt-Pt	9.05 ± 1.70	2.76 ± 0.01	5.18 ± 1.28	6.60 ± 1.64
			Pt-O	1.03 ± 0.69	1.92 ± 0.04	5.41 ± 9.29	
PtSn/DeAlBEA-0.013	53.2	0.0014	Pt-Pt	9.98 ± 1.45	2.77 ± 0.001	4.63 ± 1.32	6.34 ± 3.09
			Pt-Sn	0.74 ± 0.58	2.89±0.07		
			Pt-O	1.81±0.72	2.07±0.04	8.41±6.21	17.32± 3.49
PtSn/DeAlBEA-0.001	291.7	0.015	Pt-Pt	3.90 ± 1.92	2.74± 0.03	6.51 ± 4.48	7.56±5.27
			Pt-Sn	1.07± 0.80	2.92±0.05		
			Pt-O	3.24± 0.60	2.03± 0.02	6.14 ± 2.78	13.94±2.01
PtSn/DeAlBEA-0.013 -edh	25.42	0.0033	Pt-Pt	9 (fixed)	2.76 ± 0.01	4.06 ± 0.44	6.79± 1.27
			Pt-Sn	1 (fixed)	2.78 ± 0.05		
			Pt-O	0.37 ± 0.40	1.94 ± 0.06	8.99±3.39	12.74± 4.72
PtSn/DeAlBEA-0.001-deh	24.87	0.012	Pt-Pt	5 (fixed)	2.76±0.01	9.03 ± 0.39	5.67 ±1.01
			Pt-Sn	1 (fixed)	2.85 ± 0.02		
			Pt-O	1 (fixed)	2.02±0.02	5.66 ± 1.29	12.93±1.78

S_0^2=0.798

5.6.4 Conversion, selectivity, STY, and deactivation constant calculations

The conversion was calculated on a molar basis, using the equation below:

$$Conversion\,\% = \frac{Inlet\ mol\ C_3H_8 - Outlet\ mol\ C_3H_8}{Inlet\ mol\ C3H8} * 100\%$$

Carbon selectivity was calculated using the following equation:

$$carbon\ selectivity\ \% = \frac{mol\ of\ product * C\#}{\sum(mol\ product * C\#)} * 100\%$$

Molar selectivity was calculated using the following equation:

$$mol\ selectivity\ \% = \frac{mol\ of\ product}{\sum(mol\ product)} * 100\%$$

Net Site-Time Yield was calculated using the following equation:

$$STY\ (h^{-1}) = \frac{\frac{mol\ propylene\ formed}{h}}{mol\ metal\ in\ catalyst\ mass}$$

Deactivation constant, k_d

$$k_d[hr^{-1}] = \frac{\ln\left(\frac{1-x_{final}}{x_{final}}\right) - \ln\left(\frac{1-x_{initial}}{x_{initial}}\right)}{t[hr]}$$

5.6.5 Forward rate constant, $k_{f,app}$

Assumption:

- Propane dehydrogenation and propene hydrogenation reactions are reversible.
- The reaction occurs at low occupancy of Pt active sites, i.e., the inhibition of adsorbed products is negligible.
- The rate of propane dehydrogenation is first-order in propane partial pressure. Similar kinetics are applied for reversible hydrogenation reactions.

$$C_3H_8 \leftrightarrow C_3H_6 + H_2$$

The net rate of propane dehydrogenation can be represented as :

$$R_{PDH} = -\frac{k_{f-PDH}\, p_{C3H8} - k_{r-PDH}\, p_{C3H6}\, p_{H_2}}{\left(1 + K_{C3H8}\, p_{C3H8} + K_{C3H6} p_{C3H6} + K_{H2} p_{H2}\right)}$$

$$R_{PDH} = \frac{k_{f-PDH} p_{C3H8}}{\left(1 + K_{C3H8}\, p_{C3H8} + K_{C3H6} p_{C3H6} + K_{H2} p_{H2}\right)}\left[1 - \frac{1}{K_{ePDH}}\,\frac{\left(p_{C3H6} p_{H_2}\right)}{p_{C3H8}}\right]$$

$$p_{C3H8} = p^0_{C3H8}(1-X);\; p_{C3H6} = p^0_{C3H8} X;\; p_{H_2} = p_{C3H6} + p^0_{H_2} = p^0_{C3H8}\left(X + \theta_{H_2}\right)$$

$$R_{PDH} = -F^0_{C3H8}\frac{dX}{dW}$$

$$k_{f-PDH} = MW_{Pt}\frac{F^0_{C3H8}}{m_{Pt}}\int_0^X \frac{1}{\frac{p^0_{C3H8}(1-X)}{\left(1 + K_{C3H8} P^o_{C_3H_8}(1-X) + K_{C3H6} P^o_{C_3H_8}(X) + K_{H2}\, P^o_{C_3H_8}\left(\theta^o_{H_2} + X\right)\right)}\left(1 - \frac{(p^0_{C3H8})X\left(X + \theta_{H_2}\right)}{K_{ePDH}(1-X)}\right)} dX$$

$$k_{f-PDH} = MW_{Pt}\frac{F^0_{C3H8}}{m_{Pt}}\int_0^X \frac{1}{\frac{p^0_{C3H8}(1-X)}{(1+y_{C3H8}X)\left(1+K_{C3H8}\frac{P^o_{C_3H_8}(1-X)}{\left(1+y^o_{C_3H_8}X\right)} + K_{C3H6}\frac{P^o_{C_3H_8}(X)}{\left(1+y^o_{C_3H_8}X\right)} + K_{H2}\frac{P^o_{C_3H_8}\left(\theta^o_{H_2}+X\right)}{\left(1+y^o_{C_3H_8}X\right)}\right)}\left(1 - \frac{(p^0_{C3H8})X\left(X+\theta^o_{H_2}\right)}{K_{ePDH}(1+y^o_{C3H8}X)(1-X)}\right)} dX$$

$$\boldsymbol{k_{f-PDH} = \frac{F^0_{C3H8} MW_{Pt}}{m_{Pt} p^0_{C3H8}}\int_0^X \frac{\left(1 + y_{C3H8}X + K_{C3H8} P^o_{C_3H_8}(1-X) + K_{C3H6} P^o_{C_3H_8}(X) + K_{H2} P^o_{C_3H_8}\left(\theta^o_{H_2}+X\right)\right)}{\left((1-X) - \frac{(p^0_{C3H8})X\left(X+\theta^o_{H_2}\right)}{K_{ePDH}(1+y^o_{C3H8}X)}\right)} dX}$$

$$\boldsymbol{k_{f-PDH} = \frac{F^0_{C3H8} MW_{Pt}}{m_{Pt} p^0_{C3H8}}\int_0^X \frac{(1 + y_{C3H8}X)}{\left((1-X) - \frac{(p^0_{C3H8})X\left(X+\theta^o_{H_2}\right)}{K_{ePDH}(1+y^o_{C3H8}X)}\right)} dX}$$

5.6.5.1 Limitations of $k_{f,app}$

Although $k_{f,app}$ assumes that the PDH reaction is first-order in propane, often PDH proceeds with Langmuir-Hinshelwood kinetics.[344,345,347,350–352,363] With these kinetic models in mind, there is a possibility that kfapp is an inaccurate measure of the forward rate. Several variables affect the accuracy of this $k_{f,app}$ calculation, including 1) the true approach to equilibrium, 2) the effect of hydrogen on the structure of Pt under reaction conditions and PDH rates, and 3) appreciable adsorption of reactants or products. $k_{f,app}$ may be underestimated because of the denominator term (e.g., propane or propene site blocking).

5.6.5.1.1 Estimation of errors in the Approach to equilibrium

Because $k_{f,app}$ is calculated by dividing by one minus the approach to equilibrium, as the reaction conditions get closer to equilibrium, the $k_{f,app}$ will increase significantly. In order to account for this, $k_{f,app}$ values were not included for comparison if the approach to equilibrium was greater than 0.6. It's important to also consider that as the approach to equilibrium increases, the effects of partial pressure of propene and hydrogen also become more significant.

5.6.5.1.2 Estimation of P_{C3H6} Effects

$$r_{C3H6} = k_f^{calc} P_{C3H8}$$

$$r_{C3H6}^{act} = \frac{k_f^{act.} P_{C3H8}}{1 + K_{C3H6} * P_{C3H6}}$$

$$k_f^{calc} = \frac{k_f^{act.}}{1 + K_{C3H6} * P_{C3H6}}$$

$$k_f^{act.} = (1 + K_{C3H6} * P_{C3H6}) * k_f^{calc}$$

If K_{C3H6} =2.80-4.2 bar^{-1} [345,350–352,364] and the range of P_{C3H6} is 0.001-0.30 bar in this data set, then $K_{C3H6}P_{C3H6}$=0.0028-1.26 If we consider the highest extreme, k_f only increases 2-3 fold, equivalent to ~1 ln() unit.

5.6.5.1.3 Estimation of P_{C3H8} Effects

$$\mathrm{r_{C3H6}} = \mathrm{k_f^{calc} P_{C3H8}}$$

$$r_{C3H6}^{act} = \frac{\mathrm{k_f^{act.} P_{C3H8}}}{1 + \mathrm{K_{C3H8} * P_{C3H8}}}$$

$$\mathrm{k_f^{calc}} = \frac{\mathrm{k_f^{act.}}}{1 + \mathrm{K_{C3H8} * P_{C3H8}}}$$

$$\mathrm{k_f^{act.}} = (1 + \mathrm{K_{C3H8} * P_{C3H8}}) * \mathrm{k_f^{calc}}$$

If K_{C3H8} =3.19 bar^{-1} [364] and the range of P_{C3H8} in this data set is 0.007-1 bar, then $K_{C3H8}P_{C3H8}$=0.0022-3.19. If we consider the highest extreme, k_f can increase 4-fold or ~1.4 ln() unit.

5.6.5.1.4 Estimation of P_{H2} Effects

$$r_{C3H6} = k_f^{calc} P_{C3H8}$$

$$r_{C3H6}^{act} = \frac{k_f^{act.} P_{C3H8}}{1 + (K_{H2} * P_{H2})^{0.5}}$$

$$k_f^{calc} = \frac{k_f^{act.}}{1+(K_{H2}*P_{H2})^{0.5}}$$

$$k_f^{act.} = (1 + (K_{H2} * P_{H2})^{0.5}) * k_f^{calc}$$

If K_{H2} =0.81-18 $bar^{-0.5}$ [351,352] and the range of P_{H2} in this data set is 0.001-0.31 bar, then the maximum value of $\left(K_{H_2} P_{H_2}\right)^{0.5}$ is 0.0285-2.4. Considering this highest extreme, k_f can increase 2.4-fold or ~1 ln() unit. In addition to potential site blocking, hydrogen also has the potential to inhibit coke formation and restructure PtSn particles.[324] For these reasons, studies where hydrogen was co-flown with propane were not considered for comparison.

5.6.6 PDH Equilibrium and Activity

A) B)

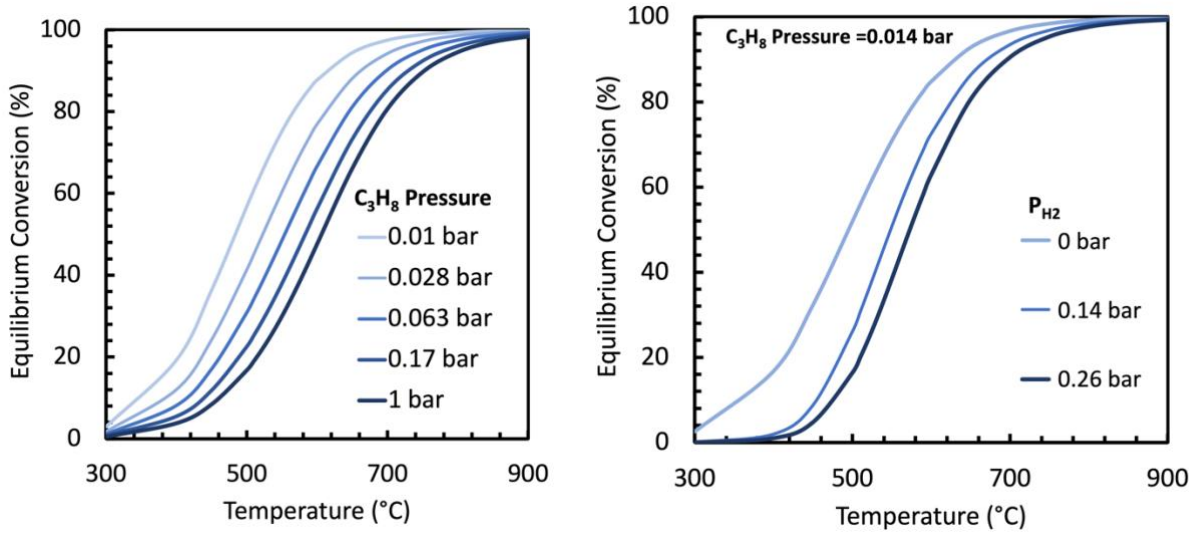

Figure S5.5. Equilibrium conversion for A) without H_2 addition to the feed at different partial pressures of propane, B) with the addition of H_2 to a feed containing P_{C3H8}= 0.014 bar.

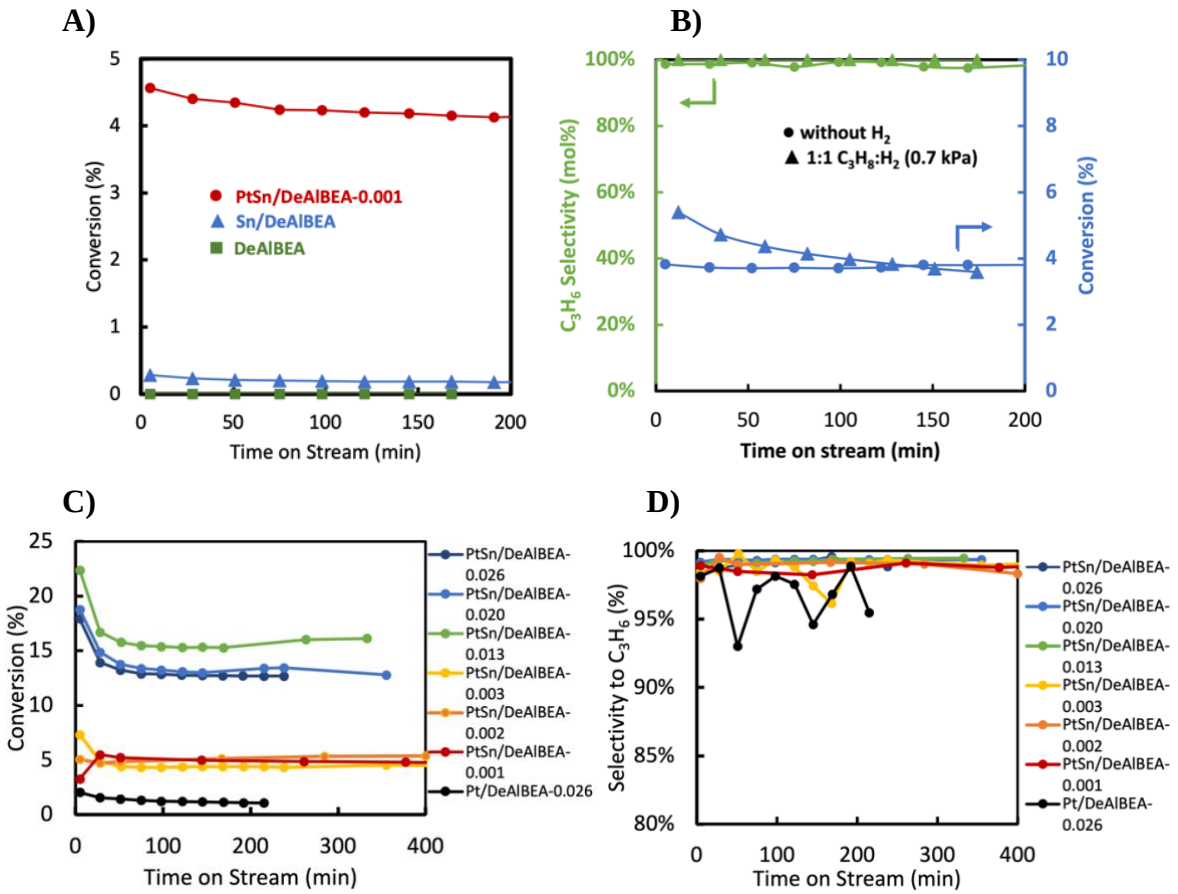

Figure S5.6. (A) Propane dehydrogenation activity over PtSn/DeAlBEA-0.001, Sn/DeAlBEA, and DeAlBEA. Reaction Conditions: 823 K, 0.7 kPa C_3H_8, 200 mL/min total flow. (B) Effect of H_2 co-feed (1:1 C_3H_8:H_2 (0.7 kPa)) for PtSn/DeAlBEA-0.001 at 823K. Catalyst pretreated in 9% H_2 in He for 1 h at 823 K prior to reaction. (C) The PDH activity and (D) selectivity to propene over PtSn/DeAlBEA catalysts vs. TOS at 823 K and 0.7 kPa C_3H_8.

Table S5.3. Deactivation constants for PtSn/DeAlBEA and Pt/DeAlBEA catalysts.

Catalyst	k_d (h^{-1})
PtSn/DeAlBEA-0.001	0.011
PtSn/DeAlBEA-0.002	0.004
PtSn/DeAlBEA-0.003	0.002
PtSn/DeAlBEA-0.013	0.021
PtSn/DeAlBEA-0.015	0.021
PtSn/DeAlBEA-0.020	0.027
PtSn/DeAlBEA-0.026	0.071
Pt/DeAlBEA-0.026	0.187

5.6.7 Literature Comparison Data set of PDH Catalysts

A) B) C)

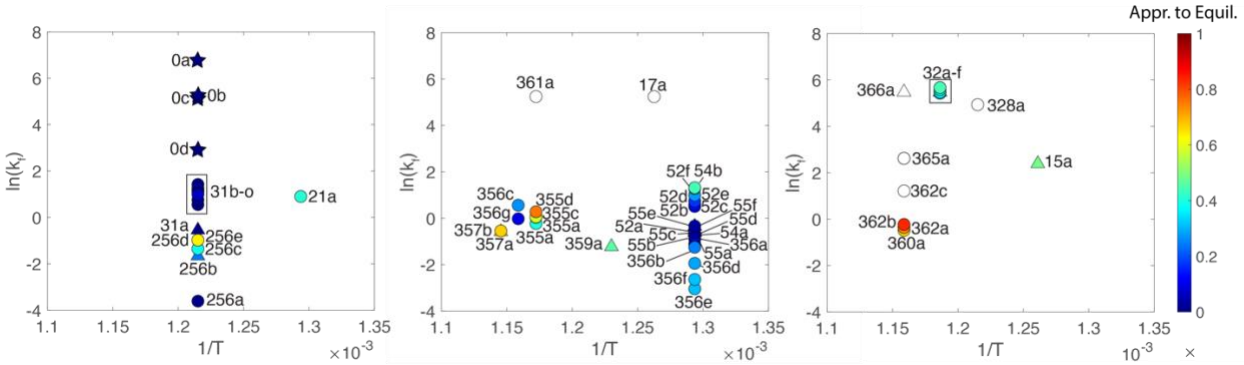

Ref	Catalyst	Ref	Catalyst	Ref	Catalyst	Ref	Catalyst	Ref	Catalyst
0a	$Pt_{0.03}Sn_2$/DeAlBEA-0.001	[31]e	$Pt_{0.29}/Sn_{0.26}$DeAlBEA	[355]a	$Pt_1Sn_{1.58}$/SBA-15	[356]a	$Pt_{0.3}Sn_{0.6}$/SBA-15	[362]a	$Pt_{0.5}Sn_1$/MFI
0b	$Pt_{0.32}Sn_2$/DeAlBEA-0.026	[31]f	$Pt_{0.26}/Sn_{1.3}$DeAlBEA	[355]b	$Pt_1Sn_{0.43}$/SBA-15	[356]b	$Pt_{0.5}Sn_1$/SBA-15	[362]b	$Pt_{0.5}Sn_1$/MFI
0c	$Pt_{0.62}Sn_2$/DeAlBEA-0.013	[31]g	$Pt_{0.28}/Sn_{1.21}$DeAlBEA	[355]c	$Pt_1Sn_{0.8}$/SBA-15	[356]c	$Pt_{0.5}Sn_1$/SBA-15	[362]c	$Pt_{0.5}Na/Sn_1$-ZSM-5
0d	$Pt_{0.62}$/DeAlBEA-0.026	[31]h	$Pt_{0.26}/Sn_{0.47}$DeAlBEA	[355]d	$Pt_1Sn_{0.39}$/SBA-15	[356]d	Pt_1Sn_2/SBA-15	[365]a	$Pt_{0.43}Sn_{0.81}Na_{1.38}$/Al-SBA-15
[21]a	$Pt_{0.375}Sn_{2.3}$/DeAlBEA	[31]i	$Pt_{0.29}/Sn_{0.8}$DeAlBEA	[54]a	Pt_3/SiO_2	[356]e	Pt_3Sn_6/SBA-15	[365]b	$Pt_{0.46}Sn_{0.85}$/Al-SBA-15
[256]a	$Pt_{0.5}Sn_{0.5}$/DeAlBEA	[31]j	$Pt_{0.28}/Sn_{0.63}$DeAlBEA	[55]d	$Pt_1Sn_{2.4}/SiO_2$	[356]f	Pt_2Sn_4/SBA-15	[32]a	$Pt_{0.5}Sn_{0.12}$/DeAlBEA
[256]b	$Pt_{0.5}$/DeAlBEA	[31]k	$Pt_{0.28}/Sn_{0.42}$DeAlBEA	[52]a	Pt_3/SiO_2	[357]a	$Pt_{0.5}/Al_2O_3$	[32]b	$Pt_{0.5}Sn_{0.14}$/DeAlBEA
[256]c	$Pt_{0.5}Sn_2$/DeAlBEA	[31]l	$Pt_{0.3}Sn_{0.4}$/DeAlBEA	[55]e	$Pt_{0.94}Sn_{0.61}/SiO_2$	[357]b	$Pt_{0.5}Sn_{1.5}/Al_2O_3$	[32]c	$Pt_{0.5}Sn_{0.27}$/DeAlBEA
[256]d	$Pt_{0.5}Sn_{0.5}$/DeAlBEA	[31]m	$Pt_{0.38}/Sn_{0.44}$DeAlBEA	[355]f	Pt_1/SiO_2	[17]a	$Pt_{0.35}Sn_{1.26}/Al_2O_3$	[32]d	$Pt_{0.5}Sn_{0.57}$/DeAlBEA
[256]e	$Pt_{0.5}Sn_1$/DeAlBEA	[31]n	$Pt_{0.47}/Sn_{0.46}$DeAlBEA	[356]g	$Pt_{0.5}Sn_1/SiO_2$	[52]c	$Pt_3Sn_{3.5}/SiO_2$		
[31]a	$Pt_{0.27}$/DeAlBEA	[31]o	$Pt_{0.55}/Sn_{0.42}$DeAlBEA	[52]b	$Pt_3Sn_{0.6}/SiO_2$	[52]d	$Pt_3Sn_{0.9}/SiO_2$	[32]e	$Pt_{0.5}Sn_{0.7}$/DeAlBEA
[31]b	$Pt_{0.08}/Sn_{0.44}$DeAlBEA	[55]a	$Pt_1Sn_{2.4}/Al_2O_3$	[358]a	Pt_1Sn_3/CeO_2	[52]e	$Pt_3Sn_{1.8}/SiO_2$	[32]f	$Pt_{0.55}$/DeAlBEA
[31]c	$Pt_{0.28}/Sn_{0.07}$DeAlBEA	[55]b	$Pt_1Sn_{0.6}/Al_2O_3$	[359]a	$Pt_{0.5}$/NaBEA	[52]f	$Pt_3Sn_{1.8}/SiO_2$	[328]a	$Pt_{0.5}Sn_{0.3}/MgAl_2O_4$
[31]d	$Pt_{0.19}/Sn_{0.47}$DeAlBEA	[55]c	Pt_1/Al_2O_3	[360]a	$Pt_{0.5}Sn_1$/MFI	[54]b	Pt_3Sn_1/SiO_2	[366]a	$PtSn/Al_2O_3$
						[361]a	$Pt_1Sn_{0.6}/SiO_2$	[15]a	$Pt_{1.3}$/SBA-15

Figure S5.7. Comparison of apparent first-order forward rate constant ($k_{f,app}$) for various Pt and PtSn catalysts. Stars note catalysts from this work. A) Pt/DeAlBEA and Pt-S/-DeAlBEA catalysts, B) Pt and Pt-Sn catalysts on other supports, C) Pt and Pt-Sn catalysts with H_2 co-flow. Triangles are Pt-based catalysts, and circles are PtSn catalysts. The color of the symbol represents the approach to equilibrium. Details concerning catalyst composition/structure and reaction conditions are reported in Table S5.4.

Table S5.4. Literature PDH Results for Pt and PtSn Catalysts

ref #	Cat.	Pt wt.%	Sn wt. %	Sn/Pt	PDH T (K)	P_{C3H8} (kPa)	Θ_{H2}	Cat mass (g)	Conv. (%)	C_3H_6 Select (%)	k_f(mol C_3H_6/(s.bar.mol Pt)	appr to equil	1/T	ln(k_f)	Pt disp. (%)	Cluster size? (nm)	Pt or PtSn?	Pt-Sn inter.
359	Pt/NaBEA	0.5	0	0	813	80	0	0.4	22.7	63.4	0.29	0.464	0.00123	-1.23	n.r.	n.r.	Pt NPs	n/a
55	1Pt/Al_2O_3	1	0	0	773	25	0	0.3	5.4	99	0.54	0.018	0.00129	-0.61	0.51	2.5 +- 1.8	Pt NP	n/a
52	Pt/SiO_2	3	0	0	773	20	0	0.05	6	0	0.61	0.017	0.00129	-0.50	54.9 micro Mol CO/g	1.1+/- 0.7	Pt NPs	XRD, XAS, HAADF STEM, XPS
55	1Pt/SiO_2	1	0	0	773	25	0	0.3	6.9	99	0.70	0.029	0.00129	-0.35	-	-	Pt Clusters	-
256	Pt/DeAlBEA	0.5	0	0	823	101	0	0.3	17	90.4	0.19	0.243	0.00122	-1.66	n.r.	n.r.	Pt	n/a
54	Pt/SiO_2	3	0	0	773	20	0	0.05	5.4	94.9	0.54	0.014	0.00129	-0.61	40.3 molCO/g	2.6+/- 1.2	Pt NPS	CO IR, XRD
357	Pt/Al_2O_3	0.5	0	0	873	100	0	0.3	35	72.1	0.56	0.641	0.00115	-0.58	n.r.	0.6+/- 0.2	Pt Clusters	n/a
31	0.3Pt/DeAlBEA	0.27	0	0	823	5	0	0.1	5.24	100	0.58	0.001	0.00122	-0.55	-	-	-	-
15	Pt/SBA-15-DP	1.3	0	0	793	8	1.625	0.03	13.5	85	10.89	0.486	0.00126	2.39	16.6	3(XRD, TEM) 6.8 (H_2)	Pt NPs	XRD, STEM
31	0.3Pt/0.1SnDeAlBEA	0.28	0.07	0.413	823	5	0	0.1	15.32	99.5	1.73	0.007	0.00122	0.55	-	-	-	-
32	PtSn/DeAlBEA	0.5	0.12	0.397	793	10	1	0	42	95	227.02	0.333	0.00119	5.43	45.46	n.r.	Pt NPs	Sn anchors: XRD, STEM, XPS, CO-IR, TPR, Py-IR
32	PtSn/DeAlBEA	0.5	0.14	0.463	793	10	1	0	43	96	236.36	0.350	0.00119	5.47	42.55	n.r.	Pt NPs	Sn anchors: XRD, STEM, XPS, CO-IR, TPR, Py-IR
31	0.3Pt/0.3SnDeAlBEA	0.29	0.26	1.482	823	5	0	0.1	18.95	99.5	2.12	0.011	0.00122	0.75	-	-	-	-
32	PtSn/BEA	0.5	0.27	0.892	793	10	1	0	46	97	266.92	0.403	0.00119	5.59	48.14	n.r.	Pt NPs	Sn anchors: XRD, STEM, XPS, CO-IR, TPR, Py-IR
355	PtSn/SBA-15	1	0.39	0.644	853	70	0	0.2	43.8	98	1.32	0.757	0.00117	0.28	n.r.	n.r.	Pt NP (XRD)	XPS, TPR
31	PtSn/DeAlBEA	0.3	0.4	2.203	823	5	0	0.1	30	99	3.52	0.032	0.00122	1.26	75	1.6	PtSn	EDX, CO FTIR, TPR
31	0.6Pt/0.5SnDeAlBEA	0.55	0.42	1.262	823	5	0	0.1	39.07	95.7	2.70	0.062	0.00122	0.99	-	-	-	-
31	0.3Pt/0.5SnDeAlBEA	0.28	0.42	2.479	823	5	0	0.1	27.24	99.6	3.35	0.025	0.00122	1.21	-	-	-	-
355	PtSn/SBA-15	1	0.43	0.711	853	70	0	0.2	39.6	95	1.05	0.576	0.00117	0.04	n.r.	n.r.	Pt NP (XRD)	XPS, TPR
31	0.4Pt/0.5SnDeAlBEA	0.38	0.44	1.913	823	5	0	0.1	31.18	98.2	2.91	0.035	0.00122	1.07	-	-	-	-
31	0.1Pt/0.5SnDeAlBEA	0.08	0.44	9.089	823	5.066	0	0.1	10.75	100	4.14	0.003	0.00122	1.42	-	-	-	-
31	0.5Pt/0.5SnDeAlBEA	0.47	0.46	1.617	823	5	0	0.1	35.48	97.8	2.78	0.048	0.00122	1.02	-	-	-	-
31	0.2Pt/0.5SnDeAlBEA	0.19	0.47	4.088	823	5	0	0.1	18.28	100	3.11	0.010	0.00122	1.13	-	-	-	-
31	0.3Pt/0.5SnDeAlBEA	0.26	0.47	2.987	823	5	0	0.1	25.81	99.2	3.38	0.022	0.00122	1.22	-	-	-	-
256	PtSn/DeAlBEA	0.5	0.5	1.653	823	101	0	0.3	3	74.4	0.03	0.006	0.00122	-3.61	n.r.	n.r.	PtSn	PDH Act.
256	PtSn/DeAlBEA	0.5	0.5	1.653	823	101	0	0.3	26	98.6	0.38	0.637	0.00122	-0.98	n.r.	n.r.	PtSn	PDH Act.
32	PtSn/DeAlBEA	0.5	0.57	1.884	843	10	1	0	48	98	289.83	0.443	0.00119	5.67	51.47	1.26+- 0.2	Pt NPs	Sn anchors: XRD, STEM, XPS, CO-IR, TPR, Py-IR

[55]	1Pt0.6Sn/Al_2O_3	1	0.6	0.992	773	25	0	0.3	4.1	99	0.41	0.010	0.00129	-0.90	0.61	2.9+-3.1	PtSn NP	CO FTIR, TPR, XRD, Rxn
[356]	PtSn/SBA-15	0.3	0.6	3.305	773	25	0	0.15	14.3	98	0.48	0.135	0.00129	-0.74	-	-	-	-
[52]	PtSn/SiO_2	3	0.6	0.331	773	20	0	0.05	15	0	1.66	0.117	0.00129	0.51	26.3 micro Mol CO/g	1.4+/-0.6	PtxSny (x/y>3) NPs	XRD, XAS, HAADF STEM, XPS
[55]	1Pt0.6Sn/SiO_2	0.94	0.61	1.072	773	25	0	0.3	6.6	99	0.71	0.026	0.00129	-0.34	-	-	-	-
[31]	0.3Pt/0.7SnDeAlBEA	0.28	0.63	3.718	823	5	0	0.1	27.02	99.2	3.32	0.025	0.00122	1.20	-	-	-	-
[32]	PtSn/DeAlBEA	0.5	0.7	2.314	843	10	1	0	48	99	289.83	0.443	0.00119	5.67	52.23	n.r.	Pt NPs	Sn anchors: XRD, STEM, XPS, CO-IR, TPR, Py-IR
[355]	PtSn/SBA-15	1	0.8	1.322	853	70	0	0.2	39.8	96	1.06	0.584	0.00117	0.06	n.r.	n.r.	Pt NP (XRD)	XPS, TPR
[31]	0.3Pt/1SnDeAlBEA	0.29	0.8	4.559	823	5	0	0.1	27.02	99.2	3.20	0.025	0.00122	1.16	-	-	-	-
[52]	PtSn/SiO_2	3	0.9	0.496	773	20	0	0.05	18	0	2.08	0.175	0.00129	0.73	26. micro Mol CO/g	1.4+/-0.6	Pt3Sn NPs	XRD, XAS, HAADF STEM, XPS
[356]	PtSn/SBA-15	0.5	1	3.305	773	25	0	0.15	18.8	98	0.29	0.247	0.00129	-1.25	-	-	-	-
[256]	PtSn/DeAlBEA	0.5	1	3.305	823	101	0	0.3	26	98.8	0.38	0.637	0.00122	-0.98	n.r.	n.r.	PtSn	PDH Act.
[360]	PtSn/MFI	0.5	1	3.305	863	80	0.25	0.2	35	96.5	0.62	0.658	0.00116	-0.48	n.r.	n.r.	Disp. Pt (no XRD)	n.r.
[362]	PtSn/MFI	0.5	1	3.305	863	80	0.25	2	37	97	0.70	0.742	0.00116	-0.36	n.r.	n.r.	Disp. Pt (no XRD)	n.r.
[362]	PtSn/MFI	0.5	1	3.305	863	80	0.25	2	39	98	0.79	0.834	0.00116	-0.23	n.r.	n.r.	Disp. Pt (no XRD)	n.r.
[356]	PtSn/SiO_2	0.5	1	3.305	863	25	0	0.2	33.9	96.9	0.98	0.097	0.00116	-0.02	n.r.	n.r.	PtSn	PDH Act.
[356]	PtSn/SBA-15	0.5	1	3.305	863	25	0	0.2	49.5	98.5	1.75	0.270	0.00116	0.56	n.r.	21.4	Pt NP (XRD, EDS)	TPR, XPS, UV-vis
[54]	PtSn/SiO_2	3	1	0.551	773	20	0	0.05	27	99.5	3.73	0.442	0.00129	1.32	6.5 molCO/g	2.6+/-1.4	Pt_3Sn (80% Pt), PtSn (20% Pt)[XRD] Pt_3Sn(75% Pt), PtSn(25% Pt), SnO[XAFS}	XRD, XAFS, CO FTIR
[31]	0.3Pt/1.3SnDeAlBEA	0.28	1.21	7.141	823	5	0	0.1	25	99.2	3.02	0.021	0.00122	1.11	-	-	-	-
[31]	0.3Pt/1.5SnDeAlBEA	0.26	1.3	8.263	823	5	0	0.1	24.19	99.6	3.13	0.019	0.00122	1.14	-	-	-	-
[357]	PtSn/Al_2O_3	0.5	1.5	4.958	873	100	0	0.3	35.6	88.5	0.58	0.670	0.00115	-0.55	n.r.	0.8+/-0.2	PtSn clusters(majority), some Pt clusters	EDS, Rxn,
[355]	PtSn/SBA-15	1	1.58	2.611	853	70	0	0.2	34.4	92	0.80	0.400	0.00117	-0.22	n.r.	n.r.	Pt NP (XRD)	XPS, TPR
[52]	PtSn/SiO_2	3	1.8	0.992	773	20	0	0.05	22	99	2.72	0.275	0.00129	1.00	6.5 micro Mol CO/g	1.8+/-0.9	Pt3Sn and PtSn NPs	XRD, XAS, HAADF STEM, XPS
[52]	PtSn/SiO_2	3	1.8	0.992	773	20	0	0.05	26.5	99.4	3.61	0.423	0.00129	1.28	6.5 micro Mol CO/g	1.7+/-0.7	Pt3Sn and PtSn NPs	XRD, XAS, HAADF STEM, XPS
-	PtSn/DeAlBEA-0.001	0.033	1.93	96.65	823	0.7	0	0.005	4.997	98.3	878.16	0.000	0.00122	6.78	-	-	Pt-Sn	FTIR, XAS
[356]	PtSn/SBA-15	1	2	3.305	773	25	0	0.15	20.1	98	0.14	0.287	0.00129	-1.94	-	-	-	-
[256]	PtSn/DeAlBEA	0.5	2	6.61	823	101	0	0.3	21	98.9	0.26	0.389	0.00122	-1.35	n.r.	n.r.	PtSn	PDH Act.
[21]	PtSn/DeAlBEA	0.375	2.3	10.14	773	5	0	0.3	48	98	2.47	0.414	0.00129	0.90	70	n.r.	Pt cluster	XAS, CO IR, 119Sn NMR

[55]	1Pt2.4Sn/Al_2O_3	1	2.4	3.966	773	25	0	0.3	3.3	99	0.33	0.006	0.00129	-1.12	0.49	2.8+-2.1	PtSn NP	CO FTIR, TPR, XRD, Rxn
[55]	1Pt2.4Sn/SiO_2	1	2.4	3.966	773	25	0	0.3	5.2	99	0.53	0.016	0.00129	-0.64	-	-	PtSn Clusters	-
-	PtSn/DeAlBEA-0.013	0.32	2.44	12.6	823	0.7	0	0.005	14.68	99.23	190.79	0.001	0.00122	5.25	-	-	Pt-Sn	FTIR, XAS
-	PtSn/DeAlBEA-0.026	0.62	2.49	6.637	823	0.7	0	0.005	12.85	99.15	168.98	0.000	0.00122	5.13	-	-	Pt-Sn	FTIR, XAS
[52]	PtSn/SiO_2	3	3.5	1.928	773	20	0	0.05	16	0	1.80	0.135	0.00129	0.59	9.7 micro Mol CO/g	2.3+/-1.3	Pt3Sn and PtSn NPs	XRD, XAS, HAADF STEM, XPS
[356]	PtSn/SBA-15	2	4	3.305	773	25	0	0.15	20.9	98	0.07	0.314	0.00129	-2.64	-	-	-	-
[356]	PtSn/SBA-15	3	6	3.305	773	25	0	0.15	20.8	98	0.05	0.310	0.00129	-3.04	-	-	-	-
[32]12/13/2023 7:49:00 PM	Pt/SnDeAlBEA	0.55	0	0	843	10.13	1	0	50	92.5	237.26	0.493	0.00119	5.47	-	-	-	-
-	Pt/DeAlBEA	0.62	0	0	823	0.7	0	0.0049	2.41	91	21.45	0.000	0.00122	3.07	n.m.	n.m.	Pt Clusters	CO FTIR

5.6.8 Kinetics of PDH over PtSn/DeAlBEA Catalysts

5.6.8.1 Packed Bed Reactor Design Equation

$$W = F_{A0}\int_0^x \frac{dX}{-r}$$

Where W is the weight of Pt, F_{A0} is the initial flow rate of reactant in mol/s.
Zeroth order in propane:

$$-r_1 = k_1'$$
$$W = F_{C_3H_80}\int_0^x \frac{dX}{k_1'}$$
$$W = F_{C_3H_80}\left(\frac{x}{k_1'}\right)$$

First order in propane:

$$-r_1 = k_1 K_{C_3H_8} P_{C_3H_8} = k_1' P_{C_3H_8} = \frac{k_1' P^o_{C_3H_8}(1-x)}{1+y^o_{C3H8}x}$$
$$W = F_{C_3H_80}\int_0^x \frac{dX}{\frac{k_1' P^o_{C_3H_8}(1-x)}{1+y^o_{C3H8}x}}$$
$$W = F_{C_3H_80}\left(-\frac{y^o_{C3H8}x}{k_1' P^o_{C_3H_8}} - \frac{(1+y^o_{C3H8})\ln(1-x)}{k_1' P^o_{C_3H_8}}\right)$$
$$\frac{W P^o_{C_3H_8}}{F_{C_3H_80}} = -\frac{(y^o_{C3H8}x + (1+y^o_{C3H8})\ln(1-x))}{k_1'}$$

Solving for P

$$P^o_{C_3H_8} = -\frac{F^o_{C_3H_8}}{W k_1'} * (y^o_{C3H8}x + (y^o_{C3H8}+1) * \ln(1-x))$$

Langmuir-Hinshelwood with propane site-blocking:

$$-r_2 = \frac{k_1 K_{C_3H_8} P_{C_3H_8}}{1+K_{C_3H_8} P_{C_3H_8}}$$
$$= \frac{k_1 K_{C_3H_8} P^o_{C_3H_8}(1-x)}{(1+y^o_{C3H8}x)\left(1+\frac{K_{C_3H_8} P^o_{C_3H_8}(1-x)}{1+y^o_{C3H8}x}\right)} = \frac{k_1 K_{C_3H_8} P^o_{C_3H_8}(1-x)}{\left(1+y^o_{C3H8}x + K_{C_3H_8} P^o_{C_3H_8}(1-x)\right)}$$
$$W = F_{C_3H_80}\int_0^x \frac{dX}{\frac{k_1 K_{C_3H_8} P^o_{C_3H_8}(1-x)}{\left(1+y^o_{C3H8}x + K_{C_3H_8} P^o_{C_3H_8}(1-x)\right)}}$$
$$W = \frac{F_{C_3H_80}\left(\left(K_{C_3H_8} P^o_{C_3H_8} - y^o_{C3H8}\right)x - (1+y^o_{C3H8})\ln(1-x)\right)}{k_1 K_{C_3H_8} P^o_{C_3H_8}}$$
$$\frac{W P^o_{C_3H_8}}{F_{C_3H_80}} = \frac{\left(K_{C_3H_8} P^o_{C_3H_8} - y^o_{C3H8}\right)x - (1+y^o_{C3H8})\ln(1-x)}{k_1 K_{C_3H_8}}$$

Solving for P

$$P^o_{C_3H_8} = \frac{1}{K_{C_3H_8}\left(\frac{Wk'_1}{F^o_{C_3H_8}} + x\right)} * (y^o_{C3H8}x - (y^o_{C3H8} + 1) * ln(1-x))$$

Langmuir-Hinshelwood with propane site-blocking, 2-surface sites:

$$-r_4 = \frac{k_1 K_{C_3H_8} P_{C_3H_8}}{\left(1 + K_{C_3H_8} P_{C_3H_8}\right)^2}$$

$$= \frac{k_1 K_{C_3H_8} P^o_{C_3H_8}(1-x)}{(1 + y^o_{C3H8}x)\left(1 + \frac{K_{C_3H_8} P^o_{C_3H_8}(1-x)}{1 + y^o_{C3H8}x}\right)^2} = \frac{k_1 K_{C_3H_8} P^o_{C_3H_8}(1-x)(1 + y^o_{C3H8}x)}{\left(1 + y^o_{C3H8}x + K_{C_3H_8} P^o_{C_3H_8}(1-x)\right)^2}$$

$$W = F_{C_3H_8 0}\int_0^x \frac{dX}{\frac{k_1 K_{C_3H_8} P^o_{C_3H_8}(1-x)(1 + y^o_{C3H8}x)}{\left(1 + y^o_{C3H8}x + K_{C_3H_8} P^o_{C_3H_8}(1-x)\right)^2}}$$

$$W = \frac{F_{C_3H_8 0}\left(\left(y^0_{C_3H_8} - 1\right)\left(K_{C_3H_8} P^o_{C_3H_8}\right)^2 \ln(1 + y^o_{C3H8}x) - y^o_{C3H8} * \left(K_{C_3H_8} P^o_{C_3H_8} - y^o_{C3H8}\right)^2 x - (y^o_{C3H8} + 1)^2 {y^o_{C3H8}}^2 \ln(1-x)\right)}{k_1 K_{C_3H_8} P^o_{C_3H_8} * {y^o_{C3H8}}^2}$$

$$\frac{W P^o_{C_3H_8}}{F_{C_3H_8 0}} = \frac{\left(\left(y^0_{C_3H_8} - 1\right)\left(K_{C_3H_8} P^o_{C_3H_8}\right)^2 \ln(1 + y^o_{C3H8}x) - y^o_{C3H8} * \left(K_{C_3H_8} P^o_{C_3H_8} - y^o_{C3H8}\right)^2 x - (y^o_{C3H8} + 1)^2 {y^o_{C3H8}}^2 \ln(1-x)\right)}{k_1 K_{C_3H_8} * {y^o_{C3H8}}^2}$$

Langmuir-Hinshelwood with propene site-blocking:

$$-r_3 = \frac{k'_1 P_{C_3H_8}}{1 + K_{C_3H_6} P_{C_3H_6}} = \frac{k'_1 P^o_{C_3H_8}(1-x)}{\left(1 + y^o_{C3H8}x + K_{C_3H_6} P^o_{C_3H_8}(x)\right)}$$

$$W = F_{C_3H_8,0}\int_0^x \frac{dX}{\frac{k'_1 P^o_{C_3H_8}(1-x)}{\left(1 + y^o_{C3H8}x + K_{C_3H_6} P^o_{C_3H_8}(x)\right)}}$$

$$W = F_{C_3H_8,0}\left(-\frac{\left(\mathrm{K_{C_3H_6}} P^o_{C_3H_8} + y^o_{C3H8}\right)x + \left(K_{C_3H_6} P^o_{C_3H_8} + y^o_{C3H8} + 1\right) * ln(1-x)}{k'_1 P^o_{C_3H_8}}\right)$$

$$\frac{W P^o_{C_3H_8}}{F_{C_3H_8,0}} = (-\frac{\left(\mathrm{K_{C_3H_6}} P^o_{C_3H_8} + y^o_{C3H8}\right)x + \left(K_{C_3H_6} P^o_{C_3H_8} + y^o_{C3H8} + 1\right) * ln(1-x)}{k'_1}$$

Solving for P

$$P^o_{C_3H_8} = \frac{(y^o_{C3H8}x - (y^o_{C3H8} + 1) * \ln(1-x))}{\left(\frac{Wk'_1}{F^o_{C_3H_8}}\right) + \mathrm{K_{C_3H_6}}x + \mathrm{K_{C_3H_6}}\ln(1-x)}$$

Langmuir-Hinshelwood with propene site-blocking, 2 sites:

$$-r_5 = \frac{k'_1 P_{C_3H_8}}{\left(1 + K_{C_3H_6} P_{C_3H_6}\right)^2} = \frac{k'_1 P^o_{C_3H_8}(1-x)}{\left(1 + y^o_{C3H8}x + K_{C_3H_6} P^o_{C_3H_8}(x)\right)^2}$$

$$W = F_{C_3H_8,0}\int_0^x \frac{dX}{\frac{k'_1 P^o_{C_3H_8}(1-x)}{\left(1 + y^o_{C3H8}x + K_{C_3H_6} P^o_{C_3H_8}(x)\right)^2}}$$

$$W = F_{C_3H_8,0}\left(-\frac{\frac{1}{2}x\left(K_{C_3H_6}P^o_{C_3H_8} + y^o_{C3H8}\right) * \left(K_{C_3H_6}P^o_{C_3H_8} * (x+2) + (y^o_{C3H8}+1) * (x+2) + 4\right) + \left(K_{C_3H_6}P^o_{C_3H_8} + y^o_{C3H8} + 1\right)^2 * ln(1-x)}{k_1' P^o_{C_3H_8}}\right)$$

$$\frac{WP^o_{C_3H_8}}{F_{C_3H_8,0}} = \left(-\frac{\frac{1}{2}x\left(K_{C_3H_6}P^o_{C_3H_8} + y^o_{C3H8}\right) * \left(K_{C_3H_6}P^o_{C_3H_8} * (x+2) + (y^o_{C3H8}+1) * (x+2) + 4\right) + \left(K_{C_3H_6}P^o_{C_3H_8} + y^o_{C3H8} + 1\right)^2 * ln(1-x)}{k_1' P^o_{C_3H_8}}\right.$$

Langmuir-Hinshelwood with propane and propene site-blocking:

$$-r_6 = \frac{k_1 K_{C_3H_8} P_{C_3H_8}}{1 + K_{C_3H_8}P_{C_3H_8} + K_{C_3H_6}P_{C_3H_6}}$$

$$= \frac{k_1 K_{C_3H_8} P^o_{C_3H_8}(1-x)}{(1+y^o_{C3H8}x)\left(1 + \frac{K_{C_3H_8}P^o_{C_3H_8}(1-x)}{1+y^o_{C3H8}x} + \frac{K_{C_3H_6}P^o_{C_3H_8}(x)}{1+y^o_{C3H8}x}\right)}$$

$$= \frac{k_1 K_{C_3H_8} P^o_{C_3H_8}(1-x)}{\left(1 + y^o_{C3H8}x + K_{C_3H_8}P^o_{C_3H_8}(1-x) + K_{C_3H_6}P^o_{C_3H_8}(x)\right)}$$

$$W = F_{C_3H_8,0}\int_0^x \frac{dX}{\frac{k_1 K_{C_3H_8} P^o_{C_3H_8}(1-x)}{\left(1 + y^o_{C3H8}x + K_{C_3H_8}P^o_{C_3H_8}(1-x) + K_{C_3H_6}P^o_{C_3H_8}(x)\right)}}$$

$$W = F_{C_3H_8,0}\frac{\left(K_{C_3H_8}P^o_{C_3H_8} - y^o_{C3H8} - K_{C_3H_6}P^o_{C_3H_8}\right)x - (y^o_{C3H8} + K_{C_3H_6}P^o_{C_3H_8} + 1)\ln(1-x)}{k_1 K_{C_3H_8} P^o_{C_3H_8}}$$

5.6.8.2 Estimation of Initial Guesses

By using the lowest and highest P pressure data points, we can estimate k_1 and $K_{ads.}$

$$-r_2 = \frac{k_1 K_{C_3H_8} P_{C_3H_8}}{1 + K_{C_3H_8}P_{C_3H_8}}$$

At low P, $K_{C_3H_8}P_{C_3H_8} \ll 1$, so

$$-r_2 = k_1 K_{C_3H_8} P_{C_3H_8} = k_{app} P_{C_3H_8}$$

At high P, $1 \ll K_{C_3H_8}P_{C_3H_8}$, so

$$-r_2 = k_1$$

These data are collected over a small propane partial pressure range (0.5-3 kPa), so these estimates are just that.

The lowest two P_{C3H8} points were fit with 1st order rate law to extract k_{app} initial guesses:

$$W = F_{C_3H_8 0}\left(-\frac{y^o_{C3H8}x}{k_1' P^o_{C_3H_8}} - \frac{(1+y^o_{C3H8})\ln(1-x)}{k_1' P^o_{C_3H_8}}\right)$$

Table S5.5. Estimation of k_{app} from first-order fit at low propane partial pressure.

Catalyst	k_{app} 773K	k_{app} 798K	k_{app} 823K	k_{app} 858K	error
PtSn/DeAlBEA -0.001 (0.5-0.7 kPa)	589.9	761.3	854.7	1037.7	4.46 e-6
PtSn/DeAlBEA -0.013 (0.7-1 kPa)	159.00	207.82	249.39	289.73	1.25e-3
PtSn/DeAlBEA -0.026 (0.7-1 kPa)	62.87	82.73	97.37	117.13	6.39e-3
All 3 together	100.0	145.4	169.5	201.4	9.07e-2

The highest two P_{C3H8} points were fit with 0^{th} order rate law to extract k_1 initial guesses:

$$W = F_{C_3H_8 0}\left(\frac{x}{k_1}\right)$$

Table S5.6. Estimation of k_1 from zero-order fit at high propane partial pressure.

Catalyst	k_1 773K	k_1 798K	k_1 823K	k_1 858K	error
PtSn/DeAlBEA -0.001(2.25-3 kPa)	4.30	6.07	7.11	9.12	1.15e-6
PtSn/DeAlBEA -0.013 (1.5-3 kPa)	1.42	1.84	2.39	2.79	2.54e-4
PtSn/DeAlBEA -0.026 (1.5-3 kPa)	0.99	1.29	1.76	1.97	3.74e-3
All 3 together	0.96	1.26	1.73	1.93	5.23e-2

We can combine these to get the initial guesses for K_{C3H8}:

$$K_{C_3H_8} k_1 = k_{app}$$

$$K_{C_3H_8} = \frac{k_{app}}{k_1}$$

Table S5.7. Estimation of K_{ads} from first- and zero-order fits.

Catalyst	K_{C3H8} 773K	K_{C3H8} 798K	K_{C3H8} 823K	K_{C3H8} 858K	error
PtSn/DeAlBEA -0.001(2.25-3 kPa)	137.32	125.39	120.24	113.74	1.15E-06
PtSn/DeAlBEA -0.013 (1.5-3 kPa)	112.29	113.11	104.40	103.83	2.54E-04
PtSn/DeAlBEA -0.026 (1.5-3 kPa)	63.80	63.93	55.43	59.60	3.74E-03
All 3 together	103.67	115.03	97.74	104.48	5.23E-02

These values can be used for initial guesses. Equilibrium constants of propane adsorption were used as initial guesses for the equilibrium constants for propene adsorption. Additionally for propene inhibition rate law. The product of k_1 and K_{C3H8} was used as k_1' also known as k_{app}.

Table S5.8. Kinetic fitting parameters for PDH over PtSn/DeAlBEA Catalysts

Catalyst	Rate law	E_{a1} (kJ/mol)	$Ln(A_1)$	E_{app} (kJ/mol)	$Ln(A_{app})$	ΔH_{C3H8} (kJ/mol)	ΔS_{C3H8} (J/mol K)	ΔH_{C3H6} (kJ/mol)	ΔS_{C3H6} (J/mol K)	R^2	Red χ^2
PtSn/DeAlBEA-0.001	$\frac{k_1 K_{C_3H_8} P_{C_3H_8}}{1 + K_{C_3H_8} P_{C_3H_8}}$	50.68 ± 6.31	9.51 ± 0.94	9.78 ± 17.74	9.14 ± 2.63	-40.90 ± 11.43	-3.05 ± 14.09			0.981	0.0010
	$\frac{k_{app} P_{C_3H_8}}{1 + K_{C_3H_6} P_{C_3H_6}}$			16.70 ± 5.41	9.71 ± 0.80			-82.26 ± 11.81	-29.36 ± 14.56	0.983	0.00092
	$\frac{k_1 K_{C_3H_8} P_{C_3H_8}}{1 + K_{C_3H_8} P_{C_3H_8} + K_{C_3H_6} P_{C_3H_6}}$	52.21 ± 6.39	9.78 ± 0.95	11.33 ± 17.83	9.41 ± 2.64	-40.88 ± 11.44	-2.99 ± 14.13	-42.95 ± 11.45	-5.99 ± 14.13	0.978	0.001
PtSn/DeAlBEA-0.013	$\frac{k_1 K_{C_3H_8} P_{C_3H_8}}{1 + K_{C_3H_8} P_{C_3H_8}}$	52.53 ± 4.70	8.65 ± 0.70	1.16 ± 15.38	6.78 ± 2.28	-51.37 ± 10.68	-15.52 ± 13.16			0.996	0.0003
	$\frac{k_{app} P_{C_3H_8}}{1 + K_{C_3H_6} P_{C_3H_6}}$			7.06 ± 7.45	7.13 ± 1.10			-116.28 ± 24.03	-82.25 ± 30.14	0.993	0.0006
	$\frac{k_1 K_{C_3H_8} P_{C_3H_8}}{1 + K_{C_3H_8} P_{C_3H_8} + K_{C_3H_6} P_{C_3H_6}}$	58.35 ± 4.91	9.63 ± 0.73	6.98 ± 15.58	7.76 ± 2.31	-51.37 ± 10.67	-15.52 ± 13.14	-59.51 ± 10.93	-27.02 ± 13.47	0.923	0.0070
PtSn/DeAlBEA-0.026	$\frac{k_1 K_{C_3H_8} P_{C_3H_8}}{1 + K_{C_3H_8} P_{C_3H_8}}$	55.06 ± 3.36	8.32 ± 0.50	21.90 ± 16.48	8.51 ± 2.44	-33.16 ± 13.12	1.54 ± 16.17			0.982	0.0017
	$\frac{k_{app} P_{C_3H_8}}{1 + K_{C_3H_6} P_{C_3H_6}}$			28.86 ± 7.27	9.08 ± 1.08			-77.81 ± 15.92	-38.53 ± 18.96	0.976	0.0022
	$\frac{k_1 K_{C_3H_8} P_{C_3H_8}}{1 + K_{C_3H_8} P_{C_3H_8} + K_{C_3H_6} P_{C_3H_6}}$	60.51 ± 3.12	9.23 ± 0.46	27.35 ± 16.24	9.42 ± 2.41	-33.16 ± 13.13	1.58± 16.21	-40.23 ± 12.59	-8.48 ± 15.55	0.970	0.003

Where $k_{app} = k_1 K_{C_3H_8}$

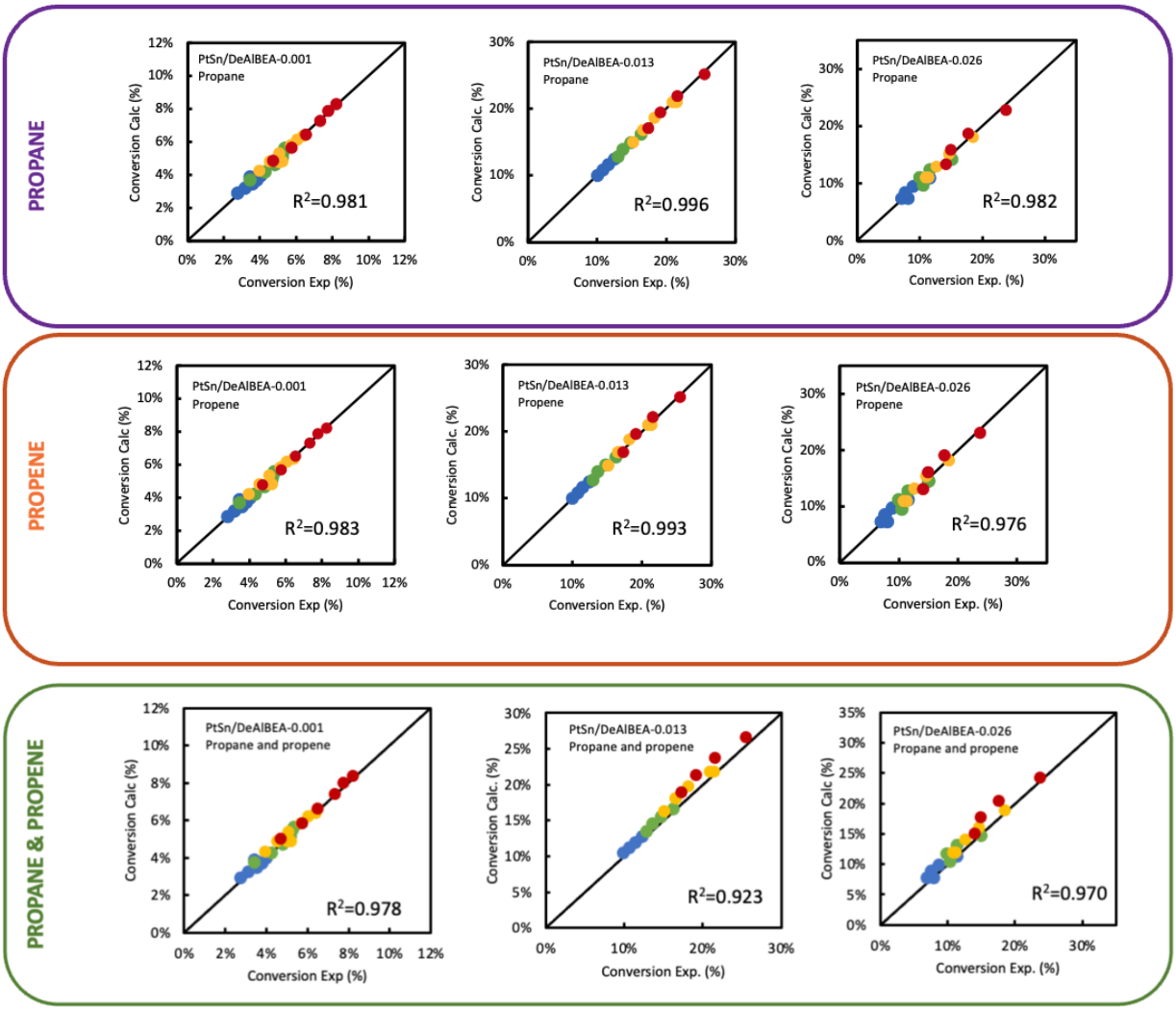

Figure S5.8. Parity plots for Langmuir-type kinetic rate laws with propane, propene, or propane and propene inhibition for PDH over PtSn/DeAlBEA-0.026, PtSn/DeAlBEA-0.013, and PtSn/DeAlBEA-0.001.

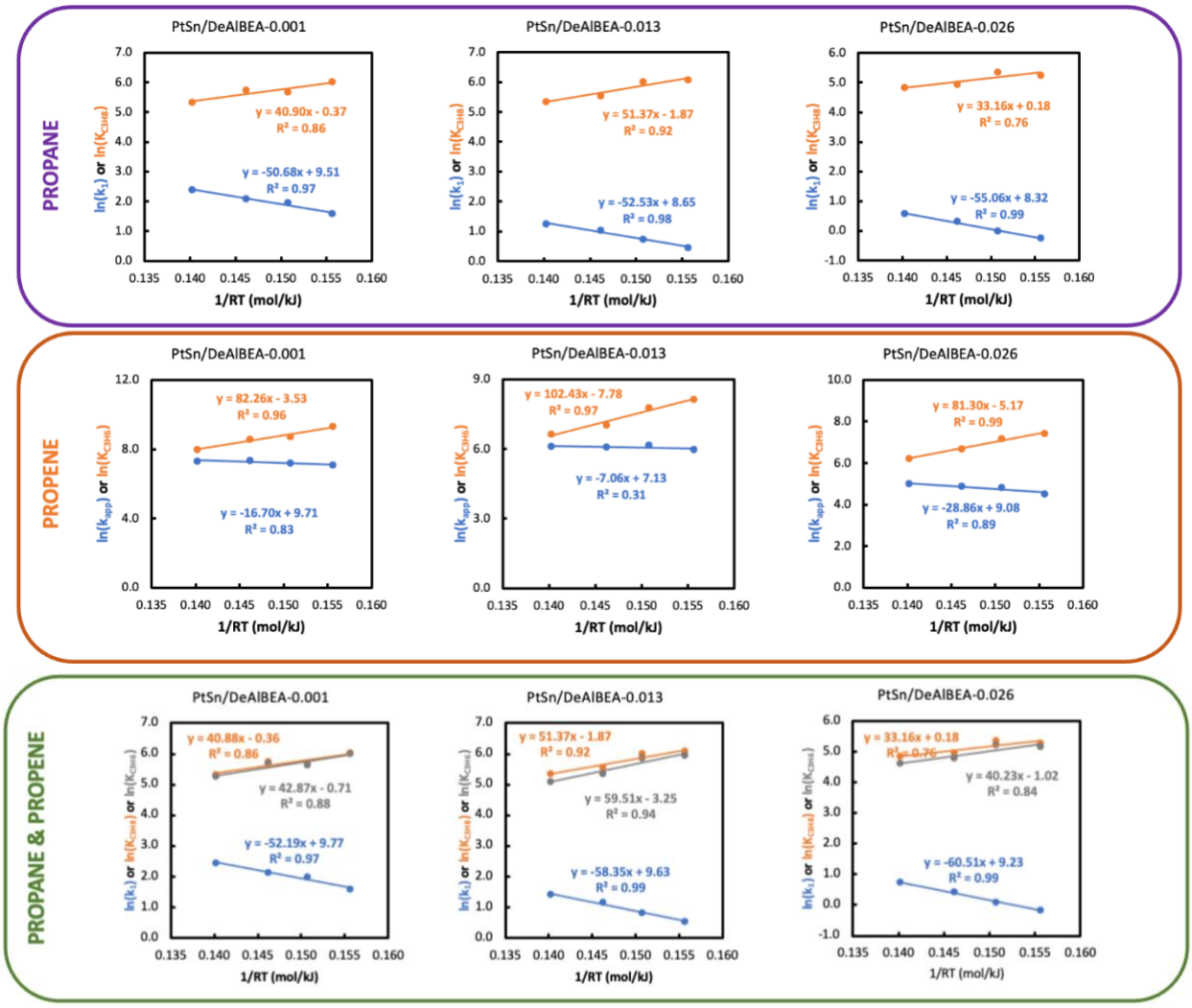

Figure S5.9. Arrhenius plots for Langmuir-type kinetic rate laws with propane, propene, or propane and propene inhibition for PDH over PtSn/DeAlBEA-0.026, PtSn/DeAlBEA-0.013, and PtSn/DeAlBEA-0.001.

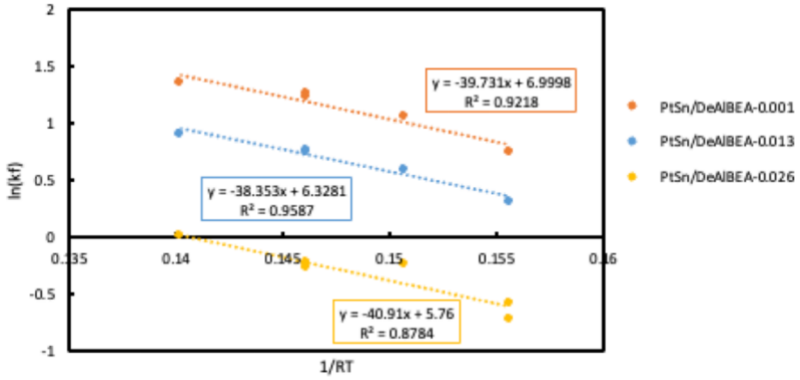

Figure S5.10. The activation energy for $k_{f,app}$ for PDH over PtSn/DeAlBEA-0.026, PtSn/DeAlBEA-0.013, and PtSn/DeAlBEA-0.001.

Table S5.9. Comparison of $k_{f,app}$ and Langmuir fitted parameters.

Catalyst	k_1	K_{C3H8}	$k_1 * K_{C3H8}$	$k_{f,app}$	**$E_{a,k1}$ (kJ/mol)**	**$E_{a,kapp}$ (kJ/mol)**	**$E_{a,kf,app}$ (kJ/mol)**
PtSn/DeAlBEA-0.001	8.03	310.8	2495.7	3.52	50.68 ± 6.31	9.78 ± 17.74	39.73
PtSn/DeAlBEA-0.013	2.83	256.3	725.2	2.12	52.53 ± 4.70	1.16 ± 15.38	38.35
PtSn/DeAlBEA-0.026	1.38	140.7	194.1	0.785	55.06 ± 3.36	21.90 ± 16.48	40.91

Rate constant values are given for 0.7 kPa and 823K for the Langmuir Hinshelwood rate law with propane inhibition.

Table S5.10. Activation energies of PDH over PtSn/DeAlBEA catalysts and Pt and PtSn catalysts reported in the literature. Here, E_{app} is the apparent activation energy of propane dehydrogenation. If heats of adsorption for propane are reported, they are lumped with a forward rate for adsorbed propane to directly compare to first-order rates.

Catalyst	Rate Law, $-r_{C3H8}$	$E_{f,app}$ (kJ/mol)	ΔH (kJ/mol) C_3H_8, C_3H_6, H_2	Ref
Pt/A_2O_3	$k_f P_{C3H8}$	86.2	-	367
$0.1\%Pt/Al_2O_3$	$k_f P_{C3H8}$	26 ±3	-	347
$0.3\%Pt/Al_2O_3$	$k_f P_{C3H8}$	41±5	-	347
$3\% Pt/Al_2O_3$	$k_f P_{C3H8}$	56±6	-	347
Pt/Al_2O_3	$-r \propto P_{H2}^{-1}$	121±19.6	-	346
Pt/Mg(Al)O	$\frac{k_2 K_1 P_{C3H8}}{\left(1+(P_{H2}^{0.5}K_5^{-0.5})\right)^2}$	81	-7.7	353
Pt/Mg(Al)O	$\frac{k_3 K_1 K_2 K_5^{0.5} P_{C3H8} P_{H2}^{0.5}}{\left(1+(P_{H2}^{0.5}K_5^{-0.5})\right)^2}$	97	-7.7	353
$PtSn/Al_2O_3$	$\frac{k_1(K_{C3H8}P_{C3H8}-\left(\frac{K_{C3H6}P_{C3H8}K_{H2}P_{H2}}{K_P}\right)}{(1+K_{C3H8}P_{C3H8}+K_{C3H6}P_{CH6}+K_{H2}P_{H2})^2}$	169.7	-85.82	349
$PtSnK/Al_2O_3$	$a*\frac{k_1\left(P_{C3H8}-\left(\frac{P_{C3H8}P_{H2}}{K_{eq}}\right)\right)}{1+\left(\frac{P_{C3H6}}{K_{C3H6}}\right)}$	34.57±9.13	-85.817 ±22.46	345
$PtSn/Al_2O_3$	$k_f P_{C3H8} - k_{rev} P_{C3H6} P_{H2}^{\gamma}$	34.8 ± 19.6	-	344
$Pt\text{-}Sn/Al_2O_3$	$\frac{k_1\left(P_{C3H8}-\frac{P_{C3H8}P_{H2}}{K_{eq}}\right)}{\left(1+K_2P_{C3H6}+(P_{H2}^{0.5}K_3^{0.5})\right)^2}$	44.7	-94.3 -238.9	352
$PtSn/Al_2O_3$	$k_f P_{C3H8}$	212.5		367
PtSn/Mg(Al)O	$a*\frac{k_1\left(P_{C3H8}-\left(\frac{P_{C3H8}P_{H2}}{K_{eq}}\right)\right)}{1+\left(\frac{P_{C3H6}}{K_{C3H6}}\right)}$	34.57	-85.82	350
PtSn/Mg(Al)O	$a*\frac{k_1\left(P_{C3H8}-\left(\frac{P_{C3H8}P_{H2}}{K_{eq}}\right)\right)}{1+\left(\frac{P_{C3H6}}{K_{C3H6}}\right)}$	30.45	-85.82	350
Pt-Sn/SAPO-34	$\frac{k_1\left(P_{C3H8}-\left(\frac{P_{C3H8}P_{H2}}{K_{eq}}\right)\right)}{(1+K_{DP}P_{C3H6}+K_{DH}^{0.5}P_{H2}^{0.5})^3}$	58.1	-36.4	351
$Pt_{1.7}NaY$	$k_f P_{C3H8}$	62.7	-	343
$Pt_{1.7}Sn_{0.75}NaY$	$k_f P_{C3H8}$	62.7	-	343
$Pt_{1.7}Sn_{0.9}NaY$	$k_f P_{C3H8}$	58.5	-	343
$Pt_{1.7}Sn_{1.4}NaY$	$k_f P_{C3H8}$	62.7	-	343
$Pt_{1.7}Sn_{2.4}NaY$	$k_f P_{C3H8}$	58.5	-	343
PtSn/DeAlBEA-0.001	$\boldsymbol{\frac{k_1 K_{C_3H_8} P_{C_3H_8}}{1+K_{C_3H_8}P_{C_3H_8}}}$	**9.78 ± 17.74**	**-40.90 ± 11.43**	**This work**
PtSn/DeAlBEA-0.001	$\boldsymbol{\frac{k_{app} P_{C_3H_8}}{1+K_{C_3H_6}P_{C_3H_6}}}$	**16.70 ± 5.41**	**-82.26 ± 11.81**	**This work**
PtSn/DeAlBEA-0.013	$\boldsymbol{\frac{k_1 K_{C_3H_8} P_{C_3H_8}}{1+K_{C_3H_8}P_{C_3H_8}}}$	**1.16 ± 15.38**	**-51.37 ± 10.68**	**This work**
PtSn/DeAlBEA-0.013	$\boldsymbol{\frac{k_{app} P_{C_3H_8}}{1+K_{C_3H_6}P_{C_3H_6}}}$	**7.06 ± 7.45**	**-116.28 ± 24.03**	**This work**
PtSn/DeAlBEA-0.026	$\boldsymbol{\frac{k_1 K_{C_3H_8} P_{C_3H_8}}{1+K_{C_3H_8}P_{C_3H_8}}}$	**3.69 ± 16.48**	**-51.37 ± 13.12**	**This work**
PtSn/DeAlBEA-0.026	$\boldsymbol{\frac{k_{app} P_{C_3H_8}}{1+K_{C_3H_6}P_{C_3H_6}}}$	**28.86 ± 7.27**	**-77.81 ± 15.92**	**This work**

5.6.9 $k_{f,app}$ vs. internal and external mass transport limitations

In order to eliminate internal mass transport limitations, the Weisz Prater criterion must be <<1. The Weisz Prater criterion, C_{WP}, is defined as

$$C_{WP} = \frac{-r_{C3H8,v}\left[\frac{mol\ C_3H_8}{m^3}\right] * (R[m])^2}{D_e\left[\frac{m^2}{s}\right] * C_{C3H8,s}\left[\frac{mol\ C_3H_8}{m^3}\right]} \ll 1$$

Where $-r_{C3H8,v}$ is the rate of propane consumption per unit volume of catalyst [mol $C_3H_8/(m^3*s)$], R is the radius of the zeolite particle [m], D_e is the effective diffusivity of the reactant [m^2/s], and $C_{C3H8,s}$is the concentration of C_3H_8 at the external surface of the catalyst [mol C_3H_8 /m^3].

$$r_{C3H8,v}\left[\frac{mol\ C_3H_6}{m^3}\right] = \mathrm{r_{C3H8}}\left[\frac{mol\ C_3H_6}{mol\ Pt\ s}\right] * \frac{\text{mol Pt}}{\text{kg cat}} * \rho_f\left[\frac{kgcat}{m^3}\right]$$

$$\frac{k_f P_{C3H8} * \frac{\text{mol Pt}}{\text{kg cat}} * \rho_f\left[\frac{kgcat}{m^3}\right] * (R[m])^2}{D_e\left[\frac{m^2}{s}\right] * C_{C3H8,s}\left[\frac{mol\ C_3H_8}{m^3}\right]} \ll 1$$

$$k_f \ll \frac{\left(D_e\left[\frac{m^2}{s}\right] * C_{C3H8,s}\left[\frac{mol\ C_3H_8}{m^3}\right]\right)}{P_{C3H8} * \frac{\text{mol Pt}}{\text{kg cat}} * \rho_f\left[\frac{kgcat}{m^3}\right] * (R[m])^2}$$

$$k_f \ll 3578.2$$

In order to eliminate external mass transport limitations, the Mears criterion must be < 0.15. The Mears criterion, C_M, is defined as

$$C_M = \frac{-r'_{C3H8}\left[\frac{mol\ C_3H_8}{kg\ cat\ *s}\right]\rho_b\left[\frac{kg}{m^3}\right]D[m]}{k_c\left[\frac{m}{s}\right]C_{C3H8,b}\left[\frac{mol}{m^3}\right]} < 0.15$$

Where $-r'_{C3H8}$ is the rate of propane consumption per unit mass of catalyst [mol $C_3H_8/(kg\ cat*s)$], D is the diameter of the zeolite particle [m], ρ_b is the bulk density of the catalyst bed [kg/m^3], n is the reaction order, kc is the mass transfer coefficient [m/s], and $C_{C3H8,b}$ is the bulk concentration of propane [mol/m^3].

$$k_c\left[\frac{m}{s}\right] = \mathrm{Sh} * \frac{\mathrm{D_{AB}}\left[\frac{\mathrm{m}^2}{\mathrm{s}}\right]}{d_p[m]}$$

Frössling correlation: $\mathrm{Sh} = 2 + 0.6 * \mathrm{Re}^{\frac{1}{2}}\mathrm{Sc}^{\frac{1}{3}}$

$$\mathrm{Re} = \mathrm{d_P[m]} * \frac{\mathrm{U}\left[\frac{\mathrm{m}}{\mathrm{s}}\right]}{v\left[\frac{\mathrm{m}^2}{\mathrm{s}}\right]}; \mathrm{Sc} = \frac{v\left[\frac{m^2}{s}\right]}{D_{AB}\left[\frac{m^2}{s}\right]}$$

$$\frac{k_f P_{C3H8} * \frac{molPt}{kgcat}\rho_b\left[\frac{kg}{m^3}\right]R[m]}{\left(2 + 0.6 * \left(\mathrm{d_P[m]} * \frac{\mathrm{U}\left[\frac{\mathrm{m}}{\mathrm{s}}\right]}{v\left[\frac{\mathrm{m}^2}{\mathrm{s}}\right]}\right)^{\frac{1}{2}}\left(\frac{v\left[\frac{m^2}{s}\right]}{D_{AB}\left[\frac{m^2}{s}\right]}\right)^{\frac{1}{3}}\right) * \frac{\mathrm{D_{AB}}\left[\frac{\mathrm{m}^2}{\mathrm{s}}\right]}{d_p[m]} C_{C3H8,b}\left[\frac{mol}{m^3}\right]} < 0.15$$

$$k_f < 0.15 * \left(\left(2 + 0.6 * \left(\mathrm{d_P[m]} * \frac{\mathrm{U}\left[\frac{\mathrm{m}}{\mathrm{s}}\right]}{v\left[\frac{\mathrm{m}^2}{\mathrm{s}}\right]}\right)^{\frac{1}{2}}\left(\frac{v\left[\frac{m^2}{s}\right]}{D_{AB}\left[\frac{m^2}{s}\right]}\right)^{\frac{1}{3}}\right) * \frac{\mathrm{D_{AB}}\left[\frac{\mathrm{m}^2}{\mathrm{s}}\right]}{d_p[m]} C_{C3H8,b}\left[\frac{mol}{m^3}\right]\right) * \frac{P_{C3H8} * \frac{molPt}{kgcat}\rho_b\left[\frac{kg}{m^3}\right]R[m]}{}$$

$$k_f < 20565$$

Table S5.11. Parameters for Weisz Prater and Mears Criteria Calculations

Parameter	Value	Units	Description
D_p	$9 \cdot 10^{-6}$	m	Particle diameter
U	0.1	m/s	Superficial velocity
v	0.000117	m^2/s	Kinematic viscosity
ρ_b	200000	kg/m^3	Bulk density
ρ_f	1836	kg cat/m^3	Density of zeolite
D_e	$1.4 \cdot 10^{-8}$	m^2/s	Diffusivity
D_{AB}	$5 \cdot 10^{-5}$	m^2/s	Diffusivity
mol Pt/kg cat	0.00154	-	

For these PtSn/DeAlBEA catalysts, k_f values range from 169 – 878 mol C_3H_6/(s • mol Pt • bar). With these calculated values, we conclude that the propane dehydrogenation reaction over PtSn/DeAlBEA is not internally or externally mass transfer limited.

6 Conclusions

This thesis began with a detailed perspective on the achievable results and the limitations of characterizing Pt and Sn materials with the infrared spectroscopy (IR) of adsorbed CO and X-ray Absorption Spectroscopy (XAS) (Chapters 2 and 3, respectively). Then, these concepts were applied to the characterization of Sn/DeAlBEA and PtSn/DeAlBEA catalysts. These materials were also evaluated for their propane dehydrogenation (PDH) activity.

In Chapter 2, IR spectroscopy of CO adsorbed on Pt sites was critically reviewed. The effects of support identity, additives/promoters (e.g., Sn, K, etc.), Pt oxidation and dispersion, and CO coverage were examined. Increasing CO coverage resulted in a blue shift in the observed IR frequency due to increased dipole-dipole repulsions between neighboring CO adsorbates and the heterogeneity of adsorption sites. Positive Pt species exhibited higher IR frequencies of adsorbed CO (> 2100 cm^{-1}) than zero valent Pt (2000-2100 cm^{-1}). These differences were rationalized with molecular orbital theory and the ability of Pt to donate electrons to the CO adsorbate. For clustered Pt, the CO frequency decreased with decreasing Pt particle size. Surprisingly, CO adsorbed to isolated Pt species exhibited high stretching frequencies (>2100 cm^{-1}). Pt on reducible supports (e.g., TiO_2, ZrO_2, CeO_2) exhibited higher IR frequencies for adsorbed CO than Pt on non-reducible supports (e.g., Al_2O_3, MgO, MgAlO). Beyond this trend, the effects of the support were complex to isolate from dispersion effects and CO coverage effects. The Sn interacting with Pt on the IR of adsorbed CO exhibited both red-shifted (Sn alloyed to Pt) and blue-shifted (framework or oxidized Sn) IR frequencies. Again, the availability of electrons for donation from Sn to Pt and, in turn, from Pt to the C-O bond rationalized these trends. The same principle also explained the observed shifts in IR of adsorbed CO on Pt with other additives (e.g., K, La, Ce). Unfortunately, separating potentially confounding effects remained difficult, making analysis complicated. Additional characterization information clarified some of the ambiguity by providing anchors for interpretation.

Chapter 3 summarized the details of evaluating Pt and Sn XAS; the concepts are universal to XAS of all elements. An increase in the oxidation state resulted in a more intense white line due to decreased electron density. Higher coordination numbers (i.e., increased metal clustering) corresponded to reductions in the white line intensity as more metal neighbors replaced oxygen neighbors, and the element of interest became more electron-rich. The support identity significantly impacted the particle size and electron density of the element of interest. Reducible supports (e.g., TiO_2, ZrO_2, CeO_2) resulted in a higher white line intensity and energy; the reverse effect was observed for non-reducible supports (e.g., Al_2O_3, MgO, MgAlO). Pt-Sn interactions resulted in changes in the lattice spacing and shifts in the white line energy and intensity. Thorough evaluation of EXAFS fits and checks for physically sensical parameters remained crucial to accurate interpretation. The interconnected nature of the EXAFS fitting parameters and intersecting effects of structural changes (i.e., support, dispersion, oxidization state, etc.) necessitate additional information from other characterization techniques to make rigorous conclusions.

Chapter 4 investigated the preparation, characterization, and PDH activity of Sn/DeAlBEA catalysts. Ethanol wetness impregnation was the most effective preparation method for incorporating Sn(IV) into DeAlBEA silanol nests. Sn was introduced as Lewis acid sites, as evidenced by CD_3CN, pyridine IR, and UV-vis spectroscopy. IR of adsorbed pyridine also confirmed the lack of Brønsted acid sites in DeAlBEA and Sn/DeAlBEA. Closed Sn framework sites were created over a range of Sn loadings (Sn/Al=0.16-0.67), as evidenced by IR spectra of

adsorbed CD_3CN, XAS, and UV-vis spectroscopy. At high Sn loadings (Sn/Al>0.4), SnO_2 particles were also present in the as-prepared catalyst samples shown in XRD and UV-vis spectroscopy. XRD also confirmed the maintenance of the BEA framework structure with dealumination and upon introduction of Sn into DeAlBEA. These Sn/DeAlBEA catalysts exhibited high stability and propane selectivity for propane dehydrogenation; however, the activity over Sn/DeAlBEA remained low. Increasing the Sn loading in Sn/DeAlBEA resulted in an increase in the STY for propane dehydrogenation. These Sn/DeAlBEA catalysts exhibited similar forward rate constants to those previously reported for Sn/DeAlBEA but lower rate constants than Sn/SiO_2.[247] A higher fraction of Sn open sites on Sn/SiO_2 relative to Sn/DeAlBEA could explain these higher values of k_f.

Chapter 5 investigated the characterization, PDH activity, and kinetic studies of PtSn/DeAlBEA. Pt species interacting with framework Sn(IV) in PtSn/DeAlBEA catalysts were found to be active and stable sites for propane dehydrogenation. These Pt-Sn interactions were evidenced by IR of adsorbed pyridine and adsorbed CO and XAS. Multiple Pt sites are present in these PtSn/DeAlBEA catalysts, including positive Pt species, Pt clusters, and Pt interacting with framework Sn. At low Pt/Al ratios, the Pt was dispersed and interacted with framework Sn (EXAFS Pt-Pt coordination number = 3). As the Pt/Al ratio increased, Pt cluster size increased, and clustered Pt interacting with framework Sn(IV) became the main Pt species (EXAFS Pt-Pt coordination number = 9). These PtSn/DeAlBEA catalysts exhibited high activity for PDH, high selectivity to propene (>97%), and good stability (k_d = 0.002-0.071 h^{-1}). PtSn/DeAlBEA catalysts were more stable, selective to propene, and active for PDH than Pt/DeAlBEA, emphasizing the influence of Sn interactions. PtSn/DeAlBEA showed higher activity on a per Pt basis with decreasing Pt/Al ratios. PDH occurred via a Langmuir-Hinshelwood type rate expression over PtSn/DeAlBEA catalysts with propane site blocking. Similar kinetic parameters were measured across Pt/Al ratios (0.001-0.026), suggesting small Pt clusters, with Sn interactions, were the dominant active sites for PDH over PtSn/DeAlBEA at all Pt/Al ratios. A first-order forward rate constant ($k_{f,app}$) for PDH was calculated to compare results from different literature studies collected at different conditions. The values of $k_{f,app}$ for these PtSn/DeAlBEA catalysts were high relative to previously reported literature. These results suggested that the increased activity of these PtSn/DeAlBEA catalysts was correlated with the presence of highly dispersed Pt species interacting with Sn.

Further work in this area should be dedicated to applying operando characterization to better understand the effects of hydrogen and PDH reaction conditions on Pt-Sn interactions. Additionally, studies that combine powerful techniques (e.g., IR and XAS) will shed better light on the Pt structures in these materials, especially under extreme reaction conditions. A combination of characterization techniques is the most comprehensive method to determine metal structure throughout these studies. Lastly, molecular Pt precursors could be employed to better control the heterogeneity of sites in PtSn/DeAlBEA catalysts. The distribution of Pt sites is an artifact from the wetness impregnation preparation, but alternative Pt introduction procedures may create more uniform sites. The silanol nests of DeAlBEA provide suitable host sites for many Lewis acid sites. While PtZn/DeAlBEA and PtSn/DeAlBEA have been studied, additional Lewis acid host metals (e.g., Ga, Cu) could be investigated. These studies would further shed light on the impact of the Lewis acid strength on the reactivity and optimal catalyst structure.

7 References

(1) *Some Industrial Chemicals*; International Agency for Research on Cancer, International Agency for Research on Cancer, Eds.; IARC monographs on the evaluation of carcinogenic risks to humans; IARC: Lyon, 1994.

(2) Ren, T.; Patel, M.; Blok, K. Olefins from Conventional and Heavy Feedstocks: Energy Use in Steam Cracking and Alternative Processes. *Energy* **2006**, *31* (4), 425–451. https://doi.org/10.1016/j.energy.2005.04.001.

(3) Sattler, J. J. H. B.; Ruiz-Martinez, J.; Santillan-Jimenez, E.; Weckhuysen, B. M. Catalytic Dehydrogenation of Light Alkanes on Metals and Metal Oxides. *Chem. Rev.* **2014**, *114* (20), 10613–10653. https://doi.org/10.1021/cr5002436.

(4) EIA. Shale Gas Production, 2023. https://www.eia.gov/dnav/ng/ng_prod_sum_dc_NUS_mmcf_a.htm.

(5) Hu, Z. P.; Yang, D.; Wang, Z.; Yuan, Z. Y. State-of-the-Art Catalysts for Direct Dehydrogenation of Propane to Propylene. *Chin. J. Catal.* **2019**. https://doi.org/10.1016/S1872-2067(19)63360-7.

(6) Sabatier, P. Catalysis Organic Chemistry.

(7) Dai, Y.; Gao, X.; Wang, Q.; Wan, X.; Zhou, C.; Yang, Y. Recent Progress in Heterogeneous Metal and Metal Oxide Catalysts for Direct Dehydrogenation of Ethane and Propane. *Chem. Soc. Rev.* **2021**. https://doi.org/10.1039/D0CS01260B.

(8) Qu, Z.; Sun, Q. Advances in Zeolite-Supported Metal Catalysts for Propane Dehydrogenation. *Inorg. Chem. Front.* **2022**. https://doi.org/10.1039/D2QI00653G.

(9) Nawaz, Z. Light Alkane Dehydrogenation to Light Olefin Technologies: A Comprehensive Review. *Rev. Chem. Eng.* **2015**, *31* (5), 413–436. https://doi.org/10.1515/revce-2015-0012.

(10) Liu, Q.; Zhang, Z. Platinum Single-Atom Catalysts: A Comparative Review towards Effective Characterization. *Catal. Sci. Technol.* **2019**, *9* (18), 4821–4834. https://doi.org/10.1039/c9cy01028a.

(11) Feng, B.; Wei, Y. C.; Song, W. Y.; Xu, C. M. A Review on the Structure-Performance Relationship of the Catalysts during Propane Dehydrogenation Reaction. *Pet. Sci.* **2022**, *19* (2), 819–838. https://doi.org/10.1016/j.petsci.2021.09.015.

(12) Chen, S.; Chang, X.; Sun, G.; Zhang, T.; Xu, Y.; Wang, Y.; Pei, C.; Gong, J. Propane Dehydrogenation: Catalyst Development, New Chemistry, and Emerging Technologies. *Chem. Soc. Rev.* **2021**, *50* (5), 3315–3354. https://doi.org/10.1039/d0cs00814a.

(13) Elgayyar, T.; Atwi, R.; Tuel, A.; Meunier, F. C. Contributions and Limitations of IR Spectroscopy of CO Adsorption to the Characterization of Bimetallic and Nanoalloy Catalysts. *Catal. Today* **2021**, *373*, 59–68. https://doi.org/10.1016/j.cattod.2021.01.009.

(14) Parkinson, G. S. Single-Atom Catalysis: How Structure Influences Catalytic Performance. *Catal. Lett.* **2019**, *149* (5), 1137–1146. https://doi.org/10.1007/s10562-019-02709-7.

(15) Santhosh Kumar, M.; Chen, D.; Walmsley, J. C.; Holmen, A. Dehydrogenation of Propane over Pt-SBA-15: Effect of Pt Particle Size. *Catal. Commun.* **2008**, *9* (5), 747–750. https://doi.org/10.1016/j.catcom.2007.08.015.

(16) Wu, J.; Peng, Z.; Bell, A. T. Effects of Composition and Metal Particle Size on Ethane Dehydrogenation over PtxSn100-x/Mg(Al)O ($70 \leq x \leq 100$). *J. Catal.* **2014**, *311*, 161–168. https://doi.org/10.1016/j.jcat.2013.11.017.

(17) Bariås, O. A.; Holmen, A.; Blekkan, E. A. Propane Dehydrogenation over Supported Pt and Pt-Sn Catalysts: Catalyst Preparation, Characterization, and Activity Measurements. *J. Catal.* **1996**, *158* (1), 1–12. https://doi.org/10.1006/jcat.1996.0001.
(18) Galvita, V.; Siddiqi, G.; Sun, P.; Bell, A. T. Ethane Dehydrogenation on Pt/Mg(Al)O and PtSn/Mg(Al)O Catalysts. *J. Catal.* **2010**, *271* (2), 209–219. https://doi.org/10.1016/j.jcat.2010.01.016.
(19) Zhang, Y.; Zhou, Y.; Qiu, A.; Wang, Y.; Xu, Y.; Wu, P. Propane Dehydrogenation on PtSn/ZSM-5 Catalyst: Effect of Tin as a Promoter. *Catal. Commun.* **2006**, *7* (11), 860–866. https://doi.org/10.1016/j.catcom.2006.03.016.
(20) Qi, L.; Babucci, M.; Zhang, Y.; Lund, A.; Liu, L.; Li, J.; Chen, Y.; Hoffman, A. S.; Bare, S. R.; Han, Y.; Gates, B. C.; Bell, A. T. Propane Dehydrogenation Catalyzed by Isolated Pt Atoms in ≡SiOZn–OH Nests in Dealuminated Zeolite Beta. *J. Am. Chem. Soc.* **2021**, *143* (50), 21364–21378. https://doi.org/10.1021/jacs.1c10261.
(21) Ma, Y.; Chen, X.; Guan, Y.; Xu, H.; Zhang, J.; Jiang, J.; Chen, L.; Xue, T.; Xue, Q.; Wei, F.; Wu, P. Skeleton-Sn Anchoring Isolated Pt Site to Confine Subnanometric Clusters within *BEA Topology. *J. Catal.* **2021**, *397*, 44–57. https://doi.org/10.1016/j.jcat.2021.03.022.
(22) Santhosh Kumar, M.; Chen, D.; Holmen, A.; Walmsley, J. C. Dehydrogenation of Propane over Pt-SBA-15 and Pt-Sn-SBA-15: Effect of Sn on the Dispersion of Pt and Catalytic Behavior. *Catal. Today* **2009**, *142* (1–2), 17–23. https://doi.org/10.1016/j.cattod.2009.01.002.
(23) Yang, M. L.; Zhu, Y. A.; Zhou, X. G.; Sui, Z. J.; Chen, D. First-Principles Calculations of Propane Dehydrogenation over PtSn Catalysts. *ACS Catal.* **2012**, *2* (6), 1247–1258. https://doi.org/10.1021/cs300031d.
(24) Sattler, J. J. H. B.; Beale, A. M.; Weckhuysen, B. M. Operando Raman Spectroscopy Study on the Deactivation of Pt/Al 2O3 and Pt-Sn/Al2O3 Propane Dehydrogenation Catalysts. *Phys. Chem. Chem. Phys.* **2013**, *15* (29), 12095–12103. https://doi.org/10.1039/c3cp50646k.
(25) Nykänen, L.; Honkala, K. Density Functional Theory Study on Propane and Propene Adsorption on Pt(111) and PtSn Alloy Surfaces. *J. Phys. Chem. C* **2011**, *115* (19), 9578–9586. https://doi.org/10.1021/jp1121799.
(26) Wang, T.; Abild-Pedersen, F. Identifying Factors Controlling the Selective Ethane Dehydrogenation on Pt-Based Catalysts from DFT Based Micro-Kinetic Modeling. *J. Energy Chem.* **2021**, *58*, 37–40. https://doi.org/10.1016/j.jechem.2020.09.034.
(27) Kitagawa, H.; Sendoda, Y.; Ono, Y. Transformation of Propane into Aromatic over ZSM-5 Zeolites. *J. Catal.* **1986**, *101*, 12–18. https://doi.org/10.1627/jpi1958.30.77.
(28) Nakai, M.; Miyake, K.; Inoue, R.; Ono, K.; Al Jabri, H.; Hirota, Y.; Uchida, Y.; Tanaka, S.; Miyamoto, M.; Oumi, Y.; Kong, C. Y.; Nishiyama, N. Dehydrogenation of Propane over High Silica ∗bEA Type Gallosilicate (Ga-Beta). *Catal. Sci. Technol.* **2019**, *9* (22), 6234–6239. https://doi.org/10.1039/c9cy00691e.
(29) Chen, C.; Zhang, S.; Wang, Z.; Yuan, Z. Y. Ultrasmall Co Confined in the Silanols of Dealuminated Beta Zeolite: A Highly Active and Selective Catalyst for Direct Dehydrogenation of Propane to Propylene. *J. Catal.* **2020**, *383*, 77–87. https://doi.org/10.1016/j.jcat.2019.12.037.

(30) Chen, C.; Hu, Z.; Ren, J.; Zhang, S.; Wang, Z.; Yuan, Z. Y. ZnO Nanoclusters Supported on Dealuminated Zeolite β as a Novel Catalyst for Direct Dehydrogenation of Propane to Propylene. *ChemCatChem* **2019**, *11* (2), 868–877. https://doi.org/10.1002/cctc.201801708.
(31) Wang, Y.; Hu, Z. P.; Tian, W.; Gao, L.; Wang, Z.; Yuan, Z. Y. Framework-Confined Sn in Si-Beta Stabilizing Ultra-Small Pt Nanoclusters as Direct Propane Dehydrogenation Catalysts with High Selectivity and Stability. *Catal. Sci. Technol.* **2019**, *9* (24), 6993–7002. https://doi.org/10.1039/c9cy01907c.
(32) Xu, Z.; Yue, Y.; Bao, X.; Xie, Z.; Zhu, H. Propane Dehydrogenation over Pt Clusters Localized at the Sn Single-Site in Zeolite Framework. *ACS Catal.* **2020**, *10* (1), 818–828. https://doi.org/10.1021/acscatal.9b03527.
(33) Dapsens, P. Y.; Mondelli, C.; Jagielski, J.; Hauert, R.; Pérez-Ramírez, J. Hierarchical Sn-MFI Zeolites Prepared by Facile Top-down Methods for Sugar Isomerisation. *Catal. Sci. Technol.* **2014**, *4* (8), 2302–2311. https://doi.org/10.1039/c4cy00172a.
(34) Bermejo-Deval, R.; Assary, R. S.; Nikolla, E.; Moliner, M.; Román-Leshkov, Y.; Hwang, S. J.; Palsdottir, A.; Silverman, D.; Lobo, R. F.; Curtiss, L. A.; Davis, M. E. Metalloenzyme-like Catalyzed Isomerizations of Sugars by Lewis Acid Zeolites. *Proc. Natl. Acad. Sci. U. S. A.* **2012**, *109* (25), 9727–9732. https://doi.org/10.1073/pnas.1206708109.
(35) Luo, H. Y.; Lewis, J. D.; Román-Leshkov, Y. Lewis Acid Zeolites for Biomass Conversion: Perspectives and Challenges on Reactivity, Synthesis, and Stability. *Annu. Rev. Chem. Biomol. Eng.* **2016**, *7*, 663–692. https://doi.org/10.1146/annurev-chembioeng-080615-034551.
(36) Wang, G.; Zhang, H.; Wang, H.; Zhu, Q.; Li, C.; Shan, H. The Role of Metallic Sn Species in Catalytic Dehydrogenation of Propane: Active Component Rather than Only Promoter. *J. Catal.* **2016**, *344*, 606–608. https://doi.org/10.1016/j.jcat.2016.11.003.
(37) Wang, G.; Wang, H.; Zhang, H.; Zhu, Q.; Li, C.; Shan, H. Highly Selective and Stable NiSn/SiO2 Catalyst for Isobutane Dehydrogenation: Effects of Sn Addition. *ChemCatChem* **2016**, *8* (19), 3137–3145. https://doi.org/10.1002/cctc.201600685.
(38) Wang, H.; Wang, H.; Li, X.; Li, C. Nature of Active Tin Species and Promoting Effect of Nickle in Silica Supported Tin Oxide for Dehydrogenation of Propane. *Appl. Surf. Sci.* **2017**, *407*, 456–462. https://doi.org/10.1016/j.apsusc.2017.02.216.
(39) Wang, G.; Zhang, H.; Zhu, Q.; Zhu, X.; Li, X.; Wang, H.; Li, C.; Shan, H. Sn-Containing Hexagonal Mesoporous Silica (HMS) for Catalytic Dehydrogenation of Propane An Efficient Strategy to Enhance Stability. *J. Catal.* **2017**, *351*, 90–94. https://doi.org/10.1016/j.jcat.2017.04.018.
(40) Liu, Q.; Luo, M.; Zhao, Z.; Zhao, Q. K-Modified Sn-Containing Dendritic Mesoporous Silica Nanoparticles with Tunable Size and SnOx-Silica Interaction for the Dehydrogenation of Propane to Propylene. *Chem. Eng. J.* **2020**, *380* (April 2019), 122423. https://doi.org/10.1016/j.cej.2019.122423.
(41) Wang, H.; Huang, H.; Bashir, K.; Li, C. Isolated Sn on Mesoporous Silica as a Highly Stable and Selective Catalyst for the Propane Dehydrogenation. *Appl. Catal. Gen.* **2020**, *590* (August 2019), 117291. https://doi.org/10.1016/j.apcata.2019.117291.
(42) Hammond, C.; Padovan, D.; Al-Nayili, A.; Wells, P. P.; Gibson, E. K.; Dimitratos, N. Identification of Active and Spectator Sn Sites in Snβ Following Solid-State Stannation, and Consequences for Lewis Acid Catalysis. *ChemCatChem* **2015**, *7* (20), 3322–3331. https://doi.org/10.1002/cctc.201500545.

(43) Bermejo-Deval, R.; Gounder, R.; Davis, M. E. Framework and Extraframework Tin Sites in Zeolite Beta React Glucose Differently. *ACS Catal.* **2012**, *2* (12), 2705–2713. https://doi.org/10.1021/cs300474x.
(44) Meunier, F. C.; Elgayyar, T.; Dembélé, K.; Kaper, H. Stability of Pt-Adsorbed CO on Catalysts for Room Temperature-Oxidation of CO. *Catalysts* **2022**, *12* (5), 532. https://doi.org/10.3390/catal12050532.
(45) Ivanova, E.; Mihaylov, M.; Thibault-Starzyk, F.; Daturi, M.; Hadjiivanov, K. FTIR Spectroscopy Study of CO and NO Adsorption and Co-Adsorption on Pt/TiO2. *J. Mol. Catal. Chem.* **2007**, *274* (1–2), 179–184. https://doi.org/10.1016/j.molcata.2007.05.006.
(46) Hadjiivanov, K. I.; Vayssilov, G. N. Characterization of Oxide Surfaces and Zeolites by Carbon Monoxide as an IR Probe Molecule. *Adv. Catal.* **2002**, *47*, 307–511. https://doi.org/10.1016/S0360-0564(02)47008-3.
(47) Resasco, J.; Yang, F.; Mou, T.; Wang, B.; Christopher, P.; Resasco, D. E. Relationship between Atomic Scale Structure and Reactivity of Pt Catalysts: Hydrodeoxygenation of m-Cresol over Isolated Pt Cations and Clusters. *ACS Catal.* **2020**, *10* (1), 595–603. https://doi.org/10.1021/acscatal.9b04330.
(48) Wang, Q.; Tichit, D.; Meunier, F.; Guesmi, H. Combined DRIFTS and DFT Study of CO Adsorption and Segregation Modes in Pt-Sn Nanoalloys. *J. Phys. Chem. C* **2020**, *124* (18), 9979–9989. https://doi.org/10.1021/acs.jpcc.0c01296.
(49) Aleksandrov, H. A.; Neyman, K. M.; Hadjiivanov, K. I.; Vayssilov, G. N. Can the State of Platinum Species Be Unambiguously Determined by the Stretching Frequency of an Adsorbed CO Probe Molecule? *Phys. Chem. Chem. Phys.* **2016**, *18* (32), 22108–22121. https://doi.org/10.1039/C6CP03988J.
(50) Meunier, F. C. Pitfalls and Benefits of: In Situ and Operando Diffuse Reflectance FT-IR Spectroscopy (DRIFTS) Applied to Catalytic Reactions. *React. Chem. Eng.* **2016**, *1* (2), 134–141. https://doi.org/10.1039/c5re00018a.
(51) Calvin, S. *XAFS for Everyone*; CRC Press, 2013.
(52) Deng, L.; Miura, H.; Shishido, T.; Hosokawa, S.; Teramura, K.; Tanaka, T. Dehydrogenation of Propane over Silica-Supported Platinum-Tin Catalysts Prepared by Direct Reduction Effects of Tin/Platinum Ratio and Reduction Temperature. *ChemCatChem* **2014**, *6* (9), 2680–2691. https://doi.org/10.1002/cctc.201402306.
(53) Dessal, C.; Len, T.; Morfin, F.; Rousset, J. L.; Aouine, M.; Afanasiev, P.; Piccolo, L. Dynamics of Single Pt Atoms on Alumina during CO Oxidation Monitored by Operando X-Ray and Infrared Spectroscopies. *ACS Catal.* **2019**, *9* (6), 5752–5759. https://doi.org/10.1021/acscatal.9b00903.
(54) Deng, L.; Miura, H.; Shishido, T.; Wang, Z.; Hosokawa, S.; Teramura, K.; Tanaka, T. Elucidating Strong Metal-Support Interactions in Pt–Sn/SiO2 Catalyst and Its Consequences for Dehydrogenation of Lower Alkanes. *J. Catal.* **2018**, *365*, 277–291. https://doi.org/10.1016/j.jcat.2018.06.028.
(55) Kaylor, N.; Davis, R. J. Propane Dehydrogenation over Supported Pt-Sn Nanoparticles. *J. Catal.* **2018**, *367*, 181–193. https://doi.org/10.1016/j.jcat.2018.09.006.
(56) Curulla, D.; Clotet, A.; Ricart, J. M. *Adsorption of Carbon Monoxide on Pt{100} Surfaces: Dependence of the CO Stretching Vibrational Frequency on Surface Coverage*; 2000; Vol. 460, pp 101–111. www.elsevier.nl/locate/susc.
(57) Chen, Y.; Sun, H.; Gates, B. C. Prototype Atomically Dispersed Supported Metal Catalysts: Iridium and Platinum. *Small* **2020**, *2004665*. https://doi.org/10.1002/smll.202004665.

(58) Cui, X.; Li, W.; Ryabchuk, P.; Junge, K.; Beller, M. Bridging Homogeneous and Heterogeneous Catalysis by Heterogeneous Single-Metal-Site Catalysts. *Nat. Catal.* **2018**, *1* (6), 385–397. https://doi.org/10.1038/s41929-018-0090-9.
(59) Ford, R. R. *Carbon Monoxide Adsorption on the Transition Metals*.
(60) Muscat, J. P.; Newns, D. M. *CHEMISORPTION ON METALS*; Pergamon Press, 1978; Vol. 9, p 143.
(61) Yates, Jr., John T. Chemisorption on Surfaces - an Historical Look at a Representative Adsorbate Carbon Monoxid. *Surf. Sci.* **1994**, *299*, 731–741.
(62) Hollins, P.; Hollins, P. *The Influence of Surface Defects on the Infrared Spectra of Adsorbed Species*; 1992.
(63) Eischens, R. P.; Pliskin, W. A. *The Infrared Spectra of Adsorbed Molecules*.
(64) Chatt, J.; Duncanson, L. A. Olefin Coordination Compounds. Part III. * Infrared Spectra and Structure - Attempted Preparation of Acetylene Complexes. **1953**, 2939` – 2947.
(65) Frenking, G.; Fröhlich, N. The Nature of the Bonding in Transition-Metal Compounds. *Chem. Rev.* **2000**, *100* (2), 717–774. https://doi.org/10.1021/cr980401l.
(66) Ziegler, T.; Tschinke, V.; Ursenbach, C. Thermal Stability and Kinetic Lability of the Metal Carbonyl Bond. A Theoretical Study on M(CO)6 (M = Chromium, Molybdenum, Tungsten), M(CO)5 (M = Iron, Ruthenium, Osmium), and M(CO)4 (M = Nickel, Palladium, Platinum). *J. Am. Chem. Soc.* **1987**, *109* (16), 4825–4837. https://doi.org/10.1021/ja00250a013.
(67) Zhou, M.; Andrews, L.; Bauschlicher, C. W. Spectroscopic and Theoretical Investigations of Vibrational Frequencies in Binary Unsaturated Transition-Metal Carbonyl Cations, Neutrals, and Anions. *Chem. Rev.* **2001**, *101* (7), 1931–1962. https://doi.org/10.1021/cr990102b.
(68) Rossomme, E.; Lininger, C. N.; Bell, A. T.; Head-Gordon, T.; Head-Gordon, M. Electronic Structure Calculations Permit Identification of the Driving Forces behind Frequency Shifts in Transition Metal Monocarbonyls. *Phys. Chem. Chem. Phys.* **2020**, *22* (2), 781–798. https://doi.org/10.1039/C9CP04643G.
(69) Blyholder, G. Molecular Orbital View of Chemisorbed Carbon Monoxide. *J. Phys. Chem.* **1964**, *68* (10), 2772–2778. https://doi.org/10.1021/j100792a006.
(70) Blyholder, G.; Allen, M. C. Infrared Spectra and Molecular Orbital Model for Carbon Monoxide Adsorbed on Metals. *J. Am. Chem. Soc.* **1969**, *91* (12), 3158–3162. https://doi.org/10.1021/ja01040a009.
(71) Price, W. C.; Potts, W. A.; Blyholder, G.; Sheets, R. *Platinum-Carbon Stretching Frequency for Chemisorbed Carbon Monoxide King's College) for Determining the Ionization Poten-Tials of Several Products The Platinum-Carbon Stretching Frequency for Chemisorbed Carbon Monoxide*. https://pubs.acs.org/sharingguidelines.
(72) Aizawa, H.; Tsuneyuki, S. *Surface Science Letters First-Principles Study of CO Bonding to Pt(111): Validity of the Blyholder Model*; 1998.
(73) Delbecq, F. General Trends in the Electronic Properties of Alloys of Transition Metals: A Semi-Empirical Study of CO Adsorption. *Surf. Sci.* **1997**, *389* (1–3), L1131–L1139. https://doi.org/10.1016/S0039-6028(97)00471-8.
(74) Hammer, B.; Morikawa, Y.; Nørskov, J. K. CO Chemisorption at Metal Surfaces and Overlayers. *Phys. Rev. Lett.* **1996**, *76* (12), 2141–2144. https://doi.org/10.1103/PhysRevLett.76.2141.

(75) Sung, S. S.; Hoffmann, R. How Carbon Monoxide Bonds to Metal Surfaces. *J. Am. Chem. Soc.* **1985**, *107* (3), 578–584. https://doi.org/10.1021/ja00289a009.
(76) Toyoshima, I.; Somorjai, G. A. Heats of Chemisorption of O_2, H_2, CO, CO_2, and N_2 on Polycrystalline and Single Crystal Transition Metal Surfaces. *Catal. Rev.* **1979**, *19* (1), 105–159. https://doi.org/10.1080/03602457908065102.
(77) Hu, P.; King, D. A.; Lee, M.-H.; Payne, M. C. Orbital Mixing in CO Chemisorption on Transition Metal Surfaces. *Chem. Phys. Lett.* **1995**, *246* (1–2), 73–78. https://doi.org/10.1016/0009-2614(95)01070-P.
(78) Greuter, F.; Heskett, D.; Plummer, E. W.; Freund, H.-J. Chemisorption of CO on Co(0001). Structure and Electronic Properties. *Phys. Rev. B* **1983**, *27* (12), 7117–7135. https://doi.org/10.1103/PhysRevB.27.7117.
(79) Nilsson, A.; Bennich, P.; Wiell, T.; Wassdahl, N.; Mårtensson, N.; Nordgren, J.; Björneholm, O.; Stöhr, J. Direct Probing of the Adsorbate-Substrate Chemical Bond Using Angle-Dependent x-Ray-Emission Spectroscopy. *Phys. Rev. B* **1995**, *51* (15), 10244–10247. https://doi.org/10.1103/PhysRevB.51.10244.
(80) Bagus, P. S.; Nelin, C. J.; Bauschlicher, C. W. Bonding of CO to Metal Surfaces: A New Interpretation. *Phys. Rev. B* **1983**, *28* (10), 5423–5438. https://doi.org/10.1103/PhysRevB.28.5423.
(81) Bagus, P. S.; Hermann, K.; Bauschlicher, C. W. On the Nature of the Bonding of Lone Pair Ligands to a Transition Metal. *J. Chem. Phys.* **1984**, *81* (4), 1966–1974. https://doi.org/10.1063/1.447818.
(82) Nilsson, A.; Hasselström, J.; Föhlisch, A.; Karis, O.; Pettersson, L. G. M.; Nyberg, M.; Triguero, L. Probing Chemical Bonding in Adsorbates Using X-Ray Emission Spectroscopy. *J. Electron Spectrosc. Relat. Phenom.* **2000**, *110–111*, 15–39. https://doi.org/10.1016/S0368-2048(00)00155-9.
(83) Nilsson, A.; Pettersson, L. G. M. Chemical Bonding on Surfaces Probed by X-Ray Emission Spectroscopy and Density Functional Theory. *Surf. Sci. Rep.* **2004**, *55* (2–5), 49–167. https://doi.org/10.1016/j.surfrep.2004.06.002.
(84) Föhlisch, A.; Nyberg, M.; Bennich, P.; Triguero, L.; Hasselström, J.; Karis, O.; Pettersson, L. G. M.; Nilsson, A. The Bonding of CO to Metal Surfaces. *J. Chem. Phys.* **2000**, *112* (4), 1946–1958. https://doi.org/10.1063/1.480773.
(85) Föhlisch, A.; Nyberg, M.; Hasselström, J.; Karis, O.; Pettersson, L. G. M.; Nilsson, A. *How Carbon Monoxide Adsorbs in Different Sites*; 2000.
(86) Primet, M. *Electronic Transfer and Ligand Effects in the Infrared Spectra of Adsorbed Carbon Monoxide*; 1984; Vol. 88, pp 273–282.
(87) Hammaker, R. M.; Francis, S. A.; Eischens, R. P. *Infrared Study of Intermolecular Interactions for Carbon Monoxide Chemisorbed on Platinum*; Pergamon Preen Ltd, 1966; Vol. 21, pp 1296–1309.
(88) De Me, L.-C.; Chaqroune, A.; Coq, B.; Francó, F. ". *Characterization of Mono-and Bi-Metallic Platinum Catalysts Using CO FTIR Spectroscopy Size Effects and Topological Segregation*; 1997; Vol. 93, pp 19–56.
(89) Browne, V. M.; Fox, S. G.; Hollins, P. Coupling Effects in Infrared Spectra from Supported Metal Catalyts. *Mater. Chem. Phys.* **1991**, *29* (1–4), 235–244. https://doi.org/10.1016/0254-0584(91)90019-Q.
(90) Severson, M. W.; Stuhlmann, C.; Villegas, I.; Weaver, M. J. Dipole–Dipole Coupling Effects upon Infrared Spectroscopy of Compressed Electrochemical Adlayers: Application

to the Pt(111)/CO System. *J. Chem. Phys.* **1995**, *103* (22), 9832–9843. https://doi.org/10.1063/1.469950.
(91) Borovkov, V. Y.; Kolesnikov, S. P.; Kovalchuk, V. I. The State of Metals in the Pt/Al2O3 and (Pt—Cu)/Al2O3 Catalysts as Indicated by IR Spectroscopy with Isotope Dilution of 12C16O with 13C18O Molecules. **2007**, *56* (5).
(92) Borovkov, V. Y.; Kolesnikov, S. P.; Kovalchuk, V. I.; d'Itri, J. L. Probing Adsorption Sites of Silica-Supported Platinum with $^{13}C\,^{16}O + ^{12}C\,^{16}O$ and $^{13}C\,^{18}O + ^{12}C\,^{16}O$ Mixtures: A Comparative Fourier Transform Infrared Investigation. *J. Phys. Chem. B* **2005**, *109* (42), 19772–19778. https://doi.org/10.1021/jp051681t.
(93) Scheffler, M. *THE INFLUENCE OF LATERAL INTERACTIONS ON THE VIBRATIONAL SPECTRUM OF ADSORBED CO*; 1979; Vol. 81, pp 562–570.
(94) Xu, Q.; Souma, Y.; Heaton, B. T.; Jacob, C.; Kanamori, K. [{Pt(CO)3}2]2+: The First Homoleptic, Dinuclear, Cationic Platinum(I) Carbonyl Complex Formed in Concentrated Sulfuric Acid. *Angew. Chem.* **2000**, *112* (1), 214–215. https://doi.org/10.1002/(SICI)1521-3757(20000103)112:1<214::AID-ANGE214>3.0.CO;2-E.
(95) Aubke, F.; Wang, C. *Carbon Monoxide as a A-Donor Ligand in Coordination Chemistry*; 1994; Vol. 137, pp 483–524.
(96) Zholobenko, V. L.; Lei, G.-D.; Carvill, B. T.; Lerner, B. A.; Sachtler, W. M. H. *Identification of Isolated Pt Atoms in H-Mordenite*; 1994; Vol. 90, pp 233–238.
(97) Benvenutti, E. V.; Franken, L.; Moro, C. C.; Davanzo, C. U. FTIR Study of Hydrogen and Carbon Monoxide Adsorption on Pt/TiO_2, Pt/ZrO_2, and Pt/Al_2O_3. *Langmuir* **1999**, *15* (23), 8140–8146. https://doi.org/10.1021/la990195s.
(98) Gu, Q.; Long, J.; Zhuang, H.; Zhang, C.; Zhou, Y.; Wang, X. Ternary Pt/SnOx/TiO2 Photocatalysts for Hydrogen Production: Consequence of Pt Sites for Synergy of Dual Co-Catalysts. *Phys. Chem. Chem. Phys.* **2014**, *16* (24), 12521–12534. https://doi.org/10.1039/c4cp01496k.
(99) Tkachenko, O. P.; Shpiro, E. S.; Zeiinsky, N. D.; Jaeger, N. I.; Lamber, R.; Schulz-Ekloff, G.; Landmesser, H. *Strong Modification of Pt-CO Interaction Caused by Alloying with Chromium in Pt-Cr / HZSM-5 Catalysts*; 1994; Vol. 23, pp 251–262.
(100) De Miguel, S.; Castro, A.; Scelza, O.; Luis, J.; Fierro, G.; Soria, J. *FTIR and XPS Study of Supported PtSn Catalysts Used for Light Paraffins Dehydrogenation*; 1996; Vol. 36, p 201.
(101) Calabrese, J. C.; Dahl, L. F.; Cavalieri, A.; Chini, P.; Longoni, G.; Martinengo, S. Synthesis and Structure of a Hexanuclear Nickel Carbonyl Dianion, Bis(Tri-.Mu.2-Carbonyl-Tricarbonyltrinickel)(2-), and Comparison with Bis(Tri-.Mu.2-Carbonyl-Tricarbonyltriplatinum)(2-). Unprecedented Case of a Metal Cluster System Possessing Different Metal Architectures for Congener Transition Metals. *J. Am. Chem. Soc.* **1974**, *96* (8), 2616–2618. https://doi.org/10.1021/ja00815a051.
(102) Masaru Ichikawa. INFRARED SPECTRA OF CARBON MONOXIDE CHEMISORBED ON SUPPORTED PLATINUM AGGREGATES PREPARED FROM Pt CARBONYL CLUSTER COMPOUNDS.Pdf. *Chem. Lett.* **1976**, 335–338.
(103) Kiindig, E. P.; McIntosh, D.; Moskovits, M.; Ozin, G. A.; Mond, L.; Langer, C.; Quincke, F. *Binary Carbonyls of Platinum, Pt(CO)" (Where = 1-4). A Comparative Study of the Chemical and Physical Properties of M(CO)" (Where M = Ni, Pd, or Pt;-1-4) Using Variable Concentration, Warm-up, and 13CieO*; 1890; Vol. 57, p 137. https://pubs.acs.org/sharingguidelines.

(104) Brandt, R. K.; Sorbello, R. S.; Greenler, R. G. *Site-Specific, Coupled-Harmonic-Oscillator Model of Carbon Monoxide Adsorbed on Extended, Single-Crystal Surfaces and on Small Crystals of Platinum*; 1992; Vol. 271, p 5.
(105) Beckerle, J. D.; Casassa, M. P.; Cavanagh, R. R.; Heilweil, E. J.; Stephenson, J. C. Ultrafast Infrared Response of Adsorbates on Metal Surfaces: Vibrational Lifetime of CO/Pt(111). *Phys. Rev. Lett.* **1990**, *64* (17), 2090–2093. https://doi.org/10.1103/PhysRevLett.64.2090.
(106) Tushaus, M.; Schweizer, E.; Hollins, P.; Bradshaw, A. M. YET ANOTHER VIBRATIONAL STUDY OF THE ADSORPTION SYSTEM Pt{111}-CO. *J. Electron Spectrosc. Relat. Phenom.* **1987**, *44*, 305–316.
(107) Crossley, A.; King, D. A. *ADSORBATE ISLAND DIMENSIONS AND INTERACTION ENERGIES FROM VIBRATIONAL SPECTRA: CO ON Pt (001) AND Pt (111)*.
(108) Olsen, C. W.; Masel, R. I. *AN INFRARED STUDY OF CO ADSORPTION ON Pt(Lll)*; 1988; Vol. 201, pp 444–460.
(109) Reutt-Robey, J. E.; Doren, D. J.; Chabal, Y. J.; Christman, S. B. CO Diffusion on Pt(111) with Time-Resolved Infrared-Pulsed Molecular Beam Methods: Critical Tests and Analysis. *J. Chem. Phys.* **1990**, *93* (12), 9113–9129. https://doi.org/10.1063/1.459202.
(110) Gardner, P.; Martin, R.; Tdshaus, M.; Bradshaw, A. M. *The Adsorbate-Induced Lifting of the Pt{ 100) Surface Reconstruc-Tion: IRAS Investigations*.
(111) R.G. Greenler; B. Hayden; K. Kretzschmar; A.M. Bradshaw. *Proc 8th Int Congr Catal.* **1984**, *IV*, 197.
(112) Bare, S. R.; Hofmann, P.; King, D. A. *VIBRATIONAL STUDIES OF THE SURFACE PHASES OF CO ON Pt{ 110) AT 300 K*; 1984; Vol. 144, p 347.
(113) Schweizer, E.; Persson, B. N. J.; Tushaus, M.; Hoge, D.; Bradshaw, A. M. *THE POTENTIAL ENERGY SURFACE, VIBRATIONAL PHASE RELAXATION AND THE ORDER-DISORDER TRANSITION IN THE ADSORPTION SYSTEM Pt{lll}-CO*.
(114) Klonker, C.; Balden, M.; Lehwald, S.; Daum, W. *CO Stretching Vibrations on Pt(111) and Pt(110) Studied by Sum-Frequency Generation*; 1996; Vol. 360, p 111.
(115) Shigeishi, R. A.; King, D. A. *CHEMISORPTION OF CARBON MONOXIDE ON PLATINUM ~iI I I}: REFLECTION-ABSORPTION INFRARED SPECTROSCOPY*; 1976; Vol. 58, pp 379–396.
(116) Krebs, H. *Evidence for Two Different Adsorption Sites of CO on Pt(Lll) from Infrared Reflection Spectroscopy*; 1977; Vol. 14, pp 337–342.
(117) K. Horn; J. Pritchard. *J. Electron Spectrosc. Relat. Phenom.* **1990**, *54155*, 619–628.
(118) DeRita, L.; Resasco, J.; Dai, S.; Boubnov, A.; Thang, H. V.; Hoffman, A. S.; Ro, I.; Graham, G. W.; Bare, S. R.; Pacchioni, G.; Pan, X.; Christopher, P. Structural Evolution of Atomically Dispersed Pt Catalysts Dictates Reactivity. *Nat. Mater.* **2019**, *18* (7), 746–751. https://doi.org/10.1038/s41563-019-0349-9.
(119) Liu, Y.; Li, Z.; Yu, Q.; Chen, Y.; Chai, Z.; Zhao, G.; Liu, S.; Cheong, W.-C.; Pan, Y.; Zhang, Q.; Gu, L.; Zheng, L.; Wang, Y.; Lu, Y.; Wang, D.; Chen, C.; Peng, Q.; Liu, Y.; Liu, L.; Chen, J.; Li, Y. A General Strategy for Fabricating Isolated Single Metal Atomic Site Catalysts in Y Zeolite. *J. Am. Chem. Soc.* **2019**, *141* (23), 9305–9311. https://doi.org/10.1021/jacs.9b02936.
(120) Ding, K.; Gulle, A.; Johnson, A. M.; Schweitzer, N. M.; Stucky, G. D.; Marks, L. D.; Stair, P. C. Identification of Active Sites in CO Oxidation and Water-Gas Shift over

Supported Pt Catalysts. *Science* **2015**, *350* (6257), 185–189. https://doi.org/10.1126/science.aab3501.
(121) Jeong, H.; Shin, D.; Kim, B.; Bae, J.; Shin, S.; Choe, C.; Han, J. W.; Lee, H. Controlling the Oxidation State of Pt Single Atoms for Maximizing Catalytic Activity. *Angew. Chem.* **2020**, *132* (46), 20872–20877. https://doi.org/10.1002/ange.202009776.
(122) Nie, L.; Mei, D.; Xiong, H.; Peng, B.; Ren, Z.; Hernandez, X. I. P.; DeLaRiva, A.; Wang, M.; Engelhard, M. H.; Kovarik, L.; Datye, A. K.; Wang, Y. Activation of Surface Lattice Oxygen in Single-Atom Pt/CeO $_2$ for Low-Temperature CO Oxidation. *Science* **2017**, *358* (6369), 1419–1423. https://doi.org/10.1126/science.aao2109.
(123) Yan, D.; Chen, J.; Jia, H. Temperature-Induced Structure Reconstruction to Prepare a Thermally Stable Single-Atom Platinum Catalyst. *Angew. Chem. - Int. Ed.* **2020**, *59* (32), 13562–13567. https://doi.org/10.1002/anie.202004929.
(124) Resasco, J.; Christopher, P. Atomically Dispersed Pt-Group Catalysts: Reactivity, Uniformity, Structural Evolution, and Paths to Increased Functionality. *J. Phys. Chem. Lett.* **2020**, *11* (23), 10114–10123. https://doi.org/10.1021/acs.jpclett.0c02904.
(125) Zhang, Z.; Zhu, Y.; Asakura, H.; Zhang, B.; Zhang, J.; Zhou, M.; Han, Y.; Tanaka, T.; Wang, A.; Zhang, T.; Yan, N. Thermally Stable Single Atom Pt/m-Al2O3 for Selective Hydrogenation and CO Oxidation. *Nat. Commun.* **2017**, *8*. https://doi.org/10.1038/ncomms16100.
(126) Chen, L.-N.; Hou, K.-P.; Liu, Y.-S.; Qi, Z.-Y.; Zheng, Q.; Lu, Y.-H.; Chen, J.-Y.; Chen, J.-L.; Pao, C.-W.; Wang, S.-B.; Li, Y.-B.; Xie, S.-H.; Liu, F.-D.; Prendergast, D.; Klebanoff, L. E.; Stavila, V.; Allendorf, M. D.; Guo, J.; Zheng, L.-S.; Su, J.; Somorjai, G. A. Efficient Hydrogen Production from Methanol Using a Single-Site Pt $_1$ /CeO $_2$ Catalyst. *J. Am. Chem. Soc.* **2019**, *141* (45), 17995–17999. https://doi.org/10.1021/jacs.9b09431.
(127) Wang, C.; Gu, X. K.; Yan, H.; Lin, Y.; Li, J.; Liu, D.; Li, W. X.; Lu, J. Water-Mediated Mars-Van Krevelen Mechanism for CO Oxidation on Ceria-Supported Single-Atom Pt1 Catalyst. *ACS Catal.* **2017**, *7* (1), 887–891. https://doi.org/10.1021/acscatal.6b02685.
(128) Wang, H.; Liu, J.-X.; Allard, L. F.; Lee, S.; Liu, J.; Li, H.; Wang, J.; Wang, J.; Oh, S. H.; Li, W.; Flytzani-Stephanopoulos, M.; Shen, M.; Goldsmith, B. R.; Yang, M. Surpassing the Single-Atom Catalytic Activity Limit through Paired Pt-O-Pt Ensemble Built from Isolated Pt1 Atoms. *Nat. Commun.* **2019**, *10* (1), 3808. https://doi.org/10.1038/s41467-019-11856-9.
(129) Yang, Y.; Perry, I. B.; Lu, G.; Liu, P.; Buchwald, S. L. Copper-Catalyzed Asymmetric Addition of Olefin-Derived Nucleophiles to Ketones. *Science* **2016**, *353* (6295), 144–150. https://doi.org/10.1126/science.aaf7720.
(130) Qiao, B.; Wang, A.; Yang, X.; Allard, L. F.; Jiang, Z.; Cui, Y.; Liu, J.; Li, J.; Zhang, T. Single-Atom Catalysis of CO Oxidation Using Pt1/FeOx. *Nat. Chem.* **2011**, *3* (8), 634–641. https://doi.org/10.1038/nchem.1095.
(131) Yang, K.; Liu, Y.; Deng, J.; Zhao, X.; Yang, J.; Han, Z.; Hou, Z.; Dai, H. Three-Dimensionally Ordered Mesoporous Iron Oxide-Supported Single-Atom Platinum: Highly Active Catalysts for Benzene Combustion. *Appl. Catal. B Environ.* **2019**, *244*, 650–659. https://doi.org/10.1016/j.apcatb.2018.11.077.
(132) Chen, Y.; Rana, R.; Huang, Z.; Vila, F. D.; Sours, T.; Perez-Aguilar, J. E.; Zhao, X.; Hong, J.; Hoffman, A. S.; Li, X.; Shang, C.; Blum, T.; Zeng, J.; Chi, M.; Salmeron, M.; Kronawitter, C. X.; Bare, S. R.; Kulkarni, A. R.; Gates, B. C. Atomically Dispersed Platinum in Surface and Subsurface Sites on MgO Have Contrasting Catalytic Properties

for CO Oxidation. *J. Phys. Chem. Lett.* **2022**, *13* (17), 3896–3903. https://doi.org/10.1021/acs.jpclett.2c00667.
(133) DeRita, L.; Dai, S.; Lopez-Zepeda, K.; Pham, N.; Graham, G. W.; Pan, X.; Christopher, P. Catalyst Architecture for Stable Single Atom Dispersion Enables Site-Specific Spectroscopic and Reactivity Measurements of CO Adsorbed to Pt Atoms, Oxidized Pt Clusters, and Metallic Pt Clusters on TiO2. *J. Am. Chem. Soc.* **2017**, *139* (40), 14150–14165. https://doi.org/10.1021/jacs.7b07093.
(134) Helali, Z.; Jedidi, A.; Syzgantseva, O. A.; Calatayud, M.; Minot, C. Scaling Reducibility of Metal Oxides. *Theor. Chem. Acc.* **2017**, *136* (9), 100. https://doi.org/10.1007/s00214-017-2130-y.
(135) De Mallmann, A.; Barthomeuf, D. *FORMATION OF CHINI TYPE Pt-CO COMPLEXES IN BASIC ZEOLITES*; 1990; Vol. 5, pp 293–300.
(136) Baranova, E. A.; Bock, C.; Ilin, D.; Wang, D.; MacDougall, B. Infrared Spectroscopy on Size-Controlled Synthesized Pt-Based Nano-Catalysts. *Surf. Sci.* **2006**, *600* (17), 3502–3511. https://doi.org/10.1016/j.susc.2006.07.005.
(137) Faisal, F.; Stumm, C.; Bertram, M.; Wähler, T.; Schuster, R.; Xiang, F.; Lytken, O.; Katsounaros, I.; Mayrhofer, K. J. J.; Schneider, M. A.; Brummel, O.; Libuda, J. Atomically-Defined Model Catalysts in Ultrahigh Vacuum and in Liquid Electrolytes: Particle Size-Dependent CO Adsorption on Pt Nanoparticles on Ordered Co_3O_4 (111) Films. *Phys. Chem. Chem. Phys.* **2018**, *20* (36), 23702–23716. https://doi.org/10.1039/C8CP03770A.
(138) Avanesian, T.; Dai, S.; Kale, M. J.; Graham, G. W.; Pan, X.; Christopher, P. Quantitative and Atomic-Scale View of CO-Induced Pt Nanoparticle Surface Reconstruction at Saturation Coverage via DFT Calculations Coupled with in Situ TEM and IR. *J. Am. Chem. Soc.* **2017**, *139* (12), 4551–4558. https://doi.org/10.1021/jacs.7b01081.
(139) Kale, M. J.; Christopher, P. Utilizing Quantitative in Situ FTIR Spectroscopy to Identify Well-Coordinated Pt Atoms as the Active Site for CO Oxidation on Al2O3-Supported Pt Catalysts. *ACS Catal.* **2016**, *6* (8), 5599–5609. https://doi.org/10.1021/acscatal.6b01128.
(140) Lentz, C.; Jand, S. P.; Melke, J.; Roth, C.; Kaghazchi, P. DRIFTS Study of CO Adsorption on Pt Nanoparticles Supported by DFT Calculations. *J. Mol. Catal. Chem.* **2017**, *426*, 1–9. https://doi.org/10.1016/j.molcata.2016.10.002.
(141) Hansen, T. K.; Høj, M.; Hansen, B. B.; Janssens, T. V. W.; Jensen, A. D. The Effect of Pt Particle Size on the Oxidation of CO, C3H6, and NO Over Pt/Al2O3 for Diesel Exhaust Aftertreatment. *Top. Catal.* **2017**, *60* (17–18), 1333–1344. https://doi.org/10.1007/s11244-017-0818-9.
(142) Barcaro, G.; Fortunelli, A. 2D Oxides on Metal Materials: Concepts, Status, and Perspectives. *Phys. Chem. Chem. Phys.* **2019**, *21* (22), 11510–11536. https://doi.org/10.1039/c9cp00972h.
(143) Pinto, F. M.; Suzuki, V. Y.; Silva, R. C.; La Porta, F. A. Oxygen Defects and Surface Chemistry of Reducible Oxides. *Front. Mater.* **2019**, *6*, 260. https://doi.org/10.3389/fmats.2019.00260.
(144) Alexeev, O. S.; Chin, S. Y.; Engelhard, M. H.; Ortiz-Soto, L.; Amiridis, M. D. Effects of Reduction Temperature and Metal−Support Interactions on the Catalytic Activity of Pt/γ-Al_2O_3 and Pt/TiO_2 for the Oxidation of CO in the Presence and Absence of H_2. *J. Phys. Chem. B* **2005**, *109* (49), 23430–23443. https://doi.org/10.1021/jp054888v.

(145) Lin, C.; Yang, Z.; Pan, H.; Cui, J.; Lv, Z.; liu, X.; Tian, P.; Xiao, Z.; Li, P.; Xu, J.; Han, Y. F. Ce-Introduced Effects on Modification of Acidity and Pt Electronic States on Pt-Sn/γ-Al2O3 Catalysts for Catalytic Reforming. *Appl. Catal. Gen.* **2021**, *617*. https://doi.org/10.1016/j.apcata.2021.118116.
(146) Zhu, X.; Wang, T.; Xu, Z.; Yue, Y.; Lin, M.; Zhu, H. Pt-Sn Clusters Anchored at Al3+penta Sites as a Sinter-Resistant and Regenerable Catalyst for Propane Dehydrogenation. *J. Energy Chem.* **2021**, *65*, 293–301. https://doi.org/10.1016/j.jechem.2021.06.002.
(147) Arteaga, G. J.; Anderson, J. A.; Rochester, C. H. *FTIR Study of CO Adsorption on Coked Pt-Sn/Al 2 O 3 Catalysts*; 1999; Vol. 58, pp 189–194.
(148) Yu, C.; Ge, Q.; Xu, H.; Li, W. Effects of Ce Addition on the Pt-Sn/γ-Al2O3 Catalyst for Propane Dehydrogenation to Propylene. *Appl. Catal. Gen.* **2006**, *315*, 58–67. https://doi.org/10.1016/j.apcata.2006.08.038.
(149) Stakheev; al. *Evidence for Monatomic Platinum Species in H-ZSM-5 from FTIR Spectroscopy of Chemisorbed CO*.
(150) Palazov, A.; Bonev, C. H.; Shopov, D.; Lietz, G.; Sarkany, ? A; And, S.; Voltert, J. *Adsorption and Hydrogenation of Ethylene, 1-Hexene, and Benzene and CO Adsorption on Pt/A1203 and Pt-Sn/A1203 Catalysts*; 1987; Vol. 103, pp 249–260.
(151) Kappers, M. J.; van der Maas, J. H. Correlation between CO Frequency and Pt Coordination Number. A DRIFT Study on Supported Pt Catalysts. *Catal. Lett.* **1991**, *10* (5–6), 365–373. https://doi.org/10.1007/BF00769171.
(152) Llorca, J.; Homs, N.; Arana, J.; Sales, J.; Ramırez De La Piscina, P. *FTIR Study of the Interaction of CO and CO with 2 Silica-Supported PtSn Alloy*; 1998; Vol. 134, pp 217–224.
(153) Barshad, Y.; Zhou, X.; Gulari, E. Carbon Monoxide Oxidation under Transient Conditions: A Fourier-Transform Infrared Transmission Spectroscopy Study. *J. Catal.* **1985**, *94* (1), 128–141. https://doi.org/10.1016/0021-9517(85)90088-0.
(154) Liu, L.; Lopez-Haro, M.; Lopes, C. W.; Rojas-Buzo, S.; Concepcion, P.; Manzorro, R.; Simonelli, L.; Sattler, A.; Serna, P.; Calvino, J. J.; Corma, A. Structural Modulation and Direct Measurement of Subnanometric Bimetallic PtSn Clusters Confined in Zeolites. *Nat. Catal.* **2020**, *3* (8), 628–638. https://doi.org/10.1038/s41929-020-0472-7.
(155) Del Angel, G.; Bonilla, A.; Peña, Y.; Navarrete, J.; Fierro, J. L. G.; Acosta, D. R. Effect of Lanthanum on the Catalytic Properties of PtSn/γ-Al 2O3 Bimetallic Catalysts Prepared by Successive Impregnation and Controlled Surface Reaction. *J. Catal.* **2003**, *219* (1), 63–73. https://doi.org/10.1016/S0021-9517(03)00140-4.
(156) Degler, D.; Pereira De Carvalho, H. W.; Kvashnina, K.; Grunwaldt, J. D.; Weimar, U.; Barsan, N. Structure and Chemistry of Surface-Doped Pt:SnO2 Gas Sensing Materials. *RSC Adv.* **2016**, *6* (34), 28149–28155. https://doi.org/10.1039/c5ra26302f.
(157) Shan, Y.; Sui, Z.; Zhu, Y.; Chen, D.; Zhou, X. Effect of Steam Addition on the Structure and Activity of Pt-Sn Catalysts in Propane Dehydrogenation. *Chem. Eng. J.* **2015**, *278*, 240–248. https://doi.org/10.1016/j.cej.2014.09.107.
(158) Degler, D.; Müller, S. A.; Doronkin, D. E.; Wang, D.; Grunwaldt, J. D.; Weimar, U.; Barsan, N. Platinum Loaded Tin Dioxide: A Model System for Unravelling the Interplay between Heterogeneous Catalysis and Gas Sensing. *J. Mater. Chem. A* **2018**, *6* (5), 2034–2046. https://doi.org/10.1039/c7ta08781k.

(159) Wang, Z.; Chen, Y.; Mao, S.; Wu, K.; Zhang, K.; Li, Q.; Wang, Y. Chemical Insight into the Structure and Formation of Coke on PtSn Alloy during Propane Dehydrogenation. *Adv. Sustain. Syst.* **2020**, *4* (9). https://doi.org/10.1002/adsu.202000092.
(160) Virnovskaia, A.; Morandi, S.; Rytter, E.; Ghiotti, G.; Olsbye, U. Characterization of Pt,Sn/Mg(Al)O Catalysts for Light Alkane Dehydrogenation by FT-IR Spectroscopy and Catalytic Measurements. *J. Phys. Chem. C* **2007**, *111* (40), 14732–14742. https://doi.org/10.1021/jp074686u.
(161) Moscu, A.; Schuurman, Y.; Veyre, L.; Thieuleux, C.; Meunier, F. Direct Evidence by in Situ IR CO Monitoring of the Formation and the Surface Segregation of a Pt–Sn Alloy. *Chem. Commun.* **2014**, *50* (62), 8590–8592. https://doi.org/10.1039/c4cc03208j.
(162) Xie, J.; Jiang, H.; Qian, Y.; Wang, H.; An, N.; Chen, S.; Dai, Y.; Guo, S. Fine Tuning the Morphology of Spinel as Ultra-Stable Catalyst Support in Propane Dehydrogenation. *Adv. Mater. Interfaces* **2021**, *8* (22). https://doi.org/10.1002/admi.202101325.
(163) Schwank, J. FTIR Study of Bimetallic Pt-Sn/AI203 Catalysts.
(164) Zheng, Y.; Wang, X.; Fu, X.; Wei, K. Preparation and Catalytic Properties of a Bimetallic Sn-Pt Complex in the Supercages of NaY Zeolite by Use of Surface Organometallic Chemistry. *Appl. Organomet. Chem.* **2007**, *21* (10), 836–840. https://doi.org/10.1002/aoc.1280.
(165) Santorf 'b, G. F.; Caseila, M. L.; Siri A'b, G. J.; Ferretti, O. A.; Fierro, J. L. G. *An Organometallic Approach for Tin Promotion Pt/y-Al203 Alkane Dehydrogenation Catalysts Enhancement Over*.
(166) Puigdollers, A. R.; Schlexer, P.; Tosoni, S.; Pacchioni, G. Increasing Oxide Reducibility: The Role of Metal/Oxide Interfaces in the Formation of Oxygen Vacancies. *ACS Catal.* **2017**, *7* (10), 6493–6513. https://doi.org/10.1021/acscatal.7b01913.
(167) Wang, Y.; Hu, Z. P.; Lv, X.; Chen, L.; Yuan, Z. Y. Ultrasmall PtZn Bimetallic Nanoclusters Encapsulated in Silicalite-1 Zeolite with Superior Performance for Propane Dehydrogenation. *J. Catal.* **2020**, *385*, 61–69. https://doi.org/10.1016/j.jcat.2020.02.019.
(168) Gao, X.; Xu, W.; Li, X.; Cen, J.; Xu, Y.; Lin, L.; Yao, S. Non-Oxidative Dehydrogenation of Propane to Propene over Pt-Sn/Al2O3 Catalysts: Identification of the Nature of Active Site. *Chem. Eng. J.* **2022**, *443*. https://doi.org/10.1016/j.cej.2022.136393.
(169) Balakrishnan, K.; Schwank, J. *FTIR Study of Bimetallic Pt-Sn/AI203 Catalysts*; 1992; Vol. 138, pp 491–499.
(170) Wang, J.; Chang, X.; Chen, S.; Sun, G.; Zhou, X.; Vovk, E.; Yang, Y.; Deng, W.; Zhao, Z. J.; Mu, R.; Pei, C.; Gong, J. On the Role of Sn Segregation of Pt-Sn Catalysts for Propane Dehydrogenation. *ACS Catal.* **2021**, *11* (8), 4401–4410. https://doi.org/10.1021/acscatal.1c00639.
(171) Mojet, B. L.; Miller, J. T.; Koningsberger, D. C. The Effect of CO Adsorption at Room Temperature on the Structure of Supported Pt Particles. *J. Phys. Chem. B* **1999**, *103* (14), 2724–2734. https://doi.org/10.1021/jp983283e.
(172) Nilsson, A.; Pettersson, L. G. M.; Nørskov, J. K. *Chemical Bonding at Surfaces and Interfaces Adsorbate Electronic Structure and Bonding on Metal Surfaces*; 2008.
(173) Yu, C.; Xu, H.; Ge, Q.; Li, W. Properties of the Metallic Phase of Zinc-Doped Platinum Catalysts for Propane Dehydrogenation. *J. Mol. Catal. Chem.* **2007**, *266* (1–2), 80–87. https://doi.org/10.1016/j.molcata.2006.10.025.
(174) Rochlitz, L.; Searles, K.; Alfke, J.; Zemlyanov, D.; Safonova, O. V.; Copéret, C. Silica-Supported, Narrowly Distributed, Subnanometric Pt–Zn Particles from Single Sites with

High Propane Dehydrogenation Performance. *Chem. Sci.* **2020**, *11* (6), 1549–1555. https://doi.org/10.1039/C9SC05599A.
(175) Sadykov, I. I.; Sushkevich, V. L.; Krumeich, F.; Nuguid, R. J. G.; van Bokhoven, J. A.; Nachtegaal, M.; Safonova, O. V. Platinum-Iron(II) Oxide Sites Directly Responsible for Preferential Carbon Monoxide Oxidation at Ambient Temperature: An Operando X-ray Absorption Spectroscopy Study**. *Angew. Chem. Int. Ed.* **2023**, *62* (1). https://doi.org/10.1002/anie.202214032.
(176) Bauer, T.; Maisel, S.; Blaumeiser, D.; Vecchietti, J.; Taccardi, N.; Wasserscheid, P.; Bonivardi, A.; Görling, A.; Libuda, J. Operando DRIFTS and DFT Study of Propane Dehydrogenation over Solid- and Liquid-Supported Ga $_x$ Pt $_y$ Catalysts. *ACS Catal.* **2019**, *9* (4), 2842–2853. https://doi.org/10.1021/acscatal.8b04578.
(177) Wang, Y.; Suo, Y.; Lv, X.; Wang, Z.; Yuan, Z.-Y. Enhanced Performances of Bimetallic Ga-Pt Nanoclusters Confined within Silicalite-1 Zeolite in Propane Dehydrogenation. *J. Colloid Interface Sci.* **2021**, *593*, 304–314. https://doi.org/10.1016/j.jcis.2021.02.129.
(178) Chen, S.; Zhao, Z. J.; Mu, R.; Chang, X.; Luo, J.; Purdy, S. C.; Kropf, A. J.; Sun, G.; Pei, C.; Miller, J. T.; Zhou, X.; Vovk, E.; Yang, Y.; Gong, J. Propane Dehydrogenation on Single-Site [PtZn4] Intermetallic Catalysts. *Chem* **2020**, 1–19. https://doi.org/10.1016/j.chempr.2020.10.008.
(179) Zhang, B.; Zheng, L.; Zhai, Z.; Li, G.; Liu, G. Subsurface-Regulated PtGa Nanoparticles Confined in Silicalite-1 for Propane Dehydrogenation. *ACS Appl. Mater. Interfaces* **2021**, *13* (14), 16259–16266. https://doi.org/10.1021/acsami.0c22865.
(180) Shpiro, E. S.; Tkachenko, O. P.; Jaeger, N. I.; Schulz-Ekloff, G.; Grünert, W. Structure and Reactivity of Platinum−Copper Alloy Particles Supported on ZSM-5. *J. Phys. Chem. B* **1998**, *102* (19), 3798–3805. https://doi.org/10.1021/jp981029g.
(181) Newville, M. Fundamentals of XAFS. **2004**.
(182) Song, Z.; Li, J.; Davis, K. D.; Li, X.; Zhang, J.; Zhang, L.; Sun, X. Emerging Applications of Synchrotron Radiation X-Ray Techniques in Single Atomic Catalysts. *Small Methods* **2022**, *6* (11), 2201078. https://doi.org/10.1002/smtd.202201078.
(183) Rana, R.; Vila, F. D.; Kulkarni, A. R.; Bare, S. R. Bridging the Gap between the X-Ray Absorption Spectroscopy and the Computational Catalysis Communities in Heterogeneous Catalysis: A Perspective on the Current and Future Research Directions. *ACS Catal.* **2022**, *12* (22), 13813–13830. https://doi.org/10.1021/acscatal.2c03863.
(184) Bare, S. R.; Ressler, T. *Chapter 6 Characterization of Catalysts in Reactive Atmospheres by X-Ray Absorption Spectroscopy*; Elsevier Inc., 2009; Vol. 52. https://doi.org/10.1016/S0360-0564(08)00006-0.
(185) Yasuhiro Iwasawa. *X-Ray Absorption Fine Structure for Catalysts and Surfaces*; World Scientific Publishing, 1996.
(186) Crozier, E. D. A Review of the Current Status of XAFS Spectroscopy. *Nucl. Instrum. Methods Phys. Res. Sect. B Beam Interact. Mater. At.* **1997**, *133* (1–4), 134–144. https://doi.org/10.1016/S0168-583X(97)00471-0.
(187) Yu, W.; Porosoff, M. D.; Chen, J. G. Review of Pt-Based Bimetallic Catalysis: From Model Surfaces to Supported Catalysts. *Chem. Rev.* **2012**, *112* (11), 5780–5817. https://doi.org/10.1021/cr300096b.
(188) Gaur, A.; Shrivastava, B. D.; Nigam, H. L. X-Ray Absorption Fine Structure (XAFS) Spectroscopy – A Review. *Proc Indian Natn Sci Acad Spl Issue Part B* **2013**, *79* (4), 921–966.

(189) Bordiga, S.; Groppo, E.; Agostini, G.; van Bokhoven, J. A.; Lamberti, C. Reactivity of Surface Species in Heterogeneous Catalysts Probed by In Situ X-Ray Absorption Techniques. *Chem. Rev.* **2013**, *113* (3), 1736–1850. https://doi.org/10.1021/cr2000898.
(190) Rehr, J. J.; Albers, R. C. Theoretical Approaches to X-Ray Adsorption Fine Structure. *Rev. Mod. Phys.* **2000**, *72* (3), 621–654. https://doi.org/10.1111/j.1440-1754.1989.tb01421.x.
(191) Aksenov, V. L.; Kuzmin, A. Y.; Purans, J.; Tyutyunnikov, S. I. EXAFS Spectroscopy at Synchrotron-Radiation Beams. **2001**, *32* (6).
(192) Ferrini, P.; Dijkmans, J.; De Clercq, R.; Van de Vyver, S.; Dusselier, M.; Jacobs, P. A.; Sels, B. F. Lewis Acid Catalysis on Single Site Sn Centers Incorporated into Silica Hosts. *Coord. Chem. Rev.* **2017**, *343*, 220–255. https://doi.org/10.1016/j.ccr.2017.05.010.
(193) Drake, I. J.; Zhang, Y.; Gilles, M. K.; Teris Liu, C. N.; Nachimuthu, P.; Perera, R. C. C.; Wakita, H.; Bell, A. T. An in Situ Al K-Edge XAS Investigation of the Local Environment of H +- And Cu+-Exchanged USY and ZSM-5 Zeolites. *J. Phys. Chem. B* **2006**, *110* (24), 11665–11676. https://doi.org/10.1021/jp058244z.
(194) Kelly, S. D. X-Ray Absorption Fine Structure Overview.
(195) Meitzner, G.; Via, G. H.; Lytle, F. W.; Sinfelt, J. H. Analysis of X-Ray Absorption Edge Data on Metal Catalysts. *J. Phys. Chem.* **1992**, *96* (12), 4960–4964. https://doi.org/10.1021/j100191a043.
(196) Gaur, A.; Shrivastava, B. D. Speciation Using X-Ray Absorption Fine Structure (XAFS). *Rev. J. Chem.* **2015**, *5* (4), 361–398. https://doi.org/10.1134/S2079978015040032.
(197) Protesescu, L.; Rossini, A. J.; Kriegner, D.; Valla, M.; de Kergommeaux, A.; Walter, M.; Kravchyk, K. V.; Nachtegaal, M.; Stangl, J.; Malaman, B.; Reiss, P.; Lesage, A.; Emsley, L.; Copéret, C.; Kovalenko, M. V. Unraveling the Core–Shell Structure of Ligand-Capped Sn/SnO $_x$ Nanoparticles by Surface-Enhanced Nuclear Magnetic Resonance, Mössbauer, and X-Ray Absorption Spectroscopies. *ACS Nano* **2014**, *8* (3), 2639–2648. https://doi.org/10.1021/nn406344n.
(198) Sayers, D. E.; Stern, E. A.; Lytle, F. W. New Technique for Investigating Noncrystalline Structures: Fourier Analysis of the Extended X-Ray—Absorption Fine Structure. *Phys. Rev. Lett.* **1971**, *27* (18), 1204–1207. https://doi.org/10.1103/PhysRevLett.27.1204.
(199) Hall, M. D.; Daly, H. L.; Zhang, J. Z.; Zhang, M.; Alderden, R. A.; Pursche, D.; Foran, G. J.; Hambley, T. W. Quantitative Measurement of the Reduction of Platinum(Iv) Complexes Using X-Ray Absorption near-Edge Spectroscopy (XANES). *Metallomics* **2012**, *4* (6), 568. https://doi.org/10.1039/c2mt20053h.
(200) Uemura, Y.; Inada, Y.; Bando, K. K.; Sasaki, T.; Kamiuchi, N.; Eguchi, K.; Yagishita, A.; Nomura, M.; Tada, M.; Iwasawa, Y. Core-Shell Phase Separation and Structural Transformation of Pt 3Sn Alloy Nanoparticles Supported on γ-Al2O 3 in the Reduction and Oxidation Processes Characterized by in Situ Time-Resolved XAFS. *J. Phys. Chem. C* **2011**, *115* (13), 5823–5833. https://doi.org/10.1021/jp111286b.
(201) Iglesias-Juez, A.; Beale, A. M.; Maaijen, K.; Weng, T. C.; Glatzel, P.; Weckhuysen, B. M. A Combined in Situ Time-Resolved UV-Vis, Raman and High-Energy Resolution X-Ray Absorption Spectroscopy Study on the Deactivation Behavior of Pt and PtSn Propane Dehydrogenation Catalysts under Industrial Reaction Conditions. *J. Catal.* **2010**, *276* (2), 268–279. https://doi.org/10.1016/j.jcat.2010.09.018.
(202) Zhang, L.; Zhou, H.; Yang, X.; Zhang, S.; Zhang, H.; Yang, X.; Su, X.; Zhang, J.; Lin, Z. Boosting Electroreduction Kinetics of Nitrogen to Ammonia via Atomically Dispersed Sn

Protuberance. *Angew. Chem. Int. Ed.* **2023**, *62* (13). https://doi.org/10.1002/anie.202217473.
(203) G Meitzner; G. H. Via; F. W. Lytle; S.C. Fung; J. H. Sinfelt. Extended X-Ray Absorption Fine Structure Studies of Platinum-Tin Catalysts. *J. Phys. Chem.* **1988**, *92* (10), 2925–2932.
(204) Mohammed, K. M. H.; Chutia, A.; Callison, J.; Wells, P. P.; Gibson, E. K.; Beale, A. M.; Catlow, C. R. A.; Raja, R. Design and Control of Lewis Acid Sites in Sn-Substituted Microporous Architectures. *J. Mater. Chem. A* **2020**. https://doi.org/10.1039/x0xx00000x.
(205) Román-Martínez, M. C.; Cazorla-Amorós, D.; Yamashita, H.; De Miguel, S.; Scelza, O. A. XAFS Study of Dried and Reduced PtSn/C Catalysts: Nature and Structure of the Catalytically Active Phase. *Langmuir* **2000**, *16* (3), 1123–1131. https://doi.org/10.1021/la990575d.
(206) Uemura, Y.; Inada, Y.; Bando, K. K.; Sasaki, T.; Kamiuchi, N.; Eguchi, K.; Yagishita, A.; Nomura, M.; Tada, M.; Iwasawa, Y. In Situ Time-Resolved XAFS Study on the Structural Transformation and Phase Separation of Pt3Sn and PtSn Alloy Nanoparticles on Carbon in the Oxidation Process. *Phys. Chem. Chem. Phys.* **2011**, *13* (35), 15833–15844. https://doi.org/10.1039/c1cp20994a.
(207) Keegan, M. B. T.; Dent, A. J.; Blake, A. B.; Conyers, L.; Moyes, R. B.; Wells, P. B.; Whan, D. A. An in Situ Energy Dispersive EXAFS Study of the Calcinatibn and Reduction of a PtZSM-5 Catalyst Precursor.
(208) Rehr, J. J.; Kas, J. J.; Vila, F. D.; Prange, M. P.; Jorissen, K. Parameter-Free Calculations of X-Ray Spectra with FEFF9. *Phys. Chem. Chem. Phys.* **2010**, *12* (21), 5503–5513. https://doi.org/10.1039/b926434e.
(209) Sun, Z.; Yan, W.; Yao, T.; Liu, Q.; Xie, Y.; Wei, S. XAFS in Dilute Magnetic Semiconductors. *Dalton Trans.* **2013**, *42* (38), 13779. https://doi.org/10.1039/c3dt50888a.
(210) Nakaya, Y.; Hirayama, J.; Yamazoe, S.; Shimizu, K. ichi; Furukawa, S. Single-Atom Pt in Intermetallics as an Ultrastable and Selective Catalyst for Propane Dehydrogenation. *Nat. Commun.* **2020**, *11* (1), 3–9. https://doi.org/10.1038/s41467-020-16693-9.
(211) Zeng, L.; Zhao, Z.; Lv, F.; Xia, Z.; Lu, S. Y.; Li, J.; Sun, K.; Wang, K.; Sun, Y.; Huang, Q.; Chen, Y.; Zhang, Q.; Gu, L.; Lu, G.; Guo, S. Anti-Dissolution Pt Single Site with Pt(OH)(O3)/Co(P) Coordination for Efficient Alkaline Water Splitting Electrolyzer. *Nat. Commun.* **2022**, *13* (1). https://doi.org/10.1038/s41467-022-31406-0.
(212) Usón, R.; Forniés, J. Synthesis and Structures of Novel Types of Heteronuclear Pt□M (M□Ag, Sn or Pb) Neutral or Anionic Organometallic Complexes. *Inorganica Chim. Acta* **1992**, *198–200*, 165–177. https://doi.org/10.1016/S0020-1693(00)92358-2.
(213) Koppaka, A.; Yempally, V.; Zhu, L.; Fortman, G. C.; Temprado, M.; Hoff, C. D.; Captain, B. Synthesis of [Pt(SnBu$^{t}_{3}$)(IBu^{t})(μ-H)]$_{2}$, a Coordinatively Unsaturated Dinuclear Compound Which Fragments upon Addition of Small Molecules to Form Mononuclear Pt–Sn Complexes. *Inorg. Chem.* **2016**, *55* (1), 307–321. https://doi.org/10.1021/acs.inorgchem.5b02441.
(214) Jain, A.; Ong, S. P.; Hautier, G.; Chen, W.; Richards, W. D.; Dacek, S.; Cholia, S.; Gunter, D.; Skinner, D.; Ceder, G.; Persson, K. A. Commentary: The Materials Project: A Materials Genome Approach to Accelerating Materials Innovation. *APL Mater.* **2013**, *1* (1), 011002. https://doi.org/10.1063/1.4812323.
(215) Fracchia, M.; Ghigna, P.; Minguzzi, A.; Vertova, A.; Turco, F.; Cerrato, G.; Meroni, D. Role of Synthetic Parameters on the Structural and Optical Properties of N,Sn-

Copromoted Nanostructured TiO2: A Combined Ti K-Edge and Sn L2,3-Edges X-Ray Absorption Investigation. *Nanomaterials* **2020**, *10* (6), 1224. https://doi.org/10.3390/nano10061224.
(216) Grandjean, D.; Benfield, R. E.; Nayral, C.; Maisonnat, A.; Chaudret, B. EXAFS and XANES Study of a Pure and Pd Doped Novel Sn/SnO $_x$ Nanomaterial. *J. Phys. Chem. B* **2004**, *108* (26), 8876–8887. https://doi.org/10.1021/jp0370627.
(217) Sordelli, L.; Psaro, R.; Vlaic, G.; Cepparo, A.; Recchia, S.; Dossi, C.; Fusi, A.; Zanoni, R. EXAFS Studies of Supported Rh–Sn Catalysts for Citral Hydrogenation. *J. Catal.* **1999**, *182* (1), 186–198. https://doi.org/10.1006/jcat.1998.2348.
(218) Hara, T.; Hatakeyama, M.; Kim, A.; Ichikuni, N.; Shimazu, S. Preparation of Clay-Supported Sn Catalysts and Application to Baeyer-Villiger Oxidation. *Green Chem.* **2012**, *14* (3), 771–777. https://doi.org/10.1039/c2gc16437j.
(219) Davis, S. R.; Chadwick, A. V.; Wright, J. D. *A Combined EXAFS and Diffraction Study of Pure and Doped Nanocrystalline Tin Oxide*; 1997. https://pubs.acs.org/sharingguidelines.
(220) Briois, V.; Santilli, C. V.; Pulcinelli, S. H.; Brito, G. E. S. EXAFS and XRD Analyses of the Structural Evolutions Involved during Drying of SnO2 Hydrogels. *J. Non-Cryst. Solids* **1995**, *191* (1–2), 17–28. https://doi.org/10.1016/0022-3093(95)00305-3.
(221) Murata, N.; Suzuki, T.; Kobayashi, M.; Togoh, F.; Asakura, K. Characterization of Pt-Doped SnO2 Catalyst for a High-Performance Micro Gas Sensor. *Phys. Chem. Chem. Phys.* **2013**, *15* (41), 17938. https://doi.org/10.1039/c3cp52490f.
(222) Kanai, H.; Mizutani, H.; Takanoc, M. X-Ray Absorption Study on the Local Structures of Fine Particles of a-Fe,O,-SnO, Gas Sensors. *J MATER CHEM* **1992**, *2*.
(223) Frenkel, A. I.; Hills, C. W.; Nuzzo, R. G. A View from the Inside: Complexity in the Atomic Scale Ordering of Supported Metal Nanoparticles. *J. Phys. Chem. B* **2001**, *105* (51), 12689–12703. https://doi.org/10.1021/jp012769j.
(224) Kip, B. Determination of Metal Particle Size of Highly Dispersed Rh, Ir, and Pt Catalysts by Hydrogen Chemisorption and EXAFS. *J. Catal.* **1987**, *105* (1), 26–38. https://doi.org/10.1016/0021-9517(87)90005-4.
(225) Greegor, R. Morphology of Supported Metal Clusters: Determination by EXAFS and Chemisorption. *J. Catal.* **1980**, *63* (2), 476–486. https://doi.org/10.1016/0021-9517(80)90102-5.
(226) Clausena, B. S.; Topsøe, H.; Hansen, L. B.; Stoltze, P.; Nørskov, J. K. Determination of Metal Particle Sizes from EXAFS. *Catal. Today* **1994**, *21* (1), 49–55. https://doi.org/10.1016/0920-5861(94)80033-2.
(227) Dai, Y.; Gorey, T. J.; Anderson, S. L.; Lee, S.; Lee, S.; Seifert, S.; Winans, R. E. Inherent Size Effects on XANES of Nanometer Metal Clusters: Size-Selected Platinum Clusters on Silica. *J. Phys. Chem. C* **2017**, *121* (1), 361–374. https://doi.org/10.1021/acs.jpcc.6b10167.
(228) Merte, L. R.; Ahmadi, M.; Behafarid, F.; Ono, L. K.; Lira, E.; Matos, J.; Li, L.; Yang, J. C.; Roldan Cuenya, B. Correlating Catalytic Methanol Oxidation with the Structure and Oxidation State of Size-Selected Pt Nanoparticles. *ACS Catal.* **2013**, *3* (7), 1460–1468. https://doi.org/10.1021/cs400234h.
(229) Song, J.; Yang, Y.; Liu, S.; Li, L.; Yu, N.; Fan, Y.; Chen, Z.; Kuai, L.; Geng, B. Dispersion and Support Dictated Properties and Activities of Pt/Metal Oxide Catalysts in Heterogeneous CO Oxidation. *Nano Res.* **2021**, *14* (12), 4841–4847. https://doi.org/10.1007/s12274-021-3443-7.

(230) Li, S.; Liu, J.; Yin, Z.; Ren, P.; Lin, L.; Gong, Y.; Yang, C.; Zheng, X.; Cao, R.; Yao, S.; Deng, Y.; Liu, X.; Gu, L.; Zhou, W.; Zhu, J.; Wen, X.; Xu, B.; Ma, D. Impact of the Coordination Environment on Atomically Dispersed Pt Catalysts for Oxygen Reduction Reaction. *ACS Catal.* **2020**, *10* (1), 907–913. https://doi.org/10.1021/acscatal.9b04558.
(231) Ankudinov, A. L.; Rehr, J. J.; Low, J.; Bare, S. R. Effect of Hydrogen Adsorption on the X-Ray Absorption Spectra of Small Pt Clusters. *Phys. Rev. Lett.* **2001**, *86* (8), 1642–1645. https://doi.org/10.1103/PhysRevLett.86.1642.
(232) Zu, X.; Li, X.; Liu, W.; Sun, Y.; Xu, J.; Yao, T.; Yan, W.; Gao, S.; Wang, C.; Wei, S.; Xie, Y. Efficient and Robust Carbon Dioxide Electroreduction Enabled by Atomically Dispersed $Sn^{\delta+}$ Sites. *Adv. Mater.* **2019**, *31* (15), 1808135. https://doi.org/10.1002/adma.201808135.
(233) Bare, S. R.; Kelly, S. D.; Sinkler, W.; Low, J. J.; Modica, F. S.; Valencia, S.; Corma, A.; Nemeth, L. T. Uniform Catalytic Site in Sn-β-Zeolite Determined Using X-Ray Absorption Fine Structure. *J. Am. Chem. Soc.* **2005**, *127* (37), 12924–12932. https://doi.org/10.1021/ja052543k.
(234) Caballero, A.; Dexpert, H.; Didillon, B.; LePeltier, F.; Clause, O.; Lynch, J. In Situ X-Ray Absorption Spectroscopic Study of a Highly Dispersed Platinum-Tin/Alumina Catalyst. *J. Phys. Chem.* **1993**, *97* (43), 11283–11285. https://doi.org/10.1021/j100145a028.
(235) N-S. Chui; W-H. Lee; Y-Xi Li; S. H. Bauer; B. H. Davis. Structures of Bimetallic Catalysts (Pt/Sn) on SiO2 vs Al2O3 Supports: NEXAFS and EXAFS Diagnostics. In *Advances in Hydrotreating Catalysts*; 1987; pp 147–163.
(236) Guggenberger, L. J. The Structure of a Platinum–Tin Cluster. *Chem Commun Lond.* **1968**, *0* (9), 512–513. https://doi.org/10.1039/C19680000512.
(237) Huang, H.; Nassr, A. B. A. A.; Celorrio, V.; Taylor, S. F. R.; Puthiyapura, V. K.; Hardacre, C.; Brett, D. J. L.; Russell, A. E. Effects of Heat Treatment Atmosphere on the Structure and Activity of Pt_3Sn Nanoparticle Electrocatalysts: A Characterisation Case Study. *Faraday Discuss.* **2018**, *208*, 555–573. https://doi.org/10.1039/C7FD00221A.
(238) Mukerjee, S.; McBreen, J. An In Situ X-Ray Absorption Spectroscopy Investigation of the Effect of Sn Additions to Carbon-Supported Pt Electrocatalysts: Part I. *J. Electrochem. Soc.* **1999**, *146* (2), 600–606. https://doi.org/10.1149/1.1391650.
(239) Borgna, A.; Stagg, S. M.; Resasco, D. E. Interference Phenomena in the EXAFS Spectra of Pt−Sn Bimetallic Catalysts. *J. Phys. Chem. B* **1998**, *102* (26), 5077–5081. https://doi.org/10.1021/jp9732571.
(240) Corma, A.; Nemeth, L. T.; Renz, M.; Valencia, S. Sn-Zeolite Beta as a Heterogeneous Chemoselective Catalyst for Baeyer-Villiger Oxidations. *Nature* **2001**, *412* (6845), 423–425. https://doi.org/10.1038/35086546.
(241) Guan, F. F.; Ma, T. T.; Yuan, X.; Zeng, H. Y.; Wu, J. Sn-Modified NaY Zeolite Catalysts Prepared by Post-Synthesis Methods for Baeyer–Villiger Oxidation. *Catal. Lett.* **2018**, *148* (1), 443–453. https://doi.org/10.1007/s10562-017-2224-0.
(242) Lei, Z.; Ma, G.; Jia, C. Montmorillonite (MMT) Supported Tin (II) Chloride: An Efficient and Recyclable Heterogeneous Catalyst for Clean and Selective Baeyer-Villiger Oxidation with Hydrogen Peroxide. *Catal. Commun.* **2007**, *8* (3), 305–309. https://doi.org/10.1016/j.catcom.2006.05.045.
(243) Clerici, A.; Alimonti, G. World Energy Resources. *EPJ Web Conf.* **2015**, *98*, 1–15. https://doi.org/10.1051/epjconf/20159801001.

(244) Harris, J. W.; Cordon, M. J.; Di Iorio, J. R.; Vega-Vila, J. C.; Ribeiro, F. H.; Gounder, R. Titration and Quantification of Open and Closed Lewis Acid Sites in Sn-Beta Zeolites That Catalyze Glucose Isomerization. *J. Catal.* **2016**, *335*, 141–154. https://doi.org/10.1016/j.jcat.2015.12.024.
(245) Vega-Vila, J. C.; Harris, J. W.; Gounder, R. Controlled Insertion of Tin Atoms into Zeolite Framework Vacancies and Consequences for Glucose Isomerization Catalysis. *J. Catal.* **2016**, *344*, 108–120. https://doi.org/10.1016/j.jcat.2016.09.011.
(246) Conrad, S.; Verel, R.; Hammond, C.; Wolf, P.; Göltl, F.; Hermans, I. Silica-Grafted SnIV Catalysts in Hydrogen-Transfer Reactions. *ChemCatChem* **2015**, *7* (20), 3270–3278. https://doi.org/10.1002/cctc.201500630.
(247) Yue, Y.; Fu, J.; Wang, C.; Yuan, P.; Bao, X.; Xie, Z.; Basset, J. M.; Zhu, H. Propane Dehydrogenation Catalyzed by Single Lewis Acid Site in Sn-Beta Zeolite. *J. Catal.* **2021**, *395*, 155–167. https://doi.org/10.1016/j.jcat.2020.12.019.
(248) Kubacka, A.; Wloch, E.; Sulikowski, B.; Valenzuela, R. X.; Cortes Coeberan, V. Oxidative Dehydrogenation of Propane on Zeolite Catalyst. *Catal. Today* **2000**, *61*, 343–352.
(249) Xia, C.; Liu, Y.; Lin, M.; Peng, X.; Zhu, B.; Shu, X. Confirmation of the Isomorphous Substitution by Sn Atoms in the Framework Positions of MFI-Typed Zeolite. *Catal. Today* **2018**, *316* (March), 193–198. https://doi.org/10.1016/j.cattod.2018.02.056.
(250) Yang, X.; Liu, Y.; Li, X.; Ren, J.; Zhou, L.; Lu, T.; Su, Y. Synthesis of Sn-Containing Nanosized Beta Zeolite As Efficient Catalyst for Transformation of Glucose to Methyl Lactate. *ACS Sustain. Chem. Eng.* **2018**, *6* (7), 8256–8265. https://doi.org/10.1021/acssuschemeng.8b00177.
(251) Van Der Graaff, W. N. P.; Li, G.; Mezari, B.; Pidko, E. A.; Hensen, E. J. M. Synthesis of SnBeta with Exclusive and High Framework Sn Content. *ChemCatChem* **2015**, *7* (7), 1152–1160. https://doi.org/10.1002/cctc.201403050.
(252) Sun, M.; Su, Y.; Du, C.; Zhao, Q.; Liu, Z. Self-Doping for Visible Light Photocatalytic Purposes: Construction of SiO_2 /SnO_2 /SnO_2 :Sn^{2+} Nanostructures with Tunable Optical and Photocatalytic Performance. *RSC Adv.* **2014**, *4* (58), 30820. https://doi.org/10.1039/C4RA04356A.
(253) Dijkmans, J.; Dusselier, M.; Janssens, W.; Trekels, M.; Vantomme, A.; Breynaert, E.; Kirschhock, C.; Sels, B. F. An Inner-/Outer-Sphere Stabilized Sn Active Site in β-Zeolite: Spectroscopic Evidence and Kinetic Consequences. *ACS Catal.* **2016**, *6* (1), 31–46. https://doi.org/10.1021/acscatal.5b01822.
(254) Popovych, N. O.; Kyriienko, P. I.; Millot, Y.; Valentin, L.; Gurgul, J.; Socha, R. P.; Żukrowski, J.; Soloviev, S. O.; Dzwigaj, S. Sn-BEA Zeolites Prepared by Two-Step Postsynthesis Method: Physicochemical Properties and Catalytic Activity in Processes Based on MPV Reduction. *Microporous Mesoporous Mater.* **2018**, *268*, 178–188. https://doi.org/10.1016/j.micromeso.2018.04.026.
(255) Sushkevich, V. L.; Ivanova, I. I.; Yakimov, A. V. Revisiting Acidity of SnBEA Catalysts by Combined Application of FTIR Spectroscopy of Different Probe Molecules. *J. Phys. Chem. C* **2017**, *121* (21), 11437–11447. https://doi.org/10.1021/acs.jpcc.7b02206.
(256) Ivanushkin, G. G.; Smirnov, A. V.; Kots, P. A.; Ivanova, I. I. Modification of Acidic Properties of the Support for Pt–Sn/BEA Propane Dehydrogenation Catalysts. *Pet. Chem.* **2019**, *59* (7), 733–738. https://doi.org/10.1134/S0965544119070077.

(257) Searles, K.; Siddiqi, G.; Safonova, O. V.; Copéret, C. Silica-Supported Isolated Gallium Sites as Highly Active, Selective and Stable Propane Dehydrogenation Catalysts. *Chem. Sci.* **2017**, *8* (4), 2661–2666. https://doi.org/10.1039/c6sc05178b.
(258) Takahara, I.; Saito, M.; Inaba, M.; Murata, K. Effects of Pre-Treatment of a Silica-Supported Gallium Oxide Catalyst with H2 on Its Catalytic Performance for Dehydrogenation of Propane. *Catal. Lett.* **2004**, *96* (1–2), 29–32. https://doi.org/10.1023/B:CATL.0000029525.33197.89.
(259) Szeto, K. C.; Jones, Z. R.; Merle, N.; Rios, C.; Gallo, A.; Le Quemener, F.; Delevoye, L.; Gauvin, R. M.; Scott, S. L.; Taoufik, M. A Strong Support Effect in Selective Propane Dehydrogenation Catalyzed by Ga(i-Bu)3 Grafted onto γ-Alumina and Silica. *ACS Catal.* **2018**, *8* (8), 7566–7577. https://doi.org/10.1021/acscatal.8b00936.
(260) Wolf, P.; Valla, M.; Núñez-Zarur, F.; Comas-Vives, A.; Rossini, A. J.; Firth, C.; Kallas, H.; Lesage, A.; Emsley, L.; Copéret, C.; Hermans, I. Correlating Synthetic Methods, Morphology, Atomic-Level Structure, and Catalytic Activity of Sn-β Catalysts. *ACS Catal.* **2016**, *6* (7), 4047–4063. https://doi.org/10.1021/acscatal.6b00114.
(261) Wolf, P.; Valla, M.; Rossini, A. J.; Comas-Vives, A.; Núñez-Zarur, F.; Malaman, B.; Lesage, A.; Emsley, L.; Copéret, C.; Hermans, I. NMR Signatures of the Active Sites in Sn-β Zeolite. *Angew. Chem. - Int. Ed.* **2014**, *53* (38), 10179–10183. https://doi.org/10.1002/anie.201403905.
(262) Shah, P.; Ramaswamy, A. V.; Pasricha, R.; Lazar, K.; Ramaswamy, V. Incorporation of Tin into Mesoporous Silica SBA-15 Molecular Sieves. *Stud. Surf. Sci. Catal.* **2004**, *154 A*, 870–877. https://doi.org/10.1016/s0167-2991(04)80897-8.
(263) Vaughan, D. E. W.; Rive, S. B. Tin Substitution into Zeolite Frameworks US Patent 4933161, 1990.
(264) Shah, P.; Ramaswamy, A. V.; Lazar, K.; Ramaswamy, V. Synthesis and Characterization of Tin Oxide-Modified Mesoporous SBA-15 Molecular Sieves and Catalytic Activity in Trans-Esterification Reaction. *Appl. Catal. Gen.* **2004**, *273* (1–2), 239–248. https://doi.org/10.1016/j.apcata.2004.06.039.
(265) Lide, D. R. et al. *CRC Handbook of Chemistry and Physics*; 2005. https://doi.org/10.1021/ja906434c.
(266) Boronat, M.; Concepción, P.; Corma, A.; Renz, M.; Valencia, S. Determination of the Catalytically Active Oxidation Lewis Acid Sites in Sn-Beta Zeolites, and Their Optimisation by the Combination of Theoretical and Experimental Studies. *J. Catal.* **2005**, *234* (1), 111–118. https://doi.org/10.1016/j.jcat.2005.05.023.
(267) Bermejo-Deval, R.; Orazov, M.; Gounder, R.; Hwang, S.-J.; Davis, M. E. Active Sites in Sn-Beta for Glucose Isomerization to Fructose and Epimerization to Mannose. *ACS Catal.* **2014**, *4* (7), 2288–2297. https://doi.org/10.1021/cs500466j.
(268) Roy, S.; Bakhmutsky, K.; Mahmoud, E.; Lobo, R. F.; Gorte, R. J. Probing Lewis Acid Sites in Sn-Beta Zeolite. *ACS Catal.* **2013**, *3* (4), 573–580. https://doi.org/10.1021/cs300599z.
(269) D. Schwartz. ITWG GUIDELINE ON POWDER X-RAY DIFFRACTION (XRD) — GENERAL OVERVIEW.
(270) Holder, C. F.; Schaak, R. E. Tutorial on Powder X-Ray Diffraction for Characterizing Nanoscale Materials. *ACS Nano* **2019**, *13* (7), 7359–7365. https://doi.org/10.1021/acsnano.9b05157.

(271) Weibel, A.; Bouchet, R.; Boulc', F.; Knauth, P. The Big Problem of Small Particles: A Comparison of Methods for Determination of Particle Size in Nanocrystalline Anatase Powders. *Chem. Mater.* **2005**, *17* (9), 2378–2385. https://doi.org/10.1021/cm0403762.
(272) Inoue, M.; Kimura, M.; Inui, T. Transparent Colloidal Solution of 2 Nm Ceria Particles. *Chem. Commun.* **1999**, No. 11, 957–958. https://doi.org/10.1039/a900930b.
(273) Zhang, Y.; Lin, L.; Zheng, X.; Liu, C.; Zhu, Q.; Guo, H. Effect of Stannic Species Modification on the Acidity of Silicalite-1 and Its Enhancement in Transforming Ethylenediamine to Heterocyclic Amines. *Catalysts* **2020**, *10* (2). https://doi.org/10.3390/catal10020211.
(274) Yuan, E.; Dai, W.; Wu, G.; Guan, N.; Hunger, M.; Li, L. Facile Synthesis of Sn-Containing MFI Zeolites as Versatile Solid Acid Catalysts. *Microporous Mesoporous Mater.* **2018**, *270* (May), 265–273. https://doi.org/10.1016/j.micromeso.2018.05.032.
(275) Marley, A.; Borrelli, F. THE ULTRAVIOLET ABSORPTION EDGE OF.
(276) Naveen Kumar, P.; Sahaya Selva Mary, J.; Chandrakala, V.; Jothi Jeyarani, W.; Merline Shyla, J. Investigation of Superior Electro-Optical Properties of SnO2/SiO2 Nanocomposite over Its Individual Counterpart SnO2 Nanoparticles. *Mater. Chem. Phys.* **2017**, *193*, 234–243. https://doi.org/10.1016/j.matchemphys.2017.02.039.
(277) Selvi, N.; Sankar, S.; Dinakaran, K. Interfacial Effect on the Structural and Optical Properties of Pure SnO2 and Dual Shells (ZnO; SiO2) Coated SnO2 Core-Shell Nanospheres for Optoelectronic Applications. *Superlattices Microstruct.* **2014**, *76*, 277–287. https://doi.org/10.1016/j.spmi.2014.10.015.
(278) Zaki, M. I.; Hasan, M. A.; Al-Sagheer, F. A.; Pasupulety, L. In Situ FTIR Spectra of Pyridine Adsorbed on SiO2-Al2O3, TiO2, ZrO2 and CeO2: General Considerations for the Identification of Acid Sites on Surfaces of Finely Divided Metal Oxides. *Colloids Surf. Physicochem. Eng. Asp.* **2001**, *190* (3), 261–274. https://doi.org/10.1016/S0927-7757(01)00690-2.
(279) Bandiera, J.; Ben Taarit, Y. Catalytic Investigation of the Dehydrogenation Properties of Pentasil Type Zeolites as Compared with Their Cracking Properties. *Appl. Catal.* **1990**, *62* (1), 309–316. https://doi.org/10.1016/S0166-9834(00)82254-X.
(280) Phadke, N. M.; Mansoor, E.; Bondil, M.; Head-Gordon, M.; Bell, A. T. Mechanism and Kinetics of Propane Dehydrogenation and Cracking over Ga/H-MFI Prepared via Vapor-Phase Exchange of H-MFI with GaCl 3. *J. Am. Chem. Soc.* **2019**, *141* (4), 1614–1627. https://doi.org/10.1021/jacs.8b11443.
(281) Josephson, T. R.; Jenness, G. R.; Vlachos, D. G.; Caratzoulas, S. Distribution of Open Sites in Sn-Beta Zeolite. *Microporous Mesoporous Mater.* **2017**, *245*, 45–50. https://doi.org/10.1016/j.micromeso.2017.02.065.
(282) Nozik, D.; Tinga, F. M. P.; Bell, A. T. Propane Dehydrogenation and Cracking over Zn/H-MFI Prepared by Solid-State Ion Exchange of $ZnCl_2$. *ACS Catal.* **2021**, *11* (23), 14489–14506. https://doi.org/10.1021/acscatal.1c03641.
(283) Andersen, I. G. K.; Andersen, E. K.; Knudsen, N.; Skou, E. Study of Preparation and Ac/Dc Conductivity of Tin-Zeolite-Y Materials. *Solid State Ion.* **1991**, *46* (1–2), 89–93. https://doi.org/10.1016/0167-2738(91)90134-W.
(284) Buniazet, Z.; Lorentz, C.; Cabiac, A.; Maury, S.; Loridant, S. Supported Oxides Catalysts for the Dehydration of Isobutanol into Butenes: Relationships between Acidic and Catalytic Properties. *Mol. Catal.* **2018**, *451*, 143–152. https://doi.org/10.1016/j.mcat.2017.12.007.

(285) Chen, S. Y.; Tsai, H. D.; Chuang, W. T.; Lee, J. J.; Tang, C. Y.; Lin, C. Y.; Cheng, S. Direct Preparation of Thermally Stable Sn-Incorporated SBA-15 Mesoporous Materials in the Self-Generated Acidic Environment. *J. Phys. Chem. C* **2009**, *113* (34), 15226–15238. https://doi.org/10.1021/jp9016129.
(286) Corcoran, E. W. J.; Vaughan, D. E. W. US5192519 Substitued Stannosilicates and Preparation Thereof, 1993.
(287) Corma, A.; Domine, M. E.; Valencia, S. Water-Resistant Solid Lewis Acid Catalysts: Meerwein-Ponndorf-Verley and Oppenauer Reactions Catalyzed by Tin-Beta Zeolite. *J. Catal.* **2003**, *215* (2), 294–304. https://doi.org/10.1016/S0021-9517(03)00014-9.
(288) Corma, A.; Navarro, M. T.; Renz, M. Lewis Acidic Sn(IV) Centers - Grafted onto MCM-41 - As Catalytic Sites for the Baeyer-Villiger Oxidation with Hydrogen Peroxide. *J. Catal.* **2003**, *219* (1), 242–246. https://doi.org/10.1016/S0021-9517(03)00190-8.
(289) Endud, S.; Wong, K. L. Mesoporous Silica MCM-48 Molecular Sieve Modified with SnCl2 in Alkaline Medium for Selective Oxidation of Alcohol. *Microporous Mesoporous Mater.* **2007**, *101* (1-2 SPEC. ISS.), 256–263. https://doi.org/10.1016/j.micromeso.2006.12.029.
(290) Fejes, P.; Nagy, J. B.; Kovács, K.; Vankó, G. Synthesis of Tin(IV) Silicalites (MFI) and Their Characterization: A Mössbauer and MAS NMR Spectroscopy Study. *Appl. Catal. Gen.* **1996**, *145* (1–2), 155–184. https://doi.org/10.1016/0926-860X(96)00167-6.
(291) Garcia Vargas, N.; Stevenson, S.; Shantz, D. F. Synthesis and Characterization of Tin(IV) MFI: Sodium Inhibits the Synthesis of Phase Pure Materials. *Microporous Mesoporous Mater.* **2012**, *152*, 37–49. https://doi.org/10.1016/j.micromeso.2011.11.036.
(292) Hagen, A.; Schneider, E.; Benter, M.; Krogh, A.; Kleinert, A.; Roessner, F. Modification of Acid Supports by Solid-State Redox Reaction Part II. Acid and Catalytic Properties. *J. Catal.* **2004**, *226* (1), 171–182. https://doi.org/10.1016/j.jcat.2004.05.027.
(293) Hammond, C.; Conrad, S.; Hermans, I. Simple and Scalable Preparation of Highly Active Lewis Acidic Sn-β. *Angew. Chem. - Int. Ed.* **2012**, *51* (47), 11736–11739. https://doi.org/10.1002/anie.201206193.
(294) Hino, M.; Arata, K. Dehydrogenation of Cyclohexanol to Cyclohexanone Catalyzed by Tin Oxide and the Sulfated Tin Oxide. *Chem. Lett.* **1990**, *19* (9), 1737–1740. https://doi.org/10.1246/cl.1990.1737.
(295) Kim, J. Y.; Heo, N. H.; Seff, K. The Pentatin Cation in Zeolite Y: Thallous Ion Exchange and Crystal Structure of |Sn 36 Cl 11 |[Si 128 Al 64 O 384]-FAU Containing Sn 5 12+ , Sn 2 Cl 3+ , and Sn 3 Cl 5+. *J. Phys. Chem. C* **2016**, *121* (1), 471–480. https://doi.org/10.1021/acs.jpcc.6b10811.
(296) Knudsen, N.; Andersen, E. K.; Andersen, I. G. K.; Norby, P.; Skou, E. Tin-Zeolites, Syntheses and Ionic Conductivity. *Solid State Ion.* **1993**, *61*, 153–161. https://doi.org/10.1111/jeb.13136.
(297) Knudsen, N.; Andersen, E. K.; Andersen, I. G. K.; Skou, E. Tin-Mordenites, Syntheses and Ionic Conductivity. *Solid State Ion.* **1989**, *35* (1–2), 51–55. https://doi.org/10.1016/0167-2738(89)90011-8.
(298) Kosmulski, M.; Mączka, E. Novel Route of Synthesis of Sn-Coated SBA-15. *J. Porous Mater.* **2019**, *26* (3), 803–811. https://doi.org/10.1007/s10934-018-0681-5.
(299) Lefebvre, F.; Basset, J. M. Surface Organometallic Chemistry of Tin, Germanium and Arsenic. *Main Group Met. Chem.* **2002**, *25* (1–2), 15–32. https://doi.org/10.1515/MGMC.2002.25.1-2.15.

(300) Mal, N. K.; Bhaumik, A.; Ramaswamy, V.; Belhekar, A. A.; Ramaswamy, A. V. Synthesis of Al-Free Sn-Containing Molecular Sieves of MFI, MEL and MTWtypes and Their Catalytic Activity in Oxidation Reactions. *Stud. Surf. Sci. Catal.* **1995**, *94* (C), 317–324. https://doi.org/10.1016/S0167-2991(06)81238-3.
(301) Mal, N. K.; Ramaswamy, V.; Ganapathy, S.; Ramaswamy, A. V. Synthesis and Characterization of Crystalline, Tin-Silicate Molecular Sieves with MFI Structure. *J. Chem. Soc. Chem. Commun.* **1994**, No. 17, 1933–1934. https://doi.org/10.1039/C39940001933.
(302) Nemeth, L.; Moscoso, J.; Erdman, N.; Bare, S. R.; Oroskar, A.; Kelly, S. D.; Corma, A.; Valencia, S.; Renz, M. Synthesis and Characterization of Sn-Beta as a Selective Oxidation Catalyst. **2004**, *154*, 2626–2631.
(303) Niphadkar, P. S.; Kotwal, M. S.; Deshpande, S. S.; Bokade, V. V.; Joshi, P. N. Tin-Silicalite-1: Synthesis by Dry Gel Conversion, Characterization and Catalytic Performance in Phenol Hydroxylation Reaction. *Mater. Chem. Phys.* **2009**, *114* (1), 344–349. https://doi.org/10.1016/j.matchemphys.2008.09.026.
(304) Pang, J.; Zheng, M.; Li, X.; Song, L.; Sun, R.; Sebastian, J.; Wang, A.; Wang, J.; Wang, X.; Zhang, T. Catalytic Conversion of Carbohydrates to Methyl Lactate Using Isolated Tin Sites in SBA-15. *ChemistrySelect* **2017**, *2* (1), 309–314. https://doi.org/10.1002/slct.201601752.
(305) Ren, L.; Guo, Q.; Orazov, M.; Xu, D.; Politi, D.; Kumar, P.; Alhassan, S. M.; Mkhoyan, K. A.; Sidiras, D.; Davis, M. E.; Tsapatsis, M. Pillared Sn-MWW Prepared by a Solid-State -Exchange Method and Its Use as a Lewis Acid Catalyst. *ChemCatChem* **2016**, *8* (7), 1274–1278. https://doi.org/10.1002/cctc.201600120.
(306) Santos, T. G.; Silva, A. O. S.; Meneghetti, S. M. P. Comparison of the Hydrothermal Syntheses of Sn-Magadiite Using Na2SnO3 and SnCl4·5H2O as the Precursors. *Appl. Clay Sci.* **2019**, *183* (May), 105293. https://doi.org/10.1016/j.clay.2019.105293.
(307) Sasidharan, M.; Kiyozumi, Y.; Mal, N. K.; Paul, M.; Rajamohanan, P. R.; Bhaumik, A. Incorporation of Tin in Different Types of Pores in SBA-15: Synthesis, Characterization and Catalytic Activity. *Microporous Mesoporous Mater.* **2009**, *126* (3), 234–244. https://doi.org/10.1016/j.micromeso.2009.05.038.
(308) Selvaraj, M.; Kawi, S. Effect of Tin Precursors and Crystallization Temperatures on the Synthesis of SBA-15 with High Levels of Tetrahedral Tin. *J. Mater. Chem.* **2007**, *17* (34), 3610–3621. https://doi.org/10.1039/b706647c.
(309) Shah, A. K.; Khan, N. U. H.; Sethia, G.; Saravanan, S.; Kureshy, R. I.; Abdi, S. H. R.; Bajaj, H. C. Tin Exchanged Zeolite as Catalyst for Direct Synthesis of α-Amino Nitriles under Solvent-Free Conditions. *Appl. Catal. Gen.* **2012**, *419–420*, 22–30. https://doi.org/10.1016/j.apcata.2012.01.001.
(310) Shah, P.; Ramaswamy, A. V.; Ramaswamy, V. Influence of Sn- and Al- Metal Sources on Post-Synthesis Modification of Mesoporous SBA-15 Molecular Sieves. *Stud. Surf. Sci. Catal.* **2005**, *158 A*, 565–572. https://doi.org/10.1016/s0167-2991(05)80386-6.
(311) Shahami, M.; Ransom, R.; Shantz, D. F. Synthesis and Characterization of Tin, Tin/Aluminum, and Tin/Boron Containing MFI Zeolites. *Microporous Mesoporous Mater.* **2017**, *251*, 165–172. https://doi.org/10.1016/j.micromeso.2017.05.049.
(312) Skeels, G. W.; Flanigen, E. M. Zeolite Chemistry VII-Framework Substitution for Aluminum in Zeolites via Secondary Synthesis Treatment. *Zeolites Facts Fig. Future* **1989**, No. 1, 1223–1231.

(313) Skoda, D.; Styskalik, A.; Moravec, Z.; Bezdicka, P.; Bursik, J.; Mutin, P. H.; Pinkas, J. Mesoporous SnO2-SiO2 and Sn-Silica-Carbon Nanocomposites by Novel Non-Hydrolytic Templated Sol-Gel Synthesis. *RSC Adv.* **2016**, *6* (73), 68739–68747. https://doi.org/10.1039/c6ra16556g.
(314) Sushkevich, V. L.; Kots, P. A.; Kolyagin, Y. G.; Yakimov, A. V.; Marikutsa, A. V.; Ivanova, I. I. Origin of Water-Induced Brønsted Acid Sites in Sn BEA Zeolites. *J. Phys. Chem. C* **2019**, *123* (9), 5540–5548. https://doi.org/10.1021/acs.jpcc.8b12462.
(315) Tolborg, S.; Katerinopoulou, A.; Falcone, D. D.; Sádaba, I.; Osmundsen, C. M.; Davis, R. J.; Taarning, E.; Fristrup, P.; Holm, M. S. Incorporation of Tin Affects Crystallization, Morphology, and Crystal Composition of Sn-Beta. *J. Mater. Chem. A* **2014**, *2* (47), 20252–20262. https://doi.org/10.1039/c4ta05119j.
(316) van Grieken, R.; Martos, C.; Sánchez-Sánchez, M.; Serrano, D. P.; Melero, J. A.; Iglesias, J.; Cubero, A. G. Synthesis of Sn-Silicalite from Hydrothermal Conversion of SiO2-SnO2 Xerogels. *Microporous Mesoporous Mater.* **2009**, *119* (1–3), 176–185. https://doi.org/10.1016/j.micromeso.2008.10.020.
(317) Wang, X. X.; de Mallmann, A.; Bayard, F.; Lefebvre, F.; Basset, J. M. Study of the Reaction of Tetramethyltin with H-Faujasite. Characterization of the Grafted Species and Thermal Stability. *Microporous Mesoporous Mater.* **2003**, *63* (1–3), 147–161. https://doi.org/10.1016/S1387-1811(03)00459-1.
(318) Calculations - 2390 Gemini VII Keypad.
(319) Brunauer, S.; Emmett, P. H.; Teller, E. Adsorption of Gases in Multimolecular Layers. *J. Am. Chem. Soc.* **1938**, *60* (2), 309–319. https://doi.org/10.1021/ja01269a023.
(320) Alper, J. *The Changing Landscape of Hydrocarbon Feedstocks for Chemical Production: Implications for Catalysis: Proceedings of a Workshop*; 1344369; 2016; p 1344369. https://doi.org/10.2172/1344369.
(321) Deng, L.; Shishido, T.; Teramura, K.; Tanaka, T. Effect of Reduction Method on the Activity of Pt-Sn/SiO2 for Dehydrogenation of Propane. *Catal. Today* **2014**, *232*, 33–39. https://doi.org/10.1016/j.cattod.2013.10.064.
(322) Deng, L.; Liu, X.; Wu, Z.; Xu, J.; Zhou, Z.; Xu, M. Effects of Synthesis Procedures on Pt–Sn Alloy Formation and Their Catalytic Activity for Propane Dehydrogenation. *Catal. Lett.* **2023**. https://doi.org/10.1007/s10562-022-04263-1.
(323) Prakash, N.; Lee, M. H.; Yoon, S.; Jung, K. D. Role of Acid Solvent to Prepare Highly Active PtSn/Θ-Al2O3 Catalysts in Dehydrogenation of Propane to Propylene. *Catal. Today* **2017**, *293–294*, 33–41. https://doi.org/10.1016/j.cattod.2017.02.027.
(324) Saerens, S.; Sabbe, M. K.; Galvita, V. V.; Redekop, E. A.; Reyniers, M. F.; Marin, G. B. The Positive Role of Hydrogen on the Dehydrogenation of Propane on Pt(111). *ACS Catal.* **2017**, *7* (11), 7495–7508. https://doi.org/10.1021/acscatal.7b01584.
(325) Hook, A.; Massa, J. D.; Celik, F. E. Effect of Tin Coverage on Selectivity for Ethane Dehydrogenation over Platinum-Tin Alloys. *J. Phys. Chem. C* **2016**, *120* (48), 27307–27318. https://doi.org/10.1021/acs.jpcc.6b08407.
(326) Lian, Z.; Ali, S.; Liu, T.; Si, C.; Li, B.; Su, D. S. Revealing the Janus Character of the Coke Precursor in the Propane Direct Dehydrogenation on Pt Catalysts from a kMC Simulation. *ACS Catal.* **2018**, *8* (5), 4694–4704. https://doi.org/10.1021/acscatal.8b00107.
(327) Huang, H.; Nassr, A. B. A. A.; Celorrio, V.; Gianolio, D.; Hardacre, C.; Brett, D. J. L.; Russell, A. E. Contrasting the EXAFS Obtained under Air and H2environments to Reveal

Details of the Surface Structure of Pt-Sn Nanoparticles. *Phys. Chem. Chem. Phys.* **2021**, *23* (20), 11738–11745. https://doi.org/10.1039/d1cp00979f.
(328) Salmones, J.; Wang, J. A.; Galicia, J. A.; Aguilar-Rios, G. H2 Reduction Behaviors and Catalytic Performance of Bimetallic Tin-Modified Platinum Catalysts for Propane Dehydrogenation. *J. Mol. Catal. Chem.* **2002**, *184* (1–2), 203–213. https://doi.org/10.1016/S1381-1169(01)00525-8.
(329) Qi, L.; Zhang, Y.; Babucci, M.; Chen, C.; Lu, P.; Li, J.; Dun, C.; Hoffman, A. S.; Urban, J. J.; Tsapatsis, M.; Bare, S. R.; Han, Y.; Gates, B. C.; Bell, A. T. Dehydrogenation of Propane and n -Butane Catalyzed by Isolated PtZn 4 Sites Supported on Self-Pillared Zeolite Pentasil Nanosheets. *ACS Catal.* **2022**, 11177–11189. https://doi.org/10.1021/acscatal.2c01631.
(330) Nakaya, Y.; Hayashida, E.; Asakura, H.; Takakusagi, S.; Yasumura, S.; Shimizu, K.; Furukawa, S. High-Entropy Intermetallics Serve Ultrastable Single-Atom Pt for Propane Dehydrogenation. *J. Am. Chem. Soc.* **2022**, *144* (35), 15944–15953. https://doi.org/10.1021/jacs.2c01200.
(331) Buzzoni, R.; Bordiga, S.; Ricchiardi, G.; Lamberti, C.; Zecchina, A.; Bellussi, G. Interaction of Pyridine with Acidic (H-ZSM5, H-β, H-MORD Zeolites) and Superacidic (H-Nafion Membrane) Systems: An IR Investigation. *Langmuir* **1996**, *12* (4), 930–940. https://doi.org/10.1021/la950571i.
(332) Mesa, M.; Ramírez, A.; Guth, J. L.; Sierra, L. Adaptation of Silanol Groups in Mesoporous Silica to Be Silylated and Their Evaluation by FTIR. *Stud. Surf. Sci. Catal.* **2004**, *154 A*, 562–567. https://doi.org/10.1016/s0167-2991(04)80851-6.
(333) Zholobenko, V. L.; Makarova, M. A.; Dwyer, J. Inhomogeneity of Brönsted Acid Sites in H-Mordenite. *J. Phys. Chem.* **1993**, *97* (22), 5962–5964. https://doi.org/10.1021/j100124a030.
(334) Sun, L.; Chai, Y.; Dai, W.; Wu, G.; Guan, N.; Li, L. Oxidative Dehydrogenation of Propane over Pt-Sn/Si-Beta Catalysts: Key Role of Pt-Sn Interaction. *Catal. Sci. Technol.* **2018**, *8* (12), 3044–3051. https://doi.org/10.1039/c8cy00712h.
(335) Virnovskaia, A.; Rytter, E.; Olsbye, U. Kinetic and Isotopic Study of Ethane Dehydrogenation over a Semicommercial Pt,Sn/Mg(Al)O Catalyst. *Ind. Eng. Chem. Res.* **2008**, *47* (19), 7167–7177. https://doi.org/10.1021/ie800361a.
(336) Thang, H. V.; Pacchioni, G.; DeRita, L.; Christopher, P. Nature of Stable Single Atom Pt Catalysts Dispersed on Anatase TiO2. *J. Catal.* **2018**, *367*, 104–114. https://doi.org/10.1016/j.jcat.2018.08.025.
(337) Miao, C.; Liu, M.; Tan, S.; Zhang, G.; Chu, S.; Song, S.; Zhang, Q.; Yu, J.; Jiang, G.; Song, W.; He, Q.; Luo, W.; Wu, Z. Pt–Sn Nanoalloys on Sn-Beta Zeolite for Efficient Propane Dehydrogenation. *Microporous Mesoporous Mater.* **2023**, *361*, 112736. https://doi.org/10.1016/j.micromeso.2023.112736.
(338) Shahid, G.; Sheppard, N. Infrared Spectra and the Structures of the Chemisorbed Species Resulting from the Adsorption of Propene and Propane on a Pt/SiO2 Catalyst. *Spectrochim. Acta Part Mol. Spectrosc.* **1990**, *46* (6), 999–1010. https://doi.org/10.1016/0584-8539(90)80017-S.
(339) Chesters, M. A.; Gardner, P.; Mccash, E. M. *THE REFLECTION-ABSORPTION INFRARED SPECTRA OF n-ALKANES ADSORBED ON Pt(Ll1)*; 1989; Vol. 209, pp 89–99.

(340) Shimanouchi, T. *Tables of Molecular Vibrational Frequencies, Consolidated Volume i*, 0 ed.; NBS NSRDS 39; National Bureau of Standards: Gaithersburg, MD, 1972; p NBS NSRDS 39. https://doi.org/10.6028/NBS.NSRDS.39.
(341) Bulánek, R.; Koudelková, E.; Solanea De Oliveira Ramos, F.; Trachta, M.; Bludský, O.; Rubeš, M.; Čejka, J. Experimental and Theoretical Study of Propene Adsorption on Alkali Metal Exchanged FER Zeolites. *Microporous Mesoporous Mater.* **2019**, *280*, 203–210. https://doi.org/10.1016/j.micromeso.2019.02.003.
(342) Sverdlov, L. M.; Kovner, M. A.; Kraĭnov, E. P. *Vibrational Spectra of Polyatomic Molecules*; Wiley: New York, 1973.
(343) Mériaudeau, P.; Thangaraj, A.; Dutel, J. F.; Naccache, C. Studies on PtxSnyBimetallics in NaY. II. Further Characterization and Catalytic Properties in the Dehydrogenation and Hydrogenolysis of Propane. *J. Catal.* **1997**, *167* (1), 180–186. https://doi.org/10.1006/jcat.1997.1531.
(344) Larsson, M.; Henriksson, N.; Andersson, B. Investigation of the Kinetics of a Deactivating System by Transient Experiments. *Appl. Catal. Gen.* **1998**, *166* (1), 9–19. https://doi.org/10.1016/S0926-860X(97)00233-0.
(345) Lobera, M. P.; Téllez, C.; Herguido, J.; Menéndez, M. Transient Kinetic Modelling of Propane Dehydrogenation over a Pt-Sn-K/Al2O3 Catalyst. *Appl. Catal. Gen.* **2008**, *349* (1–2), 156–164. https://doi.org/10.1016/j.apcata.2008.07.025.
(346) Biloen, P.; Dautzenberg, F. M.; Sachtler, W. M. H. Catalytic Dehydrogenation of Propane to Propene over Platinum and Platinum-Gold Alloys. *J. Catal.* **1977**, *50* (1), 77–86. https://doi.org/10.1016/0021-9517(77)90010-0.
(347) Zhang, W.; Wang, H.; Jiang, J.; Sui, Z.; Zhu, Y.; Chen, D.; Zhou, X. Size Dependence of Pt Catalysts for Propane Dehydrogenation: From Atomically Dispersed to Nanoparticles. *ACS Catal.* **2020**, 12932–12942. https://doi.org/10.1021/acscatal.0c03286.
(348) Liu, Y.; Zong, X.; Patra, A.; Caratzoulas, S.; Vlachos, D. G. Propane Dehydrogenation on $Pt_x Sn_y$ ($x, y \leq 4$) Clusters on Al_2O_3 (110). *ACS Catal.* **2023**, *13* (5), 2802–2812. https://doi.org/10.1021/acscatal.2c05671.
(349) Corella, J.; Asua, J. M.; Bilbao, J. Kinetics of Catalyst Deactivation. *Can. J. Chem. Eng.* **1981**, *59* (5), 647–647. https://doi.org/10.1002/cjce.5450590517.
(350) Sheintuch, M.; Liron, O.; Ricca, A.; Palma, V. Propane Dehydrogenation Kinetics on Supported Pt Catalyst. *Appl. Catal. Gen.* **2016**, *516*, 17–29. https://doi.org/10.1016/j.apcata.2016.02.009.
(351) Komasi, M.; Fatemi, S.; Mousavi, S. H. Kinetic Modelling of Propane Dehydrogenation over a Pt-Sn/Hierarchical SAPO-34 Zeolite Catalyst, Including Catalyst Deactivation. *Prog. React. Kinet. Mech.* **2017**, *42* (4), 344–360. https://doi.org/10.3184/146867817X14954764850397.
(352) Li, Q.; Sui, Z.; Zhou, X.; Zhu, Y.; Zhou, J.; Chen, D. Coke Formation on Pt-Sn/Al2O3 Catalyst in Propane Dehydrogenation: Coke Characterization and Kinetic Study. *Top. Catal.* **2011**, *54* (13–15), 888–896. https://doi.org/10.1007/s11244-011-9708-8.
(353) Zhu, J.; Yang, M. L.; Yu, Y.; Zhu, Y. A.; Sui, Z. J.; Zhou, X. G.; Holmen, A.; Chen, D. Size-Dependent Reaction Mechanism and Kinetics for Propane Dehydrogenation over Pt Catalysts. *ACS Catal.* **2015**, *5* (11), 6310–6319. https://doi.org/10.1021/acscatal.5b01423.
(354) Palfi, S. Calorimetric Studies of Hydrocarbon Adsorption on Metal Films V. Hydrocarbons on Platinum. *J. Catal.* **1984**, *88* (2), 300–312. https://doi.org/10.1016/0021-9517(84)90006-X.

(355) Li, B.; Xu, Z.; Chu, W.; Luo, S.; Jing, F. Ordered Mesoporous Sn-SBA-15 as Support for Pt Catalyst with Enhanced Performance in Propane Dehydrogenation. *Cuihua XuebaoChinese J. Catal.* **2017**, *38* (4), 726–735. https://doi.org/10.1016/S1872-2067(17)62805-5.
(356) Fan, X.; Li, J.; Zhao, Z.; Wei, Y.; Liu, J.; Duan, A.; Jiang, G. Dehydrogenation of Propane over PtSn/SBA-15 Catalysts: Effect of the Amount of Metal Loading and State. *RSC Adv.* **2015**, *5* (36), 28305–28315. https://doi.org/10.1039/c5ra01480h.
(357) Pham, H. N.; Sattler, J. J. H. B.; Weckhuysen, B. M.; Datye, A. K. Role of Sn in the Regeneration of Pt/γ-Al2O3 Light Alkane Dehydrogenation Catalysts. *ACS Catal.* **2016**, *6* (4), 2257–2264. https://doi.org/10.1021/acscatal.5b02917.
(358) Xiong, H.; Lin, S.; Goetze, J.; Pletcher, P.; Guo, H.; Kovarik, L.; Artyushkova, K.; Weckhuysen, B. M.; Datye, A. K. Thermally Stable and Regenerable Platinum–Tin Clusters for Propane Dehydrogenation Prepared by Atom Trapping on Ceria. *Angew. Chem. - Int. Ed.* **2017**, *56* (31), 8986–8991. https://doi.org/10.1002/anie.201701115.
(359) Andy, P.; Davis, M. E. Dehydrogenation of Propane over Platinum Containing CIT-6. *Ind. Eng. Chem. Res.* **2004**, *43* (12), 2922–2928. https://doi.org/10.1021/ie030357m.
(360) Zhang, Y.; Zhou, Y.; Liu, H.; Wang, Y.; Xu, Y.; Wu, P. Effect of La Addition on Catalytic Performance of PtSnNa / ZSM-5 Catalyst for Propane Dehydrogenation. *Appl. Catal.* **2007**, *333* (2), 202–210. https://doi.org/10.1016/j.apcata.2007.07.049.
(361) Motagamwala, A. H.; Almallahi, R.; Wortman, J.; Igenegbai, V. O.; Linic, S. Stable and Selective Catalysts for Propane Dehydrogenation Operating at Thermodynamic Limit. *Science* **2021**, *373* (6551), 217–222. https://doi.org/10.1126/science.abg7894.
(362) Zhang, Y.; Zhou, Y.; Huang, L.; Xue, M.; Zhang, S. Sn-Modified ZSM-5 As Support for Platinum Catalyst in Propane Dehydrogenation. *Ind. Eng. Chem. Res.* **2011**, *50* (13), 7896–7902. https://doi.org/10.1021/ie1024694.
(363) J, C. J. A. J. B. KINETICS OF CATALYST DEACTIVATION. *CAN J CHEM ENG ISSN 0008-4034 CAN 1981 VOL 59 NO 5 PP 647-648 BIBL 37 REF* **1981**.
(364) Gómez-Quero, S.; Tsoufis, T.; Rudolf, P.; Makkee, M.; Kapteijn, F.; Rothenberg, G. Kinetics of Propane Dehydrogenation over Pt-Sn/Al2O3. *Catal. Sci. Technol.* **2013**, *3* (4), 962–971. https://doi.org/10.1039/c2cy20488f.
(365) Duan, Y.; Zhou, Y.; Zhang, Y.; Sheng, X.; Xue, M. Effect of Sodium Addition to PtSn/AlSBA-15 on the Catalytic Properties in Propane Dehydrogenation. *Catal. Lett.* **2011**, *141* (1), 120–127. https://doi.org/10.1007/s10562-010-0445-6.
(366) Shi, L.; Deng, G. M.; Li, W. C.; Miao, S.; Wang, Q. N.; Zhang, W. P.; Lu, A. H. Al2O3 Nanosheets Rich in Pentacoordinate Al3+ Ions Stabilize Pt-Sn Clusters for Propane Dehydrogenation. *Angew. Chem. - Int. Ed.* **2015**, *54* (47), 13994–13998. https://doi.org/10.1002/anie.201507119.
(367) Stability and Regeneration of Supported PtSn Catalysts for Dehydrogenation.